

**THE INFLUENCE OF ACCEPTOR DOPING,  
STOICHIOMETRY AND PROCESSING ON THE  
MECHANICAL PROPERTIES AND  
MICROSTRUCTURE OF PZT CERAMICS**

by

**MARTIN ŠAFÁŘ**

A thesis submitted to the University of Birmingham

for the degree of

**DOCTOR OF PHILOSOPHY**

School of Metallurgy and Materials

College of Engineering and Physical science

University of Birmingham

June 2019

UNIVERSITY OF  
BIRMINGHAM

**University of Birmingham Research Archive**

**e-theses repository**

This unpublished thesis/dissertation is copyright of the author and/or third parties. The intellectual property rights of the author or third parties in respect of this work are as defined by The Copyright Designs and Patents Act 1988 or as modified by any successor legislation.

Any use made of information contained in this thesis/dissertation must be in accordance with that legislation and must be properly acknowledged. Further distribution or reproduction in any format is prohibited without the permission of the copyright holder.

## **ABSTRACT**

Lead zirconium titanate (PZT) is the most widely used ferroelectric ceramic material on the market. The majority of published research revolves around its piezoelectric and dielectric properties. This thesis is focused on the complex dependencies between the material's composition ( $\text{Sr}^{2+}$ ,  $\text{Fe}^{3+}$  doping and Zr/Ti ratio), microstructure, structure, physical, functional and mechanical properties. The goal was to identify the most important strength-controlling factors to create stronger and more reliable PZT products and reduce their manufacturing waste.

PZT specimens were prepared from metal oxides using an optimised conventional powder processing route and industrial processing parameters. Fracture strength was tested under equibiaxial flexural stress using a custom-designed ring-on-ring fixture and the results were evaluated using a 2-parameter Weibull distribution. Large pores and machining-induced damage were identified as the weakest flaws. The pore size distribution was affected by all studied factors. The most notable increase in strength was caused by the acceptor doping, which was linked to the changes in grain boundary strength; and by an increase in the sintering temperature (for pure PZT). The strength of the acceptor-doped PZT showed no significant change with Zr/Ti ratio or sintering temperature, unlike the undoped PZT.

## **ACKNOWLEDGMENTS**

I would like to express my most sincere gratitude to Prof. Tim W. Button for giving me the opportunity to work on this research project, for providing excellent academic guidance and for his patience and encouragement. I would also like to thank the University of Birmingham and CTS Corporation for their generous financial and material support and Dr Hana Hughes for making this project possible.

To members of the Research and Development team in Hradec Králové branch of CTS Corporation: Dr Marek Žabčík, Dr Ivana Steinfeldová, Ing. Lukáš Rusyniak, Mrs Dana Andrová and Mrs Vladimíra Krátká. Thank you for all your help over the years and all the knowledge you shared with me. I am also very grateful to Mr Bořivoj Tylš for helping me make the fixture for mechanical tests and to Ing. Miroslav Boudyš, CSc. for his valuable feedback.

I want to thank all my colleagues at the Functional Materials Group at the University of Birmingham for their encouragement and for all the discussions and meals we shared. A special thanks goes to the best technician in the world, Mr Carl Meggs, who was incredibly helpful and supportive.

I am very thankful to Dr Roger Morrell and Dr Mark Stewart from the National Physical Laboratory and Dr Antonio Feteira from the University of Sheffield for providing equipment for some of my measurements. I would further like to thank Prof. Doru Lupascu from the University of Duisburg-Essen for his useful comments and suggestions.

I must acknowledge Dr Xinyu Lu, who carried out the nanoscale observations and microscale fracture toughness tests and Dr Richard Hood, who performed some of the parallelism and flatness measurements.

Finally, I would like to thank my parents who have always encouraged me in whatever endeavour I wanted to undertake.

# TABLE OF CONTENTS

<b>1</b>	<b>Introduction .....</b>	<b>1</b>
<b>2</b>	<b>Technical background and literature review .....</b>	<b>3</b>
2.1	Mechanical properties of polycrystalline ceramics.....	3
2.1.1	Failure.....	4
2.1.2	Influence of microstructure on mechanical properties .....	9
2.2	Ferroelectrics .....	12
2.3	Piezoelectric, dielectric properties.....	14
2.4	Fracture mechanics of ferroelectrics.....	17
2.5	PZT .....	20
2.5.1	Structure and composition.....	20
2.5.2	Doping.....	26
2.5.3	Processing methods .....	30
2.5.4	Microstructure and mechanical properties .....	32
2.5.4.1	Microstructure .....	33
2.5.4.2	Mechanical properties .....	35
<b>3</b>	<b>Motivation and Objectives.....</b>	<b>39</b>
<b>4</b>	<b>Experimental methods .....</b>	<b>42</b>
4.1	Physical, structural and microstructural properties.....	42
4.1.1	Mass, density, dimensions, flatness, parallelism.....	42
4.1.2	Particle size.....	44
4.1.3	Powder X-ray diffraction.....	44
4.1.4	Pore size distribution .....	49
4.1.5	Grain size.....	50
4.1.6	Nanoscale observations .....	51

4.2	Mechanical properties .....	52
4.2.1	Surface roughness.....	52
4.2.2	Hardness .....	52
4.2.3	Elastic modulus and Poisson's ratio .....	54
4.2.4	Mechanical strength.....	56
4.2.4.1	Design of fixture used for the ROR equibiaxial flexural strength test.....	56
4.2.4.2	Testing procedure .....	60
4.2.4.3	Fractography .....	62
4.2.4.4	Fixture design optimisation.....	63
4.2.4.5	Validation of fixture used for ROR equibiaxial flexural strength test.....	67
4.2.5	Microscale fracture toughness .....	72
4.3	Piezoelectric and dielectric properties .....	74
<b>5</b>	<b>Sample preparation .....</b>	<b>77</b>
5.1	Processing optimization.....	77
5.1.1	Duration of 2 <sup>nd</sup> milling .....	78
5.1.2	Binder mixing.....	80
5.1.3	Sintering .....	83
5.1.4	Annealing .....	88
5.2	List of compositions.....	91
5.3	Optimised sample preparation .....	94
5.4	Processing results.....	98
5.4.1	Particle size distribution of calcined powders .....	98
5.4.2	Weight loss after calcination, burnout and sintering.....	100
5.4.3	Flatness, parallelism .....	103
<b>6</b>	<b>Physical properties .....</b>	<b>105</b>

6.1	Grain size .....	105
6.2	Relative density.....	108
6.3	Thickness shrinkage.....	112
6.4	Pore size distribution .....	114
6.5	Phase content and tetragonal unit cell distortion .....	131
6.6	Nanoscale homogeneity of Fe-doped sample .....	140
6.7	Summary.....	152
<b>7</b>	<b>Piezoelectric and dielectric properties.....</b>	<b>155</b>
7.1	Sintering temperature.....	155
7.2	Sr content .....	159
7.3	Fe content.....	162
7.4	Zr/Ti ratio.....	165
7.5	Summary.....	169
<b>8</b>	<b>Mechanical properties.....</b>	<b>171</b>
8.1	Elastic modulus.....	171
8.2	Hardness.....	177
8.3	Surface roughness .....	181
8.4	Equibiaxial flexural strength.....	185
8.4.1	Test sequence plots.....	186
8.4.2	Histograms.....	190
8.4.3	Fractography.....	193
8.4.4	Sintering temperature dependence .....	201
8.4.4.1	Probability distributions and fractography (0 at% Fe).....	201
8.4.4.2	Probability distributions and fractography (1.4 at% Fe).....	208
8.4.4.3	Weibull strength and reliability.....	212

8.4.5	Strontium doping dependence .....	216
8.4.5.1	Probability distributions and fractography .....	216
8.4.5.2	Weibull strength and reliability .....	219
8.4.6	Zr/Ti ratio dependence .....	221
8.4.6.1	Probability distributions and fractography (0 at% Fe) .....	221
8.4.6.2	Probability distributions and fractography (1.4 at% Fe) .....	225
8.4.6.3	Weibull strength and reliability .....	229
8.4.7	Iron doping dependence .....	234
8.4.7.1	Probability distributions and fractography .....	234
8.4.7.2	Weibull strength and reliability .....	237
8.4.8	Commercial material .....	240
8.4.8.1	Physical and mechanical properties excluding strength .....	240
8.4.8.2	Strength .....	244
8.4.9	Ferroelastic effects .....	251
8.4.10	General discussion .....	258
8.5	Microscale fracture toughness .....	272
8.6	Summary .....	275
<b>9</b>	<b>Conclusions .....</b>	<b>280</b>
<b>10</b>	<b>Future work .....</b>	<b>286</b>
	<b>Appendix I. Strength test sequence plots .....</b>	<b>288</b>
	<b>Appendix II. Strength histograms .....</b>	<b>292</b>
	<b>List of references .....</b>	<b>296</b>

## LIST OF FIGURES

Figure 2-1 Representative Weibull plot of a ceramic material.....	6
Figure 2-2 Typical dependence of crack growth ( $v$ ) on toughness ( $K_I$ ) for slow crack growth, reproduced from [13]. .....	8
Figure 2-3 Notation of axes of poled piezoelectric materials.....	15
Figure 2-4 Schematic diagram of planar vibrations $S$ in the 1-2 plane of a poled piezoelectric disc induced by an electric field $E$ in the 3-direction. ....	16
Figure 2-5 A representative stress-strain curve of a poled ferroelectric material. A-B and D-E are linearly elastic parts, B-D is a non-linear part due to ferroelastic domain switching. Upon unloading, the switching is either reversible (E-A) or irreversible (E-F). (reproduced from [30]).....	17
Figure 2-6 Illustration of a) domain switching induced by an opening crack; b) rising R-curve caused by compressive stresses created by process zone left in the wake of the crack (reproduced from [31]).....	18
Figure 2-7 A cubic perovskite unit cell of PZT illustrating a) 6-fold coordination of $Zr^{4+}/Ti^{4+}$ and b) 12-fold coordination of $Pb^{2+}$ (reproduced from [33]).....	20
Figure 2-8 Phase diagram of $Pb(Zr,Ti)O_3$ reproduced from the work of Zhang et al. [38]. $T_C$ = Curie temperature; $M_A$ , $M_B$ = two modifications of a monoclinic phase found in minor concentrations in indicated areas. ....	22
Figure 2-9 Dependence of relative permittivity ( $\epsilon_r$ ) and planar coupling factor ( $k_p$ ) on the Zr/Ti ratio showing a maximum at the morphotropic phase boundary (reproduced from [25]). ....	22
Figure 2-10 A cubic cell with directions in which it distorts to achieve tetragonal (T), rhombohedral (R) or orthorhombic (O) symmetry. $M_A$ , $M_B$ and $M_C$ distortions illustrate possible intermediate monoclinic phases. (reproduced from [43]).....	25
Figure 2-11 The dependence of tetragonal and rhombohedral unit cell distortion on the Zr/Ti ratio (reproduced from [25]). .....	25

Figure 2-12 Dependence of relative permittivity of $\text{Pb}(\text{Zr}_x\text{Ti}_{1-x})\text{O}_3$ on $x$ in pure PZT (1) and PZT doped with: 1 mol% $\text{Nd}_2\text{O}_3$ (2), 2 mol% $\text{Nd}_2\text{O}_3$ (3), 3 mol% $\text{Nd}_2\text{O}_3$ (4), 1 mol% $\text{Nb}_2\text{O}_5$ (5), 0.8 mol% $\text{Fe}_2\text{O}_3$ (6) and 1.25 mol% $\text{Cr}_2\text{O}_3$ (7) published by Thomann [65] and taken from [33].	29
Figure 4-1 Schematic of thickness measurement points.	43
Figure 4-2 Example of fitted diffraction pattern (batch 13). Crosses represent acquired data, dashed lines individual peak fits and full line their combination.	46
Figure 4-3 Image processing using ImageJ: a) original optical micrograph of the polished surface, b) thresholded image, c) outlines of analysed pores	49
Figure 4-4 Maximum Feret diameter measured on a non-equiaxed pore.	50
Figure 4-5 Thin section cut by PFIB and used for nanoscale observations.	51
Figure 4-6 Preliminary Vickers hardness (HV1/10) results for various levels of doping, loads and diagonal length measuring techniques. Error bars represent the standard deviation of mean (SDM).	53
Figure 4-7 Test apparatus for excitation and measurement of vibrations.	54
Figure 4-8 Fixture for equibiaxial strength test. Legend: 1 – top block, 2 – connector, 3 – ball bearing, 4 – load ring, 5 – test piece, 6 – support ring, 7 – bottom block.	57
Figure 4-9 Radial stress distribution on the tensile side of a disc loaded in a ring-on-ring equibiaxial flexural strength test (reproduced from [115]). The load ring diameter is 1 mm. Solid line represents an analytical solution of equations derived from the simple plate theory. Squares and dashed line show the radial stress distribution calculated by the 2D finite element analysis for symmetrical and asymmetrical loading conditions respectively.	57
Figure 4-10 Workflow for choosing ring and test-piece dimensions (from [15]), where $t$ = sample thickness (mm), $d_s$ = support ring diameter (mm), $d_L$ = load ring diameter (mm), $r_{tip}$ = support/load ring tip radius (mm), $\sigma_f$ = expected fracture strength (MPa), $Y$ = modulus of elasticity (MPa).	59

Figure 4-11 Sample arrangement prior to equibiaxial flexural strength test.....	61
Figure 4-12 Photograph of fractured sample (tensile side) with a) important features and support/load ring contact positions, b) quadrants used to classify fracture origin location. ....	63
Figure 4-13 a) Percentage of fracture origins located inside, above or outside the load ring, b) percentage of fracture origins located in each of the quadrants (see Figure 4-12). ....	65
Figure 4-14 a) first simple alignment sleeve, b) improved alignment sleeve with alignment screws, c) screw used for attaching the bottom block with support ring (with and without a shoulder), d) simple connector piece, e) connector piece with screw-on rings providing a rigid fixture-load frame connection.....	66
Figure 4-15 Weibull plot of AD-995 alumina tested in the ring-on-ring biaxial flexural strength test compared with the results of alumina tested in 4-point bend from the ARL report [123]. ....	71
Figure 4-16 SEM micrographs showing examples of fracture origins found in tested Al <sub>2</sub> O <sub>3</sub> specimens: a) Cluster of large grains, b) agglomerate likely coupled with machining damage on the surface.....	71
Figure 4-17 a) SEM micrograph of a cantilever used for nanoscale fracture toughness testing. <i>A, B, L, W</i> indicate dimensions of the pre-notch and the cantilever; <i>F</i> shows the loading direction. b) loading of the cantilever using a picoindenter (TEM micrograph).....	72
Figure 4-18 Impedance analysis arrangement. ....	75
Figure 5-1 Conventional powder processing route used in this work. ....	78
Figure 5-2 Particle size distribution curves of calcined hard doped PZT milled for 70 and 600 s. ....	79

Figure 5-3 SEM micrographs of polished surfaces of sintered hard PZT samples previously mixed with various amounts of binder (PVA-PEG-PMMA or DURAMAX) and using 2 different techniques (“DRY” and “WET”). See text for full details.....	82
Figure 5-4 Kingon and Clark’s crucible sintering arrangements reproduced from [143]. (A) was able to prevent PbO loss from the compact, while (B) resulted in a continuous loss of PbO.....	85
Figure 5-5 Schematics of the crucible arrangement for the sintering experiments.....	86
Figure 5-6 XRD patterns and ratios of (002) and (200) tetragonal peaks of a single specimen after various treatments. Note: powder was obtained by crushing and grinding a sintered sample. ....	90
Figure 5-7 Flowchart of prepared compositions of $(\text{Pb}_{1-x}\text{Sr}_x)(\text{Zr}_y\text{Ti}_{1-y})_{1-z}\text{Fe}_z\text{O}_3$ . ....	93
Figure 5-8 Schematics of 3-piece alumina crucible used for calcining and sintering.....	96
Figure 5-9 Particle size distribution curves of calcined powders milled for 2 min and grouped by Fe content.....	99
Figure 5-10 SEM micrographs of calcined and milled powders without and with Fe present (batches 4 and 13 respectively).....	100
Figure 5-11 Dependence of average weight loss of compacts after sintering on a) sintering temperature ( $T_{\text{sint}}$ ), b) Sr content, c) Zr/Ti ratio, d) Fe content of $(\text{Pb}_{1-x}\text{Sr}_x)(\text{Zr}_y\text{Ti}_{1-y})_{1-z}\text{Fe}_z\text{O}_3$ . Grey horizontal lines connect single central compositions, error bars represent SDM, $T_{\text{sint}} = 1310\text{ }^\circ\text{C}$ if not stated otherwise.....	102
Figure 5-12 Weight loss of individual samples in a stack of $(\text{Pb}_{0.95}\text{Sr}_{0.05})(\text{Zr}_{0.52}\text{Ti}_{0.48})_{0.986}\text{Fe}_{0.014}\text{O}_3$ (batch 15) after sintering at $1360\text{ }^\circ\text{C}$ . ....	103
Figure 6-1 Dependence of average grain size on a) sintering temperature ( $T_{\text{sint}}$ ), b) Sr content, c) Zr/Ti ratio, d) Fe content of $(\text{Pb}_{1-x}\text{Sr}_x)(\text{Zr}_y\text{Ti}_{1-y})_{1-z}\text{Fe}_z\text{O}_3$ . Grey horizontal lines connect single central compositions, error bars represent SDM, $T_{\text{sint}} = 1310\text{ }^\circ\text{C}$ if not stated otherwise. ....	106

Figure 6-2 Dependence of relative density on a) sintering temperature ( $T_{\text{sint}}$ ), b) Sr content, c) Zr/Ti ratio, d) Fe content of $(\text{Pb}_{1-x}\text{Sr}_x)(\text{Zr}_y\text{Ti}_{1-y})_{1-z}\text{Fe}_z\text{O}_3$ . Grey horizontal lines connect single central compositions, error bars represent SDM, $T_{\text{sint}} = 1310\text{ }^\circ\text{C}$ if not stated otherwise. ....	110
Figure 6-3 Dependence of thickness shrinkage of samples after sintering on a) sintering temperature ( $T_{\text{sint}}$ ), b) Sr content, c) Zr/Ti ratio, d) Fe content $(\text{Pb}_{1-x}\text{Sr}_x)(\text{Zr}_y\text{Ti}_{1-y})_{1-z}\text{Fe}_z\text{O}_3$ . Grey horizontal lines connect single central compositions, error bars represent SDM, $T_{\text{sint}} = 1310\text{ }^\circ\text{C}$ if not stated otherwise.....	113
Figure 6-4 Percentage of surface area covered by pores of a certain maximum Feret diameter in $(\text{Pb}_{0.95}\text{Sr}_{0.05})(\text{Zr}_{0.52}\text{Ti}_{0.48})\text{O}_3$ sintered at different temperatures. ....	117
Figure 6-5 Optical micrographs of polished surfaces of $(\text{Pb}_{0.95}\text{Sr}_{0.05})(\text{Zr}_{0.52}\text{Ti}_{0.48})\text{O}_3$ sintered at a) $1260\text{ }^\circ\text{C}$ , b) $1310\text{ }^\circ\text{C}$ , c) $1360\text{ }^\circ\text{C}$ . ....	118
Figure 6-6 Percentage of surface area covered by pores of a certain maximum Feret diameter in $(\text{Pb}_{0.95}\text{Sr}_{0.05})(\text{Zr}_{0.52}\text{Ti}_{0.48})_{0.986}\text{Fe}_{0.014}\text{O}_3$ sintered at different temperatures. ....	119
Figure 6-7 Optical micrographs of polished surfaces of $(\text{Pb}_{0.95}\text{Sr}_{0.05})(\text{Zr}_{0.52}\text{Ti}_{0.48})_{0.986}\text{Fe}_{0.014}\text{O}_3$ sintered at a) $1260\text{ }^\circ\text{C}$ , b) $1310\text{ }^\circ\text{C}$ , c) $1360\text{ }^\circ\text{C}$ . ....	120
Figure 6-8 Percentage of surface area covered by pores of a certain maximum Feret diameter in $(\text{Pb}_{1-x}\text{Sr}_x)(\text{Zr}_{0.52}\text{Ti}_{0.48})_{1-z}\text{Fe}_z\text{O}_3$ doped with various amount of Sr and Fe. ....	122
Figure 6-9 Optical micrographs of polished surfaces of $(\text{Pb}_{1-x}\text{Sr}_x)(\text{Zr}_{0.52}\text{Ti}_{0.48})_{1-z}\text{Fe}_z\text{O}_3$ doped with a) $x, z = 0$ ; b) $x = 0.05, z = 0$ ; c) $x = 0, z = 0.014$ ; d) $x = 0.05, z = 0.014$ ...	123
Figure 6-10 Percentage of surface area covered by pores of a certain maximum Feret diameter in $(\text{Pb}_{0.95}\text{Sr}_{0.05})(\text{Zr}_y\text{Ti}_{1-y})\text{O}_3$ with varying Zr/Ti fraction. ....	124
Figure 6-11 Optical micrographs of polished surfaces of $(\text{Pb}_{0.95}\text{Sr}_{0.05})(\text{Zr}_y\text{Ti}_{1-y})\text{O}_3$ with $y(\text{Zr}) =$ a) 0.49, b) 0.51, c) 0.52, d) 0.53, e) 0.55. ....	125
Figure 6-12 Percentage of surface area covered by pores of a certain maximum Feret diameter in $(\text{Pb}_{0.95}\text{Sr}_{0.05})(\text{Zr}_y\text{Ti}_{1-y})_{0.986}\text{Fe}_{0.014}\text{O}_3$ with varying Zr/Ti fraction. ....	127

Figure 6-13 Optical micrographs of polished surfaces of $(\text{Pb}_{0.95}\text{Sr}_{0.05})(\text{Zr}_y\text{Ti}_{1-y})_{0.986}\text{Fe}_{0.014}\text{O}_3$ with $y(\text{Zr}) =$ a) 0.49, b) 0.51, c) 0.52, d) 0.53, e) 0.55.....	128
Figure 6-14 Percentage of surface area covered by pores of a certain maximum Feret diameter in $(\text{Pb}_{0.95}\text{Sr}_{0.05})(\text{Zr}_{0.52}\text{Ti}_{0.48})_{1-z}\text{Fe}_z\text{O}_3$ doped with varying Fe content. ....	129
Figure 6-15 Optical micrographs of polished surfaces of $(\text{Pb}_{0.95}\text{Sr}_{0.05})(\text{Zr}_{0.52}\text{Ti}_{0.48})_{1-z}\text{Fe}_z\text{O}_3$ doped with $z(\text{Fe}) =$ a) 0, b) 0.004, c) 0.014, d) 0.020. ....	130
Figure 6-16 X-ray diffraction patterns of $(\text{Pb}_{1-x}\text{Sr}_x)(\text{Zr}_y\text{Ti}_{1-y})\text{O}_3$ (0 at% Fe). Values of variable factors are shown above each pattern. When the variable is not shown, It assumes that $y(\text{Zr}) = 0.52$ , $T_{\text{sint}} = 1310\text{ }^\circ\text{C}$ and $x(\text{Sr}) = 0.05$ . ....	132
Figure 6-17 X-ray diffraction patterns of $(\text{Pb}_{1-x}\text{Sr}_x)(\text{Zr}_y\text{Ti}_{1-y})_{1-z}\text{Fe}_z\text{O}_3$ . Values of variable factors are shown above each pattern. When the variable is not shown, It assumes that $z(\text{Fe}) = 0.014$ , $y(\text{Zr}) = 0.52$ , $T_{\text{sint}} = 1310\text{ }^\circ\text{C}$ and $x(\text{Sr}) = 0.05$ . ....	133
Figure 6-18 Dependence of a) phase content, b) tetragonal cell distortion ( $c_T/a_T-1$ ) on sintering temperature of $(\text{Pb}_{0.95}\text{Sr}_{0.05})(\text{Zr}_{0.52}\text{Ti}_{0.48})_{1-z}\text{Fe}_z\text{O}_3$ with $z(\text{Fe}) = 0.000$ or $0.014$ . ..	135
Figure 6-19 Dependence of a) phase content, b) tetragonal cell distortion ( $c_T/a_T-1$ ) on strontium content of $(\text{Pb}_{1-x}\text{Sr}_x)(\text{Zr}_{0.52}\text{Ti}_{0.48})_{1-z}\text{Fe}_z\text{O}_3$ with $z(\text{Fe}) = 0.000$ or $0.014$ , sintered at $1310\text{ }^\circ\text{C}$ . ....	136
Figure 6-20 Room temperature quaternary phase diagram of the $(\text{Pb-Sr})(\text{Ti-Zr})\text{O}_3$ system published by Ikeda [167]. $F_T$ = tetragonal, $F_R$ rhombohedral ferroelectric phases; $A_T$ = tetragonal, $A_O$ = orthorhombic anti-ferroelectric phases. Points C1 and C2 show locations of compositions investigating effects of Sr content in this work. ....	136
Figure 6-21 Dependence of a) phase content, b) tetragonal cell distortion ( $c_T/a_T-1$ ) on Zr/Ti ratio of $(\text{Pb}_{0.95}\text{Sr}_{0.05})(\text{Zr}_y\text{Ti}_{1-y})_{1-z}\text{Fe}_z\text{O}_3$ with $z(\text{Fe}) = 0.000$ or $0.014$ , sintered at $1310\text{ }^\circ\text{C}$ . ....	137
Figure 6-22 Dependence of a) phase content, b) tetragonal cell distortion ( $c_T/a_T-1$ ) on Fe content of $(\text{Pb}_{0.95}\text{Sr}_{0.05})(\text{Zr}_{0.52}\text{Ti}_{0.48})_{1-z}\text{Fe}_z\text{O}_3$ sintered at $1310\text{ }^\circ\text{C}$ . ....	139

Figure 6-23	SEM micrograph of a polished surface of $(\text{Pb}_{0.95}\text{Sr}_{0.05})(\text{Zr}_{0.52}\text{Ti}_{0.48})_{0.98}\text{Fe}_{0.02}\text{O}_3$ (batch 18, BE mode) sintered at 1310 °C.	142
Figure 6-24	Bright field TEM image of $(\text{Pb}_{0.95}\text{Sr}_{0.05})(\text{Zr}_{0.52}\text{Ti}_{0.48})_{0.98}\text{Fe}_{0.02}\text{O}_3$ (batch 18) sintered at 1310 °C. Arrows indicate potential secondary phases or submicrometric pores. Curtaining from FIB cutting is apparent.	143
Figure 6-25	EDX elemental maps of site 1 of $(\text{Pb}_{0.95}\text{Sr}_{0.05})(\text{Zr}_{0.52}\text{Ti}_{0.48})_{0.98}\text{Fe}_{0.02}\text{O}_3$ (batch 18) sintered at 1310 °C showing distribution of Pb, Sr, Ti, Zr and Fe within and near grains. Arrows indicate potential secondary phases or submicrometric pores.	144
Figure 6-26	EDX elemental map of site 2 of $(\text{Pb}_{0.95}\text{Sr}_{0.05})(\text{Zr}_{0.52}\text{Ti}_{0.48})_{0.98}\text{Fe}_{0.02}\text{O}_3$ (batch 18) sintered at 1310 °C showing distribution of Pb, Sr, Ti, Zr and Fe within and near grains. Arrows indicate a possible secondary phase.	146
Figure 6-27	EDX line scan of site 2. Arrow indicates location of the scan; dashed lines represent grain boundaries.	147
Figure 6-28	Dark field TEM image of a 300nm grain located inside a triple pocket in $(\text{Pb}_{0.95}\text{Sr}_{0.05})(\text{Zr}_{0.52}\text{Ti}_{0.48})_{0.98}\text{Fe}_{0.02}\text{O}_3$ (batch 18) sintered at 1310 °C.	148
Figure 6-29	EDX line scan of a 300nm particle located at a triple pocket in $(\text{Pb}_{0.95}\text{Sr}_{0.05})(\text{Zr}_{0.52}\text{Ti}_{0.48})_{0.98}\text{Fe}_{0.02}\text{O}_3$ (batch 18) sintered at 1310 °C.	149
Figure 6-30	EDX elemental map of $(\text{Pb}_{0.95}\text{Sr}_{0.05})(\text{Zr}_{0.52}\text{Ti}_{0.48})\text{O}_3$ (batch 4) sintered at 1310 °C showing distribution of Pb, Sr, Ti, Zr and Fe within and near grains. Fe was not detected; its elemental map only illustrates that there are no Fe-rich pockets.	150
Figure 7-1	Dependence of relative permittivity $\epsilon_r$ of $(\text{Pb}_{0.95}\text{Sr}_{0.05})(\text{Zr}_{0.52}\text{Ti}_{0.48})_{1-z}\text{Fe}_z\text{O}_3$ on sintering temperature.	156
Figure 7-2	Dependence of a) planar coupling coefficient $k_p$ , b) $d_{33}$ coefficient of $(\text{Pb}_{0.95}\text{Sr}_{0.05})(\text{Zr}_{0.52}\text{Ti}_{0.48})_{1-z}\text{Fe}_z\text{O}_3$ on sintering temperature.	157
Figure 7-3	Dependence of a) dissipation factor $\tan\delta$ , b) mechanical quality factor $Q_M$ of $(\text{Pb}_{0.95}\text{Sr}_{0.05})(\text{Zr}_{0.52}\text{Ti}_{0.48})_{1-z}\text{Fe}_z\text{O}_3$ on sintering temperature.	158

Figure 7-4 Dependence of relative permittivity $\epsilon_r$ of $(\text{Pb}_{1-x}\text{Sr}_x)(\text{Zr}_{0.52}\text{Ti}_{0.48})_{1-z}\text{Fe}_z\text{O}_3$ sintered at 1310 °C on Sr content.....	159
Figure 7-5 Dependence of a) planar coupling coefficient $k_p$ , b) $d_{33}$ coefficient of $(\text{Pb}_{1-x}\text{Sr}_x)(\text{Zr}_{0.52}\text{Ti}_{0.48})_{1-z}\text{Fe}_z\text{O}_3$ sintered at 1310 °C on Sr content.....	160
Figure 7-6 Dependence of a) dissipation factor $\tan\delta$ , b) mechanical quality factor $Q_M$ of $(\text{Pb}_{1-x}\text{Sr}_x)(\text{Zr}_{0.52}\text{Ti}_{0.48})_{1-z}\text{Fe}_z\text{O}_3$ sintered at 1310 °C on Sr content.....	161
Figure 7-7 Dependence of a) relative permittivity $\epsilon_r$ , b) dissipation factor $\tan\delta$ of $(\text{Pb}_{0.95}\text{Sr}_{0.05})(\text{Zr}_{0.52}\text{Ti}_{0.48})_{1-z}\text{Fe}_z\text{O}_3$ sintered at 1310 °C on Fe content.....	162
Figure 7-8 Dependence of a) planar coupling coefficient $k_p$ , b) $d_{33}$ coefficient of $(\text{Pb}_{0.95}\text{Sr}_{0.05})(\text{Zr}_{0.52}\text{Ti}_{0.48})_{1-z}\text{Fe}_z\text{O}_3$ sintered at 1310 °C on Fe content.....	163
Figure 7-9 a) Polarisation-electric field ( $P_E$ - $E$ ) loops of $(\text{Pb}_{0.95}\text{Sr}_{0.05})(\text{Zr}_{0.52}\text{Ti}_{0.48})_{1-z}\text{Fe}_z\text{O}_3$ doped with 0.0–2.0 at% Fe and sintered at 1310 °C; b) dependence of mechanical quality factor $Q_M$ of $(\text{Pb}_{0.95}\text{Sr}_{0.05})(\text{Zr}_{0.52}\text{Ti}_{0.48})_{1-z}\text{Fe}_z\text{O}_3$ sintered at 1310 °C on Fe content. ....	164
Figure 7-10 Relative permittivity $\epsilon_r$ and remanent polarisation $P_r$ as a function of Zr fraction in PZT replotted from [25].....	165
Figure 7-11 Dependence of a) relative permittivity $\epsilon_r$ , b) $d_{33}$ coefficient, c) planar coupling coefficient $k_p$ , of $(\text{Pb}_{0.95}\text{Sr}_{0.05})(\text{Zr}_y\text{Ti}_{1-y})_{1-z}\text{Fe}_z\text{O}_3$ sintered at 1310 °C on Zr/Ti ratio. ....	167
Figure 7-12 Dependence of a) dissipation factor $\tan\delta$ , b) mechanical quality factor $Q_M$ of $(\text{Pb}_{0.95}\text{Sr}_{0.05})(\text{Zr}_y\text{Ti}_{1-y})_{1-z}\text{Fe}_z\text{O}_3$ sintered at 1310 °C on Zr/Ti ratio.....	168
Figure 8-1 Dependence of Young's modulus $Y$ on fractional porosity $P$ of all prepared series. Each series is connected by a solid line from the lowest to the highest value of its respective variable. Fe-doped and undoped series are represented by empty and filled symbols respectively ( $\text{Fe}_z$ series itself has filled triangular symbols). Undoped $T_{\text{sint}}$ series (batches number 4–6) and a batch doped with 0.4 at% Fe (number 10) were used for the linear fit. ....	172

Figure 8-2 Dependence of dynamic Young's modulus $Y$ on a) sintering temperature ( $T_{\text{sint}}$ ), b) Sr content, c) Zr/Ti ratio, d) Fe content of $(\text{Pb}_{1-x}\text{Sr}_x)(\text{Zr}_y\text{Ti}_{1-y})_{1-z}\text{Fe}_z\text{O}_3$ . Grey horizontal lines connect single central compositions, error bars represent SDM, $T_{\text{sint}} = 1310\text{ }^\circ\text{C}$ if not stated otherwise. ....	174
Figure 8-3 Dependence of Vickers hardness $H_v$ on a) sintering temperature ( $T_c$ ), b) Sr content, c) Zr/Ti ratio, d) Fe content of $(\text{Pb}_{1-x}\text{Sr}_x)(\text{Zr}_y\text{Ti}_{1-y})_{1-z}\text{Fe}_z\text{O}_3$ . Grey horizontal lines connect single central compositions, error bars represent SDM, $T_{\text{sint}} = 1310\text{ }^\circ\text{C}$ if not stated otherwise. ....	178
Figure 8-4 Vickers hardness ( $H_v$ ) of 2 sample groups (see text for details) with similar average grain size ( $G$ ) plotted against their fractional porosity $P$ . Error bars represent SDM. ....	179
Figure 8-5 Corrected Vickers hardness $H_v$ plotted against the inverse square root of average grain size $G_a$ . Samples from batches number 1 and 9 indicate compositions with 0 at% Sr.....	180
Figure 8-6 Dependence of mean roughness depth $R_z$ on a) sintering temperature ( $T_{\text{sint}}$ ), b) Sr content, c) Zr/Ti ratio, d) Fe content of $(\text{Pb}_{1-x}\text{Sr}_x)(\text{Zr}_y\text{Ti}_{1-y})_{1-z}\text{Fe}_z\text{O}_3$ . Grey horizontal lines connect single central compositions, error bars represent SDM, $T_{\text{sint}} = 1310\text{ }^\circ\text{C}$ if not stated otherwise. ....	183
Figure 8-7 Graph of mean roughness depth $R_z$ plotted against Young's modulus $Y$ . Numbered samples correspond to batch numbers in Table 8-2.....	184
Figure 8-8 Selected test sequence graphs. Horizontal grey lines represent mean strength values $\sigma$ . Batches a) 1, b) 2, c) 4, d) 5 show location shifts; e) batch 6 represents a random scatter around the same location; f) batch 9 represents a batch with distinct outliers. ....	188
Figure 8-9 Load ring a) parallel with support ring and with correctly attached rubber bands; b) tilted due to incorrect position of 1 rubber band.....	189

Figure 8-10 Histogram of measured strength data of batch number 8 representing unimodal and slightly left skewed distribution. Histogram is overlaid by a Weibull distribution curve. ....	190
Figure 8-11 Histograms of measured strength data of batches a) 1 and b) 3 showing multimodal distributions. ....	191
Figure 8-12 Histograms of batch a) 9, b) 10, c) 11, d) 12, e) 13, f) 17, which exhibited excessively left skewed distributions of measured strength (relative to expected Weibull distributions). ....	193
Figure 8-13 General features near the fracture origin (reproduced from [120]). ....	194
Figure 8-14 Example of a surface scratch acting as a fracture origin. The primary fracture plane clearly follows a portion of the scratch.....	195
Figure 8-15 SEM micrographs of various forms of porosity acting as a fracture origin: a) pore (3-dimensional feature), b) porous seam (2-dimensional feature), c) porous region acting as a fracture origin mixed with machining damage, d) agglomerate. ....	197
Figure 8-16 SEM micrographs of fracture origins with different forms of surface damage: a) regular machining damage with no extra features, b) machining damage with an adjacent porous region, c) porous seam which likely caused chipping after fracture, d) unknown origin, possibly located in the missing piece. Dark spots on the upper half are organic contamination. ....	199
Figure 8-17 Example of a fracture origin size measurement.....	200
Figure 8-18 Probability plots with Weibull distribution fits of $(\text{Pb}_{0.95}\text{Sr}_{0.05})(\text{Zr}_{0.52}\text{Ti}_{0.48})\text{O}_3$ sintered at a) 1260 °C, b) 1310 °C, c) 1360 °C. Dashed lines represent 95% CI, marked samples had their fracture surface examined using SEM. ....	203
Figure 8-19 a) Failure stress probability (signified as F instead of $P_f$ in this figure) distribution of a model material containing both volume ( $m = 15$ ) and surface ( $m = 7$ ) defects. Grey area illustrates the portion of the distribution revealed by testing 30 specimens, $V_1$ – $V_3$ show specimen volume. Graph reproduced from an article by	

Danzer et al. [12]; b) Fit of $(\text{Pb}_{0.95}\text{Sr}_{0.05})(\text{Zr}_{0.52}\text{Ti}_{0.48})\text{O}_3$ (batch 4) to a 3-parameter Weibull distribution. ....	205
Figure 8-20 Representative SEM fracture surface micrographs of batches a) 5, b) 4, c) 6....	207
Figure 8-21 Probability plots with 2-parameter Weibull distribution fits of $(\text{Pb}_{0.95}\text{Sr}_{0.05})(\text{Zr}_{0.52}\text{Ti}_{0.48})_{0.986}\text{Fe}_{0.014}\text{O}_3$ sintered at a) 1260 °C, c) 1310 °C, d) 1360 °C. Dashed lines represent 95% CI, marked samples had their fracture surface examined using SEM; b) 3-parameter Weibull distribution fit of batch 14 sintered at 1260 °C.....	210
Figure 8-22 Strength box plots of all batches in the sintering temperature series.....	212
Figure 8-23 Plots of Weibull a) scale and b) shape factors of all batches in the sintering temperature series. Error bars represent 95% CI. Notes above the data points indicate the prevalent fracture origin: M = machining damage, P = porosity; notes below data points indicate prevalent mode of fracture: I = intergranular, T = transgranular. ....	214
Figure 8-24 Probability plots with Weibull distribution fits of a) $\text{Pb}(\text{Zr}_{0.52}\text{Ti}_{0.48})\text{O}_3$ and b) $\text{Pb}(\text{Zr}_{0.52}\text{Ti}_{0.48})_{0.986}\text{Fe}_{0.014}\text{O}_3$ sintered at 1310 °C. Dashed lines represent 95% CI, marked samples had their fracture surface examined using SEM.....	217
Figure 8-25 Strength box plots of all batches in the Sr/Fe doping series.....	219
Figure 8-26 Plots of Weibull a) scale and b) shape factors of all batches in the Sr/Fe doping series. Error bars represent 95% CI. Notes above the data points indicate the prevalent fracture origin: M = machining damage, P = porosity; notes below data points indicate prevalent mode of fracture: I = intergranular, T = transgranular. ....	220
Figure 8-27 Probability plots with Weibull distribution fits of $(\text{Pb}_{0.95}\text{Sr}_{0.05})(\text{Zr}_y\text{Ti}_{1-y})\text{O}_3$ sintered at 1310 °C. $y =$ a) 0.49, b) 0.51, c) 0.53, d) 0.55. Dashed lines represent 95% CI, marked samples had their fracture surface examined using SEM.....	223

Figure 8-28 Micrographs of fracture surfaces of $(\text{Pb}_{0.95}\text{Sr}_{0.05})(\text{Zr}_y\text{Ti}_{1-y})\text{O}_3$ samples with varying $y$ (stated in at% in the top left corner). Fracture mode changes from intergranular to transgranular at $y = 53$ and $55$ at%. .....	225
Figure 8-29 Probability plots with Weibull distribution fits of $(\text{Pb}_{0.95}\text{Sr}_{0.05})(\text{Zr}_y\text{Ti}_{1-y})_{0.986}\text{Fe}_{0.014}\text{O}_3$ sintered at $1310^\circ\text{C}$ . $y =$ a) 0.49, b) 0.51, c) 0.53, d) 0.55. Dashed lines represent 95% CI, marked samples had their fracture surface examined using SEM. ....	227
Figure 8-30 Strength box plots of all batches in Sr/Fe doping series. ....	230
Figure 8-31 SEM micrographs of fracture origins of samples a) 29 and b) 24 from batch 11. ....	230
Figure 8-32 Plots of Weibull a) scale and b) shape factors of all batches in the Zr/Ti series. Error bars represent 95% CI. Notes above the data points indicate the prevalent fracture origin: M = machining damage, P = porosity; notes below data points indicate prevalent mode of fracture: I = intergranular, T = transgranular. ....	233
Figure 8-33 Probability plots with Weibull distribution fits of $(\text{Pb}_{0.95}\text{Sr}_{0.05})(\text{Zr}_{0.52}\text{Ti}_{0.48})_{1-z}\text{Fe}_z\text{O}_3$ doped with a) 0.4 and b) 2.0 % Fe. Dashed lines represent 95% CI, marked samples had their fracture surface examined using SEM. ....	235
Figure 8-34 Strength box plots of all batches in the Fe doping series. ....	237
Figure 8-35 Volume located fracture origins in samples from batch 10. ....	238
Figure 8-36 Plots of Weibull a) scale and b) shape factors of all batches in the Fe doping series. Error bars represent 95% CI. Notes above the data points indicate the prevalent fracture origin: M = machining damage, P = porosity; notes below data points indicate prevalent mode of fracture: I = intergranular, T = transgranular. ....	239
Figure 8-37 The percentage of surface area covered by pores of certain maximum Feret diameter in a commercial PZT (CTS) compared to $(\text{Pb}_{0.95}\text{Sr}_{0.05})(\text{Zr}_{0.52}\text{Ti}_{0.48})_{1-z}\text{Fe}_z\text{O}_3$ doped with varying Fe content prepared in this work. ....	242

Figure 8-38 Optical micrographs of polished surfaces of $(\text{Pb}_{0.95}\text{Sr}_{0.05})(\text{Zr}_{0.52}\text{Ti}_{0.48})_{1-z}\text{Fe}_z\text{O}_3$ doped with $z =$ a) 0.000, b) 0.004, c) 0.014, d) 0.020 compared with commercial material in e).....	243
Figure 8-39 a) Test sequence plot, b) histogram and c) probability plot with Weibull distribution fit of strength results of commercial PZT. The vertical dashed line in the test sequence plot separates 2 datasets tested before/after testing prepared compositions, the horizontal solid line represents the mean strength value. Dashed lines in the probability plot represent 95% CI, marked samples had their fracture surface examined using SEM. ....	245
Figure 8-40 Strength box plots of all Fe-doped batches sintered at 1310 °C, commercial PZT (CTS) and polished commercial PZT (CTS-P). ....	247
Figure 8-41 Examples of fracture origins found in CTS-P (samples number 1, 4, 6 and 9)..	250
Figure 8-42 Boundary loading curves of $\text{Al}_2\text{O}_3$ and all prepared batches (boundary curves were 2 curves between which all other loading curves were located).....	252
Figure 8-43 $P_E$ - $E$ loops of prepared $(\text{Pb}_{1-x}\text{Sr}_x)(\text{Zr}_y\text{Ti}_{1-y})_{1-z}\text{Fe}_z\text{O}_3$ samples grouped by the following factors: a) sintering temperature and Fe doping, b) Sr doping and Fe doping, c) Zr/Ti ratio ( $z = 0.0$ at%), d) Zr/Ti ratio ( $z = 1.4$ at%) .....	254
Figure 8-44 Plot of coercive stress versus coercive field for soft PZT (replotted from [30])	255
Figure 8-45 Dependence of coercive field on a) sintering temperature ( $T_{\text{sint}}$ ), b) Sr content, c) Zr/Ti ratio, d) Fe content of $(\text{Pb}_{1-x}\text{Sr}_x)(\text{Zr}_y\text{Ti}_{1-y})_{1-z}\text{Fe}_z\text{O}_3$ . Grey horizontal lines connect single central compositions, $T_{\text{sint}} = 1310$ °C if not stated otherwise. ....	256
Figure 8-46 Possible directions of polarisation in samples loaded in a) 3- or 4- point flexure, b) equibiaxial flexure (loading directions are not shown). ....	257
Figure 8-47 Dependence of Weibull strength on a) sintering temperature ( $T_{\text{sint}}$ ), b) Sr content, c) Zr/Ti ratio, d) Fe content of $(\text{Pb}_{1-x}\text{Sr}_x)(\text{Zr}_y\text{Ti}_{1-y})_{1-z}\text{Fe}_z\text{O}_3$ . Grey horizontal lines connect single central compositions. Error bars represent 95% CI. T = transgranular fracture mode; fracture origin: P – porosity, M – machining damage.	

Batches with porosity as dominant fracture origin and/or intergranular fracture were left unmarked. ....	258
Figure 8-48 Dependence of Weibull strength $\sigma_0$ on porosity of $(\text{Pb}_{1-x}\text{Sr}_x)(\text{Zr}_y\text{Ti}_{1-y})_{(1-z)}\text{Fe}_z\text{O}_3$ (only batches discussed in the text are labelled).....	260
Figure 8-49 Dependence of Weibull strength $\sigma_0$ on Young's modulus $Y$ (only batches discussed in the text are labelled).....	261
Figure 8-50 Dependence of Weibull strength $\sigma_0$ on surface roughness $R_z$ (only batches discussed in the text are labelled).....	262
Figure 8-51 Dependence of Weibull strength $\sigma_0$ on average grain size $G_a$ (only batches discussed in the text are labelled).....	264
Figure 8-52 SEM micrographs of thermally etched surface of $(\text{Pb}_{0.95}\text{Sr}_{0.05})(\text{Zr}_{0.52}\text{Ti}_{0.48})\text{O}_3$ sintered at a) 1310 °C (batch 4) and b) 1360 °C (batch 6). ....	264
Figure 8-53 Dependence of Weibull strength $\sigma_0$ on Vickers hardness $H_V$ (only batches discussed in the text are labelled).....	265
Figure 8-54 Scatter of fracture toughness results of $(\text{Pb}_{0.95}\text{Sr}_{0.05})(\text{Zr}_{0.52}\text{Ti}_{0.48})_{1-z}\text{Fe}_z\text{O}_3$ doped with $z = 0$ and 2 at%.....	273
Figure 8-55 a) cantilever of $(\text{Pb}_{0.95}\text{Sr}_{0.05})(\text{Zr}_{0.52}\text{Ti}_{0.48})\text{O}_3$ (batch 4) before and after testing, Kikuchi lines confirm the presence of 2 distinct grains, fracture is intergranular; b) cantilever of $(\text{Pb}_{0.95}\text{Sr}_{0.05})(\text{Zr}_{0.52}\text{Ti}_{0.48})_{0.98}\text{Fe}_{0.02}\text{O}_3$ (batch 18) after fracture, Kikuchi lines show 2 distinct grains, but the crack did not follow the grain boundary. ....	274
Figure A1 - 1 Test sequence plots. Horizontal grey lines represent mean strength values $\sigma$ . ....	291
Figure A2 - 1 Strength histograms overlaid by Weibull distribution curves. ....	295

## LIST OF TABLES

Table 2-1 Summary of published work dealing with the strength dependence of PZT on composition, processing or microstructure.....	36
Table 2-2 Summary of published work dealing with the fracture toughness dependence of PZT on composition, processing or microstructure.....	37
Table 4-1 List of used balances .....	42
Table 4-2 Peak shape and FWHM restrictions used to achieve successful fit of XRD data of $(\text{Pb}_{1-x}\text{Sr}_x)(\text{Zr}_y\text{Ti}_{1-y})_{1-z}\text{Fe}_z\text{O}_3$ .....	47
Table 4-3 List of test-piece and support/load ring dimensions for the first version of the fixture (later denoted as “Test 1”) .....	60
Table 4-4 Dimensions used in the “Test 2” and “Test 4” arrangements with their respective allowed ranges satisfying simple plate loading conditions.....	66
Table 4-5 Reported properties of AD-995 alumina ceramics [124].....	67
Table 4-6 Mechanical test results of rotary ground AD-995 alumina (80-grit finish) .....	70
Table 5-1 Characteristics of processed calcined powder milled for 70 and 600 s .....	79
Table 5-2 Description of individual sintering arrangements .....	87
Table 5-3 Summary of sintering optimisation results .....	88
Table 5-4 List of prepared compositions of $(\text{Pb}_{1-x}\text{Sr}_x)(\text{Zr}_y\text{Ti}_{1-y})_{(1-z)}\text{Fe}_z\text{O}_3$ sintered at 1310 °C .....	92
Table 5-5 Raw materials used in this work .....	94
Table 5-6 Median particle size ( $D_{50}$ ) of calcined powders of $(\text{Pb}_{1-x}\text{Sr}_x)(\text{Zr}_y\text{Ti}_{1-y})_{(1-z)}\text{Fe}_z\text{O}_3$ ....	98
Table 8-1 Reported values of Young’s modulus for various PZT compositions .....	176
Table 8-2 Surface roughness and maximum valley depth of investigated batches of $(\text{Pb}_{1-x}\text{Sr}_x)(\text{Zr}_y\text{Ti}_{1-y})_{1-z}\text{Fe}_z\text{O}_3$ sintered at 1310 °C unless stated otherwise.....	182

Table 8-3 List of fracture origin identities .....	195
Table 8-4 Results of A-D tests and fracture origin investigations of $(\text{Pb}_{0.95}\text{Sr}_{0.05})(\text{Zr}_{0.52}\text{Ti}_{0.48})\text{O}_3$ sintered at different temperatures. ....	203
Table 8-5 Results of A-D tests and fracture origin investigations of $(\text{Pb}_{0.95}\text{Sr}_{0.05})(\text{Zr}_{0.52}\text{Ti}_{0.48})_{0.986}\text{Fe}_{0.014}\text{O}_3$ sintered at different temperatures. ....	211
Table 8-6 Results of A-D tests and fracture origin investigations of $\text{Pb}(\text{Zr}_{0.52}\text{Ti}_{0.48})\text{O}_3$ doped with 0/5 % Sr and 0.0/1.4 % Fe. ....	218
Table 8-7 Results of A-D tests and fracture origin investigations of $(\text{Pb}_{0.95}\text{Sr}_{0.05})(\text{Zr}_y\text{Ti}_{1-y})\text{O}_3$ with $y = 49-55$ at%. ....	224
Table 8-8 Results of A-D tests and fracture origin investigations of $(\text{Pb}_{0.95}\text{Sr}_{0.05})(\text{Zr}_y\text{Ti}_{1-y})_{0.986}\text{Fe}_{0.014}\text{O}_3$ with $y = 49-55$ at%. ....	228
Table 8-9 Results of A-D tests and fracture origin investigations of $(\text{Pb}_{0.95}\text{Sr}_{0.05})(\text{Zr}_{0.52}\text{Ti}_{0.48})\text{O}_3$ doped with 0.4 and 2.0 % Fe. ....	236
Table 8-10 Comparison of physical properties of commercial hard PZT (CTS) and Fe-doped compositions prepared in this work. ....	241
Table 8-11 Results of A-D tests and fracture origin investigations of commercial PZT samples. ....	246
Table 8-12 Comparison of mechanical properties of commercial hard PZT (CTS) and Fe-doped compositions prepared in this work. ....	248
Table 8-13 Results of fracture origin investigations of polished commercial PZT samples..	249
Table 8-14 Relative change of Weibull strength, physical and mechanical properties with composition of $(\text{Pb}_{1-x}\text{Sr}_x)(\text{Zr}_y\text{Ti}_{1-y})_{(1-z)}\text{Fe}_z\text{O}_3$ and processing conditions. Blue cells indicate that the value is $>2\times$ SDM. ....	270

# NOMENCLATURE AND ABBREVIATIONS

## Abbreviations

A-D	Anderson-Darling (goodness-of-fit test)
ARL	Army Research Laboratory
CI	confidence interval
EPR	Electron Paramagnetic Resonance
FWHM	full width at half maximum (peak characteristic)
HAADF	high-annular dark-field imaging in transmission electron microscopy
K-S	Kolmogorov-Smirnov (goodness-of-fit test)
MLE	Maximum Likelihood Estimation
PFIB	plasma focused ion beam
PZT	lead zirconium titanate, $\text{Pb}(\text{Zr}_y\text{Ti}_{1-y})\text{O}_3$
PSZT	Sr-doped PZT, $(\text{Pb}_{1-x}\text{Sr}_x)(\text{Zr}_y\text{Ti}_{1-y})\text{O}_3$
ROR	ring on ring
SDM	standard deviation of mean
SEM	scanning electron microscopy
TEM	transmission electron microscopy

## Symbols

$A$	depth of the pre-notch
$\alpha$	dimensionless factor between describing crack, specimen and stress field geometry
$a_0, a_1, a_2, a_3$	peak height, peak centre, FWHM, proportion of Gaussian and Lorentzian contributions
$a$	crack length
$a_c$	critical crack length
$b_f, c_f$	temperature dependent expansion coefficients (calculation of $f$ )
$a_T, c_T$	tetragonal unit cell parameters
$a_a-j_a$	polynomial coefficients in an equation for calculating Poisson's ratio. Values listed in [1].
$a_b-j_b$	polynomial coefficients in an equation for calculating geometric factors $K_i$ . Values listed in [1].
$b$	width of a rectangular specimen
$B$	cantilever thickness

$C^T$	free capacitance
$d$	disc diameter
$D$	dielectric displacement
$d_{33}$	piezoelectric charge constant (thickness direction)
$d_{50}$	median particle size
$d_{\text{diff}}$	interplanar distance
$d_V$	average length of the two diagonals of the indentation
$d_S, d_L$	support/load ring diameter
$f$	Landau free energy density
$f_0$	Landau free energy density when $P_E = 0$ (paraelectric state)
$F$	force
$f(A/W)$	finite element crack length correction term
$f_1, f_2$	1. and 2. natural resonant frequencies
$f_m, f_n$	1. minimum and maximum resonant frequency (impedance measurement)
$G$	Dynamic shear modulus (unpoled material)
$G_a$	Average grain size
$G_c$	specific fracture energy
$h$	height of a rectangular specimen
$H_V$	Vickers hardness
$h, k, l$	Miller indices of diffracting planes
$I$	Intensity of a reflection on an X-ray diffraction pattern
$I_E$	Electric current
$K_1, K_2$	geometric factors in an equation for calculating Young's modulus.
$K_c$	fracture toughness
$k_p$	planar electromechanical coupling factor
$L$	cantilever length
$L_S, L_L$	support and loading span in a 4-point bend test
$m$	disc mass
$M$	molar mass
$n$	positive integer
$N_A$	Avogadro constant
$P$	porosity
$P_E$	polarisation

$P_f$	probability of failure
$p(A-D)$	$p$ -value of Anderson-Darling goodness of fit test
$Q_M$	mechanical quality factor
$r$	disc radius
$r_A, r_B, r_O$	ionic radii of A, B and oxygen ions in the perovskite structure
$r_{tip}$	support/load ring tip radius
$R_a$	arithmetic average of the roughness profile
$R_y$	maximum valley depth
$R_z$	average distance between the highest peak and lowest valley in each sampling length of 200 $\mu\text{m}$
$s$	elastic compliance
$S$	strain
$S_E$	Effective area of material under stress
$t$	disc thickness or time
$t_G$	Goldschmidt tolerance factor
$T$	temperature
$T_0$	phase transition temperature
$T_C$	Curie temperature
$T_{sint}$	sintering temperature.
$\tan \delta$	dielectric dissipation factor
$v$	crack growth rate
$V_0$	normalising volume (failure probability calculation)
$V_{cell}$	unit cell volume
$V_E$	effective volume of material under stress
$W$	cantilever width
$Y$	dynamic Young's modulus (unpoled material)
$Y_{ij}^E$	Young's modulus (poled material) measured in closed circuit conditions
$Y_{ij}^D$	Young's modulus (poled material) measured in open circuit conditions
$Z_{min}$	absolute value of impedance at 1. minimum resonant frequency
$\alpha$	dimensionless factor describing the crack, specimen and stress field geometry
$\epsilon_r, \epsilon_{3r}^T$	relative permittivity ("free", thickness direction)
$\theta$	diffraction angle

$\lambda$	wavelength of the incident wave
$\nu$	Poisson (cross contraction) ratio (unpoled material)
$\rho_{\text{rel}}$	relative density
$\rho_{\text{t}}$	theoretical density
$\sigma$	stress
$\sigma_{\text{c}}$	critical stress (strength)
$\sigma_0$	Weibull scale factor (Weibull characteristic strength)
$\sigma_{\text{m}}$	Weibull material scale parameter
$\chi_{\text{T}}, \chi_{\text{R}}$	fraction of tetragonal/rhombohedral phase

# 1 INTRODUCTION

The discovery of polycrystalline ceramics with switchable polarisation in the 1940s started a worldwide search for new piezoelectric materials and their applications. Spark generators, acceleration, temperature or crash sensors, high-precision actuators, or transducers capable of generating and receiving ultrasound are just a few of many examples of devices developed in the last century. The global market for piezoelectric devices reached \$20 billion in 2012 and is still steadily growing [2].

Of all commercially produced piezoelectric ceramics, solid solutions of  $\text{Pb}(\text{Zr,Ti})\text{O}_3$  (lead zirconium titanate or PZT) are by far the most widely used. This is because of their unique properties combining high electromechanical coupling factors, operating temperatures, relatively low production cost and ease of their property-modification. Thanks to intensive research of the structure, phase composition, and electromechanical behaviour, scientists have been able to gain a good understanding of PZT and how it achieves its piezoelectric properties. While these properties are the most important for the use of the ceramic, there are other properties, which are also relevant, but have not received nearly as much attention.

Applications of PZT often involve high electrical and/or mechanical loads. Some of the high-power transducers for ultrasonic cleaning operate under compressive pre-load, many actuators and motors work with flexural stresses, whereas accelerometers commonly utilise shear stresses [3]. Ceramic materials generally show little to no plastic deformation at room temperature and fail in an abrupt manner. Adding the fact that, compared to other ceramics, PZT exhibits low tensile strength, components made of this material are highly susceptible to damage and failure during production, handling and use. That is why understanding the fracture behaviour of PZT

and finding ways to improve the strength are very important for both commercial producers as well as end users.

Predicting the fracture of ferroelectrics is difficult due to the combined effects of electromechanical coupling, domain switching and polarisation-induced anisotropy. In the last 30 years, scientists have developed a number of models describing crack growth in ferroelectrics under various boundary conditions and while significant progress has been made in this field, many questions remain unanswered [4]. Aside from effects specific for ferroelectrics, the strength and toughness of PZT is closely related to the microstructure and internal/external flaws. The ability to control microstructural features such as pore size distribution, pore shape, grain boundary strength or secondary phase presence can potentially enhance the strength/toughness of the material. This has been demonstrated by several researchers [5-9]. However, the individual features responsible for the enhancement are, in most cases, only hypothesised as even adjustment of a single variable such as the stoichiometry of a single element induces changes of several microstructural features.

There is a lack of studies mapping relationships between composition, processing, microstructure and strength of PZT. This thesis aims to explore this topic and extend the current knowledge in this area. The theoretical section summarizes general mechanical properties of ceramics and their microstructural dependences. Special attention is given to PZT and the relevant published work. The experimental section focuses on the influence of composition (acceptor/hard doping and Zr/Ti ratio) and sintering temperature on microstructure and strength of PZT, and attempts to elucidate their interrelationships and identify the most influential factors.

## 2 TECHNICAL BACKGROUND AND LITERATURE REVIEW

### 2.1 Mechanical properties of polycrystalline ceramics

Ceramics are generally classified as brittle materials exhibiting elastic deformation with little or no plasticity and low tensile strength at room temperature, which limit their use. Their mechanical behaviour is commonly described by several quantities such as Young's modulus  $Y$  (proportionality constant between stress and strain in stress direction), shear modulus  $G$  (relates shear stress and shear strain), hardness  $H$  (resistance of the material against plastic deformation), strength  $\sigma$  (maximum applied load without failure) or toughness  $K$  (resistance of the material against fracture) [10]. Listed properties need to be considered when choosing ceramics for certain applications or when sintered bodies need to be further processed (for example machining). Elastic moduli allow prediction of the elastic strain of the ceramic part under stress; hardness is important for wear resistant applications and machinability; strength and toughness are necessary for determining safe loading conditions and for enhancing the lifetime of ceramic parts. Many advanced ceramic materials are used primarily for reasons other than their mechanical properties, which limits the selection. In such cases, searching for ways to improve the properties often presents a better option than replacing the material itself.

Mechanical properties of polycrystalline ceramics are closely related to their microstructure as well as single-grain properties. Basic microstructural parameters include porosity, grain size and number of phases. Control of these parameters and subsequently mechanical properties can be achieved by adjusting processing parameters and composition. General effects of microstructure on mechanical properties of ceramics have been studied extensively in the past. The following sections present an overview of failure mechanisms in isotropic linearly-elastic ceramic bodies and their relation to other mechanical properties.

### 2.1.1 Failure

Brittle fracture consists of crack initiation and propagation. Microstructural inhomogeneities (flaws) present in a ceramic body can act as stress concentrators. A flaw of a critical length  $a_c$  starts propagating once the applied stress reaches a critical value  $\sigma_c$ . For linearly elastic materials, the critical stress, or ceramic strength, can be described by the Griffith-Irwin relation as follows:

$$\sigma_c = \frac{K_c}{\alpha\sqrt{\pi a_c}}, \quad (2-1)$$

where  $\alpha$  is a dimensionless factor between 0–1 describing the crack, specimen and stress field geometry and  $K_c$  is the fracture toughness quantifying the resistance of the material against crack propagation [10].  $K_c$  can be also related to the specific fracture energy  $G_c$  associated with formation of new surfaces and Young's modulus in the following way:

$$K_c = \sqrt{G_c \cdot Y}. \quad (2-2)$$

Because of inherent inhomogeneities in polycrystalline ceramic bodies, the strength is governed by the probability that a flaw of a certain size causing failure at a certain stress level is present [11]. As a consequence, when measured, ceramic materials show a scatter of strength. Several statistical theories describing the variability of strength have been developed, of which the most successful is a semi-empirical theory developed by W. Weibull in 1939 [12]. According to the theory, the probability of failure  $P_f$  at  $\sigma_c$  is given by the following relationship

$$P_f = 1 - \exp \left[ - \int_V \left( \frac{\sigma_c}{\sigma_m} \right)^m dV \right], \quad (2-3)$$

where,  $\sigma_m$  is the Weibull material scale parameter and  $m$  is the Weibull modulus [13-15]. Integrating the volume under tension containing volume distributed strength-controlling flaws yields

$$P_f = 1 - \exp \left[ -kV \left( \frac{\sigma_c}{\sigma_m} \right)^m \right], \quad (2-4)$$

where the product of  $kV$  is called the effective volume  $V_E$  and it represents the stressed volume of generally loaded material that has the same probability of failure as a hypothetical sample of the same volume tested in uniaxial tension [15]. In this case,  $\sigma_m$  is a fundamental material property independent of sample geometry and testing arrangement. Equation (2-3) and (2-4) only apply if critical flaws are inherently volume-type, such as porosity. If critical flaws are related to surface (handling damage, damage from machining), effective area  $S_E$  instead of effective volume must be used [15]. When both types are present, identification of each flaw type and separating the dataset into 2 distributions is necessary to successfully quantify  $\sigma_m$ . Because the determination of  $\sigma_m$  is very time consuming and often challenging, a sample size-dependent version of Weibull distribution is more widely used instead:

$$P_f = 1 - \exp \left[ - \left( \frac{\sigma_c}{\sigma_0} \right)^m \right]. \quad (2-5)$$

This version contains  $\sigma_0$ , which is the Weibull scale factor or the Weibull characteristic strength. Its linearized version,

$$\ln \ln \left( \frac{1}{1 - P_f} \right) = m \ln \sigma_c - m \ln \sigma_0, \quad (2-6)$$

is useful for graphical evaluation. Example of a Weibull plot is shown in Figure 2-1. Weibull strength is obtained by equating the left side of the equation (2-6) to 0, which corresponds to  $P_f$

of 0.63. Weibull modulus  $m$  quantifies the slope of the linear fit, as illustrated in Figure 2-1, and represents homogeneity and scatter of strengths. The more homogeneous the material is, the less scattered the data are, and higher the value of  $m$  is. For well-processed advanced ceramics,  $m$  is generally within the range of 15–25 [10]. As previously stated,  $\sigma_0$  is dependent on the volume of tested material and decreases when the size of the sample increases. Both  $\sigma_0$ ,  $m$  and their confidence intervals are dependent on the number of specimens tested. High  $m$  values are achieved with small datasets, which is often the case as strength tests are expensive and time-consuming [10]. ASTM standard C1499-15 [16] suggests at least 10 specimens for estimating  $\sigma_0$  and 30 specimens for determining both parameters.

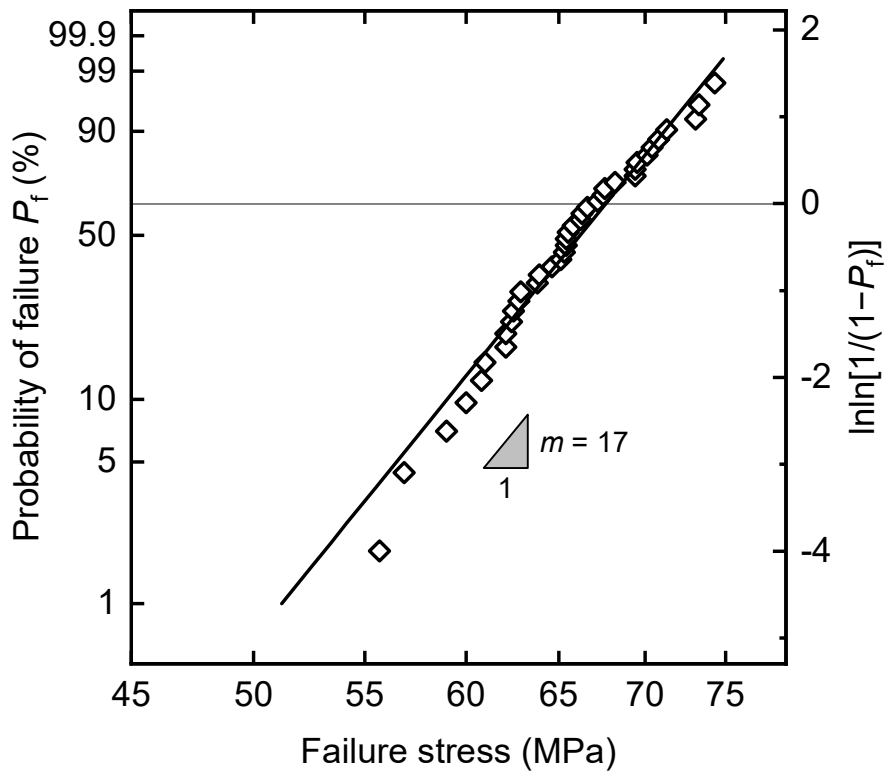


**Figure 2-1 Representative Weibull plot of a ceramic material.**

A Weibull distribution assumes a single type flaw population and that flaws do not interact. The first assumption is often violated as industrially made ceramics usually contain machining-related surface damage as well as extreme processing-related volume flaws. If that is the case,

the scatter of strength shows deviation from the linear fit in Weibull plot. The deviation however, may not be obvious for small datasets.

The discussion above has addressed unstable crack extension, where cracks propagate at near the speed of sound [14]. Stable crack extension is also not uncommon for certain ceramics under static or dynamic load with subcritical stresses. The phenomenon is described as subcritical crack growth. The rate of crack extension over time (growth rate  $v$ ) is dependent on toughness, and can be expressed as

$$v = \frac{da}{dt} = f(K). \quad (2-7)$$

Example of such a dependence is shown in Figure 2-2. The graph illustrates that crack growth usually occurs above a certain threshold  $K_{Ith}$  and can exhibit multiple regions (I–III) of different behaviour [14]. The crack starts propagating in an unstable fashion after reaching  $K_C$ . Subcritical crack growth dependence is an essential part of lifetime predictions for ceramic materials under constant/dynamic load. The underlying mechanisms behind it are still not fully understood but have been related to thermally or chemically activated breakage of atomic bonds [10]. Its testing is complex and time-consuming. Methods mostly utilise artificial macrocracks, which may not necessarily represent the behaviour of naturally-occurring microcracks [10, 14].

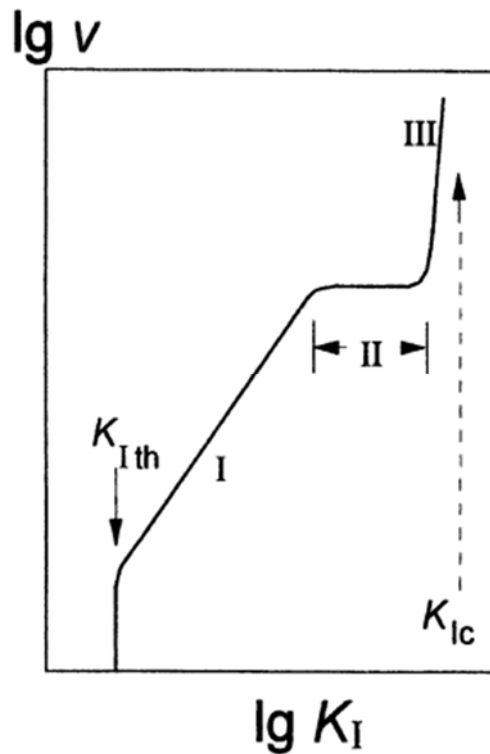


**Figure 2-2 Typical dependence of crack growth ( $v$ ) on toughness ( $K_I$ ) for slow crack growth, reproduced from [14].**

Many ceramic materials exhibit a crack growth resistance with increasing crack extension ( $\Delta a$ ). This behaviour is called the rising crack resistance curve, or the R-curve behaviour. The rising resistance can be induced by several mechanisms such as bridging effects (usually by elongated grains), phase transformations or microcracking and crack branching [14, 17]. The consequence of the R-curve behaviour is insensitivity of strength to crack length in a certain range as opposed to decreasing strength with increasing crack length in materials with a flat R-curve. This is because longer cracks start propagating in a stable manner until a certain stress/extension is reached, while shorter cracks only show unstable propagation after reaching a certain stress value [14]. R-curve behaviour affects brittle (fast) fracture as well as slow crack growth and presents another important aspect of the fracture behaviour of ceramics.

### 2.1.2 Influence of microstructure on mechanical properties

A significant number of researchers have studied the influence of microstructure on the mechanical properties of polycrystalline ceramics in the past. The majority of these studies focused on non-functional ceramics such as stoichiometric oxides, carbides and nitrides. While general effects are known, the wide range of microstructures shown by different ceramic materials and other individual structure-related effects make the prediction and computer modelling difficult.

Porosity has the widest impact on most properties. A comprehensive review can be found in a book by Rice [18], where properties are categorised based on their level of porosity dependence. Structural properties such as lattice parameters, unit cell volume and thermal expansion are not affected by porosity; density and the majority of dielectric constant data are affected only by the amount of porosity, whereas elastic, mechanical and conductive properties depend also on the character of porosity. However, there are cases where properties become independent of character or amount of porosity. In general, properties decrease with increasing porosity.

Several equations have been derived to quantify relations between elastic properties and porosity of a certain character. Dean and Lopez used various empirical relations to fit modulus-porosity data of 27 sets of 11 oxide ceramics [19]. They concluded that the relative Young's modulus of dense ceramics (>90 % theoretical density) shows approximately linear dependence on the volume fraction of porosity  $P$  and can be estimated using the following equation:

$$\frac{Y}{Y_0} = 1 - bP, \quad (2-8)$$

where  $Y_0$  is Young's modulus of a fully dense material and  $b$  is an empirical constant [19]. A similar dependence on porosity can be found for hardness [18].

Unlike elastic modulus, hardness is additionally affected by grain size. Rice et al. [20] assessed a variety of laboratory- and commercially-made ceramics (oxides, borides, carbides, nitrides) using Vickers and Knoop microhardness tests. They concluded, that within the grain size range from 1 up to tens of  $\mu\text{m}$ , which is the grain size range of interest in this work, hardness and grain size exhibit the following dependence:

$$H_V \approx G_a^{-1/2}. \quad (2-9)$$

The dependence is often described as the “Hall-Petch” dependence after two scientists who described it in metals.

The influence of porosity and grain size on fracture toughness cannot be generalised. Equation (2-2) shows that  $K_{IC}$  depends on Young’s modulus and specific fracture energy. While Young’s modulus was shown to have a defined dependence on porosity, specific fracture energy in many cases showed anomalous behaviour [18, 21]. The fracture energy is related to crack propagation and its interaction with the microstructure. Several toughness-enhancing processes can be active depending on composition and microstructure, which is what makes the toughness dependences non-trivial [22].

Strength is dependent on crack size and fracture toughness, of which the latter further depends on Young’s modulus and fracture energy as described by equations (2-1) and (2-2). When assessing effects of microstructure on strength, the first thing to consider is the prevalent fracture origin identity and its average size compared to the size of other microstructural features. When the fracture origin is large relative to natural microstructural features such as porosity and grain size, the material can be expected to follow the same trends as  $Y$  unless there is a variation in fracture energy or defect size. Examples of large flaws less size-sensitive to

processing are machining damage or large pores intentionally introduced by adding polymer beads to ceramic powder. The latter was performed on PZT in a study by Biswas [23].

When natural microstructural features are the strength-limiting flaws, the material exhibits a strength dependence on their size and shape. The flaw size generally determines the strength level, while elastic modulus and flaw shape determine the dependence [18]. Because these parameters are strongly affected by processing, they can be controlled to a certain extent. In a review of strength-grain size data of  $\text{Al}_2\text{O}_3$ ,  $\text{B}_4\text{C}$ ,  $\text{TiO}_2$ ,  $\text{Y}_2\text{O}_3$  and  $\text{SiC}$ , Rice [24] has shown that when the grain size is on the scale of the failure-causing flaws, the strength dependence follows the Hall-Petch relation,

$$\sigma \approx G_a^{-1/2}. \quad (2-10)$$

This is also true for strength-pore size dependence, as apparent from equation (2-1) and supported by the fact that both pore size and grain size scale with processing in a similar manner.

The previously described strength dependences represent simplified cases studied on pores of defined shape. Since processing affects density, pore shape, pore size, grain size and other microstructural features, strength-microstructural property dependencies can deviate from these simple relations.

## 2.2 Ferroelectrics

In 1880, Pierre and Jacques Curie discovered that certain crystals exhibit surface charge when mechanically stressed [25]. The phenomenon was later described as the direct piezoelectric effect and gave birth to many new applications. The converse piezoelectric effect, where the material is strained by the application of electric field, is also widely used in practice. The electrical/mechanical response of piezoelectrics is hysteretic and linearly dependent on the mechanical/electrical stimulation. Both effects are related to the crystal structure of the material. Only 20 out of 32 crystal classes, which exhibit a lack of centre of symmetry, are piezoelectric. Out of these classes, 10 are pyroelectric, which means they exhibit space charge under uniform heating. Furthermore, certain pyroelectrics, which possess a non-polar state not significantly less stable than their polar state, exhibit a switchable axis of polarisation. These materials are called ferroelectrics. The non-polar (paraelectric) state is stable above a certain temperature, which is described as the Curie temperature  $T_C$  [26].

Quartz was one of the first commercial piezoelectric materials and even today remains important for certain applications [27]. However, the most significant breakthrough in the field was discovery of permanently switchable polarisation in the ferroelectric ceramic  $\text{BaTiO}_3$  which sparked intense world-wide research in the fundamentals of ferroelectrics, their applications and new compositions [28]. In 1950s, a strong piezoelectric effect was found in solid solutions of lead zirconate and lead titanate  $\text{Pb}(\text{Zr,Ti})\text{O}_3$  (PZT), which has a similar structure to  $\text{BaTiO}_3$ . Due to its unique properties, which could be tailored by introducing other elements, PZT became the most heavily used piezoelectric material [3, 27].

Piezoelectricity should not be confused with electrostriction, which also describes the generation of strain in materials by the application of an electric field. Electrostriction occurs

in all dielectric materials, the strain is usually very small, and has a non-hysteretic quadratic relationship to the applied stress [29].

Piezoelectric materials are used in a large variety of applications including sensors, transducers, high voltage generators, actuators, motors, energy harvesters, frequency filters, sonars and micro-electromechanical systems. Electrostrictive materials can be used in actuators or sonars for special applications requiring non-hysteretic response [29].

### 2.3 Piezoelectric, dielectric properties

As mentioned previously stress  $\sigma$  applied to piezoelectric material generates a certain amount of charge per unit area, also known as the dielectric displacement  $D$ . The relation is expressed as follows:

$$D_i = d_{ijk}\sigma_{jk}, \quad (2-11)$$

where  $d_{ijk}$  is the proportionality constant known as the piezoelectric constant. Applied electric field  $E$  generates strain  $S$  and the phenomenon is known as the converse piezoelectric effect. This effect can be expressed by a similar equation:

$$S_{ij} = d_{kij}E_k, \quad (2-12)$$

where  $d_{kij}$  is the same proportionality constant as in the previous case. Combining the previous equations with elastic coefficient  $s_{ijkl}$  (compliance) and electric permittivity  $\epsilon_{ij}$  yields the piezoelectric constitutive equations:

$$D_i = d_{ijk}^E\sigma_{jk} + \epsilon_{ij}^\sigma E_j \quad (2-13)$$

and

$$S_{ij} = d_{kij}^\sigma E_k + s_{ijkl}^E\sigma_{kl}, \quad (2-14)$$

where superscript  $\sigma$  signifies the constant measured at constant (zero) stress (“free”) and superscript  $E$  signifies the constant measured at constant (zero) field (“short-circuit”). Additional constitutive equations can be derived for different boundary conditions [26].

Elastic and dielectric properties are direction dependent, indices  $i, j, k, l$  take values of 1, 2 or 3.  $D$  and  $E$  are vectors with 3 components, while  $\sigma$  and  $S$  are second-rank tensors with 9 components of which 6 are independent. Permittivity  $\epsilon$  is a second rank tensor, proportionality

constants  $d$  and  $s$  are third- and fourth-rank tensors respectively. To simplify the matrix notation, the indices of the 6 independent components of stress/strain, 11, 22, 33, 23 = 32, 31 = 13, and 12 = 21, can be substituted by a single index taking values of 1 to 6. Indices of components of proportionality constants are then reduced to 2 subscripts instead of 3 or 4. Reduced notation of axes used for piezoceramics is shown in Figure 2-3.

In practice, the first subscript signifies the input direction and the second subscript indicates the response direction. For example, piezoelectric constant  $d_{33}$  couples the stress or the electric field with dielectric displacement or strain in direction 3. In poled materials, axis 3 coincides with the direction of polarisation [30].

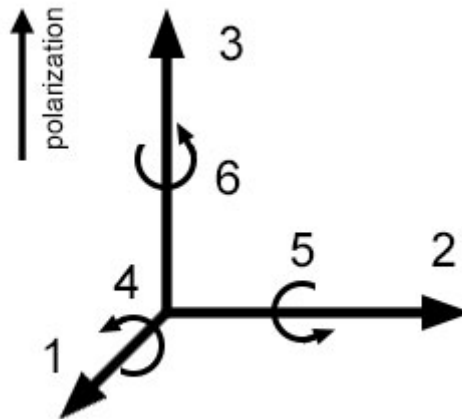


**Figure 2-3 Notation of axes of poled piezoelectric materials**

Effectiveness of energy conversion from electrical to mechanical and vice versa (i.e. electromechanical coupling) is quantified by a coupling factor  $k$  as follows:

$$k^2 = \frac{\text{electrical energy converted to mechanical energy}}{\text{input electrical energy}}. \quad (2-15)$$

As losses are always present,  $k^2$  or  $k$  is always  $< 1$  [26]. Coupling factors also uses subscripts to identify input and output directions. A planar coupling coefficient  $k_p$  is used throughout this

work, which describes conversion between an electric field in 3-direction and mechanical responses in a 1-2 plane (induced planar vibrations), as illustrated in Figure 2-4.

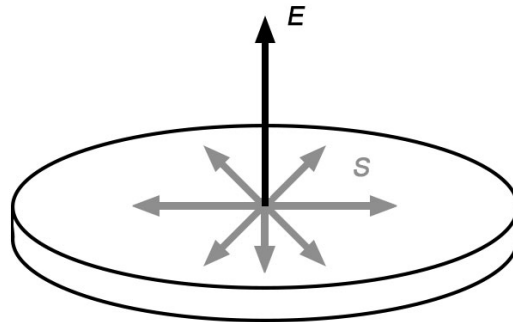


**Figure 2-4 Schematic diagram of planar vibrations  $S$  in the 1-2 plane of a poled piezoelectric disc induced by an electric field  $E$  in the 3-direction.**

Alternating voltages create charge with real (in phase) and imaginary (out-of-phase) components as a result of resistive leakage or dielectric absorption. The ratio of the imaginary to the real part is a measure of loss and is known as the dissipation (loss) factor  $\tan\delta$  [26].

The last important quantity is the mechanical quality factor  $Q_M$ , which describes sharpness (reciprocal of the relative bandwidth) of the resonance of a piezoelectric resonator. This is simply just a measure of its mechanical losses (damping). High  $Q_M$  signifies sharp resonance peaks and low losses (damping) [30].

## 2.4 Fracture mechanics of ferroelectrics

It was previously mentioned that ferroelectrics is a term used for materials with spontaneous polarisation, which can be switched by the application of electric field. Similarly, ferroelasticity refers to spontaneous polarisation switchable by the application of mechanical stress. The constitutive equations (2-13) and (2-14) illustrate that both these phenomena are highly coupled. In practice, an applied stress or an opening crack in a ferroelectric body may induce domain switching, which consumes energy and introduces a non-linearity to the fracture behaviour. A domain is a constitutive part of a piezoelectric crystal in which the polarisation direction is homogeneous. The non-linearity is illustrated in Figure 2-5, which shows a stress-strain curve of a test specimen poled in a direction parallel to that of the compressive loading, performed by Schäufele and Härdtl [31]. Part A-B is linearly-elastic; domain switching occurs between B-D until all domains have been switched, and the curve returns to being linear between D-E.

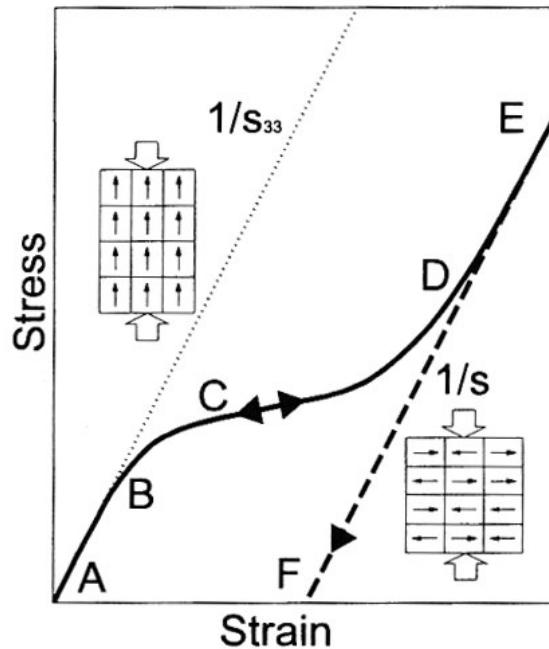
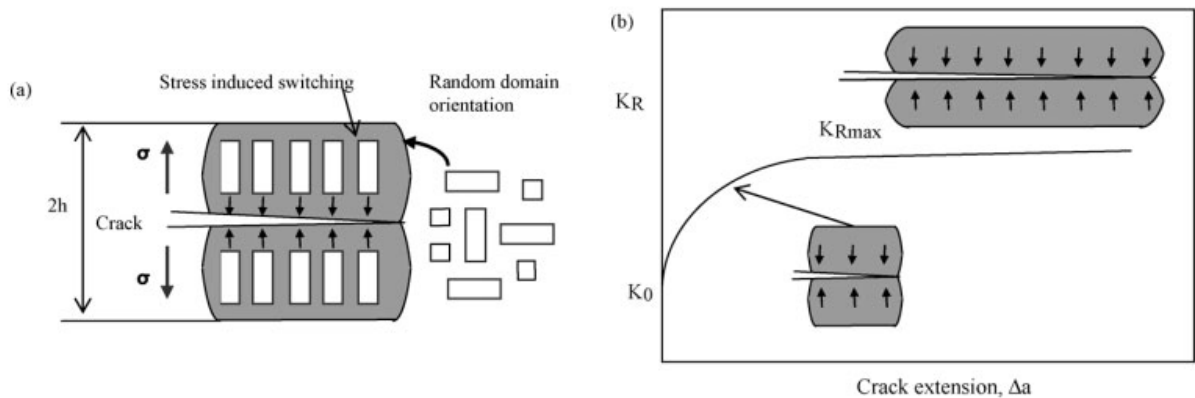


Figure 2-5 A representative stress-strain curve of a poled ferroelectric material. A-B and D-E are linearly elastic parts, B-D is a non-linear part due to ferroelastic domain switching. Upon unloading, the switching is either reversible (E-A) or irreversible (E-F). (reproduced from [31])

Domain switching is also induced at the tip of an opening crack. As the crack grows, the process zone extends. Subsequently, the part of the process zone, which gets left in the wake of the tip creates compressive stresses on the crack surfaces and shields the crack tip. The effect is similar to transformation toughening and results in the presence of a rising R-curve. An illustrative graph and diagram reproduced from the paper published by Hizebry et al. [32] are shown in Figure 2-6.



**Figure 2-6 Illustration of a) domain switching induced by an opening crack; b) rising R-curve caused by compressive stresses created by process zone left in the wake of the crack (reproduced from [32]).**

Due to ferroelastic contributions, linear elastic fracture mechanics (LEFM) does not accurately describe the fracture behaviour of ferroelectrics. The fracture mechanics of ferroelectric solids are still under development [33] and there are several aspects that make fracture predictions a complex problem:

1. Poled ferroelectric ceramics are anisotropic and the toughening is not homogeneous in all loading directions. In addition, the toughening is also affected by the direction of the crack versus the direction of loading.
2. Applied electric field affects domain switching and toughening.
3. The ease of domain reorientation is strongly affected by doping.

The study of the fracture mechanics of ferroelectrics is not the goal of this thesis. However, the aspects presented in this chapter are important and need to be considered when assessing the results. The impact of ferroelastic contributions on the results from mechanical tests in this work shall be minimised by using unpoled specimens and pure or hard-doped PZT, whose domains are not readily switchable at room temperature. Further information on the fracture mechanics of ferroelectrics can be found in the book by Fang and Liu [33] and review by Schneider [4].

## 2.5 PZT

Discovery of a permanently switchable polarisation in BaTiO<sub>3</sub> ceramics in 1944 started the search for other ABO<sub>3</sub>-type perovskites of similar properties. A few years later, strong ferroelectricity was found in the solid solution of Pb(Zr,Ti)O<sub>3</sub> and eventually other Pb-containing perovskites [28]. In the following section the structure, properties, modification, processing and current understanding of mechanical properties of this material are described.

### 2.5.1 Structure and composition

Figure 2-7 shows the basic perovskite unit cell of PZT, where Pb<sup>2+</sup> on the A site is coordinated by 12 oxygen anions and Zr<sup>4+</sup> or Ti<sup>4+</sup> on B site is coordinated by 6 oxygen anions. Both Zr<sup>4+</sup> and Ti<sup>4+</sup> cations have similar ionic radii and are interchangeable within the structure.

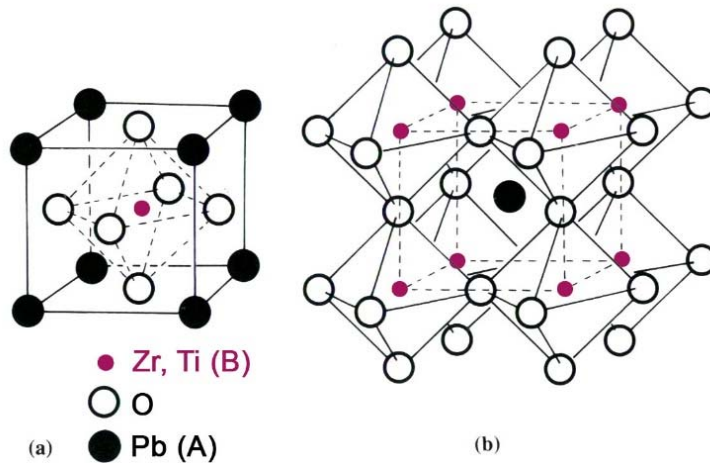


**Figure 2-7 A cubic perovskite unit cell of PZT illustrating a) 6-fold coordination of Zr<sup>4+</sup>/Ti<sup>4+</sup> and b) 12-fold coordination of Pb<sup>2+</sup> (reproduced from [34]).**

Stability of the perovskite structure is described by the Goldschmidt tolerance factor  $t_G$  [35], which is calculated from the average ionic radii of the constituting ions ( $r_A$ ,  $r_B$ ,  $r_O$ ) as follows:

$$t_G = \frac{r_A + r_O}{\sqrt{2}(r_B + r_O)}. \quad (2-16)$$

When  $t_G = 1$ , the perovskite unit cell assumes a stable cubic structure. In PZT, the cubic structure shown in Figure 2-7 is stable above the Curie temperature  $T_C$  (approximately 240–480 °C depending on the Zr/Ti ratio). Ionic displacements are observed, when the tolerance factor deviates from 1. The ionic radii of  $\text{Pb}^{2+}$ (XII),  $\text{Zr}^{4+}$ (VI) and  $\text{Ti}^{4+}$ (VI) ions are 1.49, 0.72 and  $0.61 \cdot 10^{-10}$  m respectively (numbers in brackets signify their coordination) [36]. The  $t_G$  of  $\text{PbTiO}_3$  is  $>1$ , whereas the  $t_G$  of  $\text{PbZrO}_3$  is  $<1$ , therefore, both perovskites favour different crystallographic structures below the Curie temperature. As illustrated by the  $\text{PbZrO}_3$ - $\text{PbTiO}_3$  phase diagram shown in Figure 2-8, in Ti-rich PZT, the cations displace along the [100] direction relative to the oxygen atoms, creating a tetragonal unit cell. In Zr-rich compositions, either an orthorhombic or rhombohedral phase is formed. The rhombohedral phase results from the shift of cations along the [111] direction accompanied by the tilt of oxygen octahedra. In the orthorhombic phase, cations assume an antiparallel arrangement along [110]/[ $\bar{1}\bar{1}0$ ] directions, while the oxygen octahedra rotate around the [110] axis [37, 38]. The highest piezoelectric activity of  $\text{Pb}(\text{Z}_x\text{Ti}_{1-x})\text{O}_3$  is achieved within the compositional range of  $x \approx 0.52$ – $0.55$ , near the morphotropic boundary (MPB) between the rhombohedral and tetragonal phases, as illustrated in Figure 2-9 [3]. Further discussions will be limited mostly to this range, as it contains the most of commercially used PZT compositions.

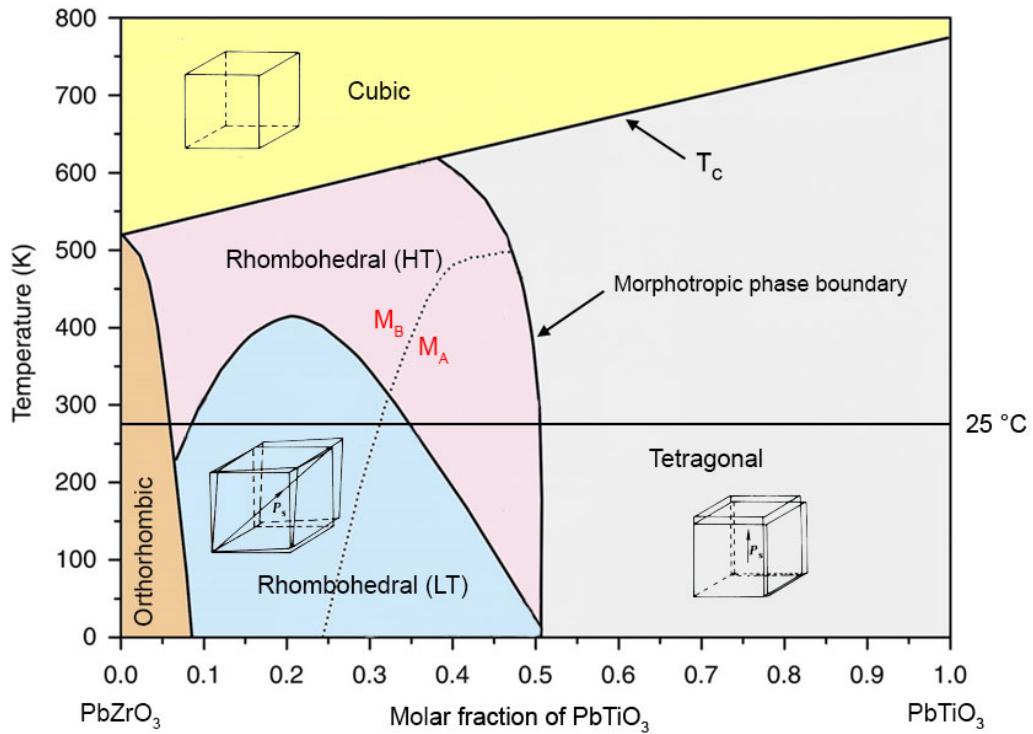


Figure 2-8 Phase diagram of Pb(Zr,Ti)O<sub>3</sub> reproduced from the work of Zhang et al. [39]. T<sub>c</sub> = Curie temperature; M<sub>A</sub>, M<sub>B</sub> = two modifications of a monoclinic phase found in minor concentrations in indicated areas.

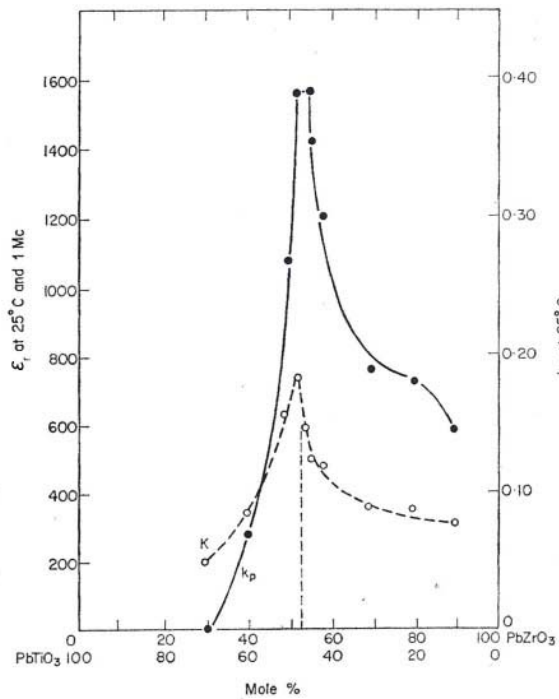


Figure 2-9 Dependence of relative permittivity ( $\epsilon_r$ ) and planar coupling factor ( $k_p$ ) on the Zr/Ti ratio showing a maximum at the morphotropic phase boundary (reproduced from [26]).

Both tetragonal and rhombohedral unit cells are non-centrosymmetric and possess a spontaneous dipole, which can be permanently switched (i.e. both phases are ferroelectric). The cubic cell does not possess a dipole and is therefore paraelectric (shows no piezoelectric response). The dipole is formed by the displacement of ions after crossing the Curie temperature. The paraelectric-ferroelectric phase transition can be described by the Landau theory, which characterises phase transitions by an order parameter, in this case polarisation  $P_E$ . The Landau free energy density can be expressed as follows:

$$f(T, P_E) = f_0(T) + \frac{1}{2} a_{f0}(T - T_0)P_E^2 + \frac{1}{4} b_f(T)P_E^4 + \frac{1}{6} c_f(T)P_E^6, \quad (2-17)$$

where  $f_0$  is the free energy when  $P_E = 0$  (paraelectric state),  $b_f$  and  $c_f$  are temperature dependent expansion coefficients,  $a_{f0}$  is a constant and  $T_0$  is the phase transition temperature. The equation is valid for homogeneous uniaxial ferroelectric systems in the absence of external electric and mechanical fields [40].

Newly formed dipoles create charges near interfaces, surfaces and defects, which gives rise to a depolarising field. To minimise this field and the energy of the system, the piezoelectric crystal is separated into regions possessing certain directions of polarisation, called domains. The direction of dipoles is homogeneous within each domain and the domains are separated by domain walls. In the case of a depolarising field, the directions of domains alternate by  $180^\circ$ , making them the  $180^\circ$  domains or  $180^\circ$  domain walls [27, 40].

In polycrystalline ceramics, each crystal is clamped and the distortion accompanying the phase transition gives rise to internal stresses. The stress can be minimised by formation of non- $180^\circ$  domains (non- $180^\circ$  domain walls). The tetragonal phase exhibits  $90^\circ$  domain walls, whereas the rhombohedral phase exhibits  $71^\circ$  and  $109^\circ$  domain walls [27].

In a polycrystalline material, although the domains have precise crystallographic directions within each crystallite, as the crystallites are randomly oriented, a polycrystalline ceramic body has zero net polarisation and shows no response to applied mechanical stress or electric field. In order to make the body piezoelectric, domains must be aligned by application of an external electric field of sufficient strength. This process is also known as poling.

A piezoelectric response originating from atomic displacements within the individual unit cells is called intrinsic. Non-180° domain wall motion is the most important extrinsic contribution to the piezoelectric response in ferroelectrics [27].

As stated previously, the piezoelectric response of PZT is much higher than that of most other ferroelectric ceramics. This phenomenon is closely related to the structure of the material near the MPB and despite several decades of research, there is still an ongoing debate about the exact mechanisms behind it. Both tetragonal and rhombohedral phases coexist near the MPB and it has been shown by Rossetti et al. [41] that the “MPB” is thermodynamically required to be a two-phase field. The presence of 2 phases increases the number of available polarisation-switching angles and increases the overall polarisation after poling. In addition to tetragonal and rhombohedral phases, Noheda et al. [42] also detected a monoclinic phase using the high-resolution synchrotron X-Ray powder diffraction. A Rietveld study by Zhang et al. [39] found long- and short-range monoclinic regions present throughout the entire rhombohedral phase region in 2 different structures –  $M_A$  and  $M_B$ . Their proposed phase diagram is shown in Figure 2-8. The presence of a monoclinic phase was also shown as thermodynamically possible [43, 44]. Further research showed that the potential barrier between tetragonal and rhombohedral phases is shallow and both phases can be reversibly transformed between one another using electric field [45-48]. The transition is facilitated by polarisation rotation, as illustrated in Figure

2-10, and all the intermediate stages of rotation can be considered as monoclinic, which explains the presence of this phase as well as the abnormally high piezoelectric response of PZT.

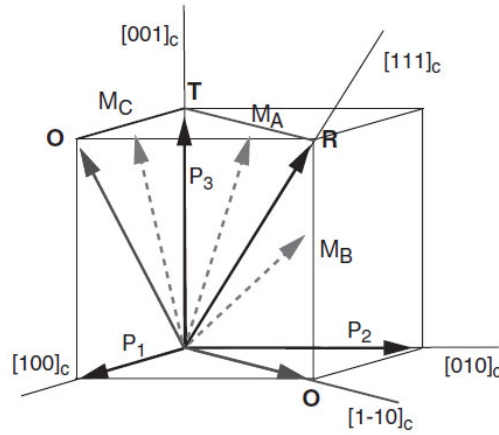


**Figure 2-10 A cubic cell with directions in which it distorts to achieve tetragonal (T), rhombohedral (R) or orthorhombic (O) symmetry.  $M_A$ ,  $M_B$  and  $M_C$  distortions illustrate possible intermediate monoclinic phases. (reproduced from [44])**

Distortion of the tetragonal unit cell  $c_T/a_T$  where  $a_T$  and  $c_T$  are lattice parameters, decreases in a linear fashion as the Zr/Ti ratio approaches the MPB, which is shown in Figure 2-11. The rhombohedral unit cell distortion ( $90 - \alpha_R$ , where  $\alpha_R$  is the rhombohedral angle) is significantly lower and shows a little change with the Zr/Ti ratio [26].

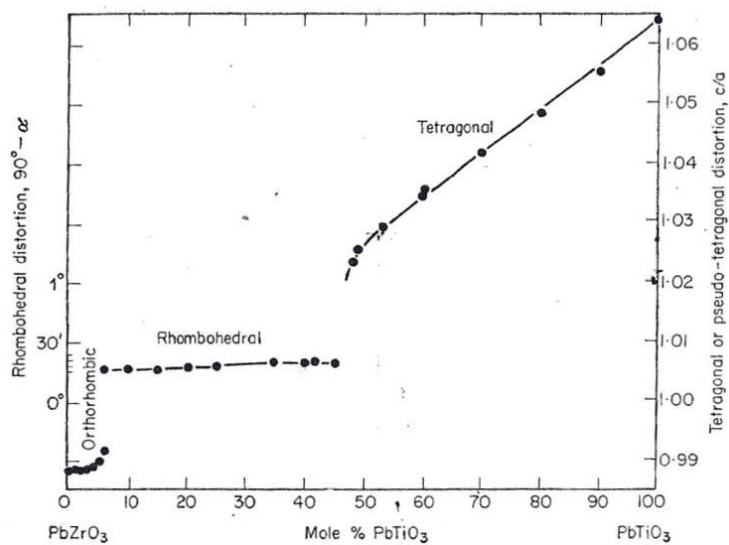


**Figure 2-11 The dependence of tetragonal and rhombohedral unit cell distortion on the Zr/Ti ratio (reproduced from [26]).**

It has been demonstrated, that the maximum unidirectional strain of PZT induced by an electric field is not achieved exactly at the MPB, but rather on the tetragonal side of it. Hoffmann and Kungl [49] found the highest strain response at the tetragonal phase volume fraction of 60–70 %. The authors speculated that the higher lattice distortion but reduced non-180° domain wall motion in the tetragonal phase are more effective at contributing to the strain response than the higher non-180° domain switching activity but smaller lattice distortion of the rhombohedral phase.

### 2.5.2 Doping

Apart from the Zr/Ti ratio, the properties of PZT can be further tailored by substituting the cations on the A or B sites by different ions (dopants) of similar size. The dopants can be either isovalent (dopants having the same charge as the ions they replace) or aliovalent (the charges of the dopants and original ions are different). Dopants can induce a range of structural and microstructural changes, including changes in lattice distortion, nature of chemical bonding, grain size, Curie temperature, domain structure, shift of the MPB and the introduction of charged lattice defects.

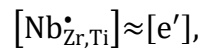
The most common isovalent dopants include  $\text{Sr}^{2+}$ ,  $\text{Ca}^{2+}$  and  $\text{Ba}^{2+}$  for the A-site. Their main effect is the decrease of the Curie temperature, which lowers the energy barrier needed to induce domain wall motion. The result is an increase of the room temperature relative permittivity and  $d_{33}$  [3, 50].

Aspects of domain wall motion (an extrinsic property) play an important role in the overall piezoelectric response. In fact, atomic displacements within individual unit cells (an intrinsic property) only contribute by less than 50 % to the piezoelectric properties [51, 52]. The ease of

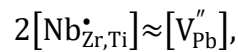
domain wall motion is governed by the proximity to the MPB as well as by the interaction of domain walls with structural and microstructural defects [27, 44, 51, 53-55]. In addition, the motion is also thermally activated and dependent on electric field and mechanical stress [27, 51].

Aliovalent dopants can either have a charge smaller than the original ion, in which case they are called acceptor or hard dopants, or their charge may be larger than the one of the original ion, in which case they are called donor or soft dopants. Terms “soft” and “hard” are frequently used throughout the field to describe donor- and acceptor-doped PZT ceramics respectively and therefore will also be used in this work. Common acceptor dopants include  $K^+$  for the A site and  $Fe^{3+}$ ,  $Mn^{2+,3+}$ ,  $Ni^{2+}$ ,  $Co^{3+}$  for the B site. For donors, these are  $Bi^{3+}$  and  $La^{3+}$  (A site) or  $Sb^{5+}$ ,  $W^{6+}$  or  $Nb^{5+}$  (B site).

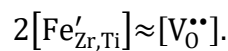
The violation of electroneutrality caused by aliovalent dopants is compensated by the formation of charged defects. In the case of donor doping, the charge is compensated by free electrons:



or the formation of lead vacancies [56]:



whereas in acceptor-doped PZT, the charge is compensated by the formation of oxygen vacancies:



Each of the two defects induces a different response in PZT. Electron paramagnetic studies suggested that defect complexes with lead vacancies are more distant, isolated and less defined.

Their movement is difficult due to the presence of surrounding oxygen ions [57, 58]. Oxygen vacancies, which are highly mobile in the oxygen sublattice, were observed to form well-defined defect complexes such as  $(\text{Fe}'_{\text{Zr,Ti}}-\text{V}_\text{O}^{\bullet\bullet})^\bullet$ . Acceptor-oxygen vacancy defect associates stabilise the domain configuration in PZT by volume effects (alignment of defect dipoles and spontaneous polarisation), domain-wall effects (fixation of domain wall position) and grain-boundary effects (secondary phases at grain boundaries stabilise domain structures) [29, 58]. Because of these effects, hard PZT materials develop “pinched” polarisation-electric field hysteresis loops, exhibit reduced relative permittivity and dissipation factor ( $\tan\delta$ ) and increased mechanical quality factor ( $Q_M$ ). Such materials show lower piezoelectric response but are more stable and resist stronger depolarizing fields [3, 59, 60]. Hard PZT is used in applications involving high power or high electric fields.

The presence of donor dopants results in an increase of domain wall mobility, but the mechanism is not well understood [56]. Recent experiments done by Fraygola et al. [61] suggest that the addition of donor dopants reduces the concentration of  $\text{V}_{\text{Pb}}''-\text{V}_\text{O}^{\bullet\bullet}$  divacancies. Soft PZT exhibits well-developed and “square”  $P_E$ - $E$  loops, enhanced relative permittivity ( $\epsilon_r$ ), coupling coefficients ( $k$ ) and elastic compliance ( $s$ ), but is more sensitive to depolarizing fields. Examples of soft PZT usage include sensors, low-power transducers, generators and actuators.

It has been shown, that dopants can affect domain wall density. Several authors reported miniaturisation of domains after doping PZT with  $\text{Fe}^{3+}$  [62, 63]. The domain size was smaller than predicted by the general parabolic scaling of domain size with the grain size observed in undoped and donor-doped PZT [64]. It was suggested that the domain size reduction (and increase in domain wall density) was caused by nucleation of domain walls at mobile ionic defects, in this case oxygen vacancies [63, 65]. However, this is still unclear as an EPR study

of the distribution of  $(\text{Fe}'_{\text{Zr,Ti}}-\text{V}_0^{\bullet\bullet})^{\bullet}$  associates did not prove that the associates concentrate near domain walls in unpoled  $\text{Fe}^{3+}$ -doped PZT [58].

As discussed in section 2.5.1, the unit cell distortion of PZT depends on the Zr/Ti ratio. In a more general sense, the distortion changes when any of the ions in the cell is removed or substituted. The substituting ion affects the unit cell size, volume and distortion by having a different size, charge or bond length with surrounding ions than the substituted ion. Changes in the local structure of PZT in relation to the Zr/Ti ratio were studied in a paper by Cooper et al. [37]. The local changes in PZT structure get more complex when aliovalent dopants are added as they additionally introduce charged vacancies.

Along with the structural changes, dopants generally also shift the position of the MPB in the  $\text{PbZrO}_3$ - $\text{PbTiO}_3$  phase diagram as each dopant may favour either a rhombohedral or tetragonal structure. This can be illustrated by the observed shift of the peak in relative permittivity to a different Zr/Ti ratio with doping, as shown in Figure 2-12.

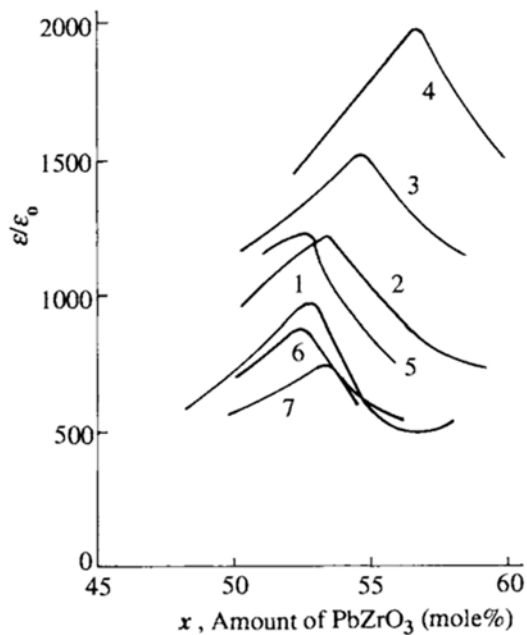


**Figure 2-12** Dependence of relative permittivity of  $\text{Pb}(\text{Zr}_x\text{Ti}_{1-x})\text{O}_3$  on  $x$  in pure PZT (1) and PZT doped with: 1 mol%  $\text{Nd}_2\text{O}_3$  (2), 2 mol%  $\text{Nd}_2\text{O}_3$  (3), 3 mol%  $\text{Nd}_2\text{O}_3$  (4), 1 mol%  $\text{Nb}_2\text{O}_5$  (5), 0.8 mol%  $\text{Fe}_2\text{O}_3$  (6) and 1.25 mol%  $\text{Cr}_2\text{O}_3$  (7) published by Thomann [66] and taken from [34].

### 2.5.3 Processing methods

As with most ceramics, PZT is processed from a powder. The easiest and most common way to achieve this is to mix respective inorganic oxide powders (e.g. PbO, TiO<sub>2</sub>, ZrO<sub>2</sub>) according to the desired stoichiometry and react them at high temperature. Purity and particle size distribution are of a high importance since impurities may contain unwanted dopants and change piezoelectric properties. The particle size distribution influences shaping, reactivity and densification during sintering. High purity oxides (> 99 %) and small particle size (< 10 μm) are usually required.

The initial mixing is generally done by high energy milling, which also serves as a way to reduce the particle size and increase reactivity. Chemical methods such as sol-gel may be used to produce nano-sized highly pure and homogeneous powders.

After initial mixing, the powder is subjected to a high temperature (≈ 800 °C in case of PZT) to form the solid solution. This process is called calcination. Several researchers have studied the reaction sequence of the formation of PZT [67-71] and while there are some discrepancies between their results, the general reaction sequence presented in available literature can be summarised as follows:

- 1) 
$$\text{PbO} + \text{TiO}_2 \longrightarrow \text{PbTiO}_3$$
- 2) 
$$\text{PbO} + \text{ZrO}_2 (+ \text{PbTiO}_3) \longrightarrow \text{PbZrO}_3 \text{ or Zr-rich Pb(Zr,Ti)O}_3$$
- 3) 
$$\text{PbTiO}_3 + \text{PbO} + \text{ZrO}_2 \longrightarrow \text{Ti-rich Pb(Zr,Ti)O}_3$$
- 4) 
$$\text{Ti-rich Pb(Zr,Ti)O}_3 + \text{Zr-rich Pb(Zr,Ti)O}_3 \longrightarrow \text{Pb(Zr,Ti)O}_3.$$

The exact mechanism depends on the stoichiometry, temperature and presence of impurities.

PZT produced by a mixed-oxide route is known to contain local compositional inhomogeneities related to the homogeneity and particle size of the initial raw-oxide mixture and the different diffusion coefficients of individual ions [27]. In addition, the presented reaction sequence doesn't reflect that a Pb-rich liquid phase is likely to be present during the reaction. The PbO-TiO<sub>2</sub> phase diagram shows that for >50 mol% PbO, a PbO-rich liquid phase forms above 838 °C [72]. The temperature of calcination would generally be achieved well before the reaction is complete. Some Zr<sup>4+</sup> and/or dopant ions may diffuse into the Pb-rich liquid phase and not readily mix with PbTiO<sub>3</sub>. Previous in-situ transmission electron microscopy (TEM) and selected-area electron diffraction observations revealed an amorphous PbO-rich phase between the grain boundaries [73]. Hammer and Hoffmann [74] found an amorphous Pb-rich phase in triple junctions between grains by means of scanning transmission electron microscopy and high-resolution TEM in PZT with either stoichiometric and overstoichiometric amount of PbO. Calcined powder is further subjected to high-energy milling to obtain a particle size distribution suitable for shaping and sintering. Most ceramic shaping methods can be applied to PZT, however, the cheapest and most common by far is dry uniaxial pressing. The method produces bulk samples of simple shapes and allows high production rate at the cost of less homogeneous density. It also usually requires the presence of a binder, which can have a significant impact on the final microstructure. Hot and/or isostatic pressing helps to alleviate some of these issues [75]. Other shaping methods include screen printing, calendaring and tape casting for thick films; physical or chemical vapour deposition for thin films; extrusion for rods and tubes; and injection moulding or slip casting for complicated shapes [3].

Conventional sintering of shaped bulk ceramic bodies is performed at temperatures between 1100–1400 °C in air. High temperature processing of PZT is complicated by the volatility of PbO above 800 °C. Careful atmosphere control must be employed in order to prevent the loss

of PbO and detrimental changes in stoichiometry. This is generally done by enclosing reacting powders or green bodies in alumina crucibles and/or adding stoichiometric excess of PbO to the initial powder. For sintering, ceramic bodies can be surrounded by a Pb-containing powder bed of higher PbO volatility (usually PbO + PbZrO<sub>3</sub>). Any organic binders are usually removed prior to sintering. The sintering process itself is complex and not fully understood [27]. Excess of PbO can facilitate liquid phase sintering and enhances densification at initial and intermediate stages [76]. Grain growth at final stages is attributed to normal Ostwald ripening [27]. Lattice diffusion is dominant in PbO deficient and doped PZT [74]. Impurities considerably decrease the sintering temperature and grain size [27].

Sintered ceramic bodies are cut and/or machined to prescribed dimensions and have electrodes applied. Sintered thick film silver electrodes are used for most commercial applications, sputtered gold or nickel-chromium electrodes can be used for special applications [3]. The last step is poling, where an electric field is applied to induce remanent polarisation of the body. The process is usually performed in a silicone oil to prevent discharge and at elevated temperatures (but below  $T_C$ ) to facilitate domain switching.

#### 2.5.4 Microstructure and mechanical properties

Section 2.4 focused on explaining how domain switching affects the general fracture of ferroelectrics. The focus of the work reported in this thesis is on the interrelationship between composition, microstructure and mechanical properties of pure and acceptor-doped PZT, as stated in the introduction. The current knowledge of this area is reviewed below.

#### 2.5.4.1 Microstructure

Many studies of PZT include information about average grain size and density, as these are also highly relevant to piezoelectric properties. Sintered PZT bodies are generally dense (> 95 % of theoretical density) with average grain size between 1–30  $\mu\text{m}$  [3]. In the previous section, the influence of PbO stoichiometry on densification was highlighted. The liquid phase present with the excess of PbO induces rapid early densification, but slows down its intermediate and late stages, which results in lower final densities [76]. Kingon and Clark [76] also reported an increase in grain size in the range of 3–11  $\mu\text{m}$  with increasing PbO content, although the grain size was only recorded for compositions with 1.6 and 0.8 mol% PbO deficiency and 19 mol% PbO excess.

Tai and Kim [77] reported that the average grain size of pure PZT decreased from 14.5 to 12.1  $\mu\text{m}$  with increasing Zr/Ti ratio from 48/52 to 52/48. La (donor) doped PZT was found independent of Zr/Ti ratio in a study by Hoffmann et al. [78]. Density changes were not significant.

Impurities and aliovalent dopants have significant impact on the sintering process and microstructure. It has been suggested that the densification of PZT is affected by the number of cation and anion vacancies, which control the volume diffusion [74, 76]. Pure PZT inherently contains certain amount of Pb vacancies, which can be enhanced or suppressed by impurities or doping. When local electroneutrality is reached, densification slows down. This can be illustrated by the study of Hammer and Hoffman [74], where a minimum density was reached with 0.1–0.2 mol% La. This concentration represented the point where most of vacancies were partially compensated by the dopant. Grain growth can proceed via surface diffusion, which is not affected by vacancy concentration [74]. When either donor or acceptor dopants are present in PZT in sufficient amount, the grain growth is inhibited, and sintered bodies achieve higher

density [74, 79-83]. This was ascribed to the reduction of grain boundary mobility by the drag effect of pinning by dopants [84].

Particle size of consolidated powder can also influence grain size, as demonstrated by Noboru and Masahiko [5]. Their study found that density did not significantly vary within the grain size range of 1–3  $\mu\text{m}$ .

While it is common to report density, studies assessing the character of porosity in PZT are very rare. Guillon et al. [85] compared the porosity of soft and hard commercial PZT by separating total porosity into macro-, meso-, and microporosity. They concluded that soft PZT contained more microporosity than hard PZT, although their methodology and calculated theoretical density ( $> 8 \text{ g}\cdot\text{cm}^{-3}$ ) raise some concerns about the validity of the statement. Malič et al. [86] found spherical intragranular pores  $< 100 \mu\text{m}$  in size present in both Nb- (donor) and Fe- (acceptor) doped PZT. Information about largest defects can be found in some strength studies. Porosity of various size (below  $50 \mu\text{m}$ ) was reported as the main fracture origin in most cases [87-89], although the characterisation was only done on selected samples and no detailed summary was given. An exception is the paper by Wang and Wereszczak [90], which gives a full fracture origin characterization. It concluded that almost 60 % of the specimens failed from volume-distributed agglomerates. This result however, may not reflect the largest defects present in the specimens as the ball-on-ring testing method was used, which concentrates stress into a singular spot below the load transferring ball. Wang et al. [91] reported microcracks emanating from pores in PZT after poling. To the author's knowledge, effects of processing on the character of porosity in PZT have not been explored yet.

#### *2.5.4.2 Mechanical properties*

Vickers hardness of pure PZT was found to be linearly dependent on the inverse root square of the average grain size for constant porosity [92]. The hardness was approximately 4 GPa for an average grain size of 1  $\mu\text{m}$ .

There are number a of studies reporting strength of PZT in relation to microstructural, compositional or processing changes. Their summary is shown in Table 2-1. None of these studies explored more than 1 factor, while even 1 factor generally influenced several microstructural features. It is therefore unclear, which one of the microstructural changes was responsible for the strength increase/decrease. Moreover, the listed studies generally show only a limited amount of microstructural information. Some of the missing features include: detailed characterisation of fracture origins (flaw populations), changes in the character/distribution of porosity or and presence of secondary phases checked by other means than XRD. Contribution of ferroelastic switching to overall strength is not addressed in most of the listed sources.

Table 2-1 Summary of published work dealing with the strength dependence of PZT on composition, processing or microstructure.

Factor(s)	Source	Conclusions	Characterised
Particle/grain size	[5]	$m$ and $\sigma_0$ increase with increasing $G_a$ .	$\rho$ , $G_a$
Hard vs soft commercial PZT	[93]	In as-received state, hard PZT showed higher $\sigma_0$ than soft.	2 examples of fracture origin
PbO content	[94]	Minimum average $\sigma$ at stoichiometric composition.	$\rho$ , $K_{IC}$
$T_{sint}$ of co-doped PZT	[8]	Multiple average $\sigma$ maxima observed, explained by competing $\rho$ and $G_a$ . (lowest $G_a$ , highest $\rho = \sigma$ maximum).	$\rho$ , $G_a$ , $K_{IC}$
Hard vs soft commercial PZT	[85, 95]	Inconclusive in terms of $\sigma_0$ , hard PZT showed higher $m$ and transgranular fracture. Hard PZT showed higher $K_{IC}$ .	$\rho$ , $G_a$ , mean pore diameter, max pore diameter, fracture origin, $Y$ , $K_{IC}$
Zr/Ti ratio	[6]	Minimum flexural strength and $K_{IC}$ at the MPB. Secondary PbO phase present.	$\rho$ , $G_a = \text{const.}$ , $K_{IC}$
Artificial spherical pores	[9]	Only total porosity, but not pore diameter controlled the median $\sigma$ as fracture origins were pore agglomerates of a constant size	$\rho$ , pore diameter
Surface treatment	[96]	Surface treatment did not significantly affect $\sigma$ . $\sigma$ was dominated by microcracks caused by PbO secondary phase.	fracture origin

A number of researchers have also reported the influence of composition, microstructure and processing of PZT on the fracture toughness; a summary is given in Table 2-2. Much of the toughening was ascribed to ferroelastic switching contributions. These are enhanced by soft doping or when approaching the MPB, although contradicting results were found in [6], where  $K_{IC}$  showed a minimum at the MPB, and in [77], where  $K_{IC}$  did not significantly changed with the Zr/Ti ratio. Yoon et al. [97] reported that a secondary phase created by excessive doping enhanced fracture toughness. Similar to strength, fracture toughness is influenced by various

factors, which are not easily distinguished. The situation is even more complex when the piece is polarized and/or in the presence of electric field.

Table 2-2 Summary of published work dealing with the fracture toughness dependence of PZT on composition, processing or microstructure.

<b>Factor(s)</b>	<b>Source</b>	<b>Conclusions</b>
Grain size	[92]	Decreases below $G_a$ of 1 $\mu\text{m}$ and is constant above.
Doping, grain size	[32]	Larger $G_a$ and soft doping enhance $K_{IC}$ ; related to ferroelastic switching.
Grain size and crack length	[98]	PZT with larger $G_a$ showed higher initial $K_{IC}$ , but same plateau $K_{IC}$ was reached at a certain crack length.
Grain boundary shape	[99]	50% increase with undulated grain boundaries
Nb <sup>5+</sup> (soft) doping	[100]	maximum at 2 at% of Nb <sup>5+</sup> due to enhanced domain switching.
Zr/Ti ratio	[77]	Slight increase towards Zr-rich PZT.
Zr/Ti for soft doped PZT	[6]	Minimum at the MPB. PbO secondary phase present.
PbO content	[94]	Maximum at 2 at% stoichiometric excess.
$T_{\text{sint}}$ of co-doped PZT	[8]	2 maxima at different $T_{\text{sint}}$ .
Co-doping of PZT by W <sup>6+</sup> and Y <sup>3+</sup>	[97]	Maximum at 3 at% of Pb(Y <sub>0.66</sub> W <sub>0.33</sub> )O <sub>3</sub> – reinforcement by secondary phase

The fracture mode of PZT ranges from intergranular, where the crack travels along grain boundaries, to transgranular, where the crack goes straight through grains. There are multiple factors affecting the path of an opening crack. The basic assumption is that the crack favours the path requiring the least amount of energy. When grains are large ( $\approx 20 \mu\text{m}$  in PZT), deflecting the crack along grain boundaries would consume too much energy, therefore the crack favours transgranular fracture [101]. Intergranular fracture is generally dominant at small grain size, as confirmed by numerical models [102, 103]. Some studies explain an observed

change in fracture mode by weakened or strengthened grain boundaries [8, 85, 95, 104, 105]. Watanabe and Tsunekawa suggested that when the fracture shows a mixed-mode, intergranular fracture increases with the fraction of random high-energy grain boundaries [106]. Porosity can also influence the path of a crack. It is known that intragranular pores enhance the transgranular fracture [18]. In PZT studies, the transition from inter- to transgranular was usually accompanied by an increase in strength, however, it was not clear whether the two changes were related.

With the exception of the work reported in [92] and [101], the referenced studies used powders made by conventional mixed oxide routes. Some researchers used overstoichiometric amount of PbO in order to enhance the sintering process [9, 96] or to compensate for PbO loss during sintering [101]. Most studies used various Pb-rich powder beds in order to control the PbO loss. However, none of these studies mentioned any results that would confirm that the lead stoichiometry did not change (apart from X-Ray diffraction, which cannot detect low amounts of secondary phases). Studies using commercial PZT [85, 92, 93, 98] did not have any control over the composition.

### 3 MOTIVATION AND OBJECTIVES

As explained in previous chapters, the mechanical properties and fracture of ferroelectric ceramics present less explored, but important areas of research. Even more so with the recent efforts to minimise waste and increase longevity of products. Higher strength and reliability of ceramic parts may also allow their use in more severe conditions. The main shortcomings of previously published studies relating processing, microstructure and mechanical properties are their limited scope and characterisation. With several microstructural and fracture-related changes induced by a single variable, it is difficult to distinguish the exact cause of the observed mechanical-property variations. Furthermore, most of the work focusing on these phenomena in PZT fails to address some important sources of bias such as ferroelastic switching or the presence of secondary phases. Extending the current knowledge in this area and addressing listed issues serves as one of the main motivations in this project.

Another purpose of this work is to find ways of improving the quality of commercial PZT ceramics produced by Noliac Ceramics s.r.o, a part of CTS Corporation, which provided partial funding for this research. To coincide with its current needs and issues, and to be able to get satisfactory results within a reasonable timeframe, the work was focused on effects of hard (acceptor) doping represented by  $\text{Fe}^{3+}$ . Additional factors, namely Zr/Ti ratio, sintering temperature and presence of  $\text{Sr}^{2+}$  isovalent dopant were also explored to induce a range of microstructural responses and match appropriate ones with observed mechanical-property variations.

The main objectives of this thesis can be summarised as follows:

- 1) To prepare PZT bulk specimens closely resembling commercially produced ceramics by using similar processing variables and methods.
- 2) To measure basic dielectric and piezoelectric properties of prepared specimens and compare them with available literature.
- 3) To design an equibiaxial flexural strength test fixture and optimise its performance to achieve reliable and repeatable strength results. The test should be suitable for further use in commercial quality control.
- 4) To determine the influence of composition, namely isovalent  $\text{Sr}^{2+}$  doping, acceptor  $\text{Fe}^{3+}$  doping and ratio of Zr/Ti as well as sintering temperature, on the physical properties of PZT such as grain size, density, pore size distribution and phase content.
- 5) To study the influence of doping, Zr/Ti ratio and sintering temperature on the mechanical properties of PZT, namely elastic modulus, hardness, surface roughness and flexural strength.
- 6) To determine whether PZT doped with  $\text{Fe}^{3+}$  responds to changes of studied factors in the same manner as undoped PZT.
- 7) To identify structural or microstructural properties responsible for any strength variations and suggest means of improving strength and reliability of the acceptor-doped PZT.
- 8) To assess the applicability of the obtained results in practice by comparing them with the commercial hard PZT.

With regards to the shortcomings of previous studies listed earlier, the emphasis shall be put on:

- Careful control of sample preparation, monitoring of PbO loss and presence of secondary phases by means of repeated weighing, X-Ray diffraction (XRD) and electron microscopy.
- Thorough characterisation of physical, structural, microstructural and mechanical properties and their interrelations.
- Development and optimisation of equibiaxial flexural strength test and strength testing of reasonably large sets of specimens to make statistical conclusions based on the Weibull probability distribution.
- Fractography of reasonable number of specimens from each tested batch in order to draw conclusions about prevalent origins of fracture.

## 4 EXPERIMENTAL METHODS

This chapter describes all the experimental methods used in this work. It is divided into 3 sections, each dealing with a different category of measured properties, namely physical, structural and microstructural properties; mechanical properties; and piezoelectric and dielectric properties. Sample preparation and its optimisation is presented later in Chapter 5.

### 4.1 Physical, structural and microstructural properties

#### 4.1.1 Mass, density, dimensions, flatness, parallelism

Several balances were used in the project. They were denoted as A–D for convenience and their parameters are summarised in Table 4-1. Balance A was used for weighing out raw oxides, calcined powders and binder. Balance B was used for measuring mass loss after calcination by weighing the completely assembled crucibles with powder prior to and after calcination. The assembly exceeded the measurement range of balance A. Balance C was used for single-sample mass measurements in order to ascertain parameters such as mass loss after binder burnout or sintering.

Table 4-1 List of used balances

Symbol	Manufacturer, model	Max load (g)	Readability (g)
A	Sartorius TE612	610	0.01
B	TSCALE QHW-6	6000	0.05
C	Mettler Toledo ML204 Newclassic	220	0.0001
D	Sartorius R300S	250	0.001

Green density was obtained by dividing the mass of the compact by its volume. Mass of each compact was measured using balance C. Thickness was measured at 5 points shown in Figure 4-1 using digital micrometer (Micromaster IP54, TESA, 0–30 mm/0.001 mm/±0.002 mm). Compact volume was calculated using average sample thickness and die diameter. The same

thickness measurement was applied to sintered samples in order to calculate thickness shrinkage after sintering.

Bulk density of sintered ceramics was determined by the Archimedes' method. Mass of samples in air/submerged in deionised water was measured using balance D. Machined samples were used for this purpose.

Thickness of machined samples was measured using a digital indicator (Absolute, Mitutoyo, 0–12.7 mm/0.001 mm/±0.002 mm) at 5 points (Figure 4-1). Diameter of machined samples was measured using digital Vernier caliper (Absolute, Mitutoyo, 0–160 mm/0.01 mm/±0.02 mm) in 2 perpendicular directions.

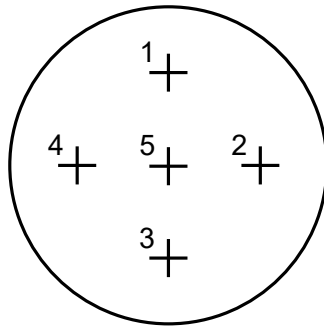


**Figure 4-1 Schematic of thickness measurement points.**

Flatness and parallelism of 2 sets of machined samples were measured by 2 separate coordinate measuring machine systems with resolution of 0.0001 mm – Mitutoyo EURO-C544 (set 1) and DeMeet-220 (set 2). 10 points on each side of the disc were used to determine both parameters using the least square method.

#### 4.1.2 Particle size

The particle size distributions of calcined and milled powders were investigated with a laser diffraction particle size analyser (Helos, Sympatec). Each sample of powder ( $\approx 0.2$  g) was dispersed in 25 ml of deionised water with 1 drop of dispersant. Ultrasonic agitation was used for 10 s prior to the measurement to separate any residual soft agglomerates. Each measurement was repeated 3 times to ensure no soft agglomerates were present.

#### 4.1.3 Powder X-ray diffraction

One machined sample from each batch was crushed and ground to fine powder using a mortar and pestle. Ground powder was passed through sieve with 36  $\mu\text{m}$  mesh size to remove any oversized particles and dried at 120 °C for 24 h. Each powder was analysed at room temperature using an X-ray diffractometer (XRD) (D2 PHASER, Bruker) with Bragg-Brentano geometry and Co-K $\alpha$  radiation (wavelength of 1.79089 Å). A range of 20–80 °2 $\theta$  with 0.02 ° step size was used to check for the presence of any secondary phases, and a range of 43–54 °2 $\theta$  with 0.02 ° step size and longer scan time per step was used for calculating lattice parameters and content of tetragonal/rhombohedral phases. A standard corundum sample supplied by Bruker was measured using the same conditions to correct for any instrument-related peak shifts. Corundum reflections were matched with a powder diffraction file from PDF-4 database ( $\text{Al}_2\text{O}_3$ , #99-500-0000).

Individual peaks from the slow scan were fitted using software Fityk 0.9.8 [107]. The range contained 6 reflections, 3 tetragonal (111)<sub>T</sub>, (002)<sub>T</sub>, (200)<sub>T</sub> and 3 rhombohedral (111)<sub>R</sub>, ( $\bar{1}11$ )<sub>R</sub>, (200)<sub>R</sub>. Only {200} reflections could be reliably resolved due to a severe overlap of {111} reflections and the limited resolution of the diffractometer. Peak shapes were described by a pseudo-Voigt function (equation (4-1)), where  $a_0$  is peak height,  $a_1$  peak centre,  $a_2$  is half width

at half maximum and  $a_3$  is a shape factor proportional to the ratio of Gaussian and Lorentzian contributions.

$$I(2\theta) = a_0 \left[ (1 - a_3) \exp\left(-\ln(2) \left(\frac{2\theta - a_1}{a_2}\right)^2\right) + \frac{a_3}{1 + \left(\frac{2\theta - a_1}{a_2}\right)^2} \right] \quad (4-1)$$

Two restrictions had to be applied to achieve a successful fit:

- 1) If a peak showed an excessive overlap, its shape factor was restricted to 0.5, making it an even mixture of the Gaussian and Lorentzian functions. Values around 0.5 gave the best fit when the shape factor did not need to be restricted.
- 2) If less than half of any tetragonal peak  $(002)_T$  or  $(200)_T$  was visible, its full width at half maximum (FWHM) was restricted to a value found in the closest composition, where the peak did not excessively overlap. Figure 4-2 shows an example of a pattern where less than a half of the  $(002)_T$  peak is visible. Its FWHM value was therefore restricted to the value of the peak found in batch 11. It was shown that the FWHM of  $\{200\}$  tetragonal reflections does not considerably change around the MPB, unlike the  $(200)_R$  rhombohedral reflection which experiences a significant broadening at the MPB [27]. Therefore, restricting tetragonal peaks should not introduce a significant error.

Example of a fit is shown in Figure 4-2, restrictions applied to specific compositions are listed in Table 4-2.

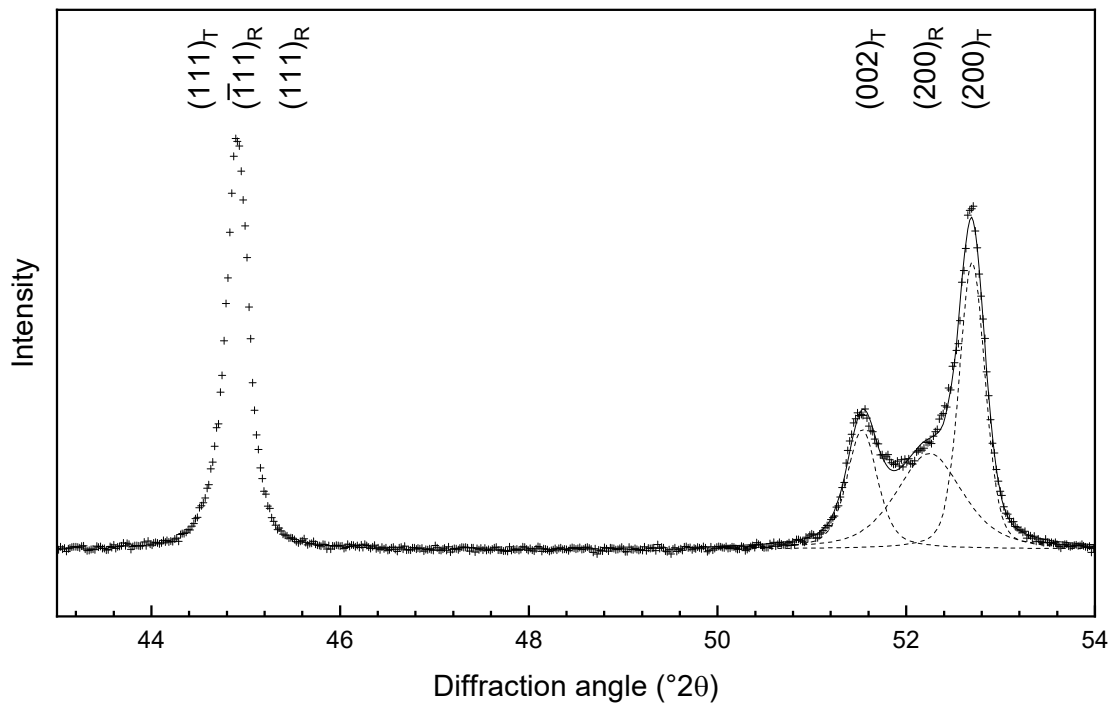


**Figure 4-2 Example of fitted diffraction pattern (batch 13). Crosses represent acquired data, dashed lines individual peak fits and full line their combination.**

Table 4-2 Peak shape and FWHM restrictions used to achieve successful fit of XRD data of  $(\text{Pb}_{1-x}\text{Sr}_x)(\text{Zr}_y\text{Ti}_{1-y})_{1-z}\text{Fe}_2\text{O}_3$

Batch no.	x (Sr)	y (Zr)	z (Fe)	Peaks with shape restricted to 0.5	Peaks with FWHM restricted to the value of peaks in (batch no.)
			(at%)		
1	0	52		(200) <sub>R</sub>	
2		49			
3		51			
4			0		
5	5	52			
6					
7		53		(002) <sub>T</sub>	
8		55		(002) <sub>T</sub> , (200) <sub>R</sub> , (200) <sub>T</sub>	(002) <sub>T</sub> , (200) <sub>T</sub> (7)
10		52	0.4	(002) <sub>T</sub> , (200) <sub>R</sub>	
9	0	52		(002) <sub>T</sub>	(002) <sub>T</sub> (11)
11		49		(200) <sub>R</sub>	
12		51			
13			1.4	(002) <sub>T</sub> , (200) <sub>R</sub>	(002) <sub>T</sub> (11)
14	5	52			
15					
16		53		(002) <sub>T</sub> , (200) <sub>R</sub> , (200) <sub>T</sub>	(002) <sub>T</sub> (11), (200) <sub>T</sub> (13)
17		55			
18		52	2.0	(002) <sub>T</sub> , (200) <sub>R</sub>	(002) <sub>T</sub> (11)

The obtained peak positions were used to calculate interplanar distance  $d_{\text{diff}}$  according to Bragg's law using equation (4-2), where  $\theta$  is the diffraction angle,  $n$  is a positive integer and  $\lambda$  is the wavelength of the incident wave.

$$2d_{\text{diff}}\sin\theta = n\lambda \quad (4-2)$$

Lattice parameters  $a_T$ ,  $c_T$  were determined according to equation (4-3), where  $h$ ,  $k$ ,  $l$  are Miller indices of diffracting planes. Only lattice parameters of the tetragonal phase could be calculated as only one rhombohedral peak was fitted, while at least two peaks are needed for the calculation.

$$\frac{1}{d_{\text{diff}}^2} = \frac{h^2 + k^2}{a_T^2} + \frac{l^2}{c_T^2} \quad (4-3)$$

Theoretical density ( $\rho_t$ ) was calculated using equation (4-4), where  $M$  is a molar mass of the unit cell,  $V_{\text{cell}}$  is the unit cell volume and  $N_A$  the Avogadro constant. Molar mass of the unit cell was obtained using the sum of atomic masses of individual atoms multiplied by their fraction according to specified composition. Unit cell volume was calculated from the lattice parameters of tetragonal phase using equation (4-5).

$$\rho_t = \frac{M}{V_{\text{cell}} N_A} \quad (4-4)$$

$$V_{\text{cell}} = a_T^2 c_T \quad (4-5)$$

Content of both phases was estimated using integrated intensities of {200} tetragonal (T) and rhombohedral (R) reflections and equation (4-6) commonly used for this purpose, in which  $\chi_T$  is the fraction of tetragonal phase [34, 63].

$$\chi_T = \frac{I(200)_T + I(002)_T}{I(200)_T + I(002)_T + I(002)_R} \quad (4-6)$$

#### 4.1.4 Pore size distribution

The porosity of sintered samples was studied using reflected light microscopy (Axioskop 2 MAT, Zeiss). One machined cylindrical sample from each batch of approximately 60 was ground and polished to 1 $\mu\text{m}$  finish using SiC paper and diamond suspensions. Surfaces were photographed at 5 and 10 $\times$  magnification; and the acquired images were processed using ImageJ software (the process is illustrated in Figure 4-3) [108]. The “IsoData” function was used for automatic thresholding and pore area was quantified using the “Analyze particles” function. Only pores consisting of more than 10 px were analysed to avoid large inaccuracies [109]. A total of 15 images per batch (total area of 7.4 mm<sup>2</sup>) were combined for each pore size distribution.

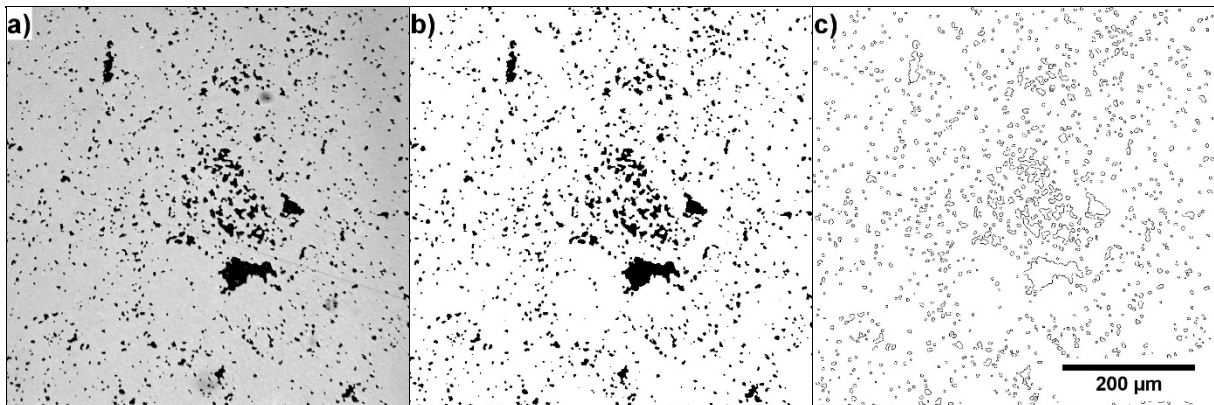


**Figure 4-3 Image processing using ImageJ: a) original optical micrograph of the polished surface, b) thresholded image, c) outlines of analysed pores**

Pore size was described by the maximum Feret diameter, which is defined as the longest possible distance between any 2 points along the pore boundary, as illustrated in Figure 4-4.

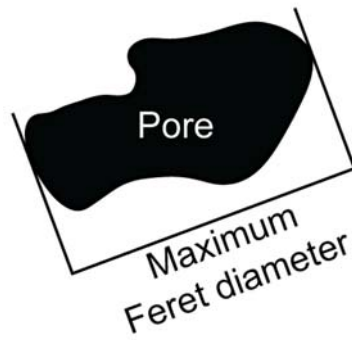


**Figure 4-4 Maximum Feret diameter measured on a non-equiaxed pore.**

#### 4.1.5 Grain size

A single cylindrical sample from each batch was ground and polished to a scratch-free surface using successive SiC papers and diamond suspensions of defined particle size (6, 3, 1  $\mu\text{m}$ ). Colloidal silica suspension was used in the final polishing step. Polished samples were thermally etched in air at suitable temperatures (generally 150  $^{\circ}\text{C}$  below the sintering temperature) for 10 min to reveal their grain structure.

Grain structure was observed with scanning electron microscopes (SEM) 6060 LV (Jeol, magnifications up to 4000 $\times$ ) and XL-30 (Philips, magnifications higher than 4000 $\times$ ). Acquired micrographs were calibrated using the ImageJ software [108]. Average grain size was calculated by the lineal intercept method described in EN ISO 13383-1 (Method A). [110] 5 lines per area and 5 areas per sample were used for the calculation, which corresponds to a total of 600–1000 analysed grains per sample.

#### 4.1.6 Nanoscale observations

Thin sections of selected materials ( $10 \times 10 \mu\text{m}$ ) were cut from their respective sintered ceramic bodies using a plasma focused ion beam (PFIB) (Helios G4 CXe, FEI). An example of a thin section is shown in Figure 4-5. The specimen was observed using a scanning electron microscope (MIRA3, TESCAN) and a transmission electron microscope (TEM) (Talos F200X, FEI).

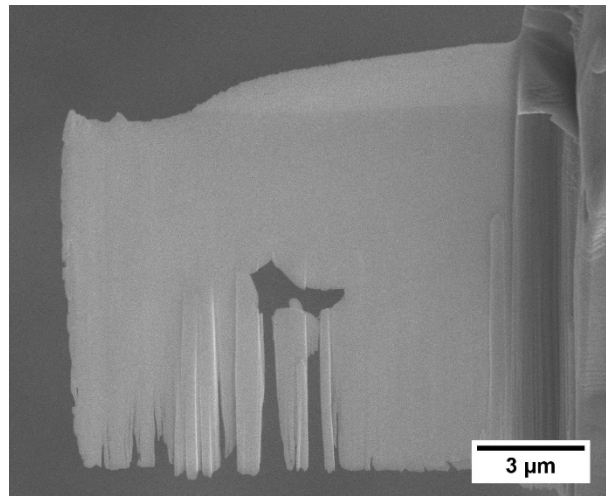


**Figure 4-5 Thin section cut by PFIB and used for nanoscale observations.**

## 4.2 Mechanical properties

### 4.2.1 Surface roughness

A high-performance stylus profilometer (XP 200, Ambios Technology) was used to describe the surface finish of the sintered samples as-received after machining. Each scan was performed on a 2mm long line at  $0.1 \text{ mm}\cdot\text{s}^{-1}$  with 10 mg stylus force. The acquired profile was levelled with a least square fit and  $500\mu\text{m}$  high pass cut off was used to obtain  $R_z$  values. The surface profile was described by parameters  $R_a$  (arithmetic average of the roughness profile),  $R_z$  (average distance between the highest peak and lowest valley in each sampling length of  $200 \mu\text{m}$ ) and  $R_v$  (maximum valley depth). At least 2 samples per batch were used for these measurements and their arithmetic average values and standard deviations are reported.

### 4.2.2 Hardness

The hardness of sintered samples was measured using a Vickers indenter (5030 SKV, Indentec). The surface of a single sample from each batch was ground and polished to a  $1\mu\text{m}$  surface finish using SiC paper and diamond suspensions. Polished samples were annealed at  $650 \text{ }^\circ\text{C}$  for 4 h prior to indentation in order to remove any residual strain effects from the polishing. 22 indentations were made in each sample using a load of 1 kg (9.81 N) for 10 s. A load of 1 kg is recommended for advanced ceramics by ASTM C1327-15 and EN 843-4 standards [111, 112]. The hardness was calculated using the following equation:

$$H_V = 0.0018544 \left( \frac{F}{d_V^2} \right), \quad (4-7)$$

where  $F$  is the used force and  $d_V$  is the average length of the two diagonals of the indentation. Indentation diagonals were measured using a built-in microscope of the indenter as well as separately, by SEM micrographs (6060 LV, Jeol). This measurement is crucial for hardness

determination and recorded values depend heavily on the user's judgement as the corners of the indent are not often as clear in ceramics, compared to other materials. Measurement by SEM is generally not recommended because of the low topographic contrast of the indentation and the need for careful image calibration [112]. However, preliminary hardness measurements on iron doped and undoped samples at different loads showed that SEM measurements were in fact more reliable than optical measurements as illustrated in Figure 4-6. In this case, the Vickers hardness does not change with increasing load. Similar results from both methods were obtained for the sample with 0 at% Fe. The variation in Vickers hardness from optical microscope observations was possibly caused by the operator's lack of experience as well as the inability to precisely determine the size of small indentations due to the limited resolution of the microscope. As a result, SEM was chosen as the main method of measurement of indentation diagonals.

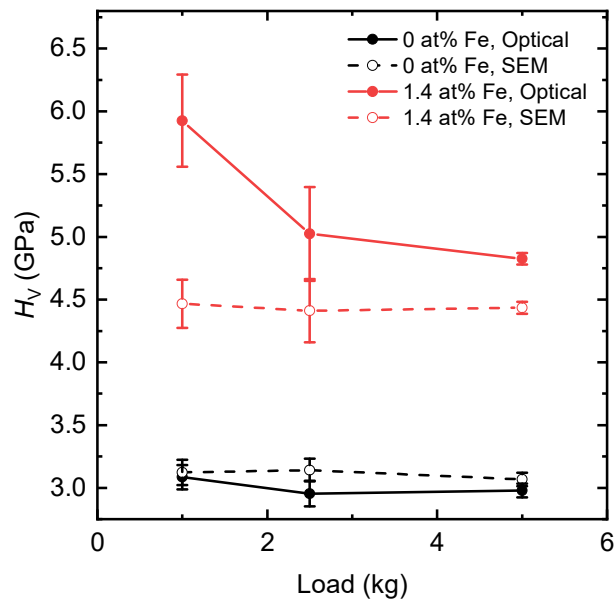


**Figure 4-6 Preliminary Vickers hardness (HV1/10) results for various levels of doping, loads and diagonal length measuring techniques. Error bars represent the standard deviation of mean (SDM).**

#### 4.2.3 Elastic modulus and Poisson's ratio

Dynamic Young's modulus, shear modulus and Poisson's ratio were measured using the impulse excitation of vibration method (RFDA, IMCE) located in National Physical Laboratory, Teddington, UK [1, 113, 114]. As-machined disc specimens were placed on a polymer string support system and were struck with an impulse tool (steel ball glued to a flexible polymer rod). Excited vibrations were picked up by a microphone, signal was processed using Fourier Transformation and resonant frequencies were identified. An overview of the test apparatus is shown in Figure 4-7.

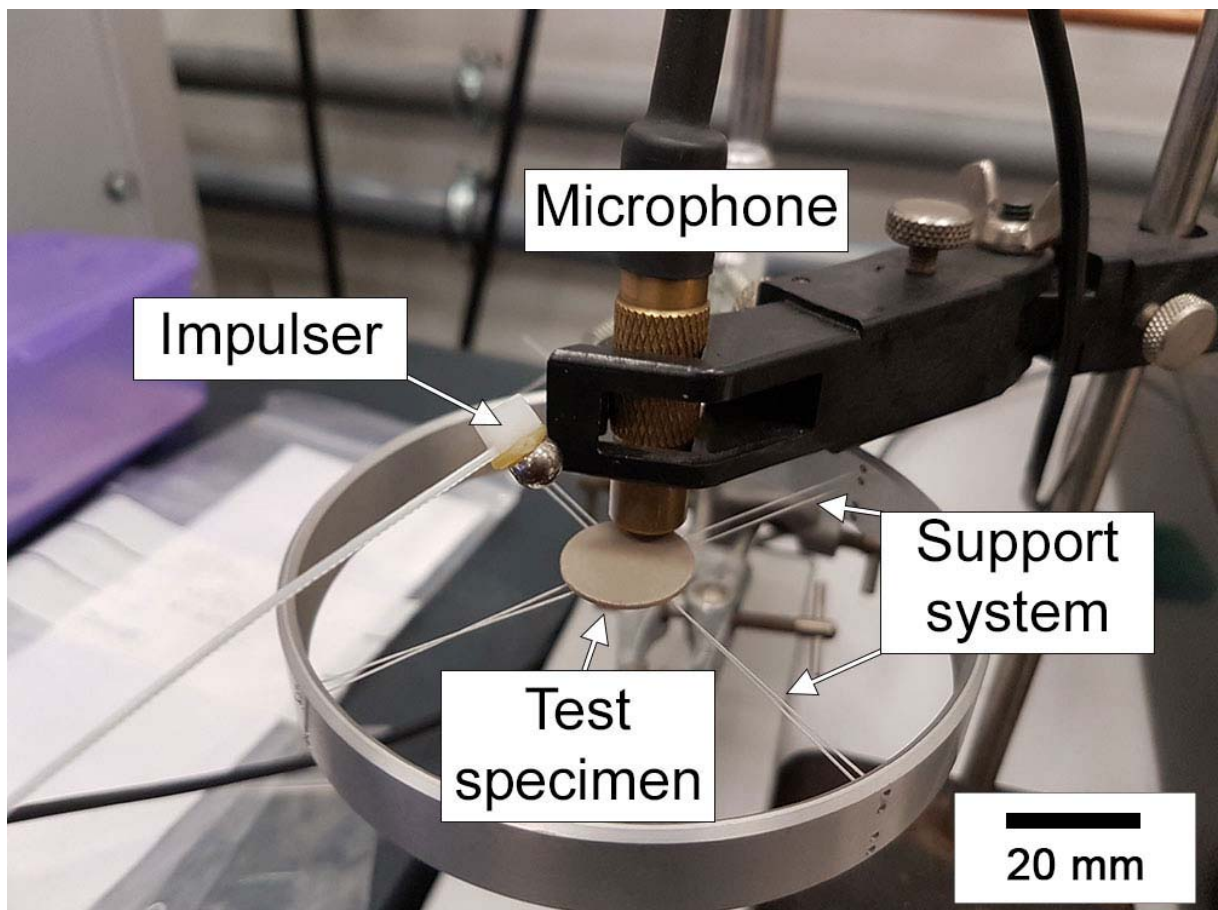


Figure 4-7 Test apparatus for excitation and measurement of vibrations.

Poisson's ratio  $\nu$  was calculated using the first and second natural resonant frequencies  $f_1$  and  $f_2$  according to the following equation:

$$\begin{aligned} \nu = & a_a + b_a \left(\frac{t}{r}\right) + c_a \left(\frac{f_2}{f_1}\right) + d_a \left(\frac{t}{r}\right)^2 + e_a \left(\frac{f_2}{f_1}\right)^2 + f_a \left(\frac{t}{r}\right) \left(\frac{f_2}{f_1}\right) + g_a \left(\frac{t}{r}\right)^3 \\ & + h_a \left(\frac{f_2}{f_1}\right)^3 + i_a \left(\frac{t}{r}\right) \left(\frac{f_2}{f_1}\right)^2 + j_a \left(\frac{t}{r}\right)^2 \left(\frac{f_2}{f_1}\right), \end{aligned} \quad (4-8)$$

where  $t$  = disc thickness,  $r$  = disc radius and  $a$ - $j$  = polynomial coefficients listed in [1].

Dynamic Young's modulus  $Y$  was obtained as an average of  $Y_1$  and  $Y_2$  calculated from the first and second resonant frequencies:

$$\begin{aligned} Y_1 &= [37.6991 f_1^2 d^2 m (1 - \nu^2)] / (K_1^2 t^3), \\ Y_2 &= [37.6991 f_2^2 d^2 m (1 - \nu^2)] / (K_2^2 t^3), \end{aligned} \quad (4-9)$$

where  $d$  = disc diameter,  $m$  = disc mass and  $K_1, K_2$  = first and second geometric factors calculated using the following equation:

$$K_i = \frac{\left( a_b + b_b \left(\frac{t}{r}\right) + c_b \left(\frac{t}{r}\right)^2 + d_b \nu + e_b \nu^2 + f_b \nu^3 \right)}{\left( 1 + g_b \left(\frac{t}{r}\right) + h_b \left(\frac{t}{r}\right)^2 + i_b \nu + j_b \nu^2 \right)}. \quad (4-10)$$

Values of polynomial coefficients  $a_b$ - $j_b$  can be found in [1].

5 individual measurements on 4 different samples per batch were performed in order to get an average value and a standard deviation of  $\nu$  and  $Y$ .

#### 4.2.4 Mechanical strength

Both tensile and flexural loading modes and their associated testing methods were considered for mechanical strength measurements. The ring-on-ring (ROR) equibiaxial flexural strength test was chosen as the most appropriate for this work as it offered the lowest requirements on specimen preparation combined with relatively large area exposed to the equibiaxial tensile stress. The design of the fixture used for the strength test, the strength testing procedure and its optimisation and validation are described in the following sections.

##### *4.2.4.1 Design of fixture used for the ROR equibiaxial flexural strength test*

The basic testing configuration, illustrated in Figure 4-8, consists of a thin cylindrical specimen inserted between 2 concentric rings of a different diameter, where the smaller ring is denoted as the “load ring” and the larger ring is denoted as the “support ring.” The rings are moved towards each other, creating equibiaxial compressive and tensile stresses at the specimen faces. The radial stress distribution on the tensile side of a specimen is illustrated in Figure 4-9, where the stress is constant inside the load ring and a sharp stress decrease is observed outside the load ring. The diagram also illustrates that the radial stress is enhanced if the load ring is off-centred. The failure of a specimen is initiated from a flaw located on or near the tensile surface; the maximum force recorded before the failure is used for the calculation of strength.

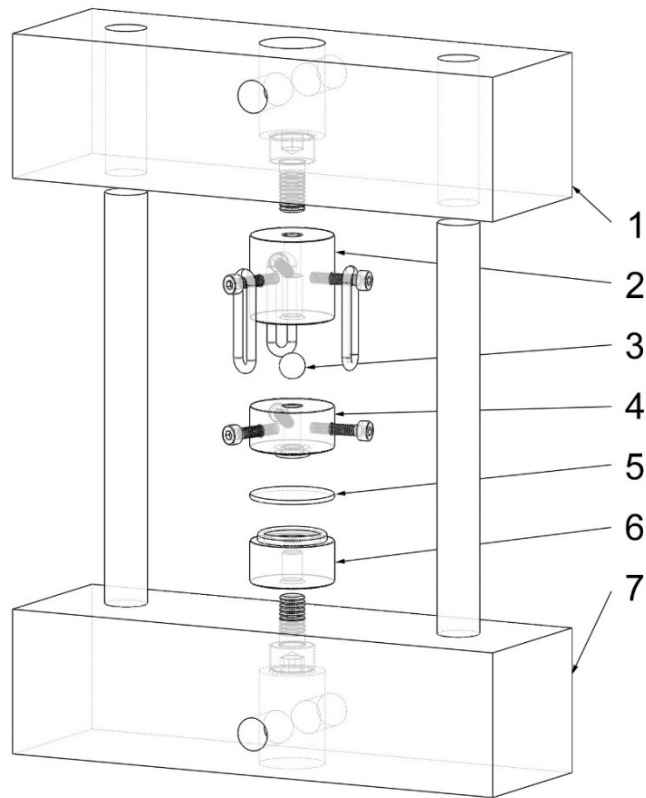


Figure 4-8 Fixture for equibiaxial strength test. Legend: 1 – top block, 2 – connector, 3 – ball bearing, 4 – load ring, 5 – test piece, 6 – support ring, 7 – bottom block.

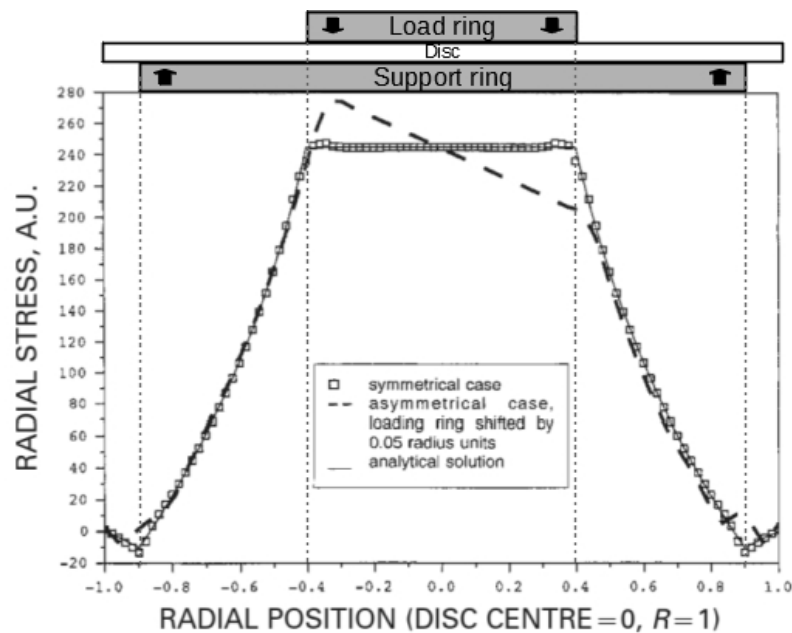


Figure 4-9 Radial stress distribution on the tensile side of a disc loaded in a ring-on-ring equibiaxial flexural strength test (reproduced from [115]). The load ring diameter is 1 mm. Solid line represents an analytical solution of equations derived from the simple plate theory. Squares and dashed line show the radial stress distribution calculated by the 2D finite element analysis for symmetrical and asymmetrical loading conditions respectively.

The ASTM C1499-15 standard [16] and Good measurement practice guide for biaxial flexural strength testing of ceramic materials written by Morrell [116] were used as primary resources for the fixture design. The fixture was made of stainless steel, rings were hardened to  $HRC > 40$  as prescribed by the standard. Hardened steel is non-compliant and may cause friction between test piece and rings. To reduce this effect, more compliant materials such as polymers [116] may be used. Steel was selected in this work due to its lower machining cost and high durability (several hundred samples were tested). Compliant layers between rings and test piece were employed to help reduce frictional effects and compensate for possible out-of-flatness of the machined samples.

In an attempt to minimise friction, more sophisticated ring geometries have also been explored by several researchers in the past, such as ring of a ball-bearings [117] or a ring made of coiled wire on a liquid-filled diaphragm [118]. When designing a ROR fixture, other important aspects, such as making sure the rings are concentric and how to attach the fixture to a load frame, also must be considered. In this work, the fixture was designed with steel blocks on the top and bottom connected by 2 guiding rods (Figure 4-8). In this way, the fixture does not rely on concentricity of the load frame connectors and does not need to be connected to the load frame at the bottom. The bottom ring is attached to the steel block by a screw. The load ring rests on a connector part with a ball bearing in between, which allows tilting and helps to compensate for any possible out-of-flatness of samples. 3 rubber “O” rings were used to keep the load ring attached to the connector.

With this chosen fixture design and the relatively small test piece diameter of 20 mm, it was deemed too difficult and costly to try adopting more elaborate ring geometry than the simple full metal rings.

Dimensions of load/support rings and the test-piece must be chosen in a way that the stress state can be reasonably described by a simple plate theory. The workflow of the selection is illustrated in Figure 4-10. Ceramic discs of 20 mm diameter and 2 mm thickness are widely used by the industrial sponsors for various tests, therefore a sample diameter of 20 mm was also adopted for strength tests. Sample thickness had to be iteratively decreased (to 1.65 mm) so that the sample diameter fell within the allowed range given by the support ring diameter. For the calculation of maximum support ring diameter range in Figure 4-10, expected fracture strength of 90 MPa [93] and elastic modulus of 80 GPa [119] were used. Calculated allowed ranges for the sample and ring dimensions and their chosen values are listed in Table 4-3. Support ring diameter and sample diameter were close to the lowest allowed values.

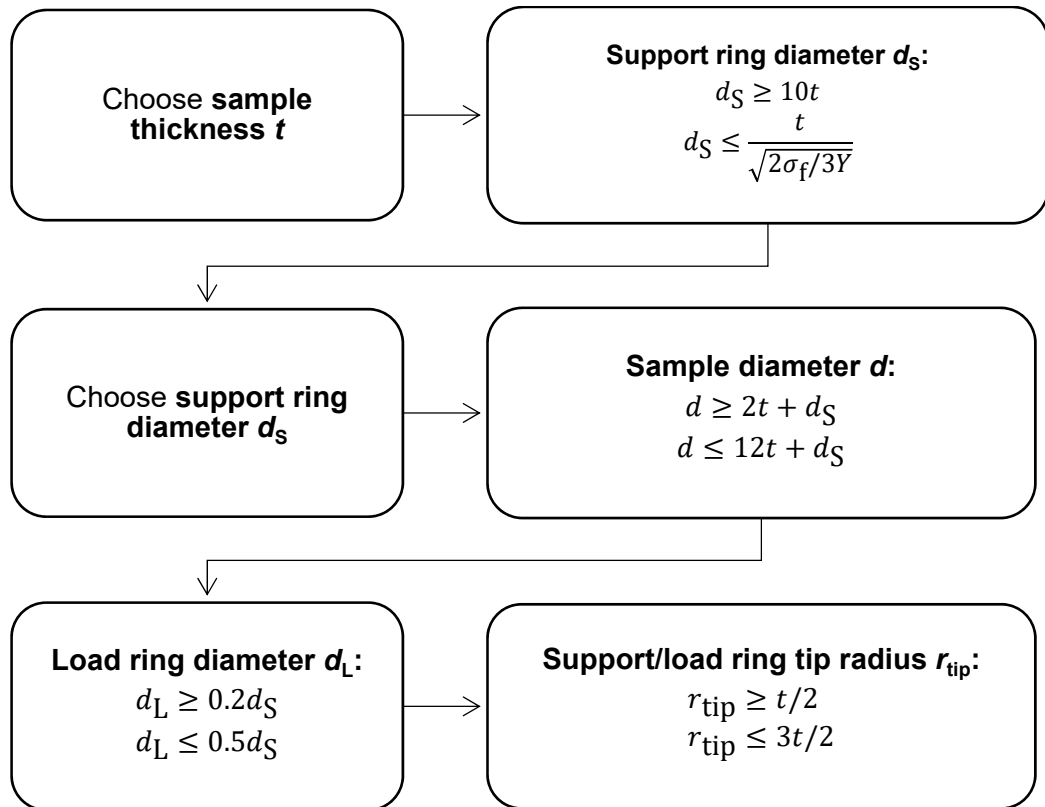


**Figure 4-10 Workflow for choosing ring and test-piece dimensions (from [16]), where  $t$  = sample thickness (mm),  $d_s$  = support ring diameter (mm),  $d_L$  = load ring diameter (mm),  $r_{tip}$  = support/load ring tip radius (mm),  $\sigma_f$  = expected fracture strength (MPa),  $Y$  = modulus of elasticity (MPa).**

Table 4-3 List of test-piece and support/load ring dimensions for the first version of the fixture (later denoted as “Test 1”)

	<b>Allowed range (mm)</b>	<b>Choice (mm)</b>
Sample thickness $t$		1.65
Support ring diameter $d_s$	16.50–57.00	16.50
Sample diameter $d$	19.80–36.30	20.00
Load ring diameter $d_L$	3.30–8.25	5.80
Support/load ring tip radius $r_{tip}$	0.825–2.475	1.65

#### 4.2.4.2 Testing procedure

As-machined ceramic samples were cleaned in an ultrasonic bath (MXB6, Grant Instruments) using water and isopropanol. Samples were visually inspected and 42 discs with the lowest handling damage and visible defects from each batch were selected and annealed at 650 °C for 4 h (see chapter 5.1.4 for annealing optimisation). The thickness and diameter of each specimen was measured according to the procedures described in chapter 4.1.1. Measured samples were stored in a sealed plastic sample box with silica gel desiccant.

Prior to testing, samples were marked and taped on the compressive side (Magic Tape, Scotch) to preserve fragments after fracture. Ceramic surfaces were cleaned by compressed air immediately prior to taping or testing (Kenair Air Duster, Kenro). A single mark on the side of the sample was made with a marker pen, which enabled consistent specimen placement on the loading ring and observation of the fracture origin location in relation to the fixture.

Individual samples were placed on the support ring with a sheet of rubber underneath (thickness of 0.62 mm) and the side mark facing the user. The sample was centred by hand using the base of the support ring as a reference (it had the same diameter as the sample). A strip of PTFE tape (thickness of 0.075 mm) was carefully placed on top of the sample (compressive side). The use of a rubber sheet is recommended by the ASTM C1499-15 standard to minimise the effects of

any misalignment between the test specimen and lower ring, the purpose of the PTFE tape is to minimise the effects of friction at the load (upper) ring interface. A photograph of the sample arrangement is shown in Figure 4-11.

The load ring was mounted to a load frame (Series 4460, Instron with Bluehill software) equipped with a 1kN static load cell (linearity of  $\pm 0.25\%$  of reading) and was positioned roughly 0.5 mm above the sample. Subsequently, the sample was loaded at a constant displacement rate of  $0.5 \text{ mm}\cdot\text{min}^{-1}$  until fracture. Force was recorded every 50 ms.

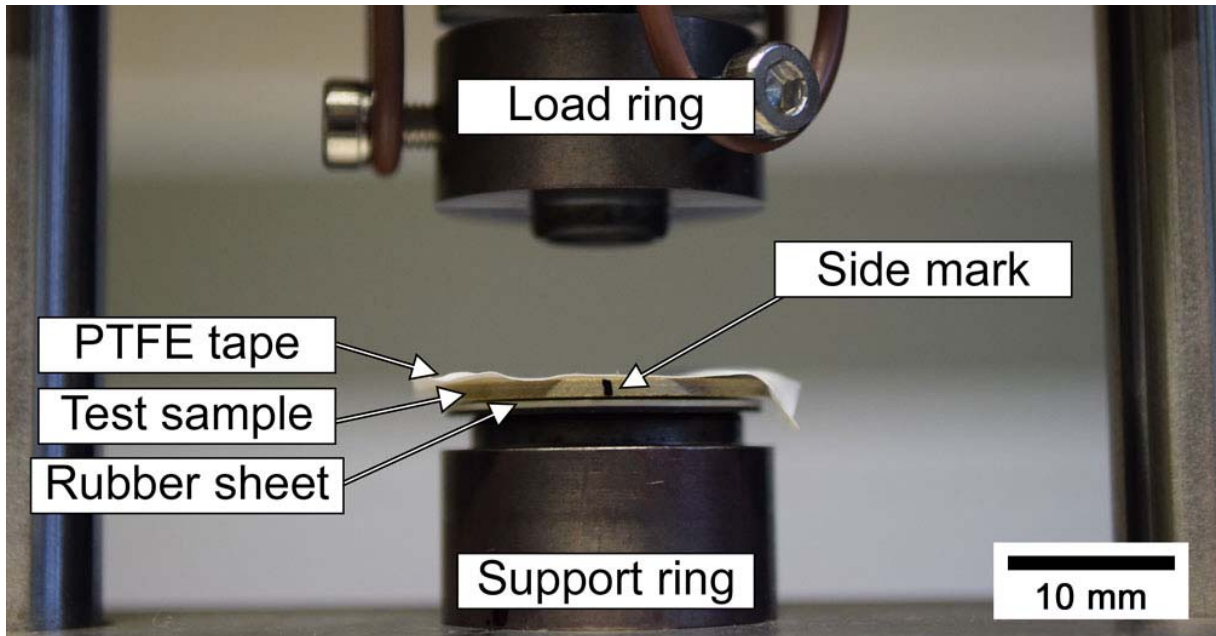


**Figure 4-11 Sample arrangement prior to equibiaxial flexural strength test.**

Equibiaxial flexural strength was calculated according to the following equation [16]:

$$\sigma_{\max} = \frac{3F}{2\pi t^2} \left[ (1 - \nu) \frac{d_s^2 - d_L^2}{2d^2} + (1 + \nu) \ln \frac{d_s}{d_L} \right], \quad (4-11)$$

where  $d_s$  = support ring diameter,  $d_L$  = load ring diameter,  $r$  – radius of a test piece,  $\nu$  = Poisson's ratio of a test piece,  $t$  = thickness of a test piece,  $F$  = fracture load. Throughout the testing programme, room temperature varied in the range 19–22 °C, relative humidity varied in the

range 30–50 %. The steel rings were periodically checked for possible damage and cleaned using ethanol and a textile polishing cloth.

#### 4.2.4.3 *Fractography*

Several publications were studied as a reference for establishing a good practice of fracture characterisation [120-122]. Specimens were always handled with latex gloves to prevent surface contamination.

The following procedure was applied:

- Visual inspection and fracture surface examination with stereo binocular microscope (Techno RZ, Meiji) at 10–75×.
- Fracture origin was located and marked by an arrow drawn with a pencil on the tensile side of the disc.
- Tensile side of discs with the lowest fracture strength were closely examined by eye for any handling damage such as scratches.
- Tensile sides of specimens were photographed with their side mark facing downwards (see Figure 4-12 a). Using the known contact area of the load ring (Figure 4-12 a), it was determined, whether the fracture originated outside the load ring, directly above it, or inside its diameter. Samples which fractured outside the load ring were discarded. Fracture locations were classified into 4 quadrants according to Figure 4-12 b). This was done to indicate any potential misalignment of rings in which case a single fracture origin location would dominate the tested set.
- As-fractured surfaces of selected samples from each batch were examined with SEM (6600 LV, Jeol) at higher magnifications (50–4000×) to characterise fracture origin by identity, location (surface or volume) and approximate size (whenever possible).

It was also determined, whether the fracture was intergranular or transgranular. Generally, the following range of samples was selected from each batch for examination: 3 samples of the lowest strength and 3 samples of the highest strength and 3 randomly chosen medium-strength samples. Extra samples were examined in some cases.

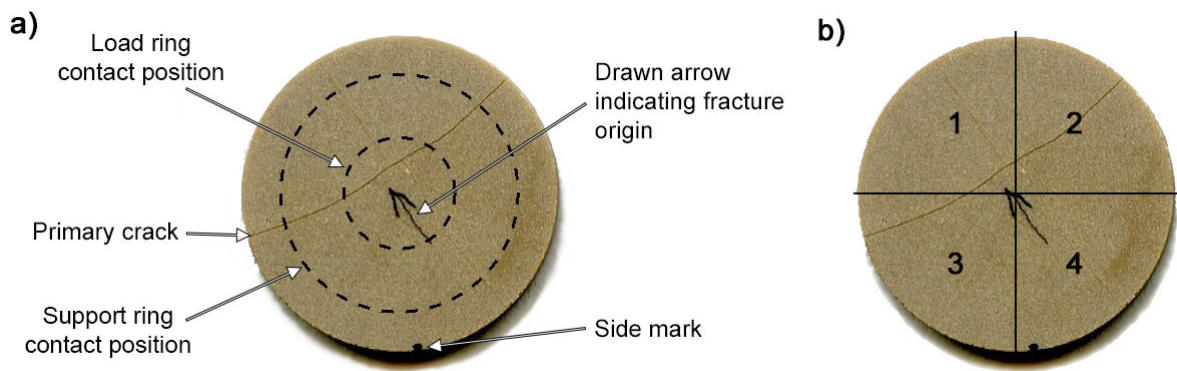


**Figure 4-12 Photograph of fractured sample (tensile side) with a) important features and support/load ring contact positions, b) quadrants used to classify fracture origin location.**

#### 4.2.4.4 Fixture design optimisation

A standard hard commercial PZT, NCE81 (CTS), was used for the fixture design optimisation, as this material is representative of the hard PZT samples prepared in this thesis. 28 ceramic pieces were tested using the fixture and specimen dimensions described in chapter 4.2.4.1 (denoted here as “Test 1”). It was noticed that the fracture often originated near the load ring contact area. The ASTM standard states that “frequent fracture at or near the load ring/test specimen interface implies excessive contact or friction stresses, or fixture/test specimen misalignment” [16]. Using a technique described in section 4.2.4.3, it was found that 53 % of samples in Test 1 showed fracture origin inside the load ring (see Figure 4-13 a). Furthermore, the fracture origin of all samples seemed to be located on the same half of the sample. In order

to verify this, all further samples were marked and oriented in a specific manner described in section 4.2.4.3. It was hypothesised that the frequent fracture near the load ring was due to fixture/specimen dimensions being near the allowed range limit (Table 4-3). For the next test (“Test 2”), samples were machined to the thickness of 1.00 mm instead of 1.65 mm, which caused ring dimensions to be well within the allowed range, except for the tip radius  $r$ , which was too large (Table 4-4).

In Test 2, only 15 % of samples fractured inside load ring and all fracture origins were located in quadrants 1 and 3 (one half of the sample) as shown in Figure 4-13. These results were interpreted as a sign of misalignment of support and load ring. As mentioned earlier, rings were attached to the steel blocks with regular screws (Figure 4-14 c) which could be moved within their sockets to a certain degree. To prevent this, fully threaded screws were replaced by screws with a shoulder (Figure 4-14 c) and rings were placed in an aluminium sleeve before the screws were tightened (Figure 4-14 a). Another batch of samples was tested using this arrangement, which was denoted as “Test 3”.

Attempts at aligning two rings in Test 3 did not significantly increase the percentage of samples fractured inside the load ring. However, in this case, fracture origins were located in all 4 quadrants, hinting that the alignment somewhat improved. Finite element analysis previously performed by Morrell et al. [115] showed a stress enhancement above load ring of 1–2 % in a frictionless case. Factors further enhancing stress above load ring are friction, specimen diameter:thickness ratio lower than 20:1 and misalignment of rings. Considering this information, it can be concluded that the fracture origin will inevitably be located near the load ring in most cases, even with a perfect ring alignment.

Because the ring tip radius in Test 2 and 3 was outside the allowed range, new rings were made with dimensions listed in Table 4-4. This fixture was denoted as Test 4. An improved alignment sleeve with screws was made (Figure 4-14 b) as well as a new attachment piece securing a rigid connection between the fixture and load frame (Figure 4-14 e). A batch of samples tested with this fixture showed 52 % of fractures inside the load ring and fracture origins located in all 4 quadrants (Figure 4-13). At this point, the fixture performance was deemed satisfactory and no further changes were made.

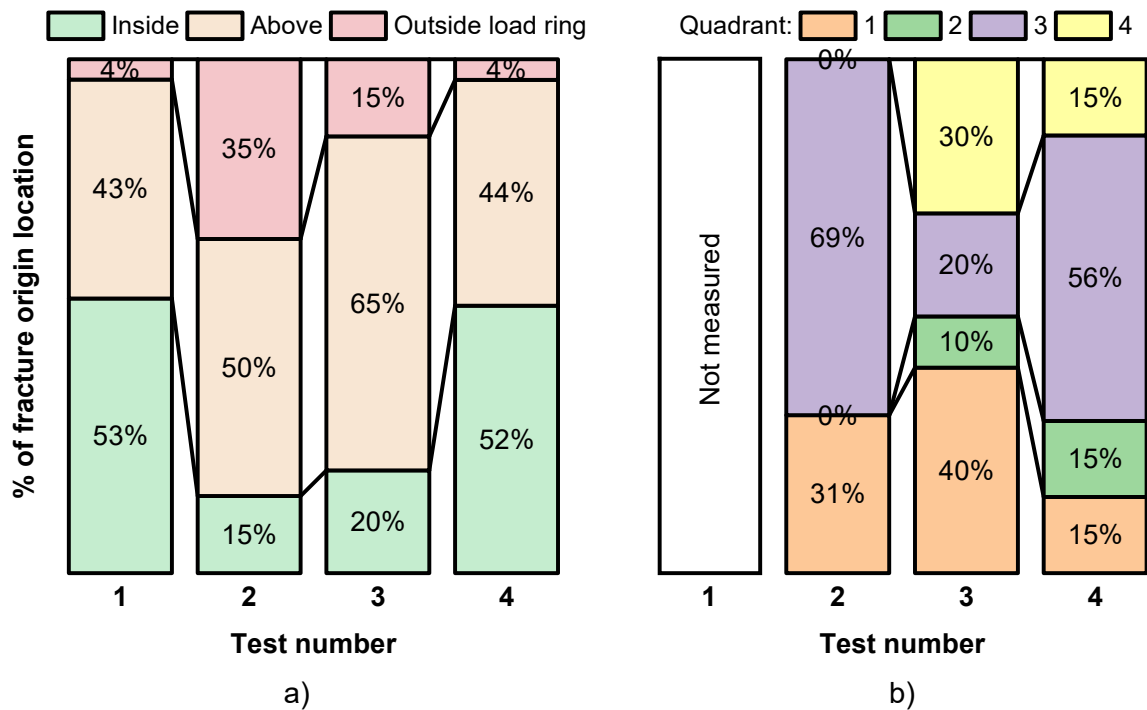


Figure 4-13 a) Percentage of fracture origins located inside, above or outside the load ring, b) percentage of fracture origins located in each of the quadrants (see Figure 4-12).

Table 4-4 Dimensions used in the “Test 2” and “Test 4” arrangements with their respective allowed ranges satisfying simple plate loading conditions

	Test 2		Test 4 (Final dimensions)	
	Allowed range (mm)	Choice (mm)	Allowed range (mm)	Choice (mm)
Sample thickness $t$		1.00		1.00
Support ring diameter $d_s$	10.00–36.51	16.5	10.00–36.51	15.00
Sample diameter $d$	18.50–28.50	20.0	17.00–27.00	20.00
Load ring diameter $d_L$	3.30–8.25	5.8	3.00–7.50	7.0
Support/load ring tip radius $r_{tip}$	0.50–1.50	1.65	0.50–1.50	0.70

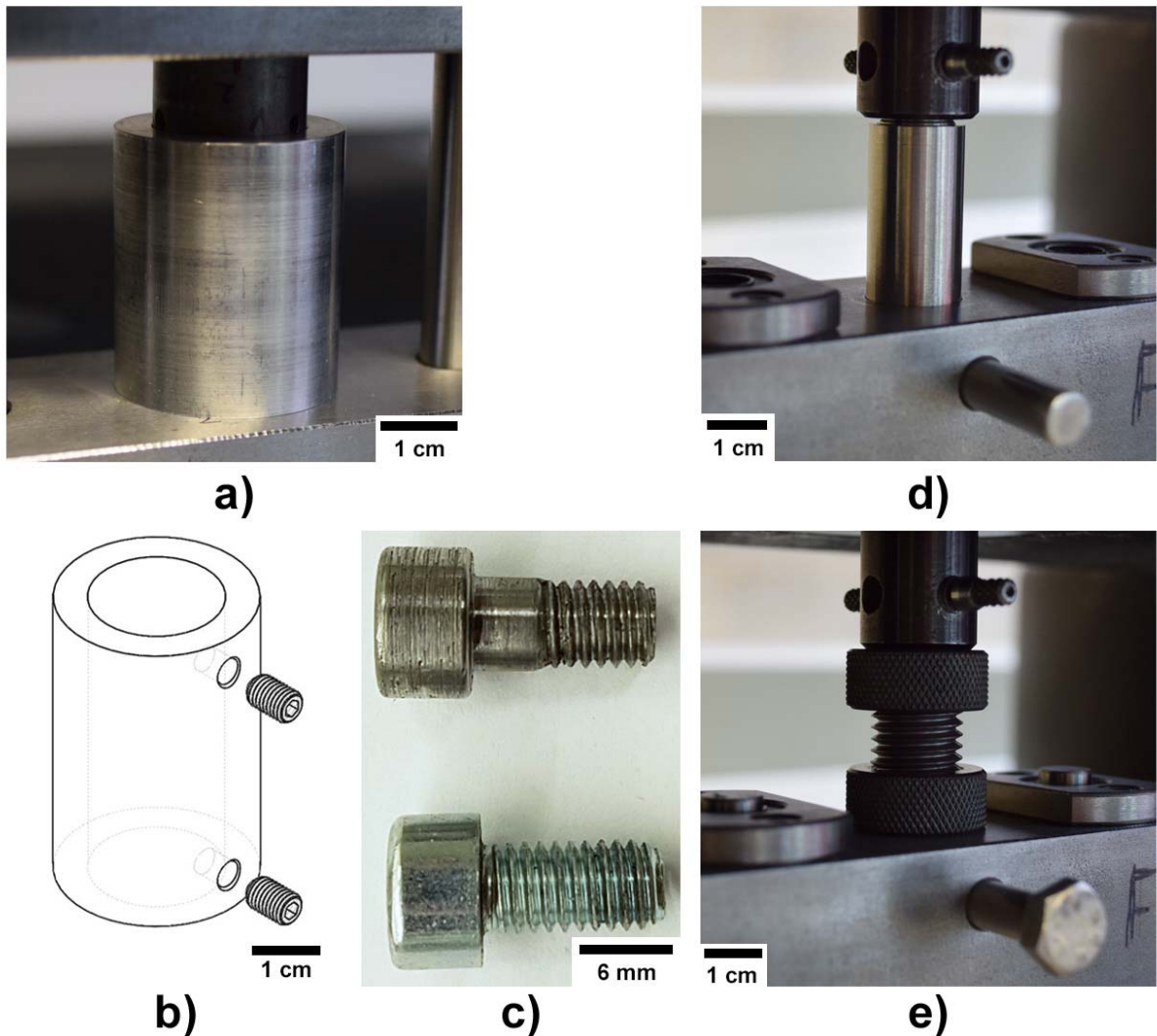


Figure 4-14 a) first simple alignment sleeve, b) improved alignment sleeve with alignment screws, c) screw used for attaching the bottom block with support ring (with and without a shoulder), d) simple connector piece, e) connector piece with screw-on rings providing a rigid fixture-load frame connection.

#### 4.2.4.5 Validation of fixture used for ROR equibiaxial flexural strength test

The flexural strength measured by the ring-on-ring configuration can be biased when test pieces are not sufficiently parallel/flat, when there is a friction between the fixture and the test-piece or when rings are not concentric. To validate the strength results obtained with the custom fixture, a set of 40 alumina samples was ordered from Coorstek Inc. for direct comparison with a published Army Research Laboratory (ARL) report from Wereszczak, Swab and Kraft [123].

The set comprised 99.5 % alumina discs (AD-995) of  $20.0 \pm 0.1$  mm diameter and  $1.00 \pm 0.05$  mm thickness. Specific properties of AD-995 are listed in Table 4-5. Tolerance for parallelism and flatness was specified as 0.01 mm (according to ASTM standard C1499-15 [16]).

Table 4-5 Reported properties of AD-995 alumina ceramics [124]

Property	Testing method	Reported value
Density ( $\text{g}\cdot\text{cm}^{-3}$ )	ASTM C20	3.90
Average grain size ( $\mu\text{m}$ )	Thin section	6.0
Flexural strength (MPa)	ASTM F417	379
Elastic modulus (GPa)	ASTM C848	370
Poisson's ratio	ASTM C848	0.22
Hardness	Rockwell 45N	83
Fracture toughness ( $\text{MPa}\cdot\text{m}^{1/2}$ )	Notched beam	4-5

Generally, the strength of specific material measured by different testing methods can be scaled using an effective area ( $S_E$ ) or effective volume ( $V_E$ ) [15, 125], which represent the portion of sample volume/surface under tensile stress that has the same probability of failure as a specimen of corresponding size tested in a simple tension. Both parameters were previously described in section 2.1.1.

It is implied that the effective surface should be used when fracture originates from surface flaws and the effective volume should be used when volume flaws are the strength-limiting

features. To satisfy this criterion, every fracture origin must be properly determined, and results must be strictly censored. In the case of the ARL report, effective surface was used despite some of the critical flaws being volume type, as it would be too laborious to characterize the fracture origin of every test piece. Moreover, some of the critical flaws such as machining damage and porosity seemed to be combined. Since alumina discs used in this work presumably contained the same flaws, a similar approach was taken, and effective surface was used for estimated strength scaling.

The effective area of a specimen tested in 4-point flexure can be calculated using the following equation:

$$S_E(4PB) = L_S \left[ \frac{h}{m+1} + b \right] \left[ \frac{L_L}{L_S} m + 1 \right] \left[ \frac{1}{m+1} \right], \quad (4-12)$$

where  $L_S$ ,  $L_L$  is the support/loading span,  $h$  is the height of the specimen,  $b$  is the width of the specimen and  $m$  is the Weibull modulus [15].

For multiaxial stresses, equation (2-3) must be changed using one of the available multiaxial failure models. These include the Principle of Independent Action (PIA), the Batdorf model and the Multiaxial Elemental Strength model [15, 126-128]. The principle of independent action states that the 3 principle stresses operate independently in their respective directions. It doesn't consider shear/compressive stresses, combined local principle stresses or the nature of defects. Therefore, the PIA failure model is phenomenological. The Batdorf model incorporates the effect of multiaxial stresses into the weakest-link theory based on linear elastic fracture mechanics (LEFM). Flaws are randomly oriented and non-interacting, shear and normal forces are incorporated [128, 129]. Lamon argued in his paper that the Batdorf theory does not consider compressive components [128]. These components were considered in the multiaxial

elemental strength model, which he developed. There are no closed-form expressions of effective surface or volume available for his model.

The Batdorf theory was used to calculate the effective area of biaxially stressed discs in this work as it was previously successful in predicting biaxial strength from 4-point bend test results [127, 130]. This theory was also used in the ARL report [123].

According to Batdorf [125], the effective area of a specimen tested in a ring-on-ring equibiaxial flexure configuration can be approximated using the following expression:

$$S_E(ROR) = 2\pi \left(\frac{D_L}{2}\right)^2 m^{0.45}, \quad (4-13)$$

where  $D_L$  is the load ring diameter and  $m$  is the Weibull modulus.

Calculated effective surface of specimen 1 ( $S_{E,1}$ ) and its Weibull characteristic strength ( $\sigma_{0,1}$ ) can be subsequently used to predict the Weibull characteristic strength of specimen 2 ( $\sigma_{0,2}$ ) with effective surface  $S_{E,2}$  using the following expression:

$$\frac{\sigma_{0,1}}{\sigma_{0,2}} = \left(\frac{S_{E,2}}{S_{E,1}}\right)^{1/m}. \quad (4-14)$$

The mechanical test results are summarized in Table 4-6. Results from the current work are compared to the ARL report results of AD-995 alumina specimens tested in 4-point bend (chamfered rectangular section blocks of  $3 \times 4 \times 50$  mm, where 3 mm is the height). Surfaces of both batches were rotary ground to 80-grit finish. Calculated effective surfaces of the two configurations were very similar. Using equation (4-14), the predicted strength of specimens tested in current work was the same as measured in 4-point bend, 294 MPa. ROR strength was 2.3 % lower (287 MPa). This can be interpreted as a good match considering that both materials were produced at different locations and 12 years apart. There is also some inaccuracy present

in the Batdorf scaling model itself and its approximated form that has been used. Weibull moduli can be compared directly and show a good agreement, since their values are well within their respective 95 % confidence intervals. Based on these observations, it can be concluded that the custom-made jig was well designed and gives satisfactory results.

Table 4-6 Mechanical test results of rotary ground AD-995 alumina (80-grit finish)

Source	Test type	Effective surface (mm <sup>2</sup> )	No. of pieces	Relative humidity (%)	Uncensored characteristic strength, $\sigma_0^\dagger$ (MPa)	Uncensored Weibull modulus, $m^\dagger$
Current work	ROR	84.2	32	50	287 [283, 291]	26.7 [20.4, 35.1]
ARL report [123]	4-point bend	85.8	30	55	294 [290, 299]	23.7 [17.1, 31.4]

<sup>†</sup> [ $\pm$  95% confidence intervals]

Figure 4-15 shows the Weibull plot of the alumina pieces tested in this work and from the ARL report. It appears that points measured in this work could be fitted with multiple lines of different slopes which suggests a presence of multiple strength-limiting flaw populations. A general discussion of deviations from Weibull distribution can be found later in section 8.4.4. The results from the ARL report do not exhibit such behaviour. The discrepancy might be caused by differences in stress conditions, character of flaws, or by unknown testing issues. Fractography revealed that most strength-limiting flaws were volume type – porosity, large grains and agglomerates, some also hybridized with machining damage, similar to findings in the ARL report. Unfortunately, no distinct strength-limiting flaw populations were identified. A few examples of strength-limiting flaws are shown in Figure 4-16.

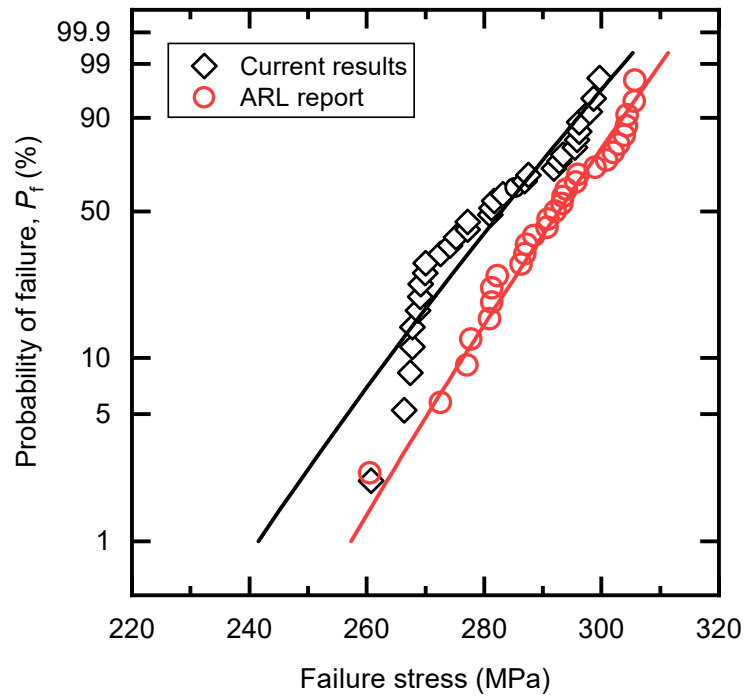


Figure 4-15 Weibull plot of AD-995 alumina tested in the ring-on-ring biaxial flexural strength test compared with the results of alumina tested in 4-point bend from the ARL report [123].

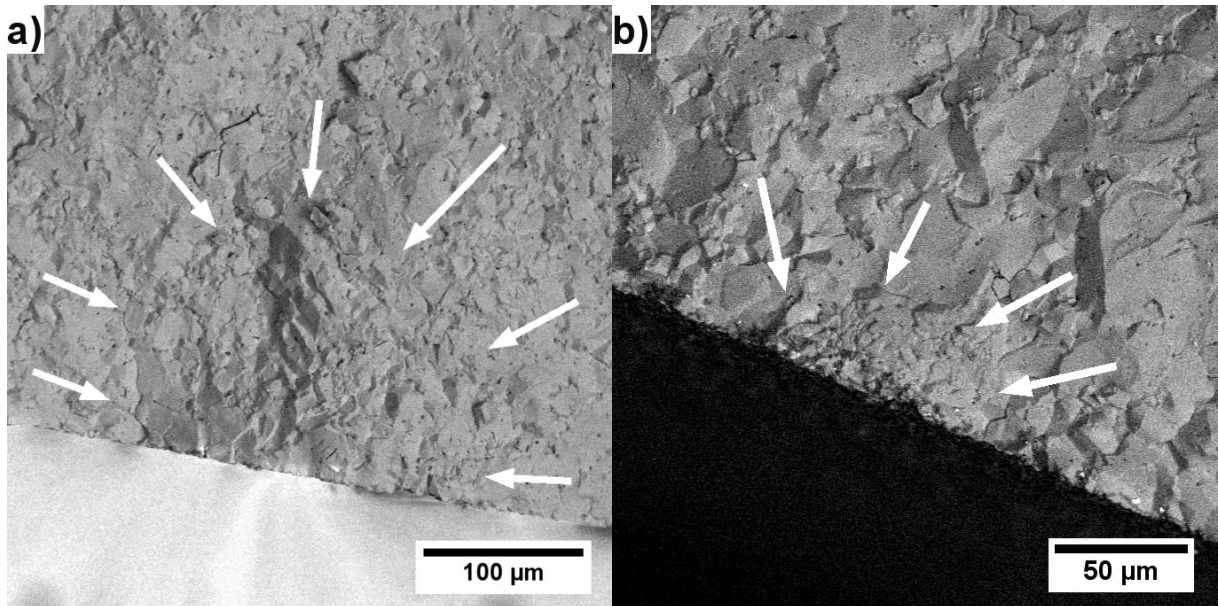
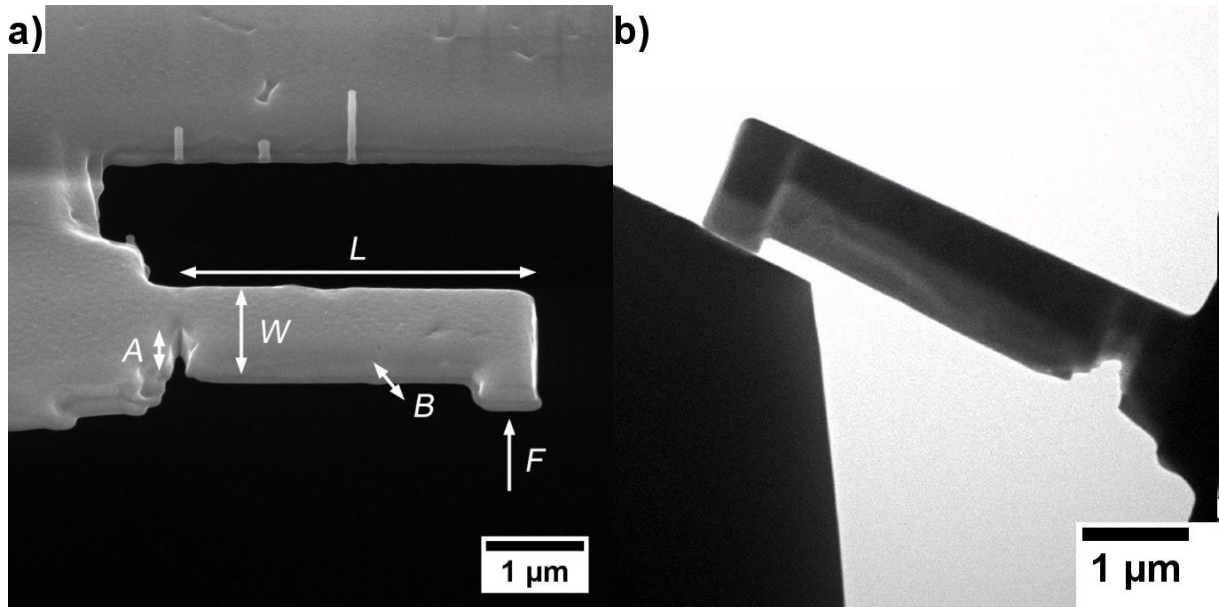


Figure 4-16 SEM micrographs showing examples of fracture origins found in tested  $\text{Al}_2\text{O}_3$  specimens: a) Cluster of large grains, b) agglomerate likely coupled with machining damage on the surface.

#### 4.2.5 Microscale fracture toughness

The fracture toughness of single grain boundaries was studied using cantilevers with a cross-section of roughly  $0.4 \times 1.0 \mu\text{m}$  and the length of  $3.0 \mu\text{m}$ . Cantilevers were prepared in a similar fashion to sections for nanoscale observations (section 4.1.6). A pre-notch was made near the base to serve as a defined fracture origin and a point of stress concentration. Example of a prepared cantilever is shown in Figure 4-17 a). When cutting the cantilever, an effort was made to have a straight grain boundary parallel with the loading direction near the cantilever base. The pre-notch was then placed directly into the boundary. Presence of 2 distinct grains on each side of the notch was confirmed by observation of Kikuchi patterns.

Each specimen was mounted on a special holder and inserted into a Hysitron PI95 TEM pico-indenter, which in turn was inserted into a TEM (2100, Jeol). The flat protruding area at the end of the cantilever served as a loading point. Figure 4-17 b) shows the loading setup.



**Figure 4-17 a) SEM micrograph of a cantilever used for nanoscale fracture toughness testing. *A, B, L, W* indicate dimensions of the pre-notch and the cantilever; *F* shows the loading direction. b) loading of the cantilever using a picoindenter (TEM micrograph).**

Fracture toughness was calculated using the following equation:

$$K_{IC} = \frac{6FL}{W^2B} \sqrt{\pi A} \cdot f(A/W), \quad (4-15)$$

where  $A$  is the depth of the pre-notch,  $B$ ,  $L$ ,  $W$  dimensions of the cantilever according to Figure 4-17 a) and  $F$  is the maximum force.  $f(A/W)$  is the finite crack length correction term – a dimensionless geometry factor determined by finite element analysis. The following approximation assuming sharp notch was used [131]:

$$f(A/W) = 1.122 - 1.4 \left(\frac{A}{W}\right) + 7.33 \left(\frac{A}{W}\right)^2 - 13.08 \left(\frac{A}{W}\right)^3 + 14 \left(\frac{A}{W}\right)^4. \quad (4-16)$$

Three cantilevers were tested for each material; two materials with different Fe content were tested.

### 4.3 Piezoelectric and dielectric properties

Samples used for piezoelectric/dielectric-property measurements were sputtered with gold electrodes (K575X, Quorum Technologies), poled in a silicone oil bath at 125 °C/3 kV·mm<sup>-1</sup> for 3 minutes and cleaned in acetone. Basic dielectric and piezoelectric properties were measured using an impedance analyser (4294A, Agilent Technologies) and Berlincourt type d<sub>33</sub> meter (YE2730A, Sinocera). 5 samples per batch were measured unless there was a significant variation in results, in which case additional samples were analysed. Measurements were carried out at intervals of 1, 3, 7 and 30 days after poling. Samples were stored in a sample box with silica gel desiccant.

Measurements followed methods described in European standards EN 50324 [30, 132] and recommendations given by the measurement good practice guides published by the National Physical Laboratory [133, 134]. The measuring process with the analyser used in this work has been previously optimised elsewhere [135]. Optimised settings from the referenced work were adopted in relevant cases. Temperature and humidity of the room was recorded prior to measurements.

For impedance analysis, the test sample was placed into a custom-made fixture consisting of a flat bottom electrode and a spring-loaded pin top electrode. Both electrodes were coated with gold. The arrangement is shown in Figure 4-18.

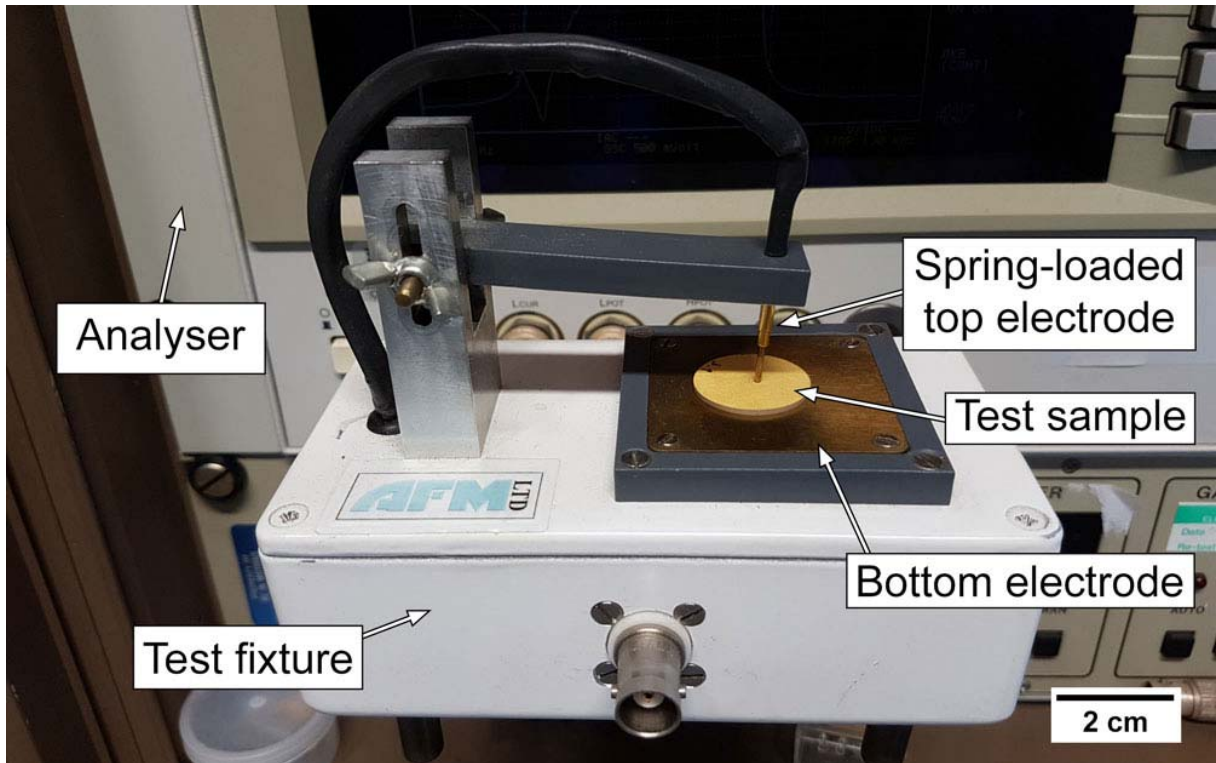


Figure 4-18 Impedance analysis arrangement.

The analyser was calibrated by a  $50\Omega$  resistor to compensate for the impedance of the fixture. Non-resonance measurements of free capacitance ( $C^T$ ) and dielectric dissipation factor ( $\tan \delta$ ) were carried out at 1 kHz. Point averaging was applied and repeated until stable values were found.

Resonance measurements were always performed using the maximum number of points (801) on the analyser and as narrow frequency range as possible. Maximum ( $f_n$ ) and minimum ( $f_m$ ) resonant frequencies and the minimum impedance ( $Z_{\min}$ ) were obtained from recorded frequency sweeps. The free relative permittivity (dielectric constant)  $\epsilon_r$  was calculated as follows:

$$\epsilon_r = \epsilon_{3r}^T = \frac{C^T t}{\epsilon_0 \pi r^2}, \quad (4-17)$$

where  $\epsilon_0$  is the vacuum permittivity,  $t$  is the specimen thickness and  $r$  is the specimen radius. Planar electromechanical coupling factor  $k_p$  and the mechanical quality factor  $Q_M$  were calculated using the following equations:

$$k_p = \sqrt{2.51 \frac{f_n - f_m}{f_n} - \left( \frac{f_n - f_m}{f_n} \right)^2}, \quad (4-18)$$

$$Q_M = \frac{1}{2\pi f_m |Z| C^T \frac{f_n^2 - f_m^2}{f_n^2}} \quad (4-19)$$

The  $d_{33}$  meter was calibrated prior to measurements using a standard test-piece supplied by the manufacturer (measured value as well as 0 point). Samples were clamped between hemispherical probes with as low clamping force as possible. Every measurement was taken approximately 5 s after clamping, when the value became stable. To make the measurement more reliable, 5 points around the central area of the sample (similar to locations shown in Figure 4-1) were recorded and their arithmetic average was used.

Polarisation and current versus electric field ( $P_E$ - $E$  and  $I_E$ - $E$ ) hysteresis loops were measured by a 2000 E analyser supplied by aixACCT on specimens previously used for piezoelectric measurements. Specimens were depoled at 500 °C for 1 h two weeks prior to the loop measurements. Hysteresis loops were measured at a maximum electric field of 4 kV·mm<sup>-1</sup> and frequency of 1 Hz. Loops were recorded after 1 cycle as this was the most representative condition of samples used for the mechanical tests.

## **5 SAMPLE PREPARATION**

This chapter describes how certain steps of the sample preparation were optimised, lists the compositions used in this work and presents the results of the measured processing variables, namely particle size distribution, weight loss after calcination, binder burnout and sintering, and flatness/parallelism of the sintered and machined specimens. The optimised sample preparation is described in section 5.3, following the optimisation and composition list in sections 5.1 and 5.2.

While some of the optimisation steps were performed in a laboratory, the sample preparation was carried out in a commercial environment (CTS) to obtain specimens closely resembling the commercial products and make the results commercially relevant.

### **5.1 Processing optimization**

A conventional powder processing route was used to prepare samples in this work. The process is shown in Figure 5-7. A series of experiments focused on finding the most appropriate processing conditions was conducted at the early stages of this work. All optimization experiments were performed using a PZT composition containing 2 hard dopants, Fe and Ni. Only Fe was later selected for the optimised route to simplify the composition and avoid possible hard dopant interactions. Three main processing aspects were optimised: duration of 2<sup>nd</sup> milling, binder mixing and sintering. The duration of 2<sup>nd</sup> milling can affect particle and agglomerate sizes and thus influence green and sintered densities, and it was thus checked if the recommended time of 70 s was sufficient for the materials produced in this work. Issues with pore clusters related to binder mixing and a secondary phase formed during sintering were encountered during test batch preparation, so the binder mixing was also considered worthy of further investigation. The optimisation will be briefly discussed in subsequent sections along with annealing optimisation.

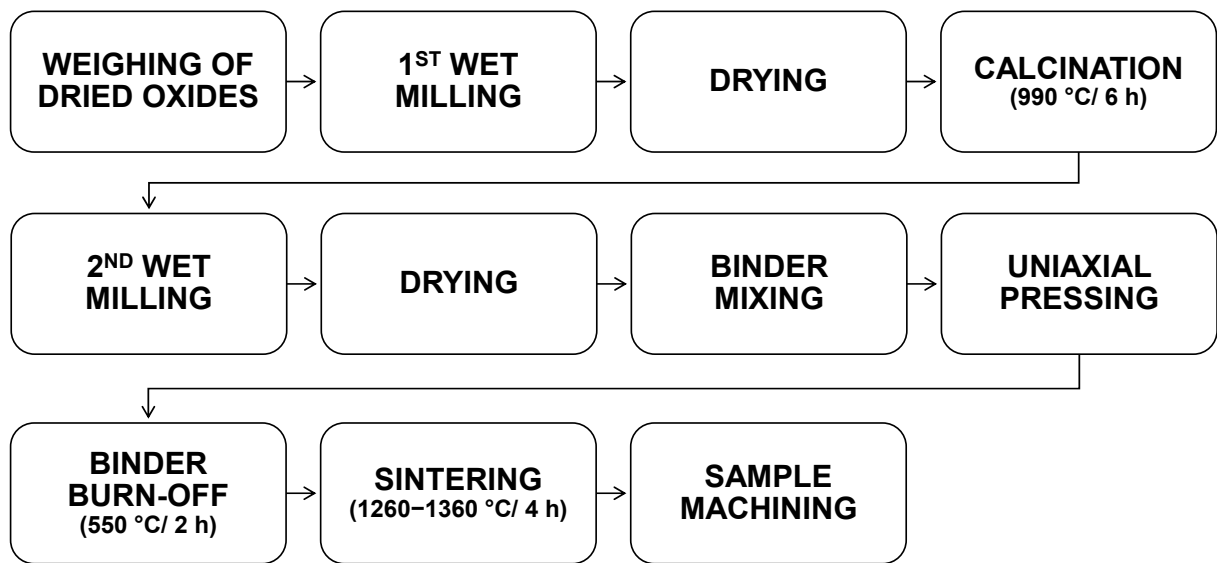


**Figure 5-1 Conventional powder processing route used in this work.**

### 5.1.1 Duration of 2<sup>nd</sup> milling

To assess the influence of particle size on density and average grain size, a batch of hard PZT powder  $((\text{Pb}_{0.95}\text{Sr}_{0.05})(\text{Zr}_{0.52}\text{Ti}_{0.48})_{0.986}\text{Fe}_{0.014}\text{O}_3)$ , prepared by mixing and milling dried raw oxides in a laboratory agitator bead mill and calcining the dried mixture at 920 °C for 6 h in an alumina crucible, was split into 2 halves of which one was milled for 70 s (suggested value) and the other for 10 min (arbitrarily chosen to obtain significantly lower median particle size). Rest of the preparation process was identical to optimised process except for sintering, where no powder bed was present.

The characteristics of the processed calcined powder milled for 70 and 600 s are shown in Table 5-1. Particle size distributions of respective batches are shown in Figure 5-2.

Table 5-1 Characteristics of processed calcined powder milled for 70 and 600 s

	Duration of 2 <sup>nd</sup> milling		Standard deviation
	70 s	600 s	
Median particle size $d_{50}$ ( $\mu\text{m}$ )	2.5	1.3	0.2
Density of green body ( $\text{g}\cdot\text{cm}^{-3}$ )	4.92	4.59	0.01
Density of sintered body ( $\text{g}\cdot\text{cm}^{-3}$ )	7.62	7.57	0.01
Average grain size ( $\mu\text{m}$ )	2.1	2.1	0.3

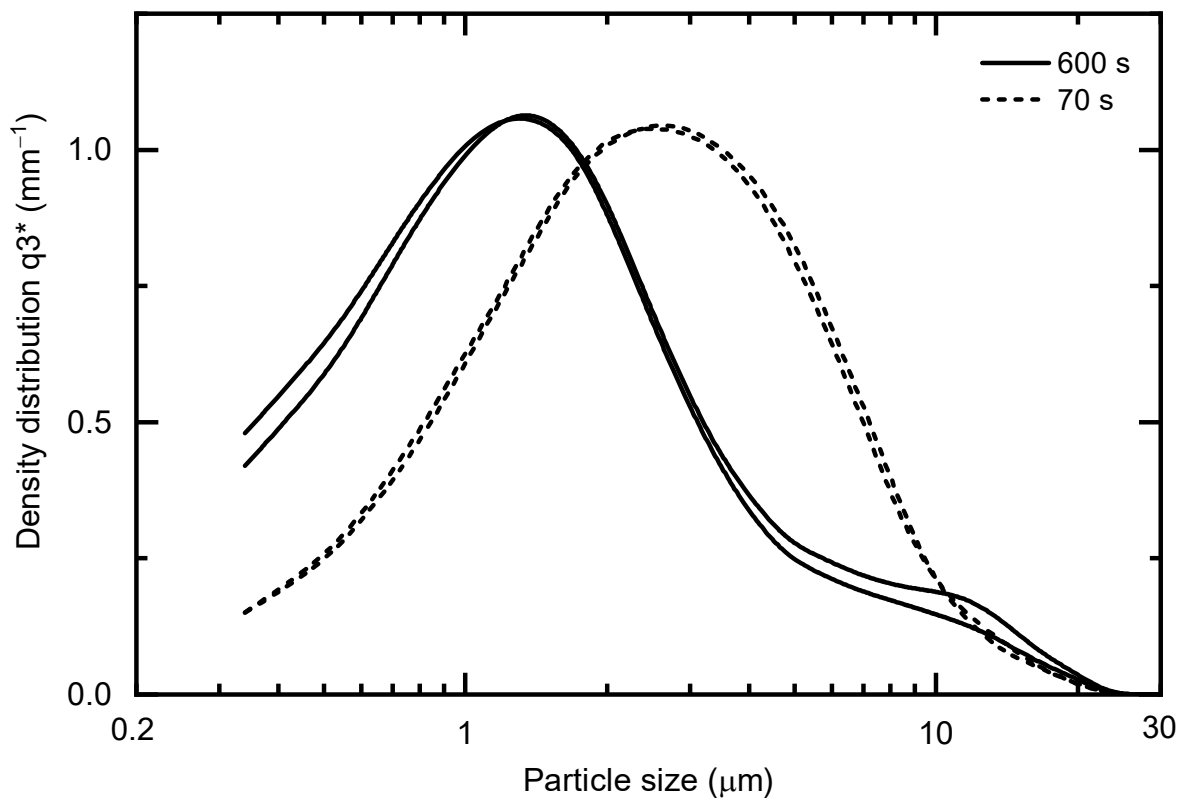


Figure 5-2 Particle size distribution curves of calcined hard doped PZT milled for 70 and 600 s.

Longer milling time reduced the median particle to almost the half of its value obtained after the 70-second milling. As expected, the particle size distribution also gets narrower with longer milling times. It has been shown, that wider particle size distribution gives a higher packing density [75], which was confirmed by measured green body density. The difference in the

densities of the green bodies (6.7 %) is significantly reduced after sintering (to 0.7 %). The average grain size 2.1  $\mu\text{m}$  was identical for both batches of sintered ceramic.

Because it was shown that longer milling time did not improve density of the final product nor it was able to change its average grain size, an intermediate milling time of 2 minutes was selected for all compositions.

### 5.1.2 Binder mixing

Spray drying of calcined powder-binder slurries, conventionally used for industrial powders, could not be adopted in this work as the powder batch sizes ( $\approx 550$  g) were too small for the equipment available (required minimum is 50 kg). Two alternative mixing techniques were explored, where the goal was to obtain a pore microstructure similar to the one of spray dried and sintered commercial hard PZT (NCE81) shown in Figure 5-3 a).

In the first technique (marked as WET), binder was added to the slurry of calcined and milled powder with  $\text{ZrO}_2$  beads (beads:powder:water = 2:1:1 by weight). The mixture was further milled (mixed) at slow speed for 15 min and subsequently dried in an oven. Final powder-binder mixtures were sieved through a mesh with 400 $\mu\text{m}$  opening. The original binder, a proprietary solution of PVA-PEG-PMMA, did not remain homogeneously dispersed after drying and created a hard crust on top of the powder. The dried mixture had to be manually crushed and milled using a mortar and pestle. Polished surfaces of samples sintered with 5 and 3 wt% of PVA-PEG-PMMA binder incorporated in this way are shown in Figure 5-3 b, c). Pore microstructure was significantly different from the spray-dried one and large pores developed due to inhomogeneous binder distribution in the compact.

Using the same technique, a different binder system was used, namely PVA based Duramax B-1000 and B-1007 (Dow) mixed 1:1 by weight. This system achieved a much better homogeneity

and did not create a hard crust on top of the powder after drying. However, its use still resulted in the presence of large pores in the sintered bodies (Figure 5-3 d–f), even at 1.25 wt%, below which material could not be successfully compacted.

After these unsuccessful wet-route binder mixing attempts, a second technique was employed (marked as DRY) whereby, a binder was simply sprayed on the powder and kneaded in using a mortar and pestle. After drying the powder-binder mixtures were sieved through a mesh with 400 $\mu$ m opening. Much higher similarity to the spray dried pore microstructure was achieved using this technique (Figure 5-3 g), and was therefore adopted for the preparation of samples in this work.

When experimenting with compositions not containing Ni (only Fe was present), it was found that this technique for binder incorporation resulted in the presence of pore clusters as shown in Figure 5-3 h). Due to time restrictions, additional techniques could not be explored. In order to minimise the presence and size of these pore clusters, extra steps were adopted to further homogenise the binder as described in section 5.3.

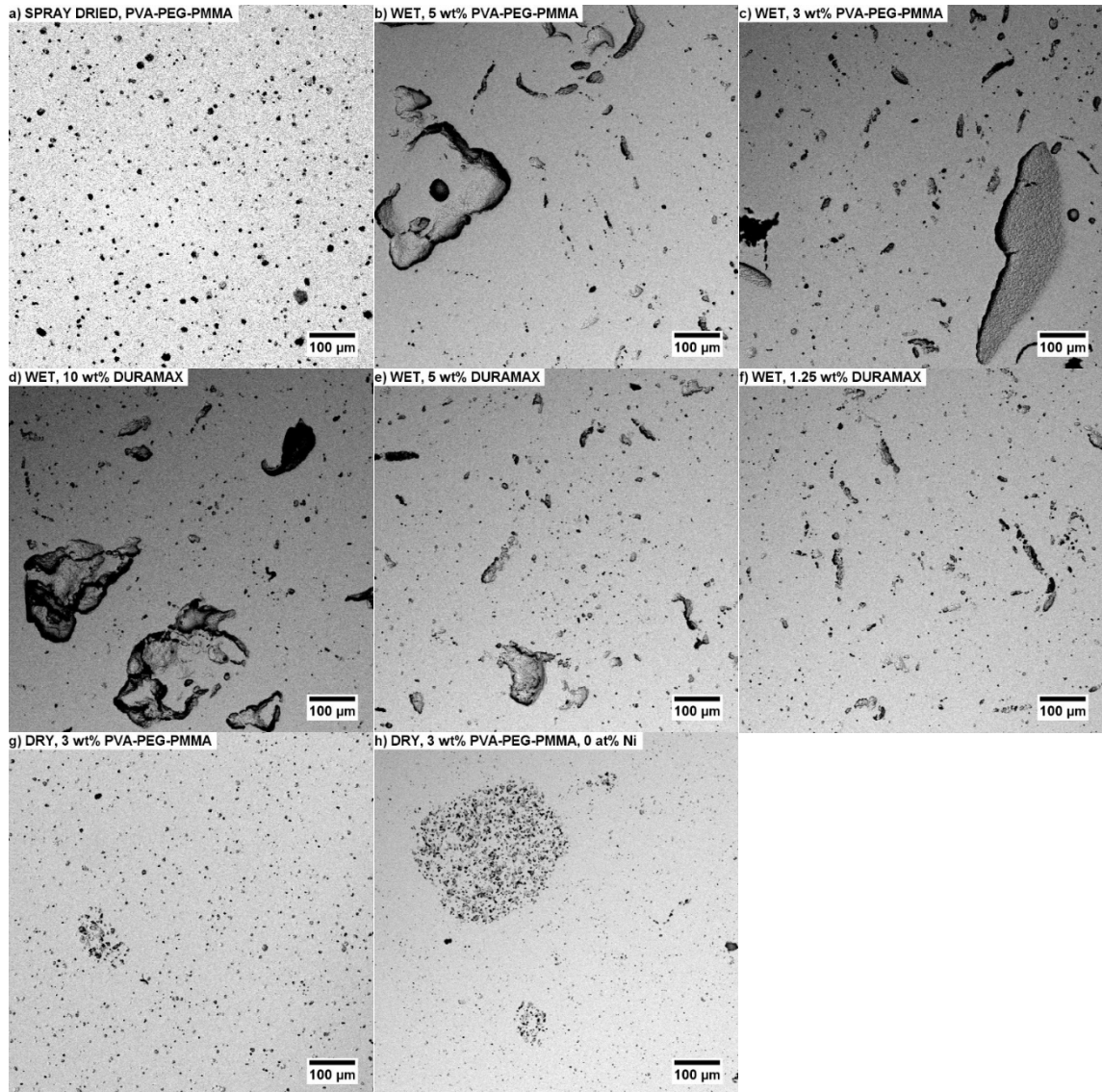
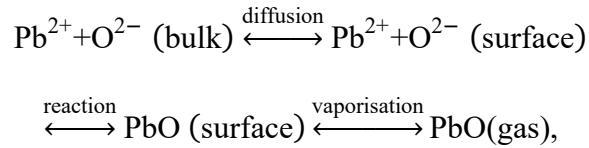


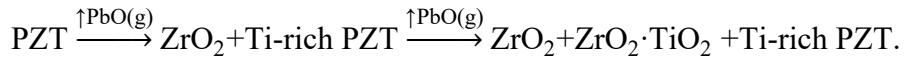
**Figure 5-3 SEM micrographs of polished surfaces of sintered hard PZT samples previously mixed with various amounts of binder (PVA-PEG-PMMA or DURAMAX) and using 2 different techniques (“DRY” and “WET”). See text for full details.**

### 5.1.3 Sintering

As discussed in section 2.5.3, the volatility of PbO at high temperatures poses one of the main processing difficulties of PZT. It has been previously shown that  $\text{Pb}^{2+}$  escapes from the surface of a ceramic piece in the form of PbO, creating a depleted layer on the surface. Vaporisation kinetics of PbO changes once the depleted layer is formed [136]. Northrop suggested the following equilibrium [137]:



where the diffusion step is the slowest. Loss of PbO creates lead vacancies and eventually leads to the formation of secondary phases. PZT with a composition around the MPB undergoes the following reactions [138, 139]:



The rate of loss depends on the surface area of the green body but is independent of its density [137].

In initial trial experiments with a supplied commercial hard PZT powder (NCE40, CTS), spots consisting entirely of zirconium and oxygen were found on the surface of as-sintered samples when investigated with SEM-EDX. These spots were only found on smaller ceramic pieces sintered in a laboratory furnace and not on industrially sintered samples. Both were sintered in enclosed alumina crucibles in air; however, laboratory-made samples were sintered using a smaller material volume and body size. It was speculated, that differences in the material volume per crucible, crucible volume and total surface of compacts were responsible for the formation of the secondary phase. It was deemed necessary to avoid the formation of the secondary phase as it could affect the results of mechanical property investigations.

In general, loss of PbO is controlled by 3 measures:

- a) Enclosed or sealed crucible.
- b) Excess of PbO in the stoichiometric PZT composition.
- c) PbO-containing powder bed inside the crucible capable of maintaining a higher vapour pressure of PbO than in the sintered compacts.

Point a) refers to the crucible arrangement. In a laboratory environment, this can range from simply covering a crucible with a lid to using ZrO<sub>2</sub> sealing pastes and double-crucible arrangements [51, 140, 141]. Changing the stoichiometry of PbO requires prior knowledge about its loss and a number of preliminary experiments, especially if the target is optimum piezoelectric/dielectric properties. The partial pressure of PbO above various powder beds has been reported by Hårdtl and Rau [142]. They found that increasing the Zr/Ti ratio increases the vapour pressure of PbO above PZT, which means that when using PbZrO<sub>3</sub> as a powder bed, PbO in the crucible atmosphere will be equilibrated from the powder bed rather than from the sintered material. For this reason, lead zirconate is often used as a powder bed, sometimes with various amounts of extra ZrO<sub>2</sub> to limit its sinterability. The crucible arrangement, however, remains unreported in most cases.

Kington and Clark's paper [143], often referenced to justify the use of lead zirconate as a powder bed, showed that crucible arrangement is also very important. Simply placing a sample on top of the bed inside an enclosed crucible did not prevent PbO loss in their experiment (Figure 5-4 (B)). Only the more complicated arrangement (A) in Figure 5-4 was able to prevent it. However, such a complicated arrangement would be too difficult and expensive to implement for large sample batches. At the same time, compacts need to be separated from the PbZrO<sub>3</sub> powder bed

to prevent the migration of Ti [143]. Lastly, sintered samples need to be separable from whichever material they are in contact with, which turned out to be a serious issue when using high sintering temperatures, slow ramp rates and long dwell times.

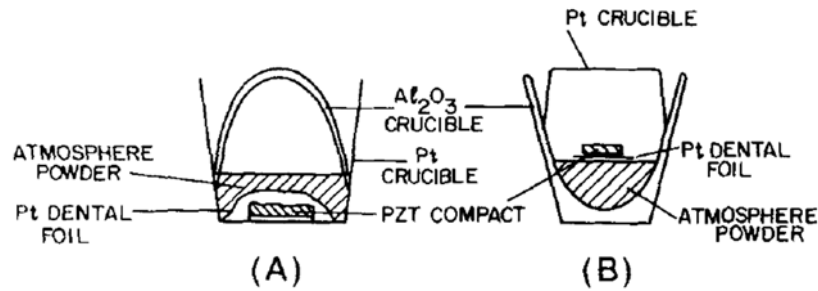


**Figure 5-4 Kingon and Clark's crucible sintering arrangements reproduced from [143]. (A) was able to prevent PbO loss from the compact, while (B) resulted in a continuous loss of PbO.**

In this work, 8 powder beds have been investigated in a series of sintering optimisation experiments to sinter compacts of industrial hard PZT powder. The goals of the optimisation were:

- To obtain a single-phase ceramic.
- To be able to easily separate samples from the powder bed.
- Composition of samples should not change significantly.
- Piezoelectric/dielectric properties should be near the values reported in the data sheet.

Schematics of the crucible arrangement are shown in Figure 5-5. Samples were made of hard doped commercial PZT powder (NCE40, CTS) using techniques described in section 5.3. A separator material was used in some cases to prevent samples and powder bed from sintering together. Powder bed and separator compositions were the following:

- $\text{PbZrO}_3$  (PZ) and  $\text{PbZrO}_3 + 10 \text{ wt } \% \text{ ZrO}_2$  (PZ+Z) powder prepared by the same solid-state route as other PZT powders (see section 5.3). Calcined powder was manually ground using a mortar and pestle to obtain an aggregate size of less than 1 mm.
- Ca-stabilised  $\text{ZrO}_2$  sand labelled as “Z sand” (Porta, 99.0 wt%, particles between 100–500  $\mu\text{m}$ )
- Hard doped PZT (labelled as PZT) – same composition as samples, with the binder burnt out prior to sintering. Samples sintered in this powder bed had to be separated by a layer of  $\text{ZrO}_2$  sand otherwise they would sinter with the powder bed.
- Ca-stabilised  $\text{ZrO}_2$  sand repeatedly used as a separator for more than 10 sintering runs in air (reacted with PbO from the samples over time). Powder bed labelled as “Air Z soaked”.
- $\text{ZrO}_2$  sand + 5 wt % PbO (labelled as 5% PZ sand) prepared by dry mixing of fresh Ca-stabilised  $\text{ZrO}_2$  sand with 5 wt % PbO followed by calcination at 920 °C for 4 h.

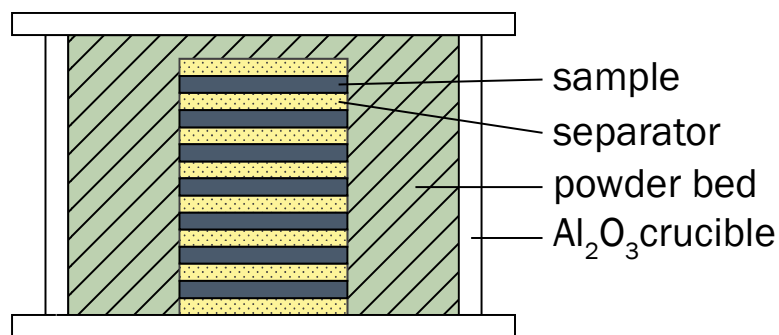


**Figure 5-5 Schematics of the crucible arrangement for the sintering experiments.**

Individual sintering arrangements are listed in Table 5-2. Samples were sintered at 1260 °C for 4 h with a heating rate of 1 °C·min<sup>-1</sup>, which means they spent a significant amount of time at temperatures high enough for PbO vaporisation.

Table 5-2 Description of individual sintering arrangements

<b>Label</b>	<b>No. of samples</b>	<b>Crucible inner volume (cm<sup>3</sup>)</b>	<b>Powder bed</b>	<b>Separator</b>
Air S	3	11	Air	Z sand
Air L	7	51	Air	Z sand
Air Z soaked	7	94	Air	Z soaked
Z sand	7	194		Z sand
PZ	7	117		PZ
PZ + Z	7	117		PZ
PZT	5	141	PZT	Z sand
5% PZ sand	7	179		5% PZ sand

Detailed discussion of the results has been published in the proceedings of the 2017 Joint IEEE ISAF-IWATMD-PFM conference [144] and only the most important results are summarised in Table 5-3. “5% PZ sand” has been chosen as the most suitable powder bed as it was easily separable from sintered samples, showed one of the lowest weight losses per sample and was the only powder bed to prevent any secondary phase formation (investigated by XRD and SEM-EDX). Piezoelectric and dielectric property results were not significant enough for discarding any of the powder beds, therefore, they were not presented here. The reader is referred to the published paper for more information. It is important to note that, in most cases, X-ray diffraction was not capable of detecting secondary phases otherwise found by SEM-EDX.

Table 5-3 Summary of sintering optimisation results

Label	Could be separated from PB?	Weight loss after sintering <sup>†</sup> (wt %)	Secondary phases found	Secondary phase abundance	
				Outer surface	Cross-section
Air S	Yes	6.4 (1.0)	ZrO <sub>2</sub>	Abundant	Entire
Air L	Yes	3.2 (0.3)	ZrO <sub>2</sub>	Abundant	Entire
Air Z soaked	Yes	1.3 (0.2)	ZrO <sub>2</sub>	Common	Near edges
Z sand	Yes	3.2 (0.8)	ZrO <sub>2</sub>	Frequent	Entire
PZ	Yes	5.4 (1.2)	PbO	Abundant	-
PZ + Z	No	N/A	N/A	N/A	N/A
PZT	Yes	1.6 (0.1)	ZrO <sub>2</sub>	Rare	Near edges
5% PZ sand	Yes	1.5 (0.2)	-	-	-

<sup>†</sup>reported with standard deviation in brackets

#### 5.1.4 Annealing

Ceramic grinding can introduce surface and subsurface cracks and residual stresses [145]. In PZT, mechanical stress can also lead to domain switching [146, 147]. The surface state of PZT can be quantified using XRD via the ratio of tetragonal reflections (002) and (200). When in a powder form or as-sintered state, domains are randomly oriented and the  $I(002)_T/I(200)_T$  ratio shows values of  $\sim 0.5$  [146, 147]. After cutting or grinding, this ratio increases, generally above 1.0 [146].

Residual stresses and microcracks on the surface can affect the strength of ceramic pieces, which is why an effort has been made to remove them as much as possible. Residual stresses and microcracks can be removed either by polishing and/or annealing at increased temperatures [147]. No polishing was employed in this work as the intention was to test as-machined surfaces. Polishing all samples would also be too time consuming and expensive. Optimum annealing conditions were explored using samples of  $(\text{Pb}_{0.95}\text{Sr}_{0.05})(\text{Zr}_{0.52}\text{Ti}_{0.48})\text{O}_3$  (batch 4, as defined in section 5.2). One sample was crushed and ground into powder using a mortar and pestle

whereas a second sample was left in an as-machined state and annealed at different temperatures. Patterns were also compared to that of the as-sintered sample.

Figure 5-6 shows the XRD patterns of the 2 tetragonal peaks of interest and their intensity ratio. It can be seen, that the as-sintered and powder samples show  $I(002)_T/I(200)_T \sim 0.5$  (Figure 5-6 (a)), which is consistent with previous studies. The as-machined sample shows  $I(002)_T/I(200)_T = 1.37$ , which reveals machining-induced domain switching. Annealing at 500 °C and 650 °C for 4 hours decreased the ratio to 1.28 and 1.00 respectively (Figure 5-6 (b)). Increasing dwell times at these temperatures did not further change the ratio. Annealing experiments were not performed above 650 °C as it would risk the loss PbO. No mass/dimension change was detected after annealing at 650 °C.

Not even the highest annealing temperature used, 650 °C, was able to revert the intensity ratios to the powder values. It was suspected that the surface is relatively rough, creating a significant surface texture which cannot be reverted simply by the heat treatment. To verify this statement, the surface was polished to a 1 μm surface finish and annealed at 500 °C for 4 h. As can be seen in Figure 5-6 (b), the statistical intensity ratio was restored to 0.61, which confirms the previous hypothesis. Because annealing at 650 °C did lower the original  $I(002)_T/I(200)_T$ , it was applied to all as-machined samples prior to mechanical testing.

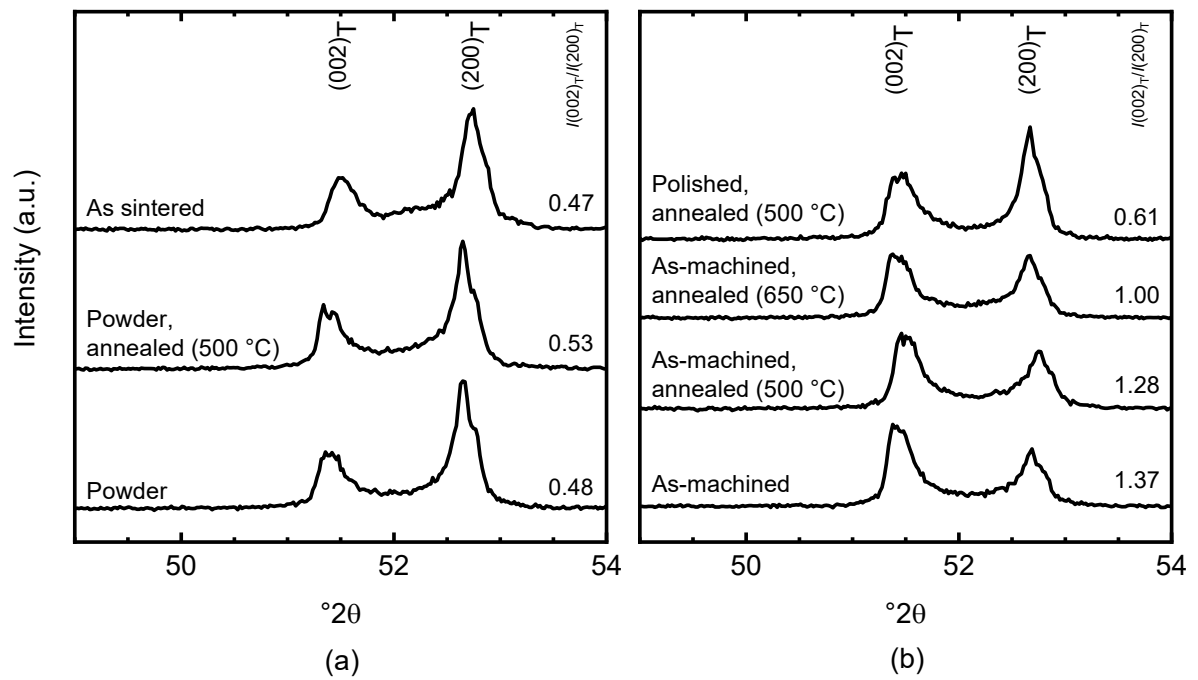


**Figure 5-6 XRD patterns and ratios of (002) and (200) tetragonal peaks of a single specimen after various treatments. Note: powder was obtained by crushing and grinding a sintered sample.**

## 5.2 List of compositions

Table 5-4 shows the list of prepared compositions designed to investigate effects of following factors:

- **Sr<sup>2+</sup> A-site isovalent doping** (0 and 5 at%)
- **Fe<sup>3+</sup> acceptor doping** (0, 0.4, 1.4 and 2 at%)
- **Zr/Ti ratio** (5 different values between 49/51–55/45)
- **Sintering temperature** (1260, 1310 and 1360 °C)

Only selected combinations of factors were used, which are illustrated by a flowchart in Figure 5-7. It should be noted that the full batch “labels” listed in Table 5-4 are only used in graphs and tables. The abbreviation “PSZT” is generally used throughout the text to refer to Sr-doped PZT.

The main goal was to study effects of hard doping, represented by Fe<sup>3+</sup>. The highest Fe<sup>3+</sup> content used (2.0 at %) was intentionally higher than its reported solubility limit in PZT solid solution (0.5–2.0 at %) [148-150]. Piezoelectric properties of PZT are very sensitive to its position in the PbZrO<sub>3</sub>-PbTiO<sub>3</sub> phase diagram relative to the MPB. As a range of Zr/Ti ratios near the MPB is used in practice, it was decided to add the Zr/Ti ratio as a factor in this study. Used Zr/Ti ratios were intended to cross the MPB between rhombohedral and tetragonal phase, which is generally considered as 52/48 for pure PZT [3]. Sr<sup>2+</sup> as well as Ba<sup>2+</sup> or Ca<sup>2+</sup> are widely used isovalent dopants for their enhancement of permittivity and piezoelectric properties in a trade-off for lower Curie temperature [3, 151]. Since they are present in most commercial compositions, it was decided to add Sr<sup>2+</sup> to all materials made in this work. Two compositions were made without Sr<sup>2+</sup> to check if it has an impact on mechanical (and other) properties. Lastly, it is well known that porosity and grain size significantly influence mechanical properties.

Sintering temperature was added as a factor to investigate effects of these properties on 2 compositions.

Table 5-4 List of prepared compositions of  $(\text{Pb}_{1-x}\text{Sr}_x)(\text{Zr}_y\text{Ti}_{1-y})_{(1-z)}\text{Fe}_z\text{O}_3$  sintered at 1310 °C

Batch no.	Label	x	y	z	Batch no.	Label	x	y	z
		(Sr)	(Zr)	(Fe)			(Sr)	(Zr)	(Fe)
		(at%)					(at%)		
1	PZT	0	52		10	PSZTF 52/48 0.4		52	0.4
2	PSZT 49/51		49		11	PSZTF 49/51		49	
3	PSZT 51/49		51		12	PSZTF 51/49		51	
4	PSZT 52/48			0	13	PSZTF 52/48			
5	PSZT 52/48 LT <sup>†</sup>	5	52		14	PSZTF 52/48 LT <sup>†</sup>	5	52	1.4
6	PSZT 52/48 HT <sup>‡</sup>				15	PSZTF 52/48 HT <sup>‡</sup>			
7	PSZT 53/47		53		16	PSZTF 53/47		53	
8	PSZT 55/45		55		17	PSZTF 55/45		55	
9	PZTF	0	52	1.4	18	PSZTF 52/48 2.0		52	2.0

<sup>†</sup>sintered at 1260 °C

<sup>‡</sup>sintered at 1360 °C

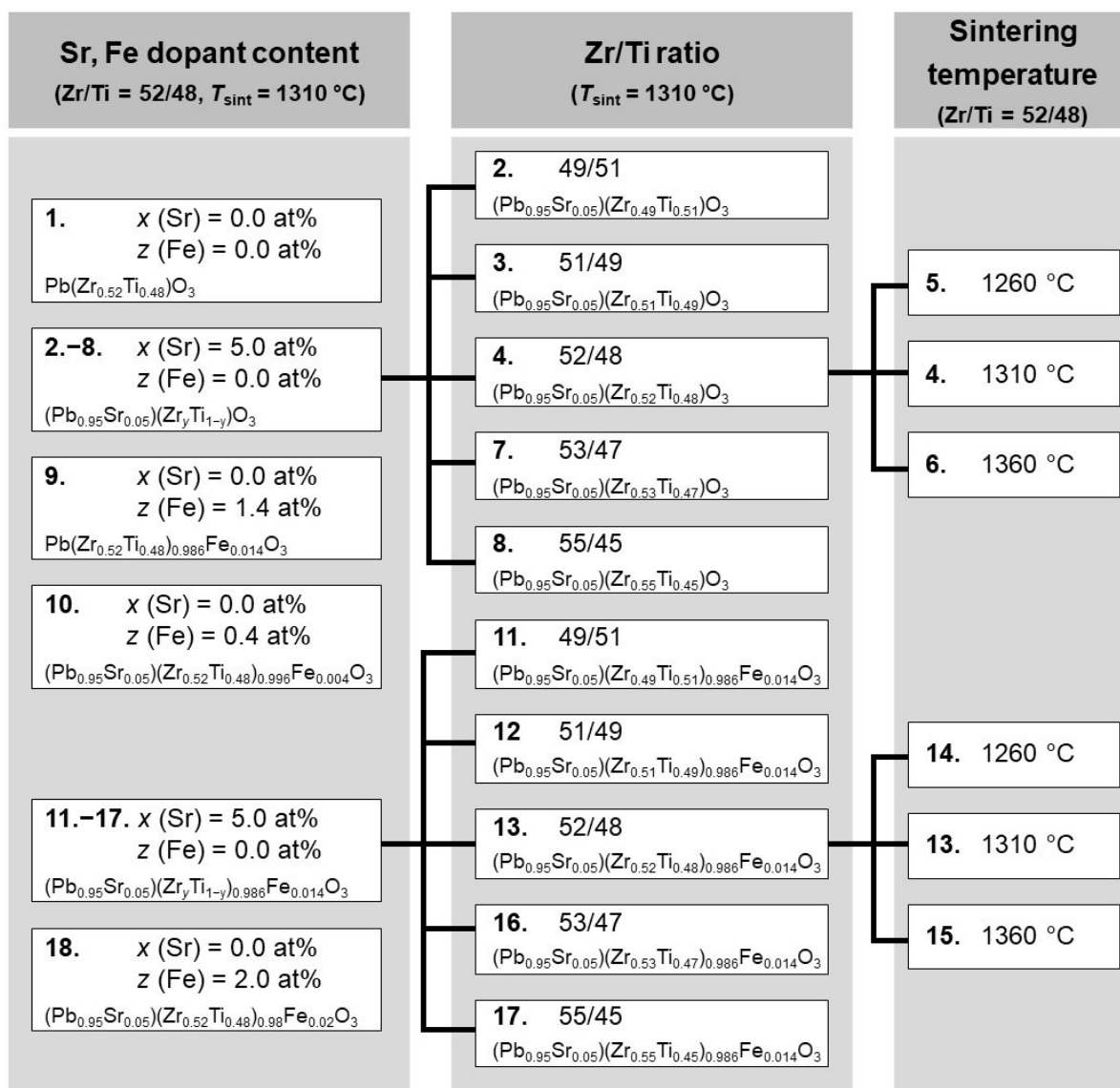


Figure 5-7 Flowchart of prepared compositions of  $(\text{Pb}_{1-x}\text{Sr}_x)(\text{Zr}_y\text{Ti}_{1-y})_{(1-z)}\text{Fe}_z\text{O}_3$ .

### 5.3 Optimised sample preparation

The optimised sample preparation followed the steps shown earlier in Figure 5-1. First, raw oxides were dried at 130 °C for 24 h in a laboratory oven (FD53, Binder) to remove any residual moisture. Purity, supplier and a median particle diameter ( $d_{50}$ ) of the raw oxides and carbonates are listed in Table 5-5. Commercial-grade raw oxides were used, because one of the objectives of this dissertation was to relate findings to a commercially used material.

Table 5-5 Raw materials used in this work

Raw material	Supplier	Purity <sup>†</sup> (%)	$d_{50}$ <sup>‡</sup> ( $\mu\text{m}$ )
PbO	Penox GmbH	99.90	8.05
SrCO <sub>3</sub>	CSC JÄKLECHEMIE Czech s.r.o.	99.80	6.15
ZrO <sub>2</sub>	Porta s.r.o.	99.50	5.45
TiO <sub>2</sub>	EUROSarm s.r.o.	99.30	0.61
Fe <sub>2</sub> O <sub>3</sub>	J. P. K. Chem	99.37	0.97

<sup>†</sup>value stated by the supplier

<sup>‡</sup>measured

The theoretical combined amount of impurities in each prepared batch calculated from the purities shown in Table 5-5 is  $\approx 0.25$  wt% compared to the 0.00–0.50 wt% of Fe<sup>3+</sup> added deliberately. The calculated value is not representative of the actual amount of impurities in the samples as a certain fraction of them is combustible and will be burnt-out during calcination. TiO<sub>2</sub> and ZrO<sub>2</sub> showed weight losses of 0.32 and 0.15 % respectively after 90 min at 950 °C. The remaining impurities probably still have some effect on the properties of the prepared samples, but their amount and nature does not considerably change from batch to batch. An attempt was made to identify the main impurities present in the oxides using X-ray fluorescence spectrometry measurements with 2 instruments (ARL 9400 XP, Thermo ARL and S8 Tiger, Bruker). Both instruments found K<sup>+</sup> (A-site acceptor) and Nb<sup>5+</sup> (B-site donor) present in TiO<sub>2</sub>

and  $\text{Ca}^{2+}$  (isovalent A-site dopant) present in  $\text{ZrO}_2$ . Some other elements were found by each instrument, but the results were inconsistent.

Dried oxides were weighed and mixed according to their purity and stoichiometric ratios given by Table 5-4. The total weight of each batch was approximately 550 g. An additional 3.3 g of PbO were added to every composition to compensate for its evaporation during calcination and sintering. The value was based on previous experiments (sample preparation for optimisation experiments described in sections 5.1.1 and 5.1.2). The weighed oxides were transferred to a laboratory agitator bead mill (LabStar, Netzsch) and milled in deionised water at 3000 rpm for 75 s using  $\text{ZrO}_2$  beads ( $\approx 0.15$  mm in diameter). The resulting slurry was then dried in an oven at 90 °C (to remove free water) and 130 °C (to remove residual moisture).

The dried agglomerated powder was manually crushed and transferred into a 3-piece alumina crucible (see Figure 5-8). The crucible, filled with powder and loosely covered with an alumina lid, was placed into a laboratory furnace (VP10/16, LAC) where it was calcined. Calcination consisted of a  $1^\circ\text{C}\cdot\text{min}^{-1}$  ramp and 6h dwell at 920 °C. After that, the heating was switched off and the furnace was left to cool naturally. The PbO loss per batch, calculated from the weight of the powder and crucible before and after calcination, was between 2.6–3.7 g.

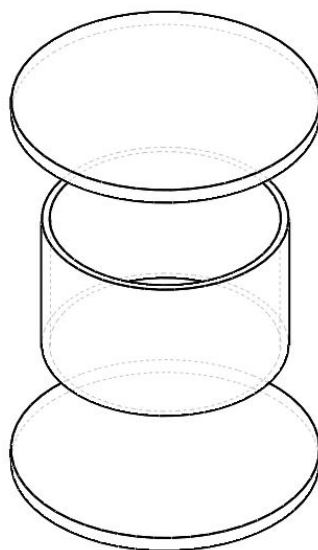


**Figure 5-8 Schematics of 3-piece alumina crucible used for calcining and sintering.**

Calcined material was manually crushed using an agate mortar and pestle to a powder sufficiently fine to use in the bead mill. Crushed powder was milled in the agitator bead mill in deionised water at 3000 rpm for 2 min. The resulting slurry was dried in an oven at 90 °C (to remove free water) and 130 °C (to remove residual moisture).

The dried agglomerated powder was crushed and sieved through a kitchen sieve. Only 400 g of the powder was used for further processing. In the next step, the powder was sieved through a 120 $\mu$ m mesh and mixed with 12 g of a proprietary solution of PVA-PEG-PMMA binder system. The mixing was performed manually with a plastic spatula in a container, which was previously evaluated as the optimal procedure as reported in section 5.1.2. In order to maximize the homogeneity of the binder, several steps have been further introduced to the mixing process. These included kneading in a bowl using a silicone spatula, sieving through kitchen and 400 $\mu$ m mesh sieves and pressing the powder into a large pellet with subsequent crushing into powder again.

The homogenized powder was uniaxially pressed into pellets (approximately 25 mm diameter and 2.3 mm thickness) using a small industrial press (PYTE 3,15, WMW Erfurt) fitted with a

custom-made stainless-steel die. The used pressure could not be measured precisely because the pressure gauge was not calibrated but was estimated to be approximately 50 MPa. Green density was used to determine, whether the pressing force was sufficient. All samples were pressed using the same force and all samples showed an average green density of  $4.86 \pm 0.04 \text{ g}\cdot\text{cm}^{-3}$ , approximately 62 % of theoretical density.

The binder was burnt out of compacts in a small custom-made laboratory furnace at 550 °C for 2 h in air. Pellets were then sintered in an arrangement described in section 5.1.3 (Figure 5-5) using the same furnace as for calcination. 70–80 samples were sintered per batch. The sintering program consisted of a  $1^\circ\text{C}\cdot\text{min}^{-1}$  ramp and 4h dwell at 1260/1310/1360 °C followed by natural cooling. The maximum temperature in the furnace was also checked with process temperature control rings (Ferro GmbH).

55–65 samples from each batch were machined by the industrial sponsor to 20 mm diameter and 1 mm thickness to be characterized by various methods and used in the mechanical tests. Thickness grinding was performed using a grinding machine with rotary table and vertical grinding spindle (to the tolerance of 0.05 mm), diameter was machined by an external centreless grinding (to the tolerance of 0.1 mm). 400-grit SiC abrasive was used in thickness grinding, both operations were water-cooled. Dimensions of several randomly chosen samples from several batches were measured to confirm their compliance with prescribed tolerances (method described in section 4.1.1).

## 5.4 Processing results

This section presents the measured values of several processing parameters of powders and sintered samples. The main goal was to investigate any significant processing differences between batches, which could affect the results of other tests.

### 5.4.1 Particle size distribution of calcined powders

All batches were milled after calcination using the same conditions. However, as shown in Table 5-6, the median particle size exhibited some differences. Particle size distribution curves are shown in Figure 5-9. The major differences appear to be correlated with Fe content as it can be seen that all batches with the same Fe content occupy narrow areas of the graph. The mode of particle size shifts to lower values as the Fe content increases. The distribution is “cut off” on the left side due to the instrument detection limit of 0.3  $\mu\text{m}$ .

Table 5-6 Median particle size ( $D_{50}$ ) of calcined powders of  $(\text{Pb}_{1-x}\text{Sr}_x)(\text{Zr}_y\text{Ti}_{1-y})_{(1-z)}\text{Fe}_z\text{O}_3$

batch no.	x (Sr)	y (Zr)	z (Fe)	$D_{50}$ ( $\mu\text{m}$ )	Batch no.	x (Sr)	y (Zr)	z (Fe)	$D_{50}$ ( $\mu\text{m}$ )
	(at%)					(at%)			
1	0	52		2.1	9	0	52		1.7
2		49		2.1	11		49		1.7
3		51		2.1	12		51		1.8
4			0	2.1	13			1.4	1.7
5	5	52		2.1	14	5	52		1.7
6				2.1	15				1.7
7		53		2.2	16		53		1.7
8		55		2.2	17		55		1.6
10		52	0.4	2.1	18		52	2.0	1.5

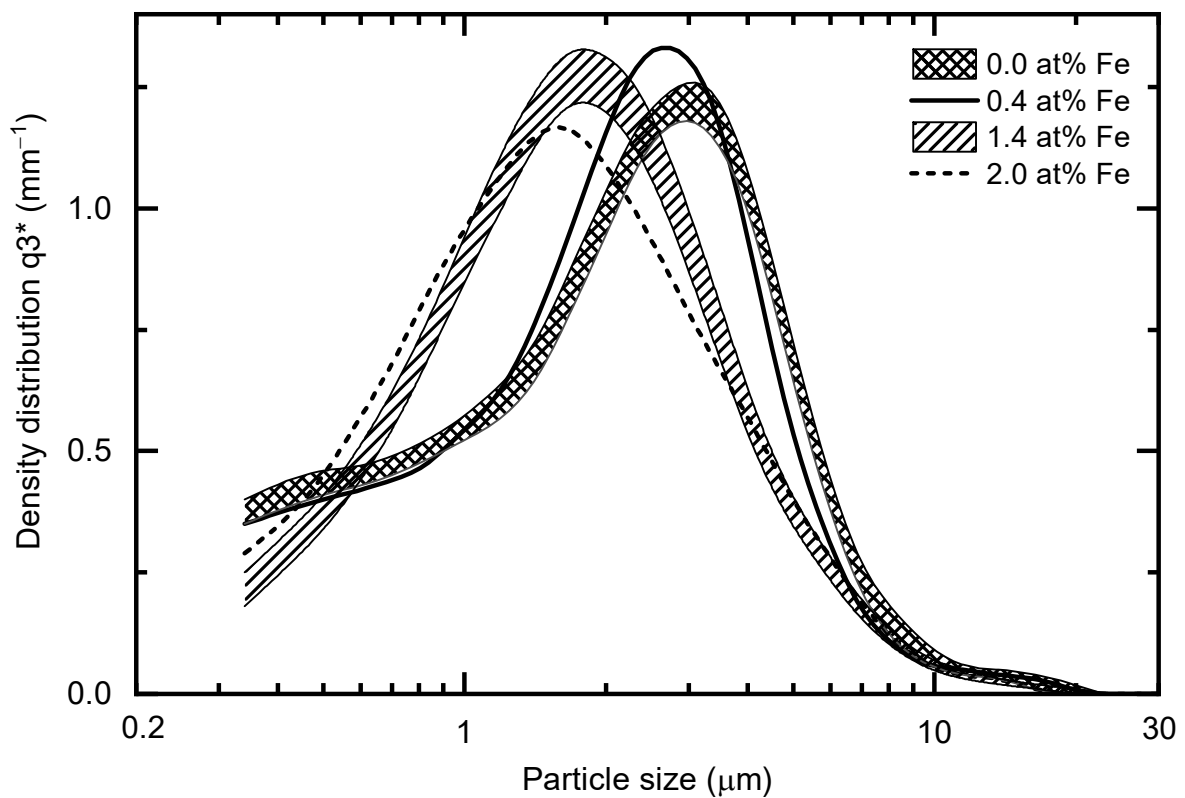


**Figure 5-9 Particle size distribution curves of calcined powders milled for 2 min and grouped by Fe content.**

It has been previously shown that dopants may affect the solid-state reaction of PZT [152]. Based on particle size measurements, it is likely that the presence of Fe noticeably affected the reaction kinetics of PZT, while Sr did not. As-calcined cake of undoped PZT was more difficult to crush compared to doped compositions. This might be related to the solute drag effect of  $\text{Fe}^{3+}$ . In undoped materials, there is more pronounced particle growth, the calcined powder has a higher initial  $d_{50}$  and therefore would take longer to get milled to the same final  $d_{50}$ .

SEM micrographs in Figure 5-10 clearly show larger particles present in the undoped composition compared to an Fe-doped material. Particles are in both cases mostly equiaxial. All batches exhibited particle size distributions suitable for further processing. Based on previous experiments described in section 5.1.1, measured differences in particle size should not affect the final grain size.

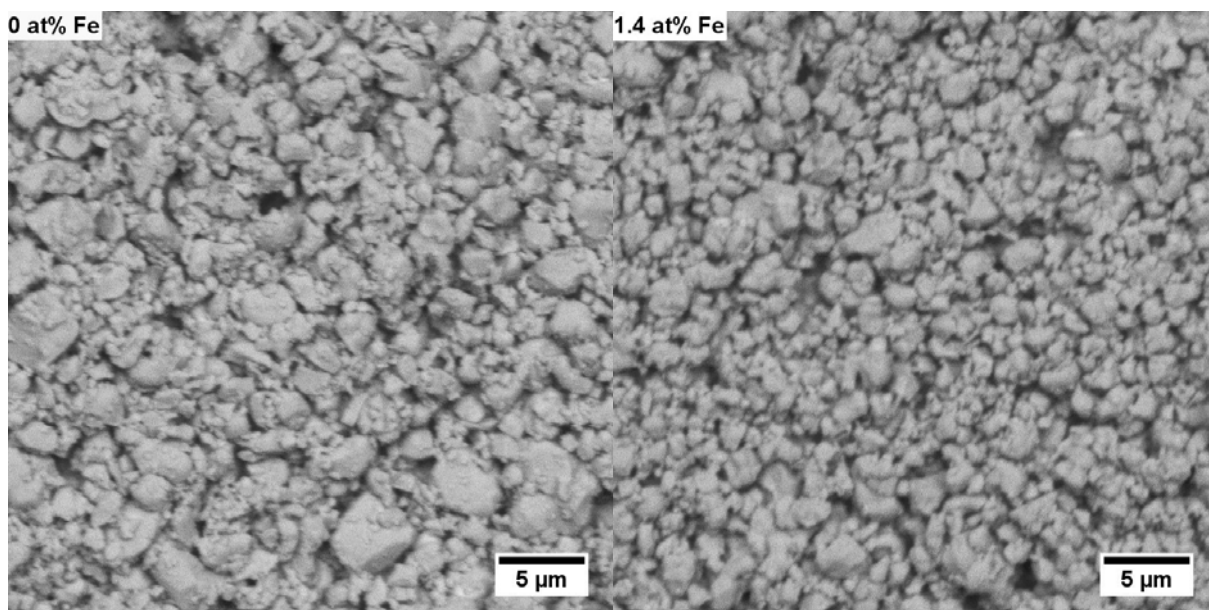


**Figure 5-10 SEM micrographs of calcined and milled powders without and with Fe present (batches 4 and 13 respectively).**

#### 5.4.2 Weight loss after calcination, burnout and sintering

All batches showed PbO loss of 2.6–3.9 g after calcination, which is approximately the overstoichiometric amount of PbO added to each batch (3.3 g). PbO loss in this case refers to the total weight loss of powder after subtracting the calculated weight of CO<sub>2</sub> generated by SrCO<sub>3</sub> decomposition. PbO loss did not show any correlation with composition.

Additional loss between 0.56–0.85 wt% was observed after binder burnout. Values were recorded for 10 individual samples (1 stack) per batch. Standard deviation per batch was no more than 0.1 wt%, showing that the binder distribution within the powder was relatively homogeneous.

Figure 5-11 shows the dependence of the average weight loss of compacts after sintering on the sintering temperature and composition. The compacts exhibited a loss of 0.3–0.7 wt%, which corresponds to 0.4–1.0 at% of Pb depending on the composition. This suggests that the sintered specimens should be slightly Pb deficient. However, these calculations don't consider the

evaporation of impurities and transport of Ti at contact points between the compacts and the powder bed. Average weight loss after sintering noticeably decreased after doping with  $\geq 1.4$  at% Fe as can be seen in Figure 5-11. Increasing sintering temperature decreased weight loss in both Fe-doped and undoped materials. The presence of Sr did not affect the weight loss of samples without Fe. It decreased the weight loss of samples when combined with Fe. The loss did not correlate with the Zr/Ti ratio.

The differences in weight loss are possibly related to the sintering kinetics and the vapour pressure of PbO inside the crucible. The powder bed used in this work should establish a PbO-rich atmosphere of a certain PbO partial pressure, depending on the temperature. A stoichiometric PZT compact should absorb a low amount of PbO from the atmosphere to match the PbO activity of the powder bed. Holman and Fulrath [139] showed that the activity of PbO above  $\text{PbZrO}_3 + \text{ZrO}_2$  increases with increasing temperature, which means that more PbO can be absorbed by the sample at higher temperatures. Similarly, if the PZT sample has a stoichiometric excess of PbO, it will release it until an equilibrium is established. Atkin and Fulrath suggested that aliovalent dopants bind A- or B-site vacancies and slow down diffusion in the material [81]. In this case,  $\text{Fe}^{3+}$  doping might have affected the diffusion of Ti into the powder bed and  $\text{Pb}^{2+}$  to/from the compact surface.

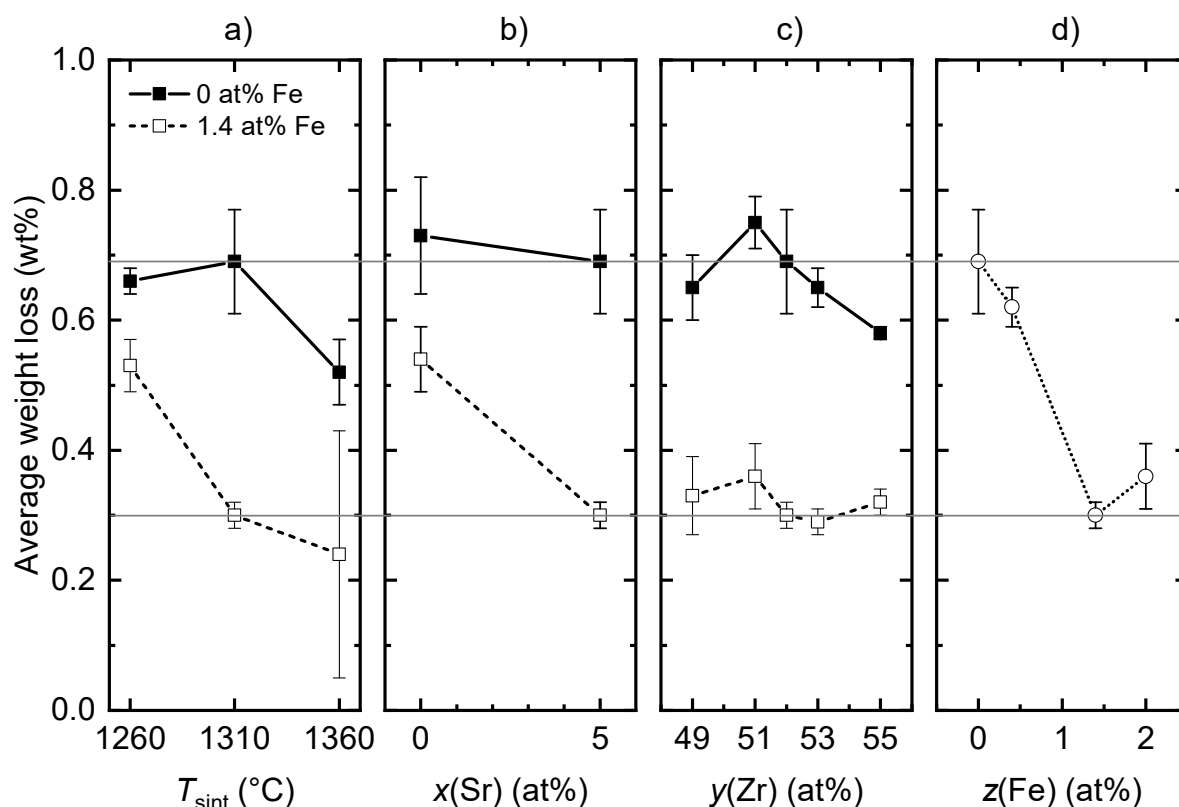


**Figure 5-11** Dependence of average weight loss of compacts after sintering on a) sintering temperature ( $T_{\text{sint}}$ ), b) Sr content, c) Zr/Ti ratio, d) Fe content of  $(\text{Pb}_{1-x}\text{Sr}_x)(\text{Zr}_y\text{Ti}_{1-y})_{1-z}\text{Fe}_z\text{O}_3$ . Grey horizontal lines connect single central compositions, error bars represent SDM,  $T_{\text{sint}} = 1310$  °C if not stated otherwise.

Fe-doped composition sintered at 1360 °C (batch 15) showed a very high standard deviation. This was due to its variability in weight loss within a single stack. Figure 5-12 shows that in this case, samples near the top showed significantly lower loss than samples on the bottom. Compositions without Fe doping did not show this variation. The most plausible explanation of this phenomenon is an incomplete crucible enclosure. Crucible pieces rested loosely on top of each other and it is possible that the middle piece was accidentally lifted when the crucible was being filled with the powder bed and some of the sand got trapped under it, creating a gap at the bottom. PbO would escape during sintering, creating a concentration gradient of PbO vapour inside the crucible.

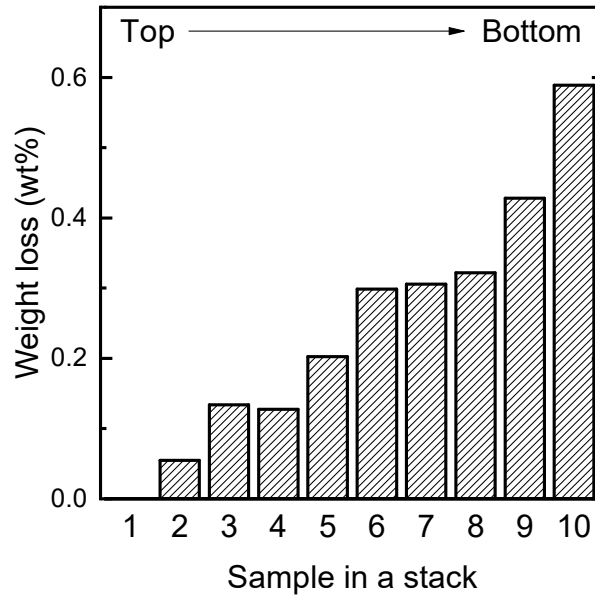


**Figure 5-12 Weight loss of individual samples in a stack of  $(\text{Pb}_{0.95}\text{Sr}_{0.05})(\text{Zr}_{0.52}\text{Ti}_{0.48})_{0.986}\text{Fe}_{0.014}\text{O}_3$  (batch 15) after sintering at 1360 °C.**

Phase purity was confirmed with XRD and SEM observations of one as-sintered sample from each batch. Depending on Fe doping and sintering temperature, there may be batch-to-batch differences in the deficiency of PbO. However, the recorded weight loss may not be entirely caused by the loss of PbO and even if it was, the differences are very small (within 1 at% of Pb). It is possible that batch 15 contains larger sample-to-sample differences, due to variable weight loss, however, it should be kept in mind that all the samples had their outer layer machined prior to carrying out any further functional or mechanical tests.

#### 5.4.3 Flatness, parallelism

Dimensions of randomly chosen machined samples from 7 batches were measured using 2 separate co-ordinate measuring machines (10 and 11 samples per machine, denoted as set 1 and set 2 as described in section 4.1.1). The average flatness including measurements from both faces of the disc was 0.003 mm with a standard deviation of 0.001 mm. Both sets of samples showed the same value, proving that both machines gave consistent results. Measured flatness

was well within the tolerance of 0.010 mm given by the ASTM standard [16] and did not significantly vary. There was no statistical difference between disc faces.

Set 1 and set 2 showed average parallelism values of 0.010 and 0.012 mm respectively, with a standard deviation of 0.003 mm. All values ranged between 0.006 to 0.019 mm, which means that some of the samples showed values outside the recommended tolerance of 0.010 mm. 29 % of samples showed parallelism values larger than 0.013 mm (tolerance + standard deviation). It is not clear, if such values pose a significant strength measurement inaccuracy. It was assumed that parallelism deviations outside the allowed tolerance range will be mitigated by the compliant layers and free tilt of the load ring in the ROR test fixture.

## 6 PHYSICAL PROPERTIES

This chapter presents results of the measured physical properties of the prepared batches and discusses their dependence on the studied factors – composition and sintering temperature. The properties include grain size, relative density, thickness shrinkage, pore size distributions, phase contents, tetragonality, and nanoscale homogeneity.

### 6.1 Grain size

The effects of composition and sintering temperature on grain size of the sintered samples are summarised in Figure 6-1 a). As expected, grain size increases with increasing sintering temperature. Samples not doped with Fe show a linear trend and increase in average grain size by 2  $\mu\text{m}$  for sintering temperatures from 1260–1360  $^{\circ}\text{C}$ . On the other hand, Fe-doped compositions showed grain size increase by 0.6  $\mu\text{m}$  only at 1360  $^{\circ}\text{C}$ , less than in the previous case. The difference is most likely caused by the effect of  $\text{Fe}^{3+}$  on the grain boundary movement discussed further in subsequent chapters.

Addition of  $\text{Sr}^{2+}$  did not affect the average grain size of pure PZT. Average grain size decreased from 2.4 to 1.2  $\mu\text{m}$  when Sr was added to Fe-doped PZT as shown in Figure 6-1 b). Previous reports report conflicting results. Pure PZT exhibited grain growth inhibition [50] or no change in grain size [153] when Sr was added, while donor-doped [154] and donor-acceptor co-doped PZT [155] showed a grain size increase. This suggests that the effect of Sr on sintering kinetics depends on its interaction with other dopants.

Grain size somewhat decreased towards Zr-rich compositions in Fe-free compositions. This is not surprising since  $\text{PbZrO}_3$  exhibits a higher melting point than  $\text{PbTiO}_3$  [156] and the decrease was also observed elsewhere [77]. Diffusion of Zr during sintering was reported as slower compared to Ti [157, 158], which could possibly lead to a reduced rate of grain growth and

densification. The work of Chung [140] showed that Ti-rich compositions exhibit higher average grain size than Zr-rich compositions. Fe-doped PZT does not show any variation of average grain size with increasing Zr/Ti ratio, which is probably due to the grain size of these compositions being already close to the particle size of starting powder.

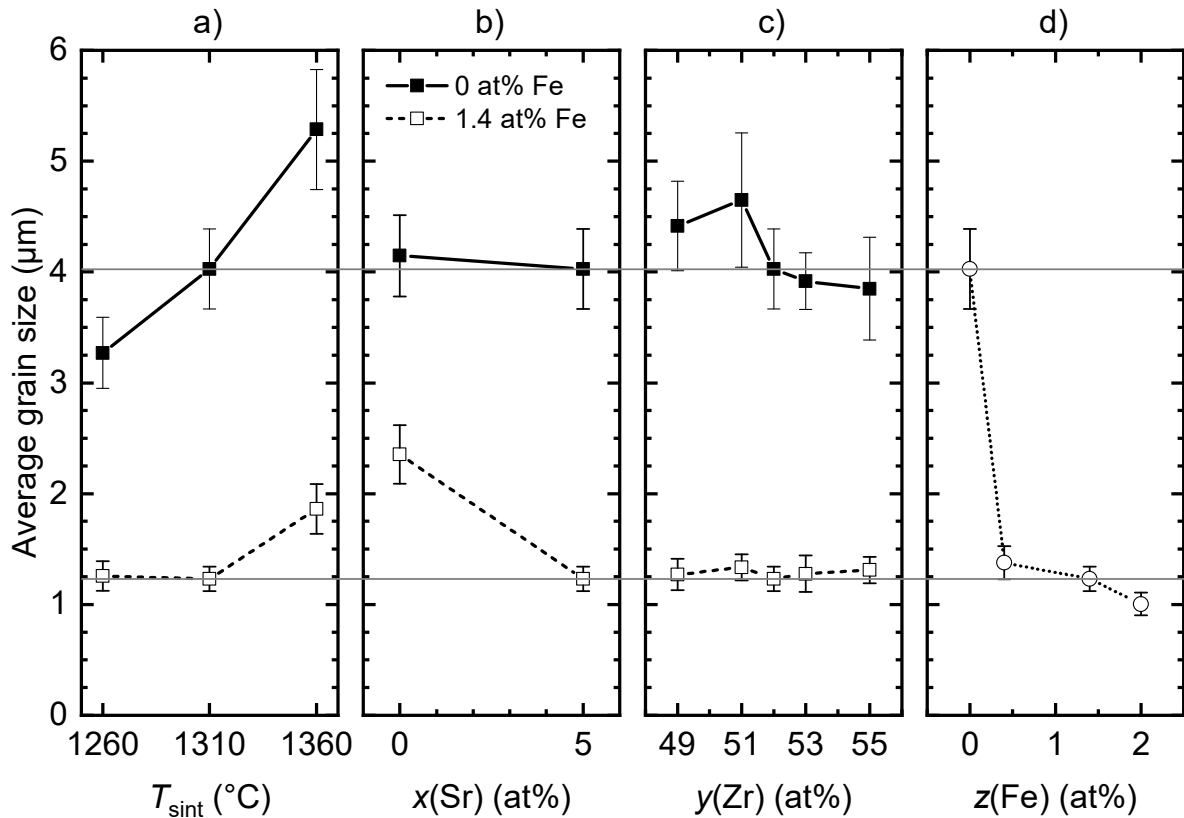


**Figure 6-1** Dependence of average grain size on a) sintering temperature ( $T_{\text{sint}}$ ), b) Sr content, c) Zr/Ti ratio, d) Fe content of  $(\text{Pb}_{1-x}\text{Sr}_x)(\text{Zr}_y\text{Ti}_{1-y})_{1-z}\text{Fe}_z\text{O}_3$ . Grey horizontal lines connect single central compositions, error bars represent SDM,  $T_{\text{sint}} = 1310$  °C if not stated otherwise.

It is well established that aliovalent dopants often inhibit grain growth, although the mechanism is still not completely understood. It is generally attributed to the disruption of defect equilibria at the grain surface at high temperatures [27]. Also, Fernández et al. [159] demonstrated that some cations ( $\text{Fe}^{3+}$  in his experiment) are not readily incorporated into the PZT lattice.

Atkin and Fulrath [81] speculated that aliovalent dopants concentrate near grain boundaries and associate with their respective vacancies (either lead or oxygen) via Coulombic forces. Grain boundary movement is then inhibited by a solute drag mechanism. Single doping with  $\text{Nb}^{5+}$  (donor) or  $\text{Al}^{3+}$  (acceptor) decreased grain size, while their combination did not. The authors hypothesised that in this case, dopants formed associates with each other rather than with charged vacancies and these associates were not strongly adsorbed by the moving grain boundary.

Hammer and Hoffmann [74] studied La-doped PZT (donor) and observed that La concentrated in the grain core. They also reported an inhomogeneous Zr/Ti distribution, where the grain core was enriched in Ti, while the outer shell contained more Zr. It was hypothesised that  $\text{La}^{3+}$  preferentially substituted Ti and the grain growth was inhibited by the solute drag of a Zr-enriched layer, rather than by dopant-defect associates. It should be noted that the reaction mechanism and the potential presence of a Pb-rich liquid phase (see section 2.5.3) could have been responsible for this phenomenon.

Addition of 0.4 at% of Fe to Sr-doped PZT significantly reduced the average grain size from 4.0 to 1.4  $\mu\text{m}$  as shown in Figure 6-1 d). Further increase in Fe content resulted only in a marginal decrease to 1.0  $\mu\text{m}$  for 2.0 at% Fe. Average grain size values of all acceptor-doped compositions are lower than the median particle size of their respective calcined powders, which signifies that the grain growth was effectively suppressed. It is possible that the grain size decrease between 0.4–2.0 at% Fe is related to the decrease in starting particle size, rather than the effect of Fe doping. Calcined powder median particle size ranged between 2.1–1.5  $\mu\text{m}$  for 0.4–2.0 at% Fe. The same trend of grain size dependence on Fe content was observed by Weston et al. [80].

## 6.2 Relative density

The sintering behaviour of PZT is not trivial, mostly due to the presence of PbO with a relatively low melting point. Because the presence and quantity of a liquid phase during sintering significantly affects the onset temperature and the shape of the sintering curve, final densities and microstructure depend strongly on the stoichiometric excess or deficiency in PbO [74, 76, 160]. Stoichiometric excess of PbO in the starting compositions was shown to reduce the onset sintering temperature [74] and to enhance densification by accelerating mass transport by the liquid phase. However, when the excess of PbO is too high (reported as  $\geq 3$  mol%), final densities are reduced as the rapid early densification creates inhomogeneous microstructure and large, thermodynamically stable pores [76].

All compositions in this work were prepared with 3.3g ( $\approx 0.86$  mol%) excess of PbO, which should have been roughly the amount lost during calcination and sintering. However, as discussed in section 5.4.2, the measured weight loss might be biased by other volatile substances or diffusing species and is generally not accurate enough to support this claim. The PbO loss is also likely to be inhomogeneous during sintering, where the volatilisation is expected primarily at the sample surface. Considering all these factors, PbO liquid phase is expected to be present during the sintering of samples used in this work. As indicated in chapter 5.4.2, there are most likely small differences in PbO content among the different batches. However, it is not possible to assess their effect on final densities from the available data.

The relative density of sintered samples ( $\rho_{rel}$ ) exhibited a maximum for samples sintered at 1310 °C, irrespective of acceptor doping (Figure 6-2 a). For compositions containing 0 at% Fe, no statistically significant change in density with sintering temperature was found when the temperature was raised to 1360 °. In contrast, acceptor-doped compositions showed a relative density decrease of  $\approx 1$  % at this temperature. It was shown in the previous section, that Fe

inhibits grain growth. The average grain size of acceptor-doped samples increased for samples sintered at at 1360 °C, indicating enhancement of grain growth as well as pore coalescence, and formation of larger and more stable pores. This would explain the decrease in relative density. A similar phenomenon could be expected in samples with no added Fe, however, their grain growth is not nearly as inhibited, which means that larger pores appear even at 1310 °C and porosity changes accompanying an increase in sintering temperature are not as significant.

It should be noted, that the measured relative densities of the Fe-doped composition sintered at 1260 °C exhibited a very high standard deviation, which was likely related to microstructural inhomogeneities introduced by solid state processing.

Kulcsar reported that  $\text{Ca}^{2+}$  and  $\text{Sr}^{2+}$  exhibit fluxing effects up to 5 at%, which increases density of sintered compacts [50]. In his study, an approximately 2 % increase in relative density was achieved with 5 at% of Sr doping. An increase of between 2–3 % relative density was observed when 1 at% of Sr was added to La, Mn co-doped PZT in [155]. A similar increase was observed for the addition of 1.5 at% of Sr to La, Nb co-doped PZT in [154].

As shown in Figure 6-2 b), addition of 5 at% of Sr to pure PZT induced a relative density decrease of  $\approx 0.4$  %, which disagrees with previous studies. It is speculated that the positive fluxing effect of Sr was lost due to impurities and excess of PbO. XRF analysis of raw oxides repeatedly detected the presence of Ca, which was shown to exhibit similar behaviour. In Kulcsar's study, increasing the Sr content above 5 at% led to a significant decrease in density. The study did not provide any microstructural information, but it could be hypothesised that above a certain threshold, fluxing effects of  $\text{Sr}^{2+}$  lead to enhanced pore coalescence, creating larger and more stable pores. This theory will be further investigated in section 6.4.

A combination of Sr and Fe doping induced a decrease in average grain size, suggesting an interaction between dopants and inhibition of grain growth. Reduction in coarsening would lead to higher relative densities. More insight can be gained from the porosity results presented in section 6.4.

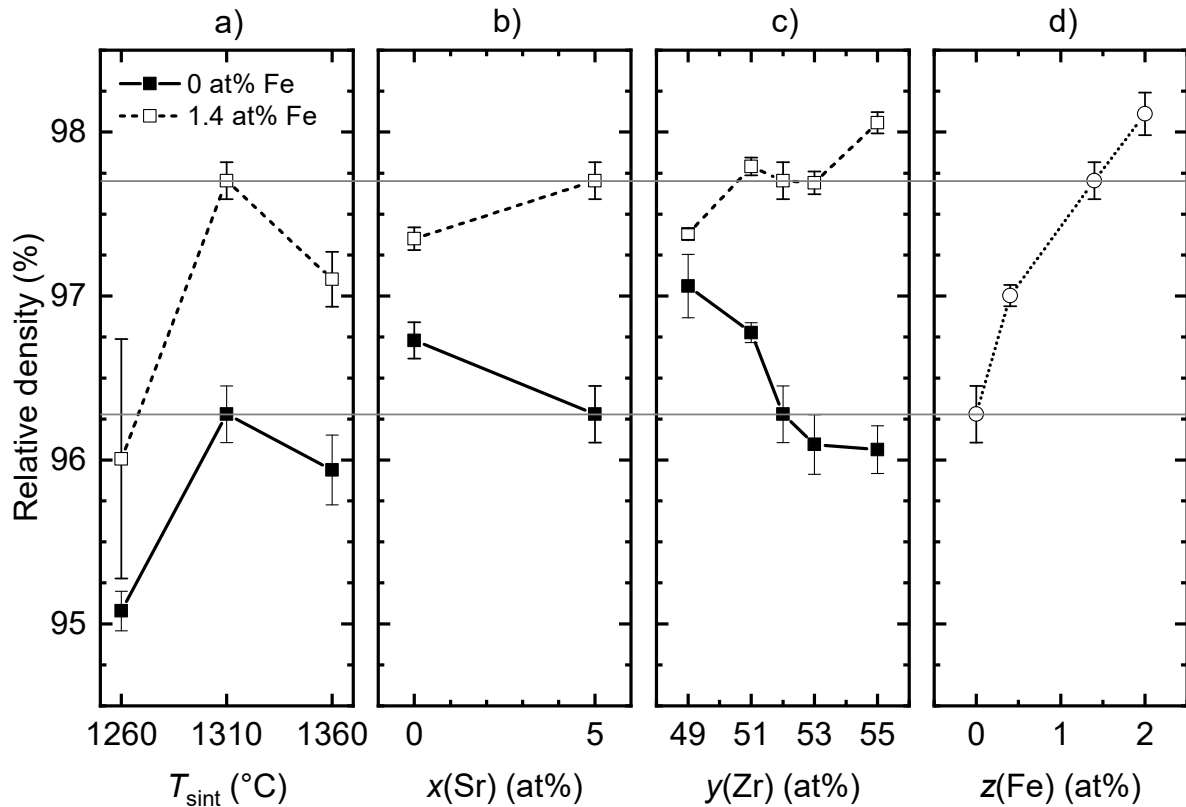


**Figure 6-2** Dependence of relative density on a) sintering temperature ( $T_{sint}$ ), b) Sr content, c) Zr/Ti ratio, d) Fe content of  $(\text{Pb}_{1-x}\text{Sr}_x)(\text{Zr}_y\text{Ti}_{1-y})_{1-z}\text{Fe}_z\text{O}_3$ . Grey horizontal lines connect single central compositions, error bars represent SDM,  $T_{sint} = 1310$  °C if not stated otherwise.

The dependence of relative density on the  $y$  in  $(\text{Pb}_{1-x}\text{Sr}_x)(\text{Zr}_y\text{Ti}_{1-y})_{1-z}\text{Fe}_z\text{O}_3$  showed opposite trends depending on the presence of Fe, which is illustrated in Figure 6-2 c). The relative density of Fe-free samples showed a decrease of 1 % with increasing  $y(\text{Zr})$  from 49 to 55 at%, while acceptor-doped PZT showed an increase of 0.7 %. The variation in density is small overall and grain size was not significantly affected by the Zr/Ti ratio. Hoffmann et al. [78] observed a lower relative density in rhombohedral La-doped PZT. They suggested that Ti-rich

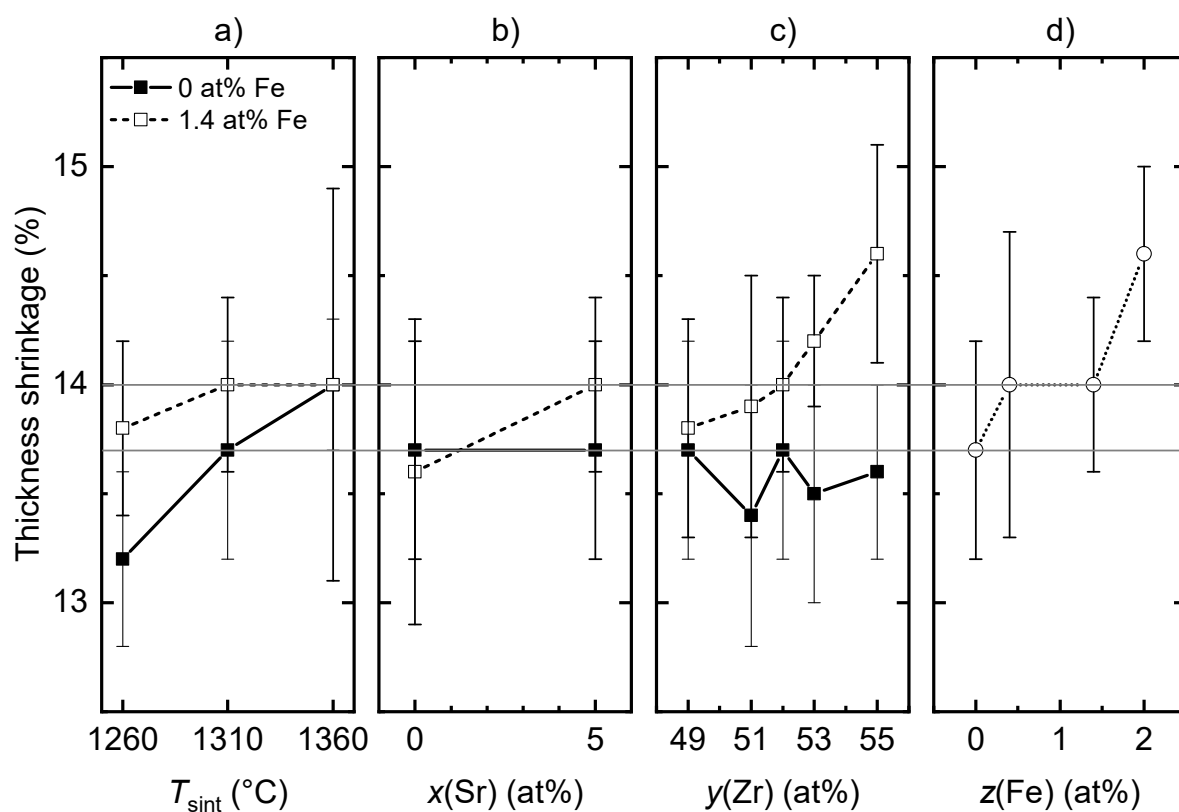
compositions tend to react with the PbO rich atmosphere inside the crucible, leaving a secondary phase at grain boundaries and triple points. This cannot be confirmed in this work as the recorded weight loss was similar regardless of Zr/Ti ratio. The opposing density trends will be further discussed in section 6.4.

Figure 6-2 d) shows that the relative density increased monotonically with increasing Fe content. As shown in the previous section, Fe inhibits grain growth. Since densification and grain growth are competing mechanisms, inhibition of grain growth enhances densification, which explains the raise in relative density.

### **6.3 Thickness shrinkage**

The thickness shrinkage of PZT discs was expected to follow the relative density trends. Results showed relatively high standard deviation, which was most likely caused by several factors such as sample warpage and sintering in a stack, where the bottom samples experienced the most significant load.

Thickness shrinkage plots are shown in Figure 6-3. Shrinkage trends cannot be confidently compared to trends in density due to the high standard deviation of the shrinkage measurements. Fe-doped PZT sintered at 1360 °C showed an exceptionally high standard deviation. Variable PbO loss within the stack discussed in chapter 5.4.2 was probably responsible for this phenomenon (the average value was calculated from samples in a single stack). It should be noted that the high standard deviation found here was not reflected in the relative density results, which suggests that a density difference may have been significant only in the surface layer removed by machining.



**Figure 6-3** Dependence of thickness shrinkage of samples after sintering on a) sintering temperature ( $T_{\text{sint}}$ ), b) Sr content, c) Zr/Ti ratio, d) Fe content ( $\text{Pb}_{1-x}\text{Sr}_x(\text{Zr}_y\text{Ti}_{1-y})_{1-z}\text{Fe}_z\text{O}_3$ ). Grey horizontal lines connect single central compositions, error bars represent SDM,  $T_{\text{sint}} = 1310 \text{ °C}$  if not stated otherwise.

## 6.4 Pore size distribution

Characterisation of porosity in dense ceramic materials is not trivial as the porosity is mostly closed and therefore not accessible by intrusion and adsorption techniques. This was confirmed to be the case for the current samples as none of the trial tests utilising mercury intrusion porosimetry or nitrogen gas adsorption produced any consistent or reliable results. Samples would have to be powdered in order to make enough pores accessible and gain information about micropores (<2 nm), mesopores (2–50 nm) or macropores (>50 nm). The pore size distribution would likely depend on the particle size as large macropores would gradually get destroyed with decreasing particle size of the powder. Open porosity determination methods also assume a certain pore shape, which may not necessarily reflect reality [161].

Analysis of two-dimensional cross sections or fractured surfaces is one of the simplest method suitable for the analysis of the pore structure [18]. It was considered that large macropores above 1  $\mu\text{m}$  should provide information useful for speculations involving sintering kinetics and fracture as the largest defects are responsible for the fracture initiation and preliminary investigations showed significant presence of pores in this size range. Optical microscopy of polished sections (1 sample per batch) was used in this work as described in section 4.1.4. Due to limitations of this method, only a certain size range of pores could be reliably examined. Pores and pore clusters ranging in size from less than 1  $\mu\text{m}$  to more than 200  $\mu\text{m}$  were found using SEM. When a porous solid contains a wide range of porosity, increasing image magnification leads to increased bias associated with the choice of areas of investigation. The only way to overcome this issue is to capture and analyse many images, which can be tedious and time consuming. In addition, the largest pores/clusters can be too large to fit in the image at high magnifications. Conversely, if the magnification is too low, small pores cannot be resolved and some pores may appear interconnected. Considering these limitations, images

captured at 10× magnification were chosen for the analysis. This method allowed pore quantification in the range of 2–50 μm, where the minimum pore size was limited by the number of pixels per pore (pores consisting of less than 10 px were not counted) and the maximum was chosen arbitrarily; at least 1 pore in the range of 40–50 μm was found in every sample.

The percentage of area covered by pores of a certain range of maximum Feret diameter was selected to quantify porosity, Feret diameter intervals followed an exponential function  $f(x) = 10^x$ . This allowed a balanced observation of the entire range of pore diameters within a single graph. As with other methods describing pore diameter, maximum Feret diameter does not reflect the pore shape. Therefore, the distribution plots somewhat simplify the real microstructure. A representative image of each batch is included below the respective graphs, illustrating the original pore structure. To make distributions comparable and avoid bias as much as possible, each distribution was compiled from 15 randomly chosen areas; brightness of microscope images was controlled automatically by the AxioVision software supplied with the AxioCam HR3 camera; and thresholding was performed using a built-in automatic algorithm, the “IsoData” function, in ImageJ software. Variability of the surface coverage was quantified by calculation of the standard deviation of mean from the 15 photographed areas per each batch.

Porosity was intergranular in all examined samples, suggesting that sintering path did not cross the separation region, where pores get trapped inside rapidly growing grains [75]. Pore clusters ranging from tens to hundreds of μm were found on polished sections of all prepared samples. Binder optimisation experiments described in section 5.1.2 attributed their presence to the manual binder mixing process. The size and frequency of pore clusters varied among batches, implying that their original size and shape in the powder compacts were different. Individual

pores making up clusters were likely more dispersed in the green bodies and they coalesced during sintering in a process affected by sintering kinetics. Unfortunately, the largest pores/pore clusters, which are the potential critical fracture initiating defects, could not be reliably quantified as their frequency and the probability of finding them was low. The particle analysis algorithm in ImageJ cannot distinguish pore clusters, therefore their size and occurrence were only evaluated by visual comparison of images of polished sections at 5× magnification. Information about largest defects present in the microstructure were obtained from fractographical observations.

Pore size distributions of  $(\text{Pb}_{0.95}\text{Sr}_{0.05})(\text{Zr}_{0.52}\text{Ti}_{0.48})\text{O}_3$  (0 at% Fe) sintered at different temperatures are shown in Figure 6-4. Optical micrographs of their polished surfaces are shown in Figure 6-5. It is evident that increasing sintering temperature shifts the maximum % of covered area towards larger pore diameters. This is consistent with monotonous increase in grain size as a response to increasing sintering temperature. It also confirms that pore coalescence intensifies at higher temperatures, which was previously suggested as the reason for a decrease in relative density at 1360 °C. In the studied range of pore diameters, samples sintered at 1310 °C showed less porosity than samples sintered at 1260 °C, which agrees with the relative density trend. No significant difference in the presence and size of pore clusters was observed between the batches.

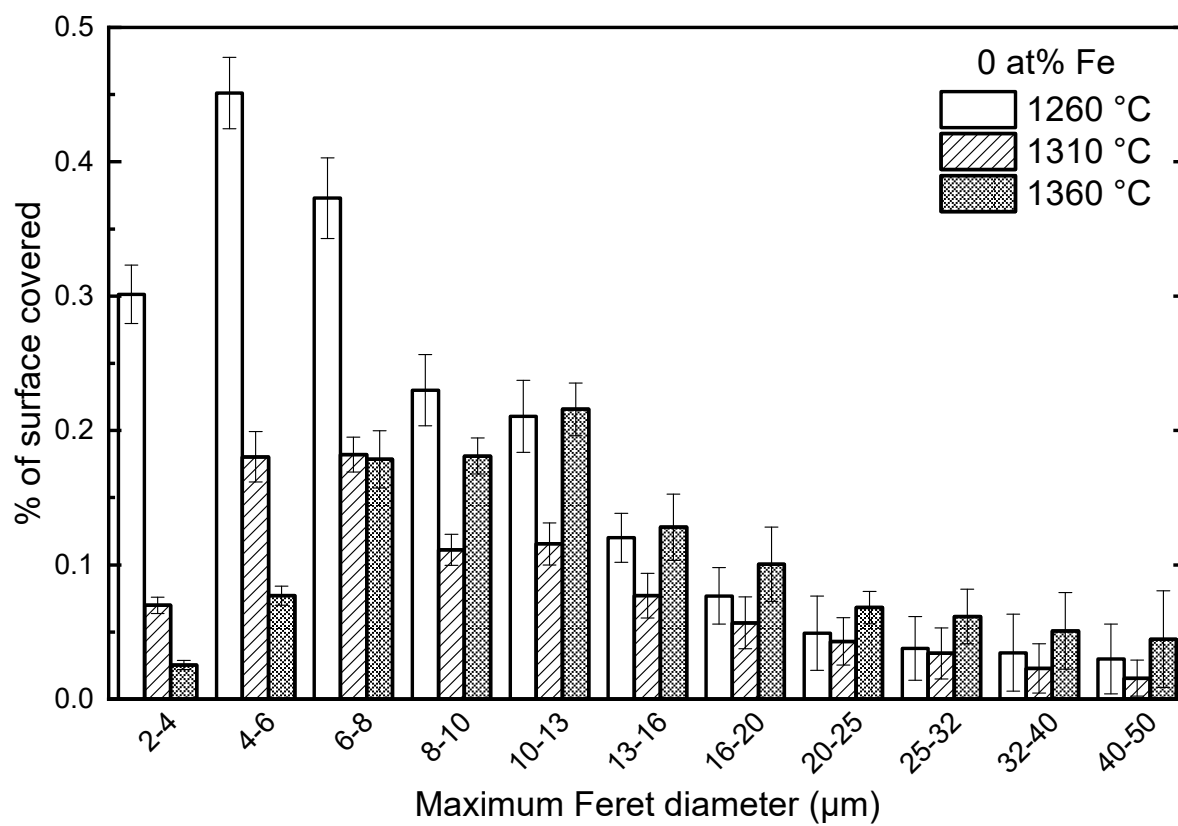
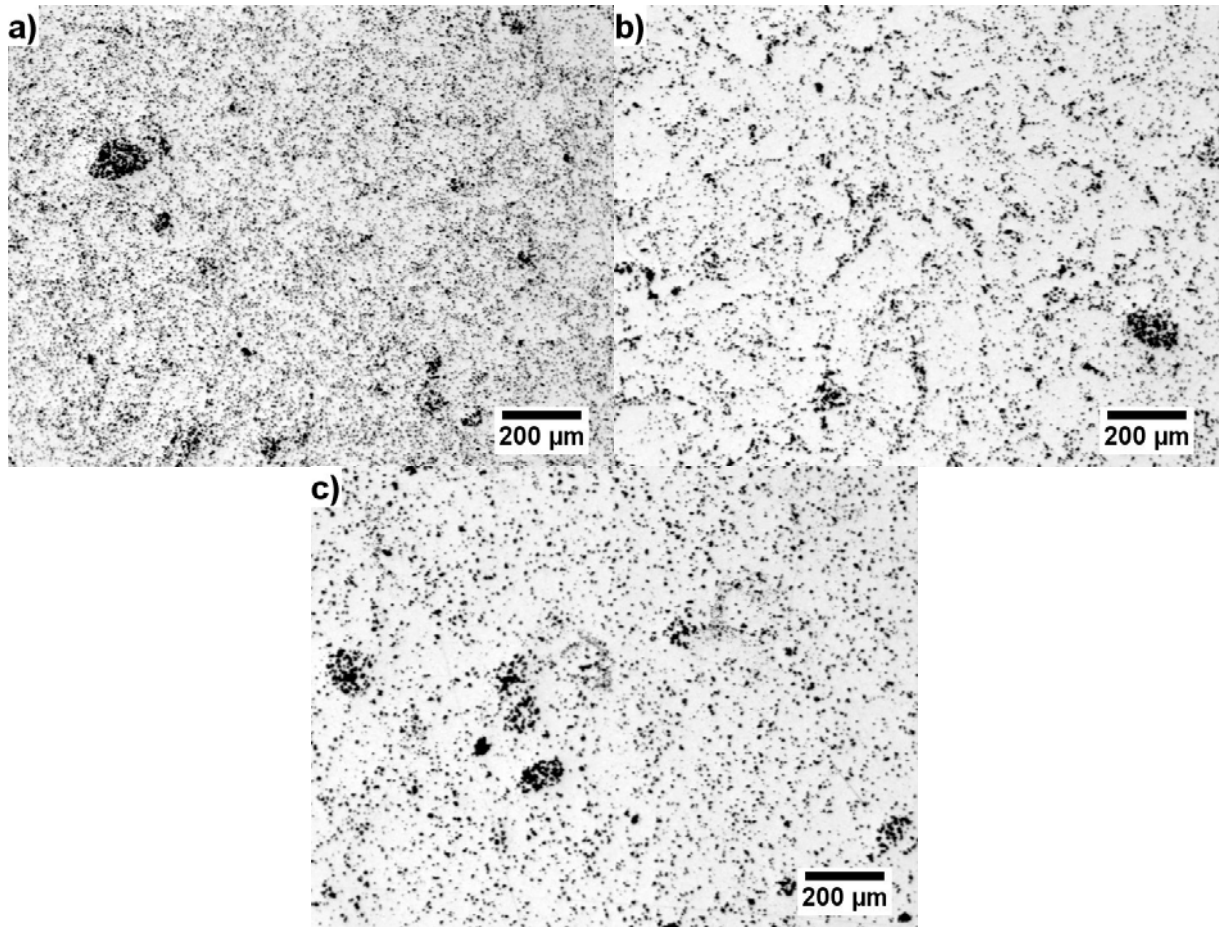


Figure 6-4 Percentage of surface area covered by pores of a certain maximum Feret diameter in  $(\text{Pb}_{0.95}\text{Sr}_{0.05})(\text{Zr}_{0.52}\text{Ti}_{0.48})\text{O}_3$  sintered at different temperatures.



**Figure 6-5 Optical micrographs of polished surfaces of  $(\text{Pb}_{0.95}\text{Sr}_{0.05})(\text{Zr}_{0.52}\text{Ti}_{0.48})\text{O}_3$  sintered at a) 1260 °C, b) 1310 °C, c) 1360 °C.**

Pore size distributions and surface micrographs of  $(\text{Pb}_{0.95}\text{Sr}_{0.05})(\text{Zr}_{0.52}\text{Ti}_{0.48})_{0.986}\text{Fe}_{0.014}\text{O}_3$  sintered at different temperatures are shown in Figure 6-6 and Figure 6-7 respectively. Findings are similar to the previous case with some notable differences. When the sintering temperature is increased to 1310 °C, only the smallest pores (2–6 μm) are removed, while the percentage of larger pores does not significantly change. This corresponds to an increase in relative density as the grain size remains the same. However, sintering at 1360 °C shows that the area covered by pores larger than 8 μm is clearly larger than at lower sintering temperatures. It is suggested that pore coalescence becomes significant at this temperature, which is in agreement with the observed increase in grain size and reduction in relative density.

Visual observations of polished surfaces revealed that Fe-doped samples contain less pore clusters than undoped compositions. It is unclear whether this is related to the binder distribution in the compacts or the sintering kinetics.

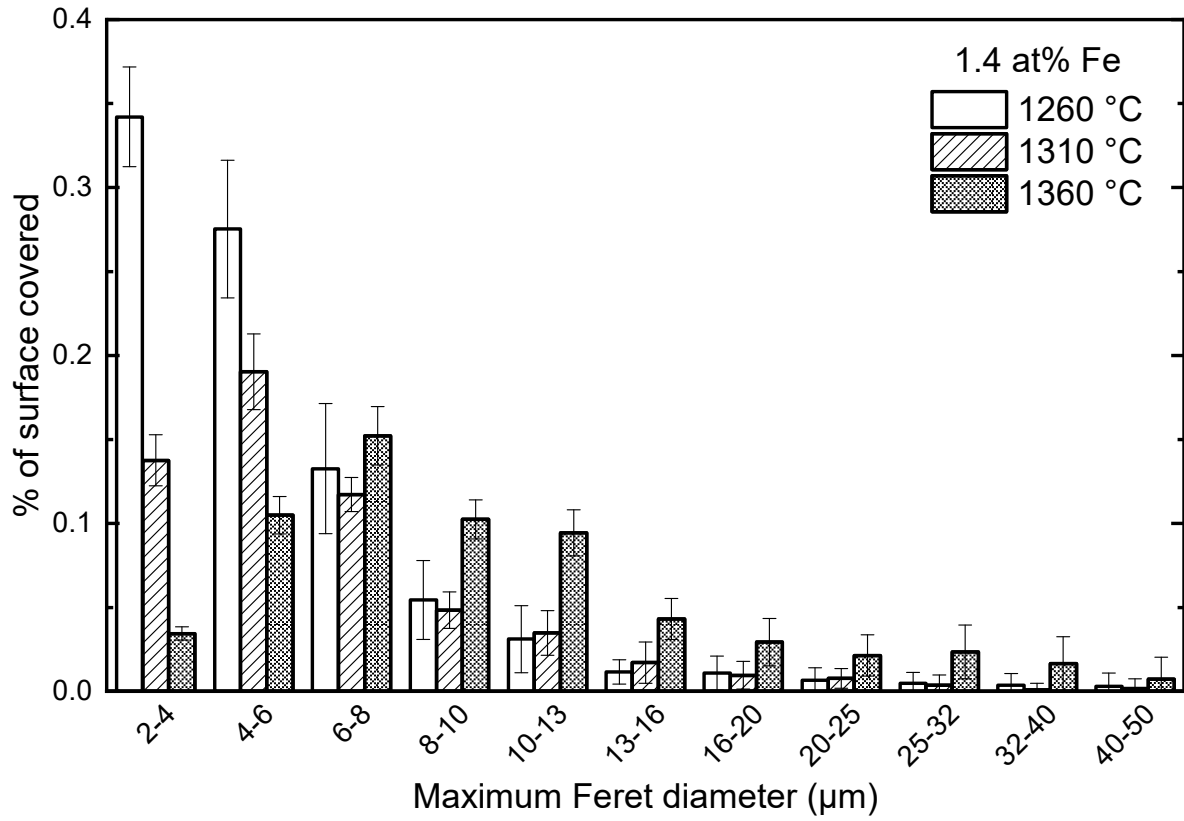
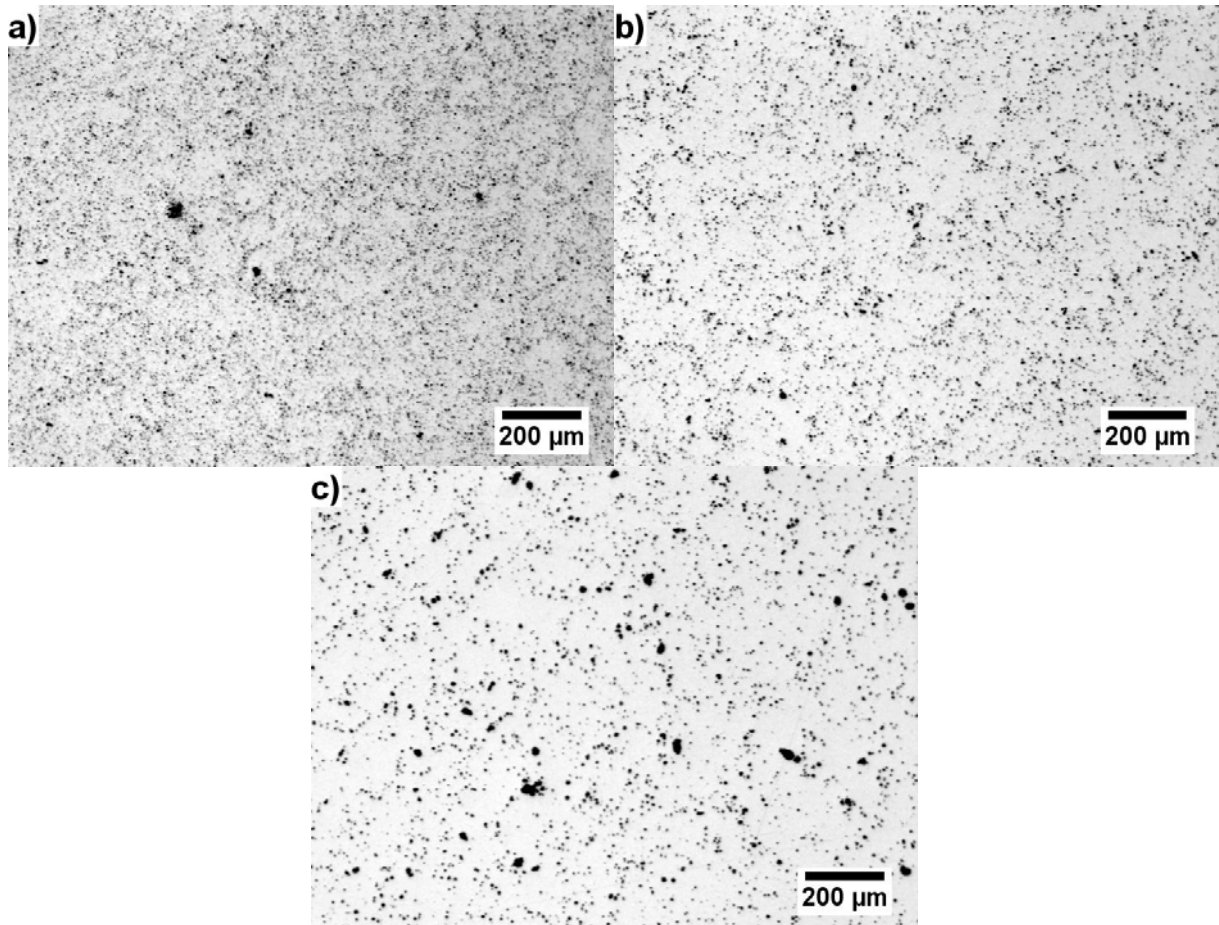


Figure 6-6 Percentage of surface area covered by pores of a certain maximum Feret diameter in  $(\text{Pb}_{0.95}\text{Sr}_{0.05})(\text{Zr}_{0.52}\text{Ti}_{0.48})_{0.986}\text{Fe}_{0.014}\text{O}_3$  sintered at different temperatures.



**Figure 6-7 Optical micrographs of polished surfaces of  $(\text{Pb}_{0.95}\text{Sr}_{0.05})(\text{Zr}_{0.52}\text{Ti}_{0.48})_{0.986}\text{Fe}_{0.014}\text{O}_3$  sintered at a) 1260 °C, b) 1310 °C, c) 1360 °C.**

The influence of Fe and Sr doping on the character of porosity can be deduced from the pore size distribution in Figure 6-8 and optical micrographs of polished sections in Figure 6-9. Doping  $\text{Pb}(\text{Zr}_{0.52}\text{Ti}_{0.48})\text{O}_3$  with Sr does not introduce any significant differences to the pore size distribution within the observed range of Feret diameters.

Different behaviour is observed in Fe-doped PZT. When only Fe is present, grain growth is inhibited, and the sintered compact achieves higher relative density. However, larger pores between 20–50 μm are still present in this composition at similar percentages as in Fe free samples. The surface micrograph shown in Figure 6-9 c) reveals that this porosity is likely to be present as pore clusters, suggesting some degree of pore coalescence. When Sr is added, finer and more homogeneous porosity is achieved as shown in Figure 6-9 d). This is also

apparent from the pore size distribution, where the percentage of pores between 2–8  $\mu\text{m}$  is increased and percentage of pores between 20–50  $\mu\text{m}$  is decreased. The absence of pore clusters in the  $(\text{Pb}_{0.95}\text{Sr}_{0.05})(\text{Zr}_{0.52}\text{Ti}_{0.48})_{0.986}\text{Fe}_{0.014}\text{O}_3$  composition is unexpected, as the pore clusters were considered to be already present in the compacts. Since the binder incorporation process was the same for all batches, pore clusters of a similar size would be expected to be present in all sintered bodies. As this was not the case, it is hypothesised that the binder is distributed inhomogeneously throughout the compacts, but the clusters are not well defined. They are formed by pore diffusion and coalescence during sintering. This would explain why, in some cases, clusters (in sintered bodies) are not present or have varying size. The porosity observations discussed in this paragraph are consistent with the data presented earlier (sections 6.1 and 6.2), which showed that co-doping PZT with both Sr and Fe results in a smaller average grain size and higher relative density. It is likely that dopant interaction is responsible for this behaviour.

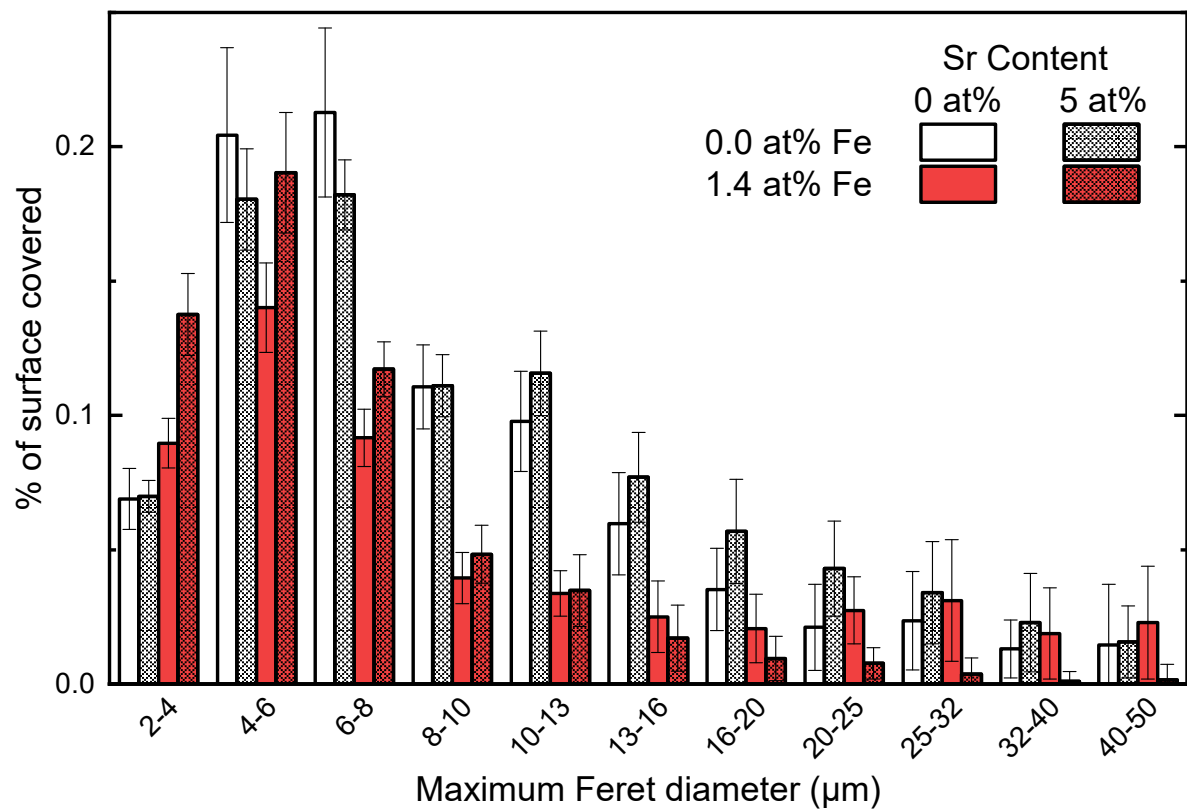
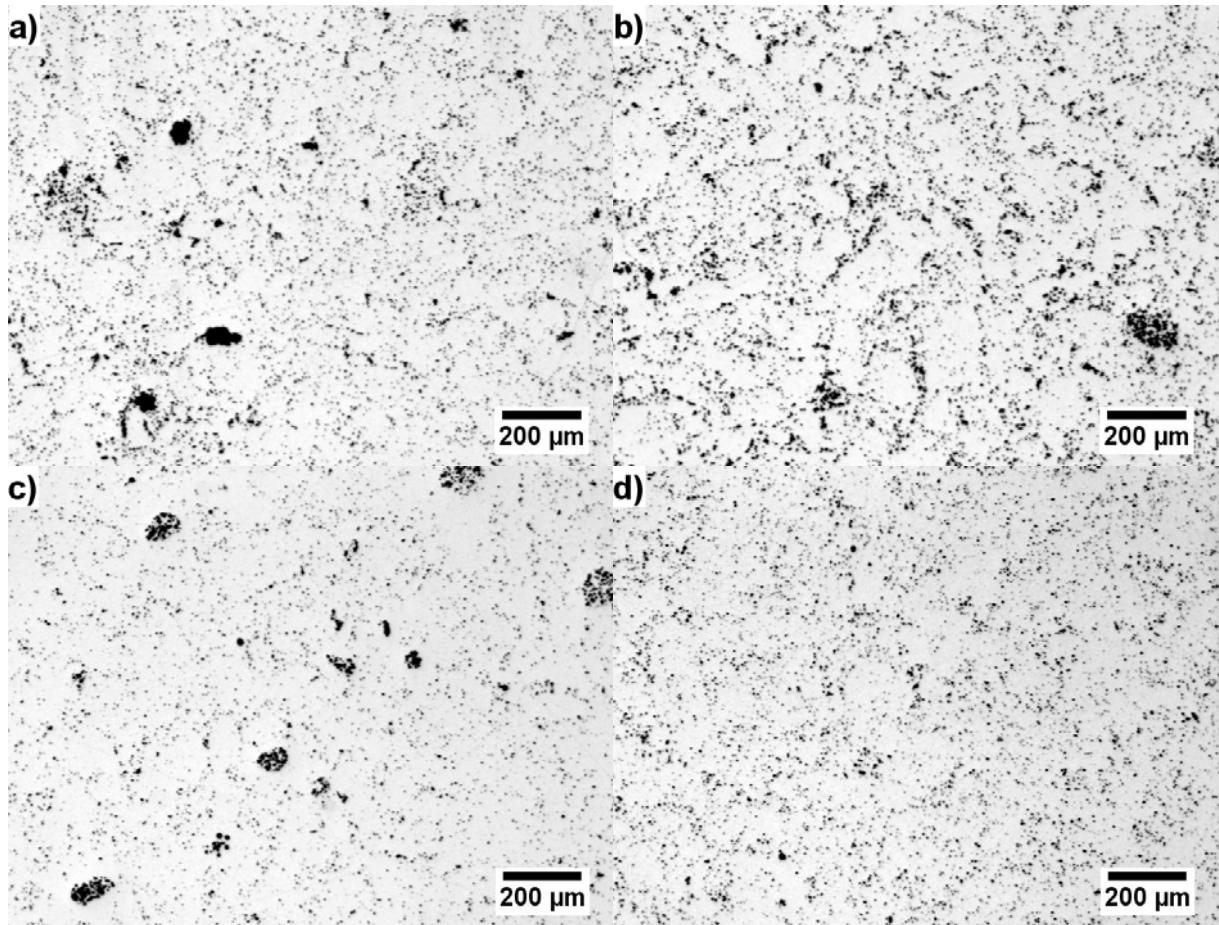


Figure 6-8 Percentage of surface area covered by pores of a certain maximum Feret diameter in  $(\text{Pb}_{1-x}\text{Sr}_x)(\text{Zr}_{0.52}\text{Ti}_{0.48})_{1-z}\text{Fe}_2\text{O}_3$  doped with various amount of Sr and Fe.



**Figure 6-9 Optical micrographs of polished surfaces of  $(\text{Pb}_{1-x}\text{Sr}_x)(\text{Zr}_{0.52}\text{Ti}_{0.48})_{1-z}\text{Fe}_z\text{O}_3$  doped with a)  $x, z = 0$ ; b)  $x = 0.05, z = 0$ ; c)  $x = 0, z = 0.014$ ; d)  $x = 0.05, z = 0.014$ .**

The pore size distribution shown in Figure 6-10 revealed that the porosity noticeably changed after the  $y$  in  $(\text{Pb}_{0.95}\text{Sr}_{0.05})(\text{Zr}_y\text{Ti}_{1-y})\text{O}_3$  reached 53 at%. This is highlighted in the figure by red bars. Compositions with  $y(\text{Zr}) = 0.53, 0.55$  clearly exhibit an increase in the number of pores between 2–10  $\mu\text{m}$ , while larger pores up to 50  $\mu\text{m}$  in size remain unaffected. This is consistent with the decrease in relative density observed in Zr-rich compositions. It appears that increasing the  $y$  affects sintering kinetics and increases the percentage of finer porosity. The change is not as significant as in the case of Sr doping or sintering temperature series and is not easily distinguishable in the micrographs shown in Figure 6-11.

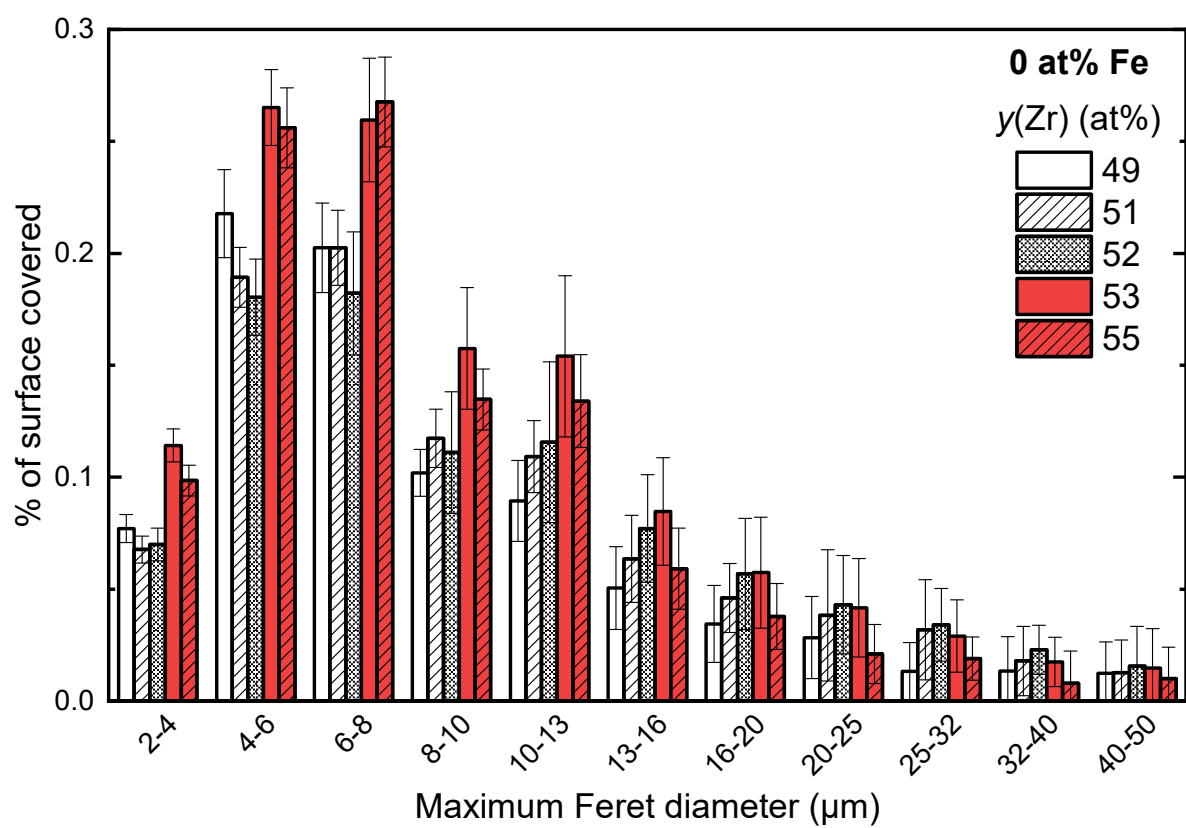
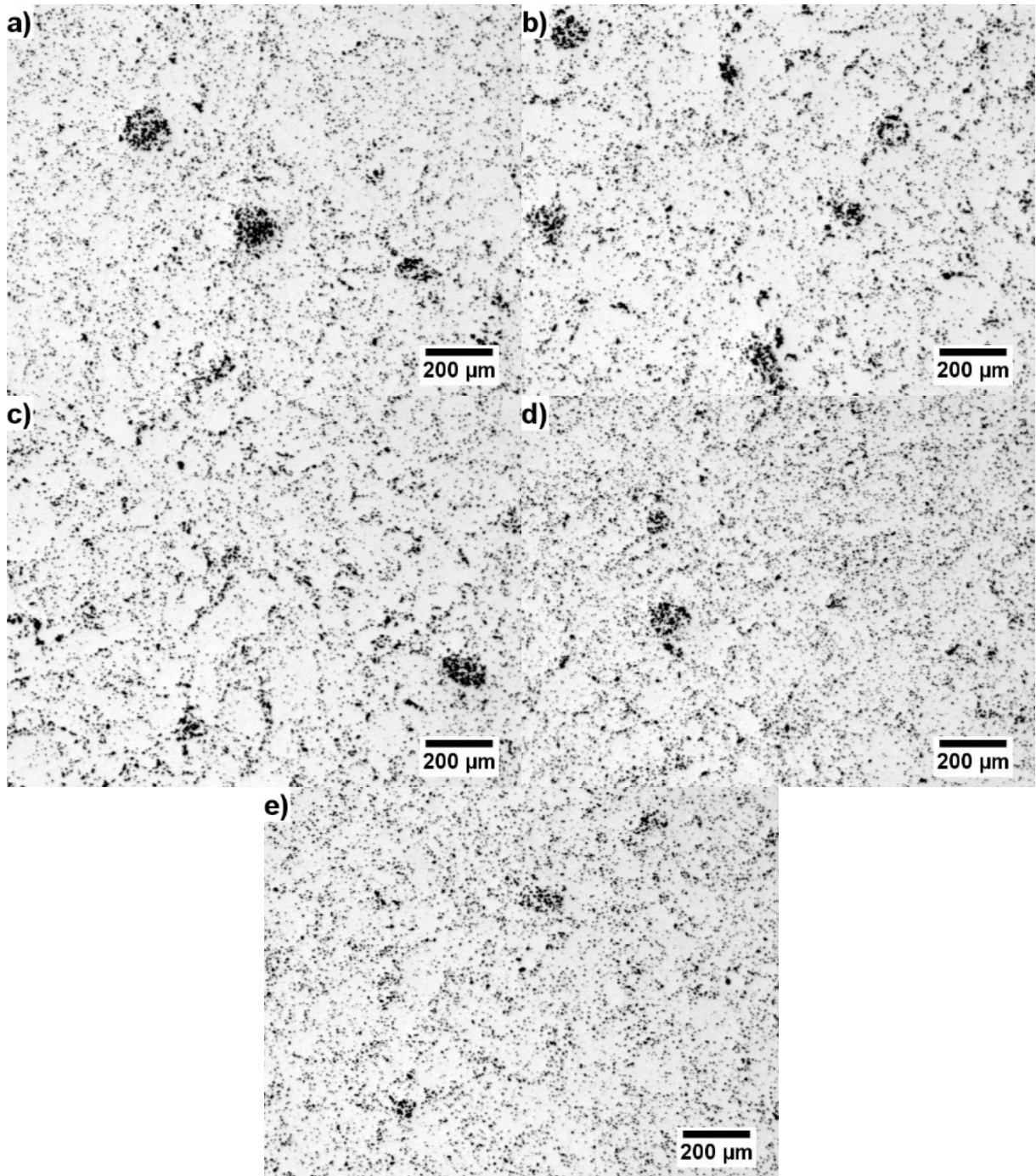


Figure 6-10 Percentage of surface area covered by pores of a certain maximum Feret diameter in  $(\text{Pb}_{0.95}\text{Sr}_{0.05})(\text{Zr}_y\text{Ti}_{1-y})\text{O}_3$  with varying Zr/Ti fraction.



**Figure 6-11 Optical micrographs of polished surfaces of  $(\text{Pb}_{0.95}\text{Sr}_{0.05})(\text{Zr}_y\text{Ti}_{1-y})\text{O}_3$  with  $y(\text{Zr}) =$  a) 0.49, b) 0.51, c) 0.52, d) 0.53, e) 0.55.**

The pore size distributions of Fe-doped PZT with variable Zr/Ti ratio are shown in Figure 6-12, micrographs of their polished sections are shown in Figure 6-13. As in the case of compositions without Fe, porosity exhibits 2 distinct distributions depending on the  $y$  in  $(\text{Pb}_{1-x}\text{Sr}_x)(\text{Zr}_y\text{Ti}_{1-y})_{1-z}\text{Fe}_z\text{O}_3$ , although the transition occurs at slightly lower  $y$  of 52 at%.

Compositions with  $y \geq 52$  at% (highlighted in red in Figure 6-12) exhibit a higher percentage of pores between 4–6  $\mu\text{m}$  (a significantly narrower range than in the previous case) and a considerable decrease in pores  $>13$   $\mu\text{m}$ . Visual inspection of polished sections revealed that  $(\text{Pb}_{0.95}\text{Sr}_{0.05})(\text{Zr}_y\text{Ti}_{1-y})_{0.986}\text{Fe}_{0.014}\text{O}_3$  with  $y = 0.49, 0.51$  contains significantly more pore clusters of larger size than other compositions, which is likely the cause of the observed larger-sized porosity. Since all compositions showed the same particle size distribution and were prepared in the same way, it can be assumed that the binder distribution in green compacts should also be identical. This would support the previous hypothesis that the pore clusters form and coalesce during the sintering process. It appears that densification and pore transport along boundaries is affected by the Zr/Ti ratio; however, the mechanism is unclear. Fe-doped compositions appear more sensitive than undoped compositions to this effect, where the grain growth is not inhibited.

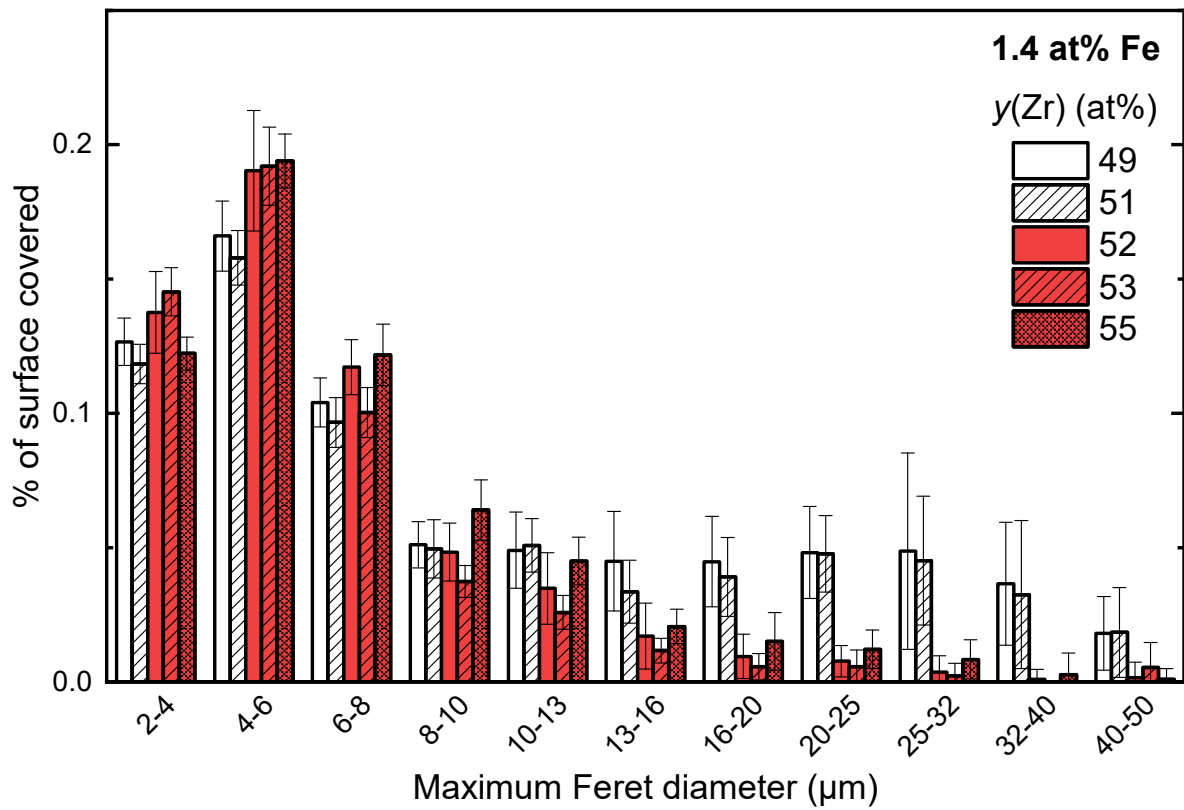


**Figure 6-12 Percentage of surface area covered by pores of a certain maximum Feret diameter in  $(\text{Pb}_{0.95}\text{Sr}_{0.05})(\text{Zr}_y\text{Ti}_{1-y})_{0.986}\text{Fe}_{0.014}\text{O}_3$  with varying Zr/Ti fraction.**

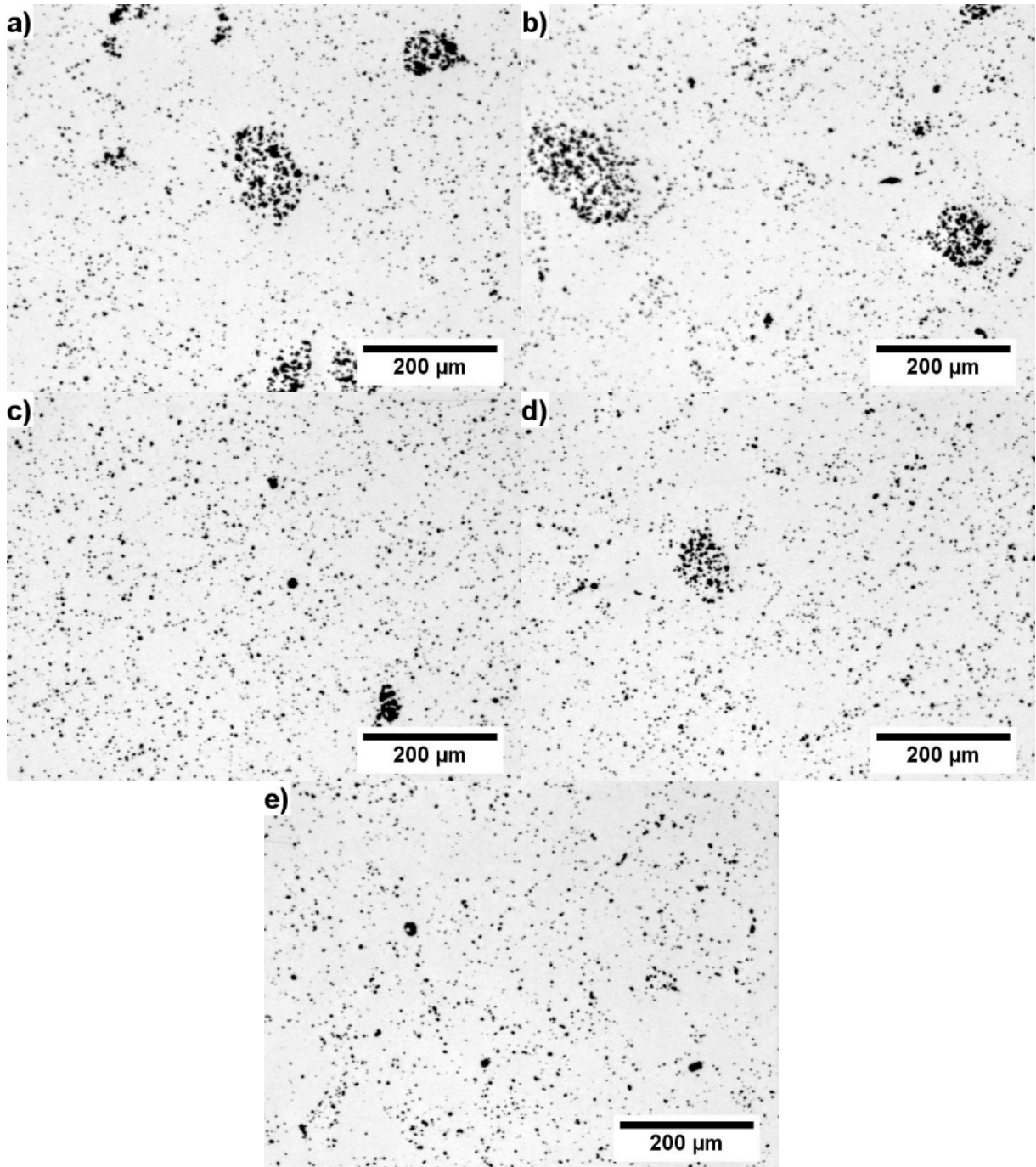


**Figure 6-13 Optical micrographs of polished surfaces of  $(\text{Pb}_{0.95}\text{Sr}_{0.05})(\text{Zr}_y\text{Ti}_{1-y})_{0.986}\text{Fe}_{0.014}\text{O}_3$  with  $y(\text{Zr}) =$  a) 0.49, b) 0.51, c) 0.52, d) 0.53, e) 0.55.**

The influence of Fe doping on the pore size distribution of  $(\text{Pb}_{0.95}\text{Sr}_{0.05})(\text{Zr}_{0.52}\text{Ti}_{0.48})_{1-z}\text{Fe}_z\text{O}_3$  is shown in Figure 6-14; micrographs of polished sections are in Figure 6-15. The presence of Fe significantly lowered the percentage of pores between 6–25  $\mu\text{m}$  and increased percentage of the finest observed pores between 2–4  $\mu\text{m}$ . This is not unexpected as the average grain size

dropped considerably when Fe was added. Increasing the Fe content further decreases porosity but does not affect the shape of the distribution. Figure 6-15 d) shows that there are pores larger than 50  $\mu\text{m}$  present in the composition with 2 at% Fe, which were not observed in the composition with 1.4 at% Fe. This suggests that there might be a change in densification and pore transport between the batches, possibly related to the presence of a secondary phase (Fe should have exceeded its solubility limit at 2 at% as discussed previously in section 5.2). The overall decrease in porosity agrees with the increase in relative density with increasing Fe content.

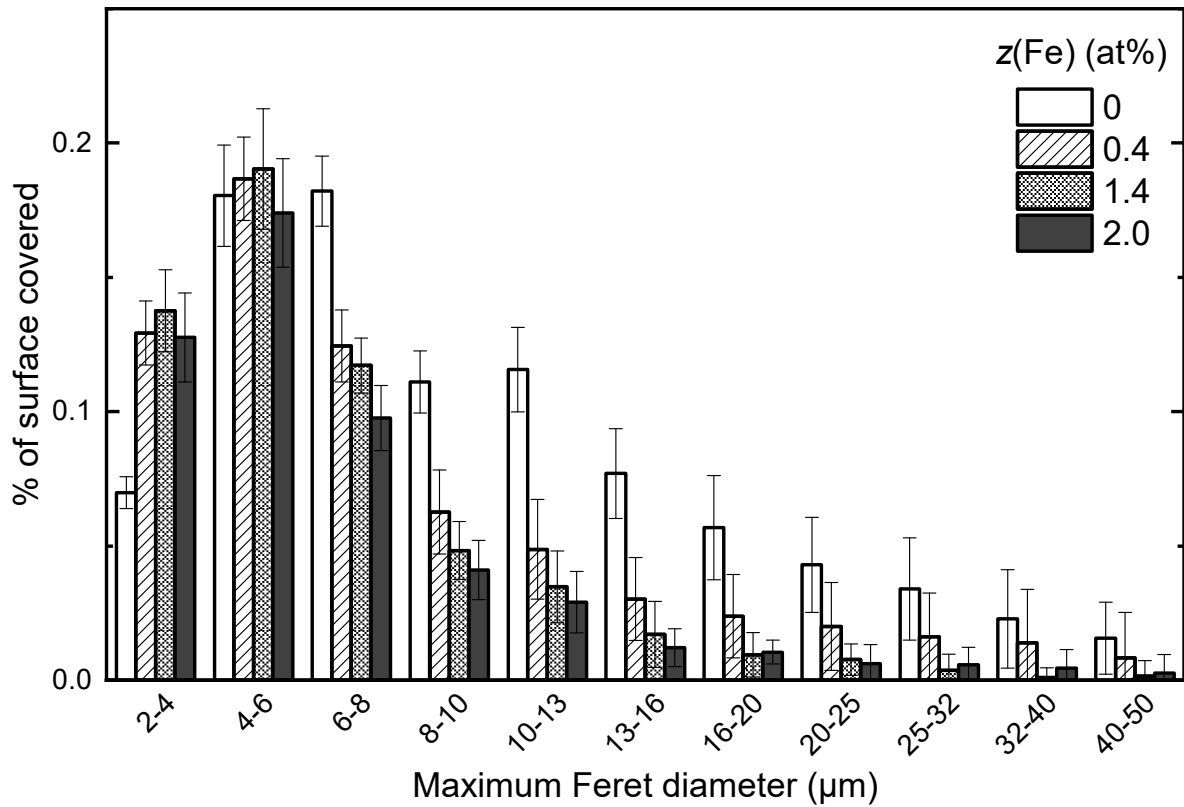


**Figure 6-14** Percentage of surface area covered by pores of a certain maximum Feret diameter in  $(\text{Pb}_{0.95}\text{Sr}_{0.05})(\text{Zr}_{0.52}\text{Ti}_{0.48})_{1-z}\text{Fe}_z\text{O}_3$  doped with varying Fe content.

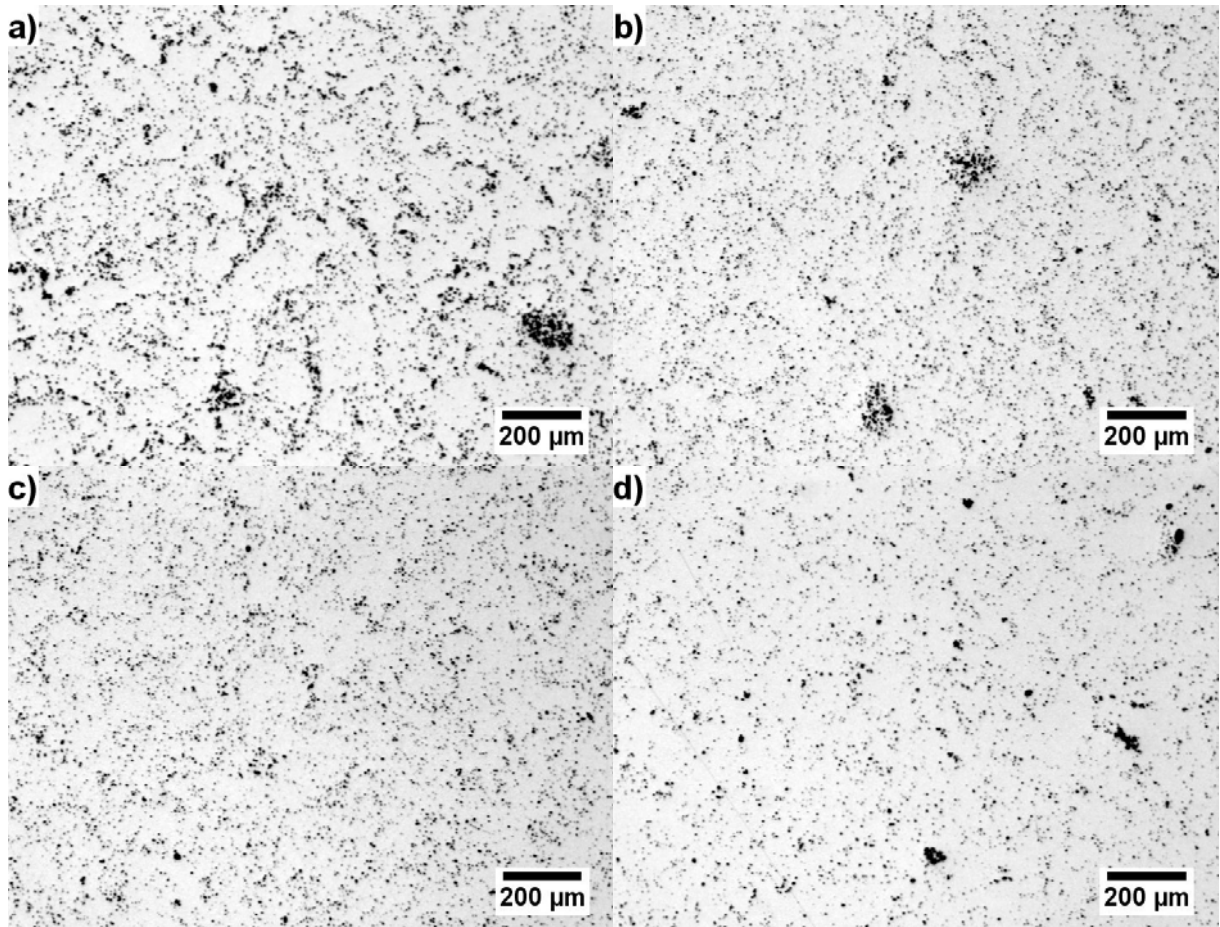


Figure 6-15 Optical micrographs of polished surfaces of  $(\text{Pb}_{0.95}\text{Sr}_{0.05})(\text{Zr}_{0.52}\text{Ti}_{0.48})_{1-z}\text{Fe}_z\text{O}_3$  doped with  $z(\text{Fe}) =$  a) 0, b) 0.004, c) 0.014, d) 0.020.

## 6.5 Phase content and tetragonal unit cell distortion

The results from XRD pattern fitting of the tetragonal/rhombohedral phase content and distortion of the tetragonal unit cell are presented in this section. XRD patterns of prepared compositions are shown in Figure 6-16 and Figure 6-17. The patterns from all compositions could be indexed entirely on the peaks expected from a pure perovskite phase. Restrictions placed on pattern fitting were discussed in section 4.1.3. Due to the purely graphical and mathematical nature of peak fitting and the significant overlap of some peaks which was observed, absolute calculated values of phase content may contain significant error. However, the deconvolution was performed in a consistent manner and should allow observation of trends. Error bars could not be estimated for the calculated phase content as the software only calculates the standard error of the peak position, height and half width at half maximum. The error bars for the tetragonal cell distortions computed from values given by the software were below 0.0002 units (smaller than the datapoints shown in the graphs). Therefore, the unit cell distortions should be considered representative as it only relies on positions of (200) and (002) tetragonal peaks, which was clear in most cases.

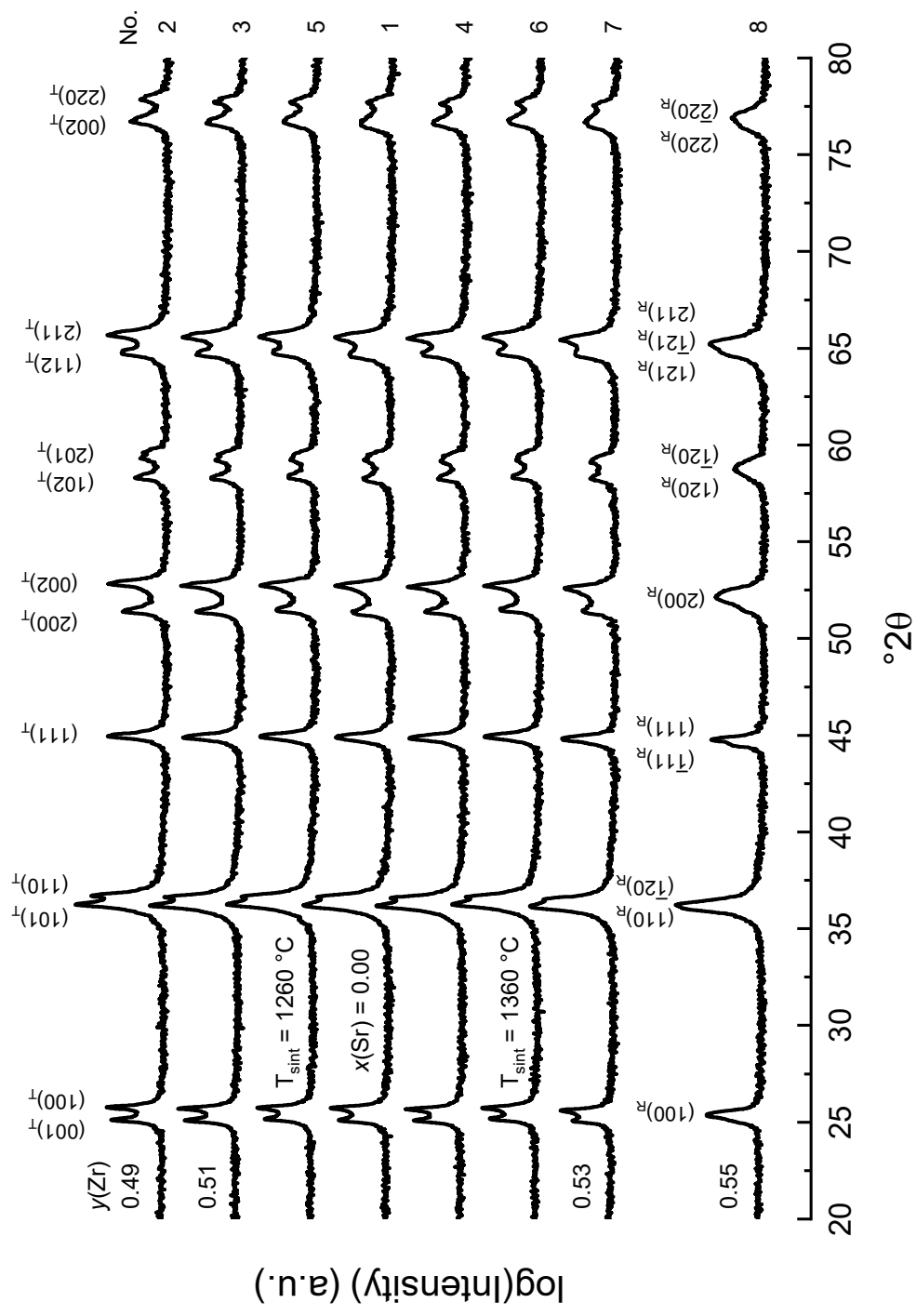


Figure 6-16 X-ray diffraction patterns of  $(\text{Pb}_{1-x}\text{Sr}_x)(\text{Zr}_y\text{Ti}_{1-y})\text{O}_3$  (0 at% Fe). Values of variable factors are shown above each pattern. When the variable is not shown, it assumes that  $y(\text{Zr}) = 0.52$ ,  $T_{\text{sint}} = 1310$  °C and  $x(\text{Sr}) = 0.05$ .

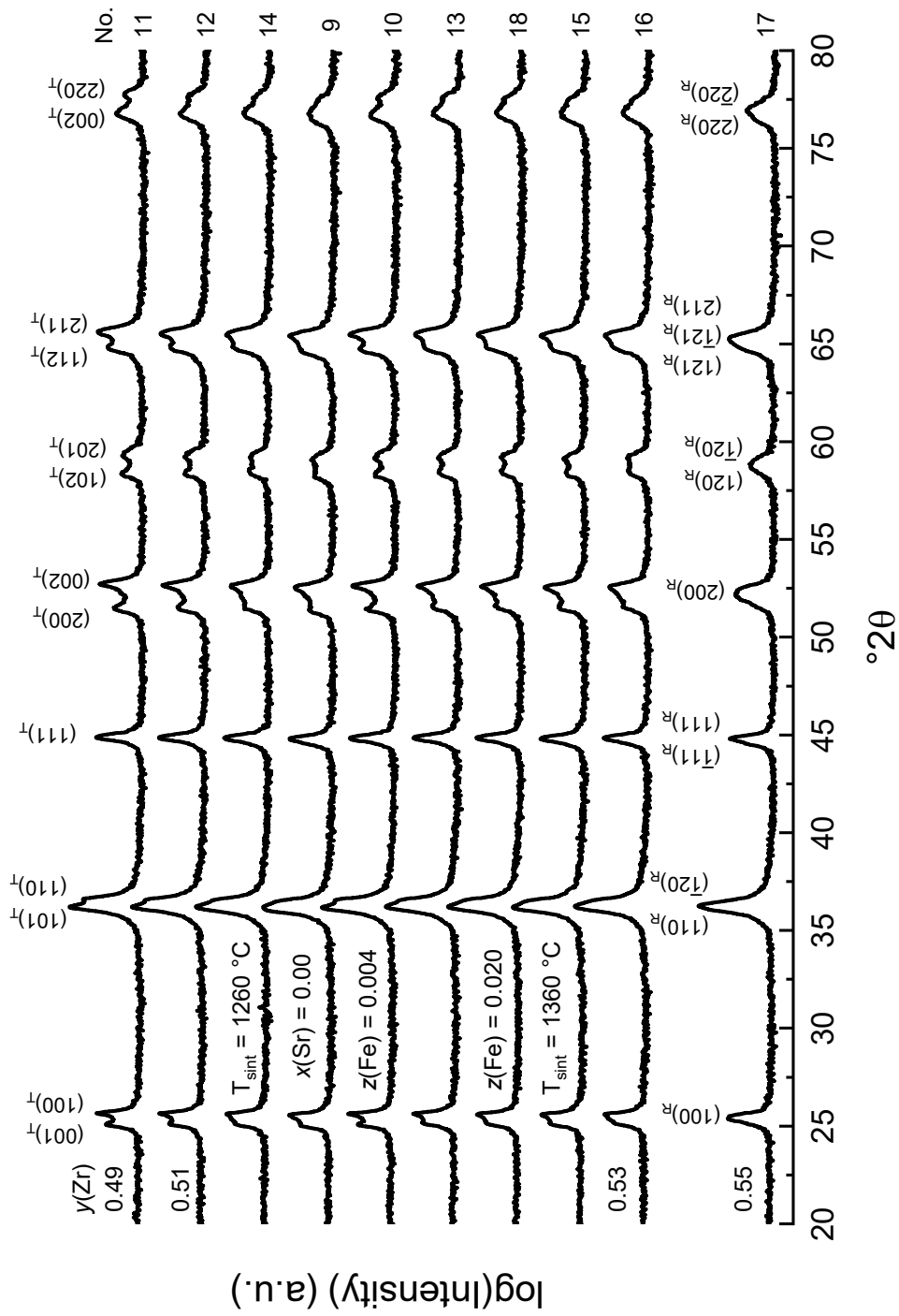
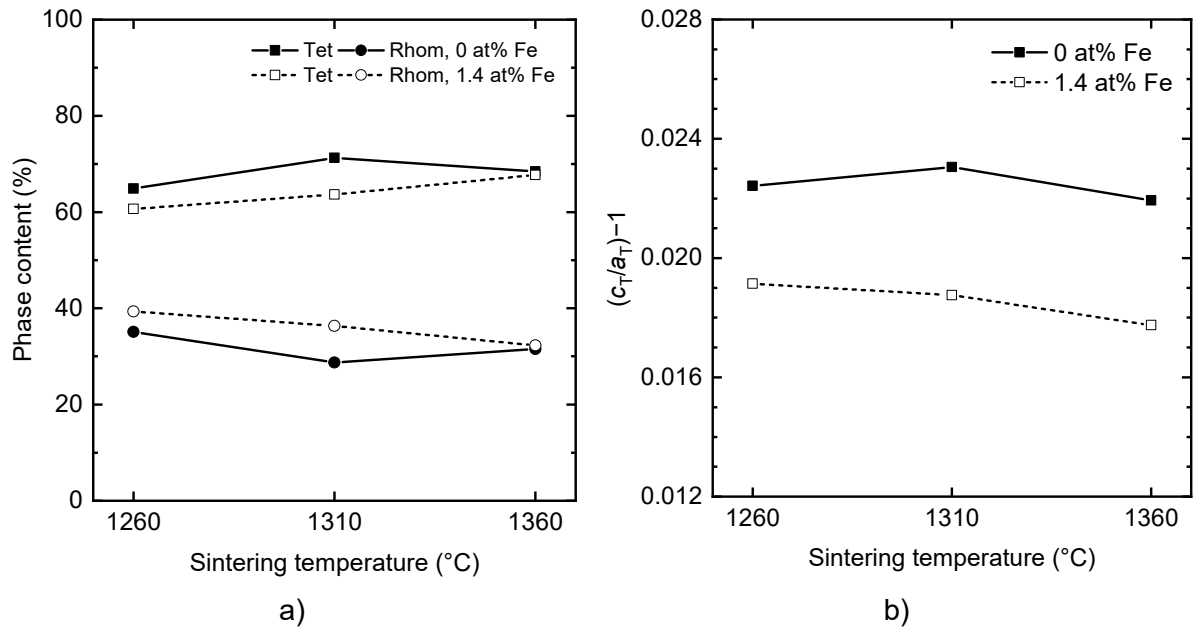


Figure 6-17 X-ray diffraction patterns of  $(\text{Pb}_{1-x}\text{Sr}_x)(\text{Zr}_y\text{Ti}_{1-y})_{1-z}\text{Fe}_2\text{O}_3$ . Values of variable factors are shown above each pattern. When the variable is not shown, it assumes that  $z(\text{Fe}) = 0.014$ ,  $y(\text{Zr}) = 0.52$ ,  $T_{\text{sint}} = 1310 \text{ }^\circ\text{C}$  and  $x(\text{Sr}) = 0.05$ .

The phase content did not show significant variation with increasing sintering temperature as shown in Figure 6-18. Fe-doped samples contained slightly more rhombohedral content. This has been observed in other studies [63, 80, 162] and attributed to either an MPB shift by Fe doping or a decrease in the micro-/nanohomogeneity of the material induced by Fe doping. It was previously suggested that Fe inhibits diffusion, therefore Zr-rich rhombohedral microregions take longer to mix with Ti-rich tetragonal microregions. Phase content reaches the same value for doped/undoped samples at 1360 °C, which supports this theory as increasing temperature facilitates diffusion.

The phase content may be also influenced by grain size. Previous research has shown that the width of the phase coexistence region increases as the grain size decreases [163, 164]. Fe-doped samples exhibit much smaller grain size, therefore, their phase coexistence range should be wider, and they should contain more rhombohedral phase. This theory does not agree well with the data presented in Figure 6-18 a), because for a sintering temperature of 1360 °C, both compositions regardless of Fe doping and difference in grain size show the same amount of both phases. On the other hand, one must consider that possible inaccuracies in the data as discussed above.

The tetragonal distortion of the unit cell decreased for the samples at 1360 °C (Figure 6-18 b), which has also been observed previously [165, 166] and could be explained by compositional fluctuations. When Zr-rich regions mix with Ti-rich regions at the highest sintering temperature, overall distortion of tetragonal phase decreases. The effect is more pronounced in Fe-doped compositions, which agrees with the previous reasoning that Fe inhibits diffusion.



**Figure 6-18** Dependence of a) phase content, b) tetragonal cell distortion  $(c_T/a_T)-1$  on sintering temperature of  $(\text{Pb}_{0.95}\text{Sr}_{0.05})(\text{Zr}_{0.52}\text{Ti}_{0.48})_{1-z}\text{Fe}_z\text{O}_3$  with  $z(\text{Fe}) = 0.000$  or  $0.014$ .

Incorporation of  $\text{Sr}^{2+}$  into the PZT lattice increased the tetragonal content and decreased tetragonal cell distortion as shown in Figure 6-19. Ikeda showed that substituting  $\text{Pb}^{2+}$  with  $\text{Sr}^{2+}$  up to approximately 15 at% continuously shifts the MPB towards a higher Zr/Ti ratio, which is illustrated in Figure 6-20 [167]. This agrees with results from other studies [50, 154, 168-170]. In the experiment reported in this thesis, compositions with a constant Zr/Ti ratio of 52/48 were used and only the Pb/Sr fraction was varied from 100/0 to 95/5 (as illustrated by points C1 and C2 in Figure 6-20). It is apparent, that the shift of MPB should have increased the tetragonal content, as was observed. Reduction of cell distortion is associated with the replacement of  $\text{Pb}^{2+}$  ion by smaller  $\text{Sr}^{2+}$  ion. With an increasing fraction of Sr/Pb, the cell distortion decreases until the material becomes cubic [50, 167].

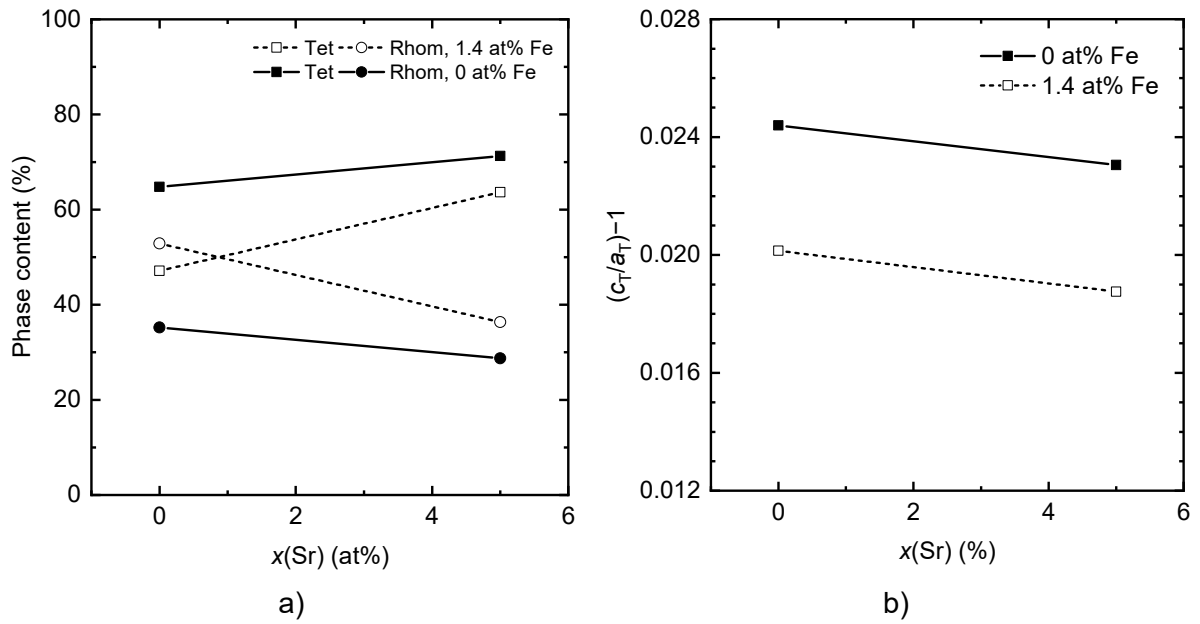


Figure 6-19 Dependence of a) phase content, b) tetragonal cell distortion ( $c_T/a_T-1$ ) on strontium content of  $(Pb_{1-x}Sr_x)(Zr_{0.52}Ti_{0.48})_{1-z}Fe_zO_3$  with  $z(Fe) = 0.000$  or  $0.014$ , sintered at  $1310\text{ }^\circ\text{C}$ .

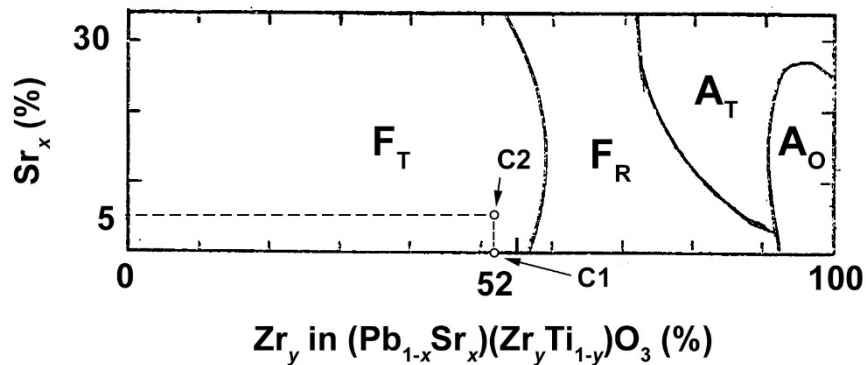
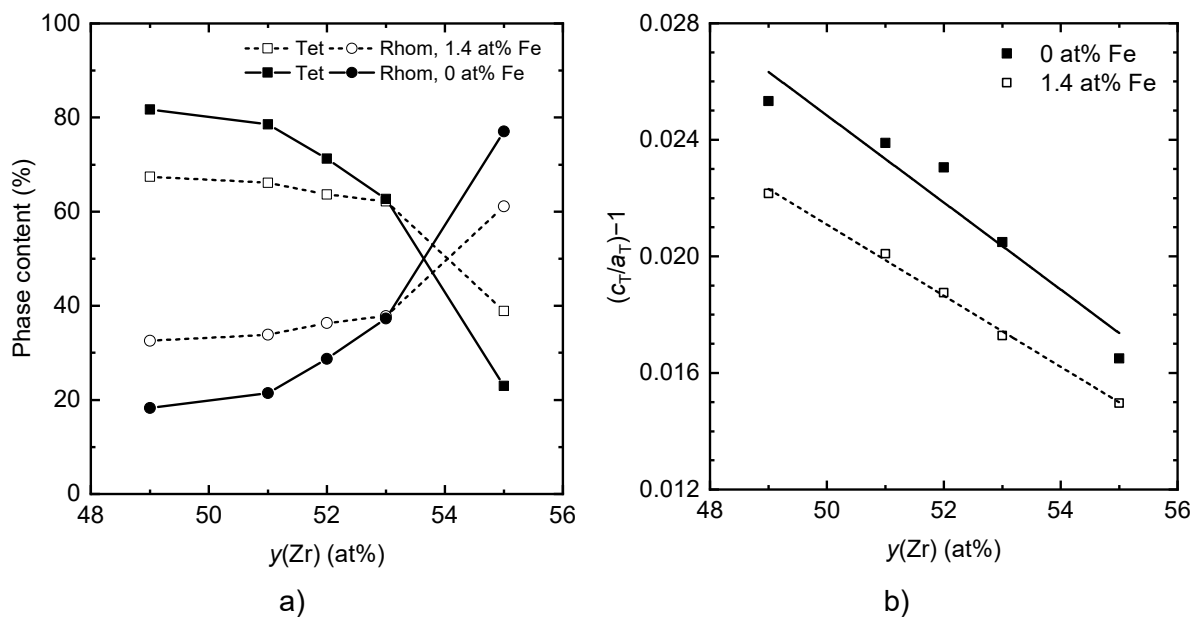


Figure 6-20 Room temperature quaternary phase diagram of the  $(Pb-Sr)(Ti-Zr)O_3$  system published by Ikeda [167].  $F_T$  = tetragonal,  $F_R$  rhombohedral ferroelectric phases;  $A_T$  = tetragonal,  $A_O$  = orthorhombic anti-ferroelectric phases. Points C1 and C2 show locations of compositions investigating effects of Sr content in this work.

The dependence of phase content on Zr/Ti ratio is plotted in Figure 6-21 a). Regardless of Fe content, both series show a decrease of tetragonal phase and eventual transition into a majority rhombohedral phase as the  $y$  in  $(Pb_{1-x}Sr_x)(Zr_yTi_{1-y})_{1-z}Fe_zO_3$  is increased. The position of the MPB appears to lie between  $y = 53$  and  $55$  at%. However, this should be treated with caution as the phase content values are likely to be less accurate near the MPB due to the severe peak

overlap, especially on the rhombohedral side, where maxima of the tetragonal peaks could not be distinguished. Fe-doped samples seem to show an increased amount of rhombohedral phase in all compositions and their phase content variation with  $y(\text{Zr})$  is less pronounced. Increased presence of rhombohedral phase in all Fe-doped compositions suggests that the coexistence region widened, rather than a shift in MPB position. This can be rationalised either by the phase coexistence width dependence on grain size or by the local inhomogeneities in Fe-doped samples as suggested earlier.

The tetragonal cell distortion exhibited a linear decrease with increasing  $y(\text{Zr})$  (see Figure 6-21 b), which agrees well with previous research [27, 140]. Fe-doped samples generally show lower distortion, which will be further discussed in next paragraphs. It should be noted that unlike tetragonal distortion, phase content did not show a linear dependence on Zr/Ti fraction as one would expect, and which was demonstrated in other studies [49, 169, 171]. It suggests that phase content measurements may not be accurate enough possibly due to the resolution of the diffractometer or the peak fitting process.



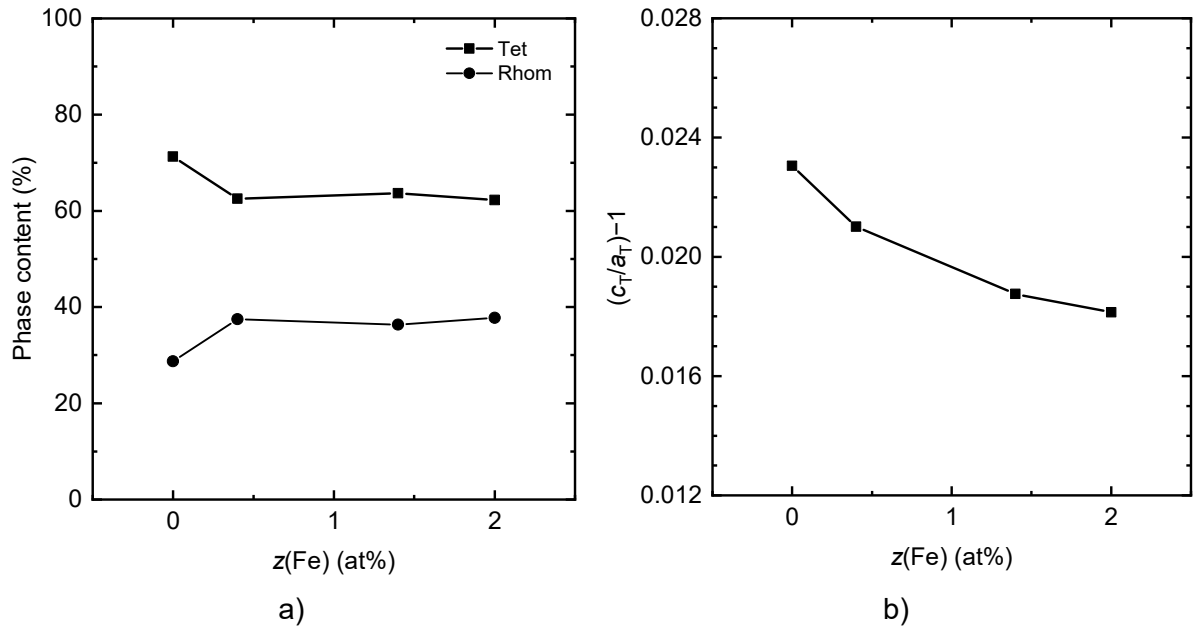
**Figure 6-21** Dependence of a) phase content, b) tetragonal cell distortion ( $c_T/a_T - 1$ ) on Zr/Ti ratio of  $(\text{Pb}_{0.95}\text{Sr}_{0.05})(\text{Zr}_y\text{Ti}_{1-y})_{1-z}\text{Fe}_z\text{O}_3$  with  $z(\text{Fe}) = 0.000$  or  $0.014$ , sintered at  $1310^\circ\text{C}$ .

Figure 6-22 a) shows the dependence of tetragonal and rhombohedral phase content on Fe doping. The rhombohedral phase content increased by ~10 % with 0.4 at% Fe but then remained constant with further Fe content up to 2.0 at%. Increase of the rhombohedral phase content with Fe doping has been reported in other studies [63, 80, 162, 172]. Weston et al. implied that the phase content ratio continuously changes with increasing Fe doping as the material switched from being predominantly tetragonal to being predominantly rhombohedral at a certain Fe content (2 at% Fe in [80]). This trend is not reflected in Figure 6-22 a), although this might be due to inaccuracy of the measurement as discussed previously. An increase in rhombohedral content may be explained by several reasons: 1) Fe shifted the location of the MPB, 2) width of the phase coexistence region widened due to grain growth inhibition or 3) width of the phase coexistence region widened due to a decrease in homogeneity caused by the presence of Fe.

Tetragonal distortion continuously decreased with increasing Fe content as shown in Figure 6-22 b). This general trend has been previously observed [63, 172] and is mostly related to the substitution of  $Zr^{4+}/Ti^{4+}$  by  $Fe^{3+}$ . The ionic radius of  $Fe^{3+}(VI)$  is 0.55 or  $0.65 \cdot 10^{-10}$  m depending on its spin, which is lower than that of  $Zr^{4+}(VI)$  ( $0.86 \cdot 10^{-10}$  m) [36], and the  $Fe^{3+}$  doping introduces oxygen vacancies, which result in reduction of the cell volume [26]. The presence of  $Fe^{3+}$  is expected to distort the surrounding oxygen octahedra and decrease the B-O-B coupling as well as the Curie temperature [172]. Additional factors affecting the tetragonal distortion may include the previously suggested decrease in micro-/nanohomogeneity, or an effect of grain size, where smaller grains were reported to enhance clamping of the unit cell distortion [51].

The distortion would be expected to decrease only up to the dopant's solubility limit, which should be < 2.0 at% in the case of  $Fe^{3+}$  as discussed previously in section 5.2. Contrary to this, the distortion is seen to decrease monotonously (Figure 6-22 b). This can be rationalised by

considering that the distribution of  $\text{Fe}^{3+}$  may not be perfectly homogeneous on a nanoscale level and therefore the dopant may not be fully incorporated even at lower doping concentrations due to its local saturation. Another possibility is that the distortion is affected by a newly-formed secondary phase containing the excess  $\text{Fe}^{3+}$ .



**Figure 6-22** Dependence of a) phase content, b) tetragonal cell distortion  $(c_T/a_T) - 1$  on Fe content of  $(\text{Pb}_{0.95}\text{Sr}_{0.05})(\text{Zr}_{0.52}\text{Ti}_{0.48})_{1-z}\text{Fe}_z\text{O}_3$  sintered at 1310 °C.

## 6.6 Nanoscale homogeneity of Fe-doped sample

There are several reports of nanoscale investigations of Fe-doped PZT. Kleebe et al. [150] investigated  $\text{Pb}(\text{Zr}_{0.6}\text{Ti}_{0.4})_{1-z}\text{Fe}_z\text{O}_3$  with  $z = 0.03$  prepared by a conventional mixed oxide route. Excess iron, not incorporated into PZT, segregated into magnetic grains of approximately 1–2  $\mu\text{m}$  (average PZT grain diameter was 0.5–0.8  $\mu\text{m}$ ). The secondary phase was identified as magnetoplumbite ( $\text{PbFe}_{12}\text{O}_{19}$ ). The maximum solubility of Fe in PZT was estimated at approximately 1 at% using X-band EPR (Electron Paramagnetic Resonance) spectra and numerical simulation.

Erdem et al. [148] studied  $\text{Pb}(\text{Zr}_y\text{Ti}_{1-y})_{1-z}\text{Fe}_z\text{O}_3$  with  $z = 0.005$  and  $0.010$  prepared by a conventional mixed oxide route. A secondary nanocrystalline phase containing an increased concentration of Pb and Fe was found in triple pockets of a sample doped with 1 at% Fe. Zr and Ti were also present in the secondary phase at lower concentration, with their ratio remaining the same as in the matrix. An amorphous grain boundary film was also detected. However, it showed no compositional shift from the bulk. It was reported that the microstructure was homogeneous, with no residual porosity and did not change significantly when the Fe content was increased from 0.5 to 1.0 at%.

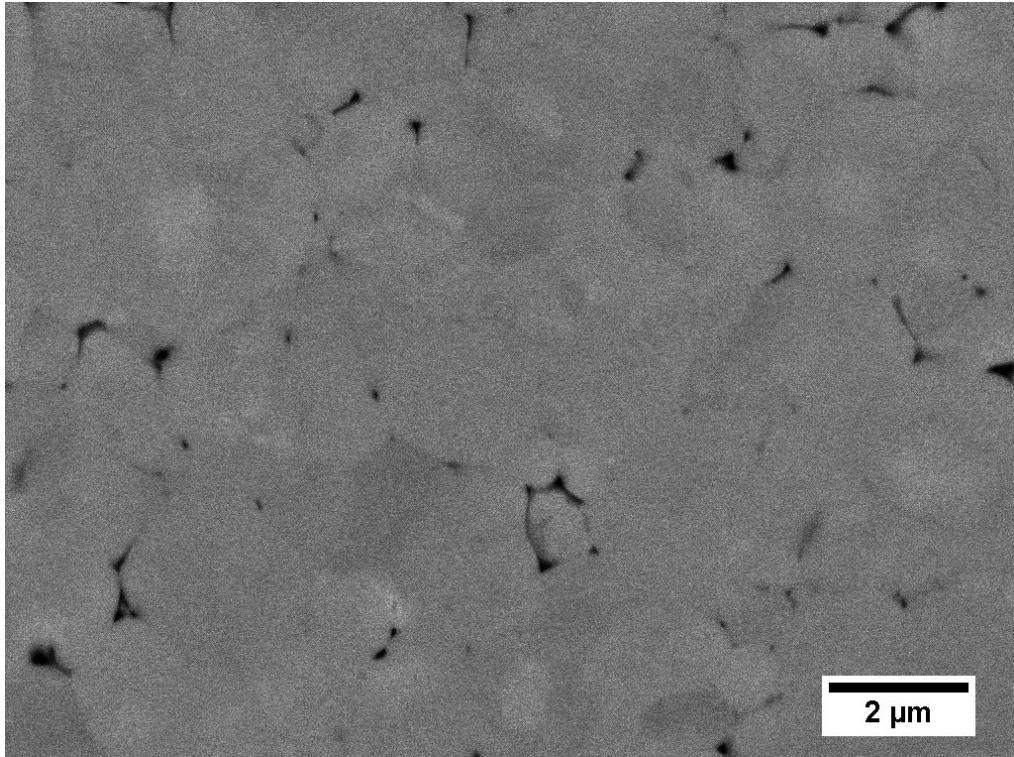
Fernández et al. [159] prepared  $\text{Pb}(\text{Zr}_{0.530}\text{Ti}_{0.458}\text{Fe}_{0.010}\text{Nb}_{0.002})\text{O}_3$  via a conventional mixed oxide route and sintering at 1070–1190 °C for 1–5 h. No excess PbO was used, only  $\text{PbZrO}_3 + 5\text{wt}\%$   $\text{ZrO}_2$  was used as a powder bed for sintering. Similar high density was achieved at all conditions, which was attributed to the small particle size (high reactivity) of the starting powder ( $d_{50} = 0.85 \mu\text{m}$ ). Small spherical particles of  $\text{ZrO}_2$  (<100 nm) were found inside grains of all samples and interpreted as unreacted residues of starting powder. For sintering temperatures up to 1150 °C, a PbO-rich secondary phase was detected in triple junctions (size up to 30 nm), which was hypothesised to be a result of  $\text{Fe}^{3+}$  not being incorporated into the lattice at that

temperature. The hypothesis was based on measured electrical properties. For samples sintered at 1150 °C, 0.5 μm ZrO<sub>2</sub> grains were found at triple junctions, surrounded by a PbO rich phase. The authors speculated that the ZrO<sub>2</sub> phase precipitated from the PbO-rich secondary phase shortly after Fe<sup>3+</sup> incorporated into PZT lattice. For sintering temperatures above 1150 °C, only a PbO-rich secondary phase containing both Ti and Zr was found, suggesting that the ZrO<sub>2</sub> phase redissolved once the liquid was enriched by Ti<sup>4+</sup> from surrounding grains.

Malič et al. [86] examined Pb(Zr<sub>0.53</sub>Ti<sub>0.47</sub>)<sub>1-x</sub>X<sub>x</sub>O<sub>3</sub>, where X = Fe or Nb and x = 0.02, prepared by sol-gel processing, which should yield better homogeneity of sintered material. A TEM examination of samples sintered at 1100 °C for 1 h showed the presence of 100nm spherical intragranular pores, likely caused by the processing. 200nm ZrO<sub>2</sub> particles, either at triple junctions or inside grains, and a PbO-rich Fe-containing phase at triple junctions were detected. The presence of secondary phases was explained by citing the Fe<sup>3+</sup> incorporation process suggested by Fernández et al., which was summarised in the previous paragraph. It was concluded that the initial high homogeneity achieved by this process is lost due to the Fe<sup>3+</sup> incorporation process. The author didn't consider that the concentration of Fe might have exceeded its solubility limit in PZT.

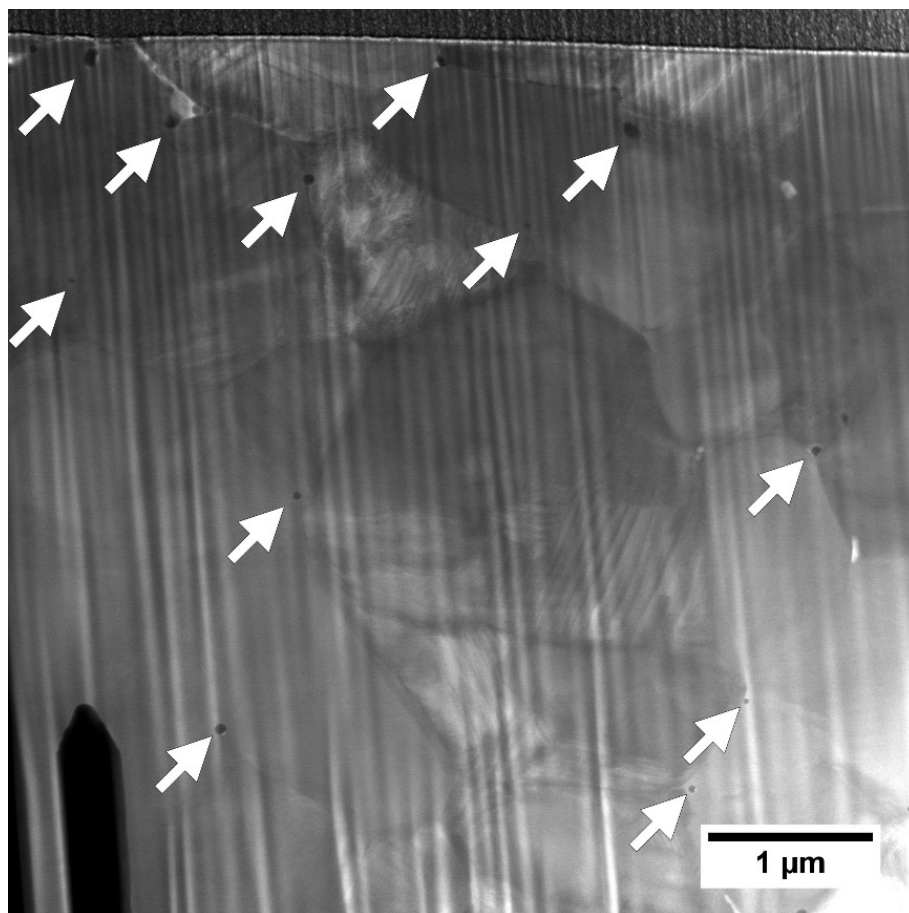
In order to explore homogeneity and features of Fe-doped material at the nanoscale level, one sample from batch 18 ((Pb<sub>0.95</sub>Sr<sub>0.05</sub>)(Zr<sub>0.52</sub>Ti<sub>0.48</sub>)<sub>0.98</sub>Fe<sub>0.02</sub>O<sub>3</sub>) was investigated using TEM. The amount of Fe in this composition should be exceeding its solubility limit of 0.5–1 at% suggested in previous studies [148, 150].

Figure 6-23 shows a polished surface of the sample. There are no apparent microstructural inhomogeneities at this magnification, only intergranular porosity is present. The measured average grain diameter is 1.0 μm.



**Figure 6-23 SEM micrograph of a polished surface of  $(\text{Pb}_{0.95}\text{Sr}_{0.05})(\text{Zr}_{0.52}\text{Ti}_{0.48})_{0.98}\text{Fe}_{0.02}\text{O}_3$  (batch 18, BE mode) sintered at 1310 °C.**

A bright field TEM image of the same material at higher magnification in Figure 6-24 revealed a dense domain structure as well as dark circular spots ranging between 8–70 nm in size (indicated by arrows). These may potentially be a secondary phase or fine pores. Dark spots are located at or near grain boundaries and triple junctions.



**Figure 6-24 Bright field TEM image of  $(\text{Pb}_{0.95}\text{Sr}_{0.05})(\text{Zr}_{0.52}\text{Ti}_{0.48})_{0.98}\text{Fe}_{0.02}\text{O}_3$  (batch 18) sintered at 1310 °C. Arrows indicate potential secondary phases or submicrometric pores. Curtaining from FIB cutting is apparent.**

EDX elemental maps of 2 selected areas (denoted as site 1 and site 2) and line scans were employed to investigate the composition of the dark spots as well as the grains and their boundaries. An elemental map of site 1 is shown in Figure 6-25. The dark spots marked by two arrows were rich in Pb, Fe segregation was apparent at the grain boundaries and triple junctions. The Fe-rich phase appears to contain Pb and Sr, while Zr and Ti concentrations are lowered compared to the stoichiometric composition. Sr and Ti show local fluctuations within grains.

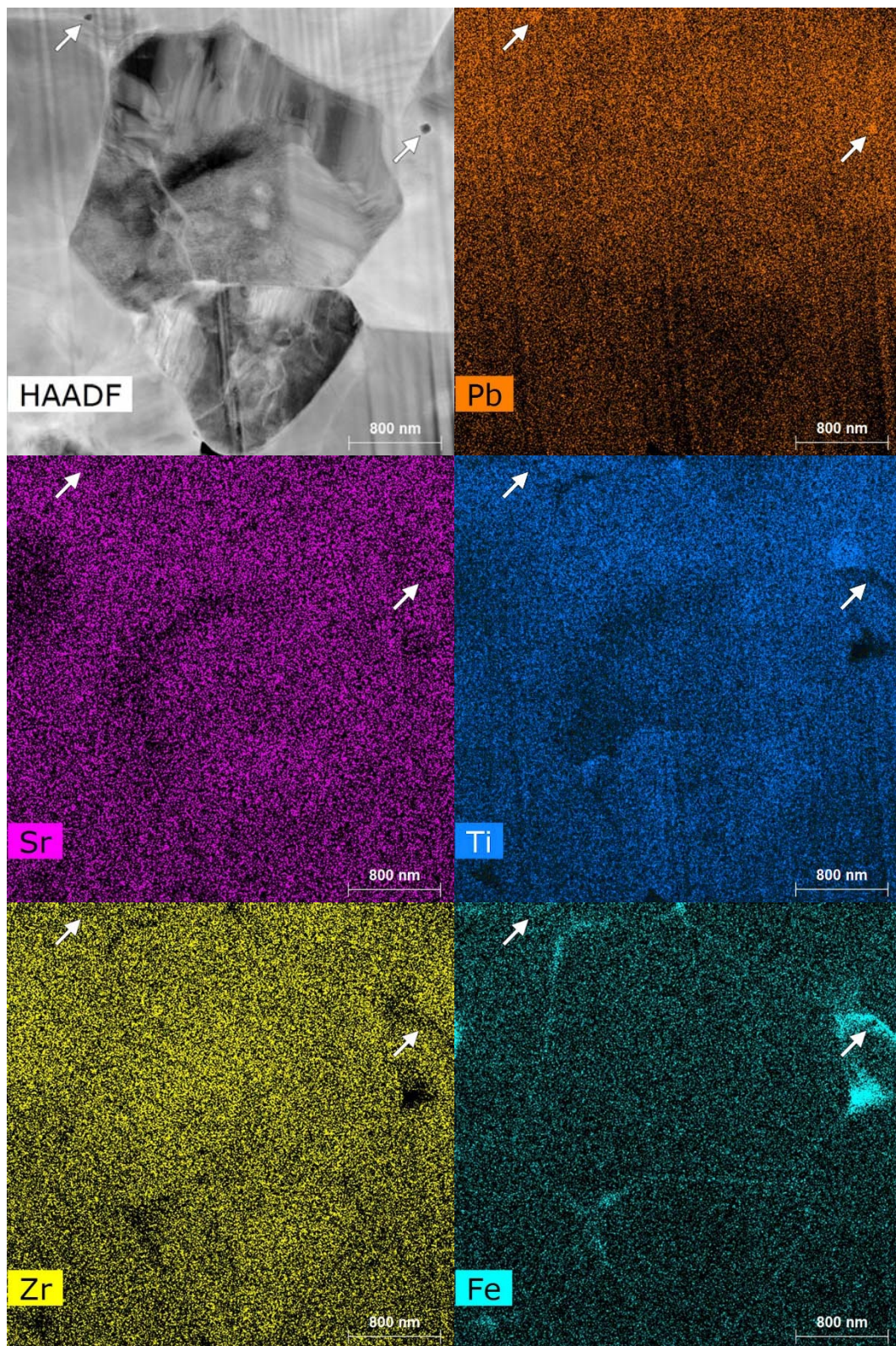


Figure 6-25 EDX elemental maps of site 1 of  $(\text{Pb}_{0.95}\text{Sr}_{0.05})(\text{Zr}_{0.52}\text{Ti}_{0.48})_{0.98}\text{Fe}_{0.02}\text{O}_3$  (batch 18) sintered at 1310 °C showing distribution of Pb, Sr, Ti, Zr and Fe within and near grains. Arrows indicate potential secondary phases or submicrometric pores.

Figure 6-26 shows an elemental map of site 2. The dark spot indicated by an arrow is rich in Pb, while other elements are present at their regular concentration. The inclusion is located inside a grain and appears to be surrounded by an Fe-rich phase. In previous studies, unreacted ZrO<sub>2</sub> particles were found inside grains, as discussed earlier [86, 159]. It is possible that such a ZrO<sub>2</sub> particle was captured by a growing grain and reacted over time. However, it is unclear how the spot became rich in PbO.

The area below the central grain exhibited decreased Zr/Ti ratio compared to its surroundings. A secondary phase rich in Fe and Pb was present at grain boundaries and triple junctions.

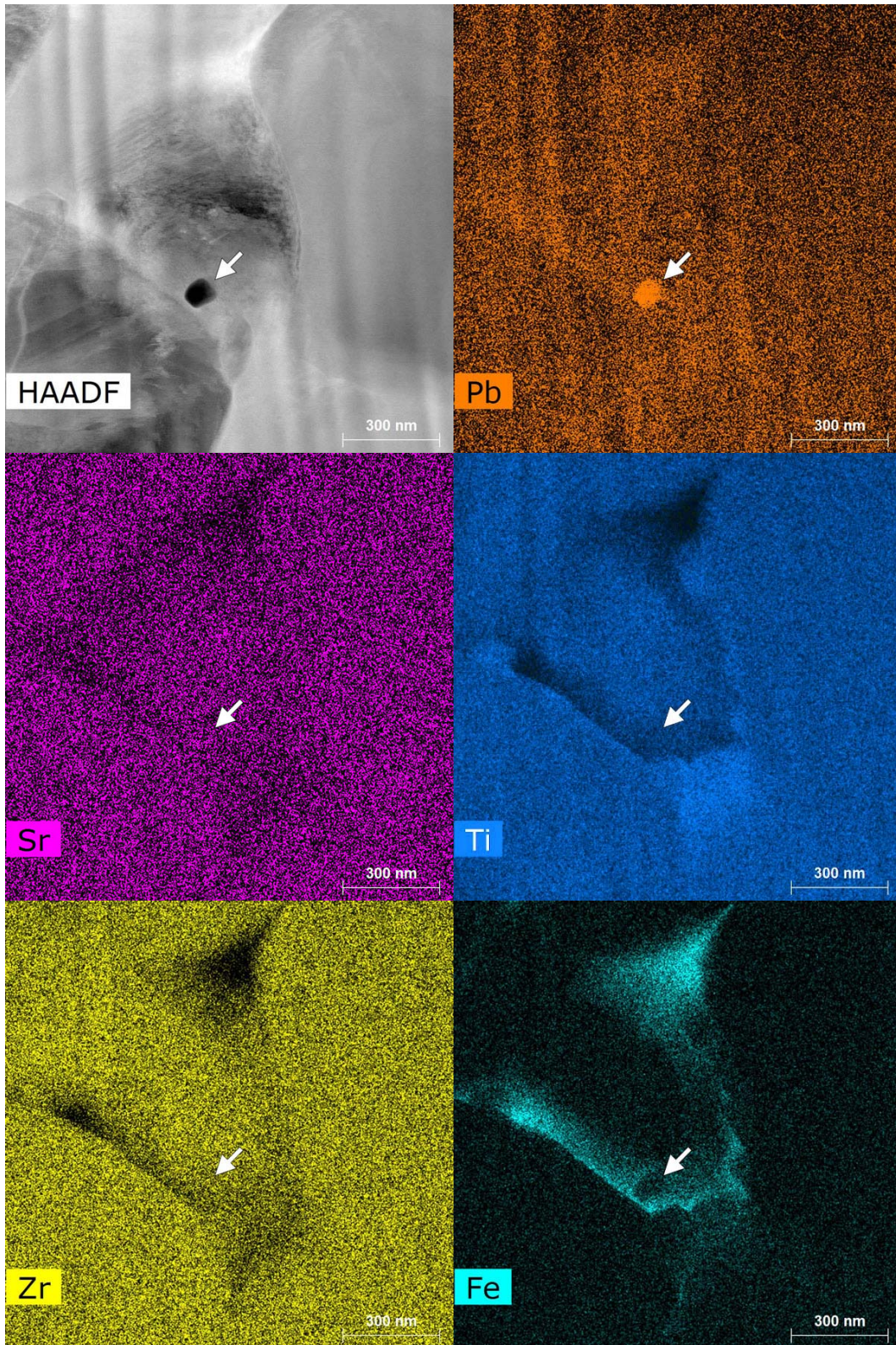


Figure 6-26 EDX elemental map of site 2 of  $(\text{Pb}_{0.95}\text{Sr}_{0.05})(\text{Zr}_{0.52}\text{Ti}_{0.48})_{0.98}\text{Fe}_{0.02}\text{O}_3$  (batch 18) sintered at 1310 °C showing distribution of Pb, Sr, Ti, Zr and Fe within and near grains. Arrows indicate a possible secondary phase.

An EDX line scan, carried out at site 2, is shown in Figure 6-27. It clearly shows an increase of Fe and decrease in Zr and Ti at the grain boundaries. The drop in Zr concentration appears smaller than the drop in Ti, which supports the Fe incorporation mechanism proposed by Fernández et al. Line scan confirms that the inclusion is rich in Pb and deficient in Ti. An Fe-rich area can be found around the inclusion. The concentration of Sr does not vary along the line.

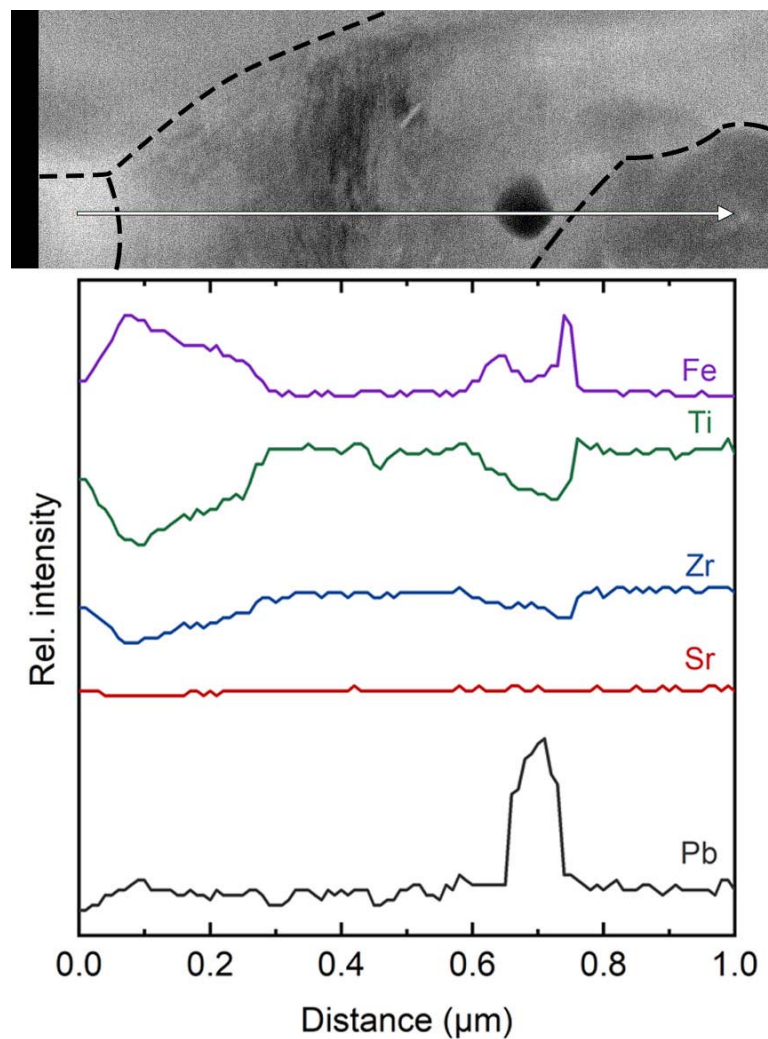
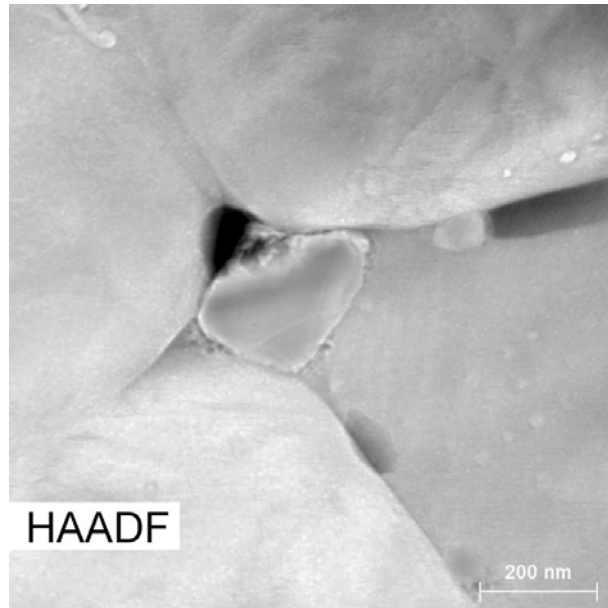
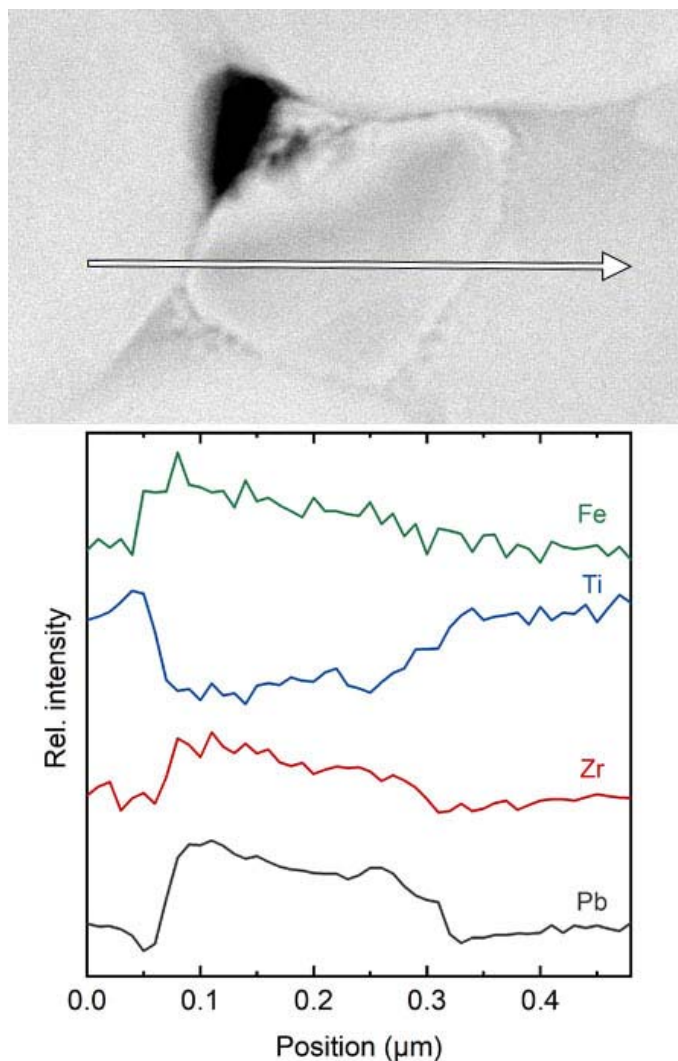


Figure 6-27 EDX line scan of site 2. Arrow indicates location of the scan; dashed lines represent grain boundaries.

A small 300nm grain has been found at one of the triple pockets (Figure 6-28). The EDX line scan shown in Figure 6-29 revealed an increased concentration of Pb, Zr and Fe. The content of Fe decreases from the left grain boundary to the right which may suggest that Fe is not inside the grain, but rather underneath it, at a triple pocket. The grain is depleted of Ti.



**Figure 6-28 Dark field TEM image of a 300nm grain located inside a triple pocket in  $(\text{Pb}_{0.95}\text{Sr}_{0.05})(\text{Zr}_{0.52}\text{Ti}_{0.48})_{0.98}\text{Fe}_{0.02}\text{O}_3$  (batch 18) sintered at 1310 °C.**



**Figure 6-29** EDX line scan of a 300nm particle located at a triple pocket in  $(\text{Pb}_{0.95}\text{Sr}_{0.05})(\text{Zr}_{0.52}\text{Ti}_{0.48})_{0.98}\text{Fe}_{0.02}\text{O}_3$  (batch 18) sintered at 1310 °C.

One sample of  $(\text{Pb}_{0.95}\text{Sr}_{0.05})(\text{Zr}_{0.52}\text{Ti}_{0.48})\text{O}_3$  (0 at% Fe, batch 4) was studied by TEM to make a comparison with previous results. A representative EDX map of a site from this sample is shown in Figure 6-30. The HAADF image reveals much larger domains compared to the doped sample, which is in agreement with previous research. All elemental maps show low intensity in the bottom-right corner, which indicates an uneven thickness or tilt of the sample. There appear to be some notable fluctuations in Pb concentration. Other elements appear homogeneously distributed. The bottom-right image confirms that no Fe is present and the studied PSZT sample did not show any inclusions or nanoporosity inside the grains.

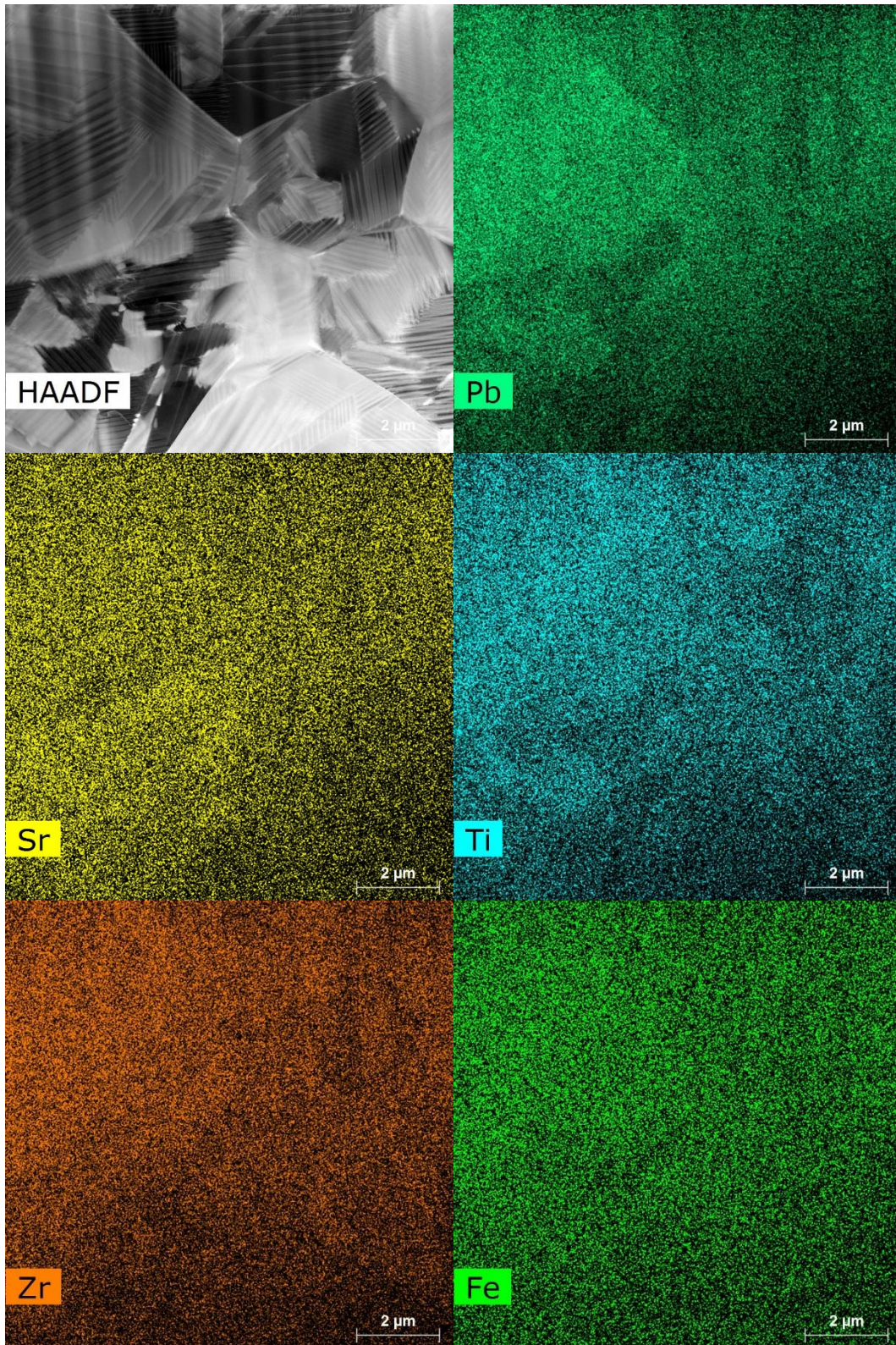


**Figure 6-30 EDX elemental map of  $(\text{Pb}_{0.95}\text{Sr}_{0.05})(\text{Zr}_{0.52}\text{Ti}_{0.48})\text{O}_3$  (batch 4) sintered at 1310 °C showing distribution of Pb, Sr, Ti, Zr and Fe within and near grains. Fe was not detected; its elemental map only illustrates that there are no Fe-rich pockets.**

The TEM analysis has proved that the solubility limit of Fe in PZT is less than 2 at%. In samples with 2 at% Fe, segregation was apparent at grain boundaries as well as triple junctions. The segregated phase was also rich in Pb and depleted of Ti and Zr.

The following compositional inhomogeneities were found:

- Zr- and Pb-rich grains at triple junctions.
- Areas with decreased Zr/Ti ratio.

These are likely the result of the processing route. Solid state processing is generally considered as a method producing less homogeneous ceramics and Fe affects grain growth as well as the diffusion of species. Zr- and Pb-rich phases may be related to the Fe<sup>3+</sup> incorporation process described by Fernández et al. Compositional inhomogeneity in Fe-doped sample supports previous observations of trends of various properties. However, disregarding grain boundary areas and triple junctions, both Fe-doped and undoped materials showed local elemental fluctuations and it can't be concluded that one is less homogeneous than the other.

Pb-rich inclusions between 8–70 nm were found inside grains, near grain boundaries in Fe-doped samples. The location suggests that these were incorporated during the initial grain growth and reacted over time, however their original composition is unknown. Inclusions showed an increased Zr/Ti ratio and were surrounded by Fe rich phase. It is unclear, whether the Fe came from the near grain boundary or the inclusion itself.

## 6.7 Summary

An increase in temperature from 1260 °C to 1360 °C was linked to an absolute increase in average grain size of 2 μm for PSZT with 0 at% Fe and 0.7 μm for PSZT with 1.4 at% Fe. Grain growth was inhibited by Fe doping, leaving the grain size of sintered bodies similar to the particle size of the starting powder. Relative density exhibited a maximum for samples sintered at 1310 °C irrespective of Fe doping, which was explained by a low densification rate at 1260 °C and early formation of larger and more stable pores at 1360 °C. The phase content did not significantly change with sintering temperature, tetragonal distortion decreased at 1360 °C possibly due to better homogeneity at this temperature. TEM nanoscale investigations revealed local compositional fluctuations in specimens sintered at 1310 °C.

Strontium doping only affected the grain size of Fe-doped PZT; decreased it by  $\approx 1 \mu\text{m}$ . A previously reported density increase with Sr doping was not confirmed in this work for pure PZT. Interaction of Sr and Fe inhibited formation of pore clusters, which resulted in a density increase. The MPB was likely shifted to higher Zr/Ti ratio, which caused the observed increase in tetragonal phase content. The tetragonal distortion decreased due to substitution of  $\text{Pb}^{2+}$  by smaller  $\text{Sr}^{2+}$ .

Increasing  $y$  in  $(\text{Pb}_{0.95}\text{Sr}_{0.05})(\text{Zr}_y\text{Ti}_{1-y})\text{O}_3$  (0 at% Fe) induced an average grain size decrease of 0.8 μm, which was rationalised by a decrease in sinterability with increasing  $\text{PbZrO}_3$  due to its higher melting point compared to  $\text{PbTiO}_3$ . This argument was supported by microscopic observations which revealed an increase in porosity between 2–10 μm (maximum Feret diameter) for samples with  $y = 53$  and 55 at%, and by the absolute decrease of relative density by 1 % between  $y = 49$ –55 at%.

The grain size of Fe-doped compositions was not affected by changes in  $y(\text{Zr})$ , as grain growth was already effectively inhibited by Fe. The density of Fe-doped compositions slightly increased towards Zr-rich compositions (absolute change of 0.7 %). In this case, a higher Zr content inhibited pore movement and the creation of pore clusters, allowing better densification. Increase in density was correlated with decrease in porosity above 13  $\mu\text{m}$  (maximum Feret diameter).

The tetragonal phase content and distortion decreased when approaching the MPB. Fe-doped samples exhibited higher rhombohedral content at any Zr/Ti ratio, suggesting the widening of the MPB. The widening could also be possibly caused by grain size or local inhomogeneities. TEM revealed local compositional fluctuations in PSZT regardless of Fe presence, but the differences could not be quantified, and the observed areas were not representative enough to make a conclusion. According to the XRD results, the MPB was located between  $y(\text{Zr}) = 53\text{--}55$  at%.

The presence of Fe inhibited grain growth of PSZT, while achieving higher density and thickness shrinkage. Microscopic observations revealed an increase in finer porosity and decrease of pores above 6  $\mu\text{m}$  (maximum Feret diameter). The tetragonal distortion decreased monotonously with increasing Fe content suggesting that more  $\text{Fe}^{3+}$  atoms get incorporated into the crystal lattice of PZT, even after exceeding its reported solubility limit. Possible explanations include local fluctuations of  $\text{Fe}^{3+}$  at lower concentrations or the effect of the secondary phase containing segregated  $\text{Fe}^{3+}$  on surrounding grains. Nanoscale investigations confirmed segregation of Pb- and Fe- or Zr-rich phase in PSZT at triple junctions of samples with 2 at% Fe. An increased concentration of Fe was also detected in the grain boundaries and Pb-rich inclusions of 8–70 nm were found near grain boundaries. Their origin is unknown.

The results and conclusions presented in this chapter will be revisited when discussing the impact of physical properties on piezoelectric, dielectric and mechanical properties in the following chapters.

## 7 PIEZOELECTRIC AND DIELECTRIC PROPERTIES

This chapter presents results from piezoelectric and dielectric measurements of samples 3 days after poling. Measured values are presented in graphs plotted against the studied factors, as in the previous chapter.

### 7.1 Sintering temperature

Sintering temperature was varied for each fixed composition, with and without Fe-doping:  $(\text{Pb}_{0.95}\text{Sr}_{0.05})(\text{Zr}_{0.52}\text{Ti}_{0.48})_{0.986}\text{Fe}_{0.014}\text{O}_3$  and  $(\text{Pb}_{0.95}\text{Sr}_{0.05})(\text{Zr}_{0.52}\text{Ti}_{0.48})\text{O}_3$  respectively. Therefore, the piezoelectric and dielectric properties should be mainly affected by microstructural parameters – relative density, grain size and phase composition. As shown in chapter 5.4.2, the average PbO loss was similar for all sintering temperatures, only the Fe-doped samples sintered at 1360 °C exhibited variable loss within the crucible, which was attributed to an imperfect enclosure. Inspection of the graphs in Figure 7-1, Figure 7-2 and Figure 7-3 show that there is clearly no abnormal standard deviation shown by the Fe-doped batch 15 sintered at 1360 °C. The most likely explanations are that either the PbO loss difference was not large enough to induce property changes or the affected layer was removed by machining prior to the characterisation measurements.

The relative permittivity of  $(\text{Pb}_{0.95}\text{Sr}_{0.05})(\text{Zr}_{0.52}\text{Ti}_{0.48})\text{O}_3$  slightly increased with increasing sintering temperature, while  $\epsilon_r$  of the Fe-doped compositions was not significantly affected, as shown in Figure 7-1. Randall et al. reviewed published reports of grain size effects on the relative permittivity and concluded that they showed opposing trends [51]. They hypothesised that other factors such as processing, homogeneity and PbO loss may affect room temperature permittivity more than grain size. The initial increase in relative permittivity can be attributed to an increase in relative density, as previously shown in Figure 6-2 a). The relative permittivity

increase in undoped samples sintered at 1360 °C is likely the result of the other factors mentioned earlier as the relative density decreases slightly at this temperature.

While relative permittivity is not significantly affected by grain size at the room temperature, it has been reported to show a dependence at elevated temperatures [51, 64, 173, 174]. However, the temperature dependence of relative permittivity was not measured in this work.

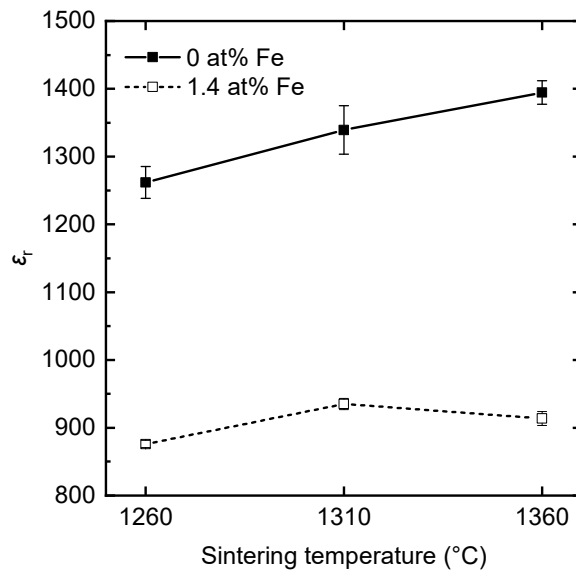


**Figure 7-1 Dependence of relative permittivity  $\epsilon_r$  of  $(\text{Pb}_{0.95}\text{Sr}_{0.05})(\text{Zr}_{0.52}\text{Ti}_{0.48})_{1-z}\text{Fe}_z\text{O}_3$  on sintering temperature.**

Unlike  $\epsilon_r$  at room temperature, planar coupling and  $d_{33}$  coefficients appear to be significantly affected by sintering temperature (see Figure 7-2), which can be correlated with the changes in grain size shown in Figure 6-1 a). Both  $k_p$  and  $d_{33}$  are linked with polarisation. Grain boundaries pin domain walls, reducing their mobility (one of the extrinsic contributions to polarisation) [51, 175-178]. As grain size decreases and the number of grain boundaries increases, domain wall motion is impeded and  $k_p$  and  $d_{33}$  are reduced. The results presented here reflect this dependence.

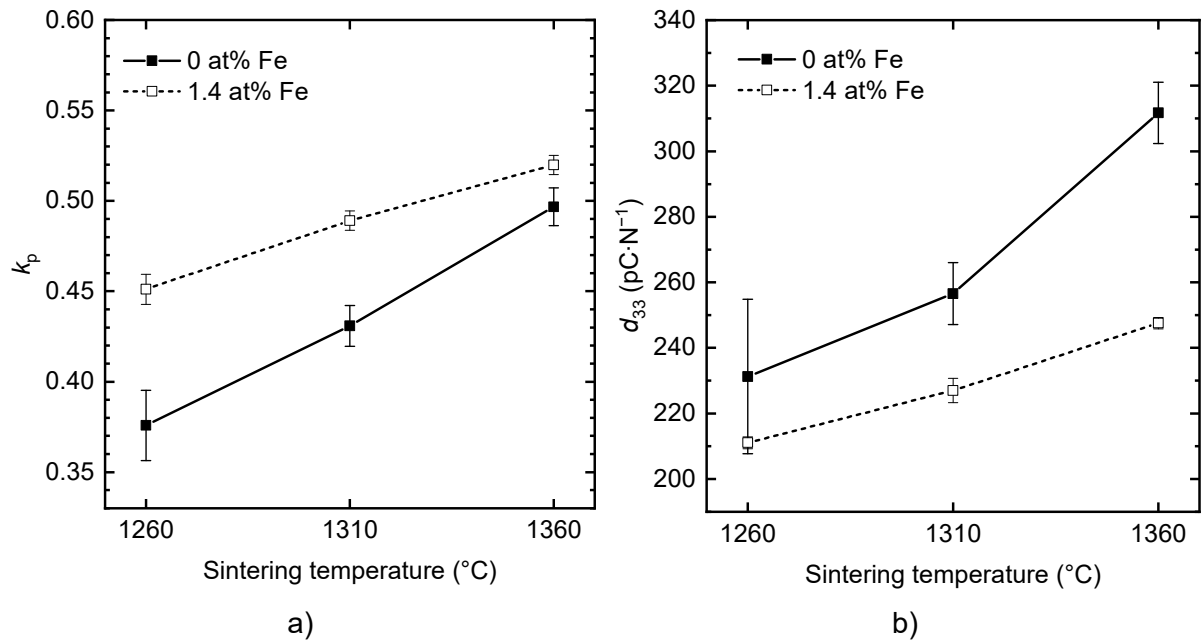
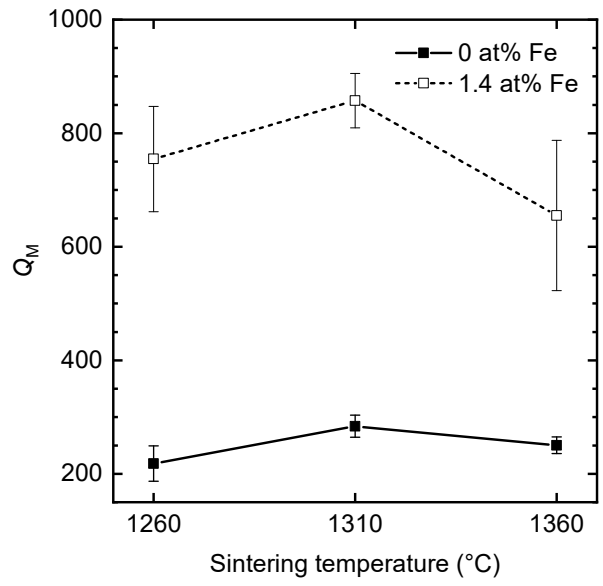
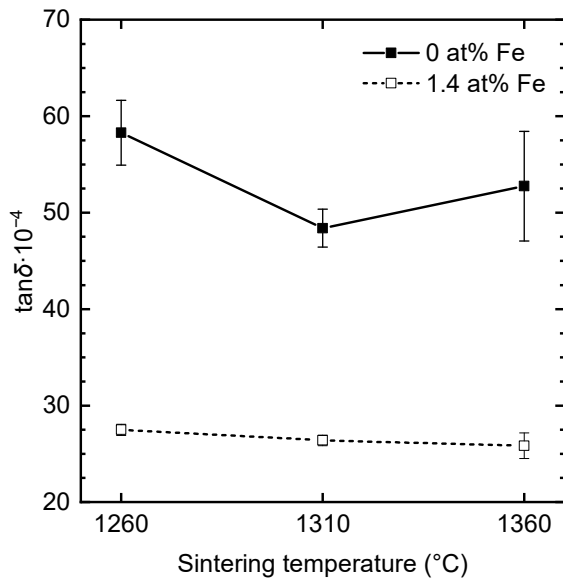


**Figure 7-2 Dependence of a) planar coupling coefficient  $k_p$ , b)  $d_{33}$  coefficient of  $(\text{Pb}_{0.95}\text{Sr}_{0.05})(\text{Zr}_{0.52}\text{Ti}_{0.48})_{1-z}\text{Fe}_z\text{O}_3$  on sintering temperature.**

The dissipation factor was unaffected by sintering temperature in the Fe-doped composition and showed only a small variation in the undoped composition (Figure 7-3 a)).

The mechanical quality factor  $Q_M$  of PZT with 0 at% Fe was generally low and showed almost no change with increasing sintering temperature (Figure 7-3 b)). On the other hand, the Fe-doped composition showed a small increase and then a more substantial decrease of  $Q_M$  with increasing sintering temperature. This can be explained by 2 competing factors: relative density and grain size. Increased domain wall motion caused by increasing grain size reduces  $Q_M$ , while increased relative density enhanced it.



a)

b)

**Figure 7-3 Dependence of a) dissipation factor  $\tan\delta$ , b) mechanical quality factor  $Q_M$  of  $(\text{Pb}_{0.95}\text{Sr}_{0.05})(\text{Zr}_{0.52}\text{Ti}_{0.48})_{1-z}\text{Fe}_2\text{O}_3$  on sintering temperature.**

## 7.2 Sr content

The presence of Sr increased relative permittivity in both the Fe-doped and undoped compositions (Figure 7-4). The enhancement of relative permittivity is a side effect of Sr doping caused by the lowering of the Curie temperature [26, 179]. However, the observed permittivity change of 100–200 shown in Figure 7-4 was not as significant as reported elsewhere (absolute increase of 300–500 with 5–6 at% of Sr in [26, 50]). This may have been caused by impurities in the raw oxides.

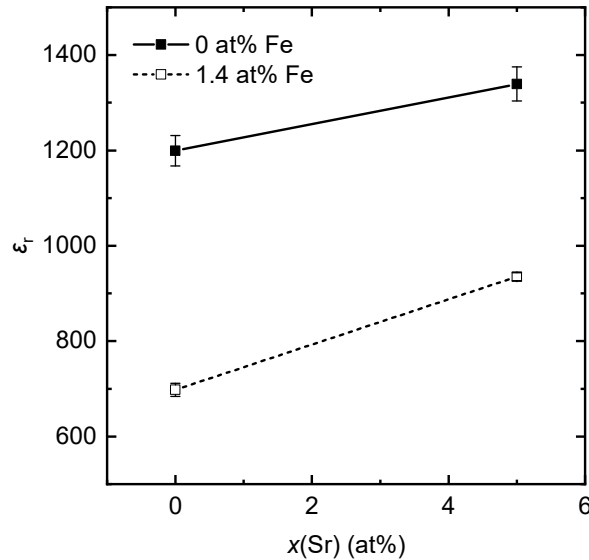


**Figure 7-4 Dependence of relative permittivity  $\epsilon_r$  of  $(\text{Pb}_{1-x}\text{Sr}_x)(\text{Zr}_{0.52}\text{Ti}_{0.48})_{1-z}\text{Fe}_z\text{O}_3$  sintered at 1310 °C on Sr content.**

Another effect of  $\text{Sr}^{2+}$  doping is an increase in electromechanical coupling [26, 50, 155, 180]. However, an opposite trend was observed in this work as can be seen in Figure 7-5 a). It should be noted that in the referenced work an increase in relative density with Sr doping was always observed [155, 180]. Kulcsar stated that small amount of Sr acts as a flux [50]. In the previous section, a clear increase of  $k_p$  with increasing grain size and density was shown. However, Sr-doped samples showed < 1% change in relative density, suggesting that Sr did not significantly alter densification, but the grain size of Fe-doped samples was decreased, which would be

expected to lead to a decrease in  $k_p$ . It was previously suggested that raw oxide impurities as well as excess PbO created a liquid phase at high temperatures, overshadowing any densification effects of Sr.

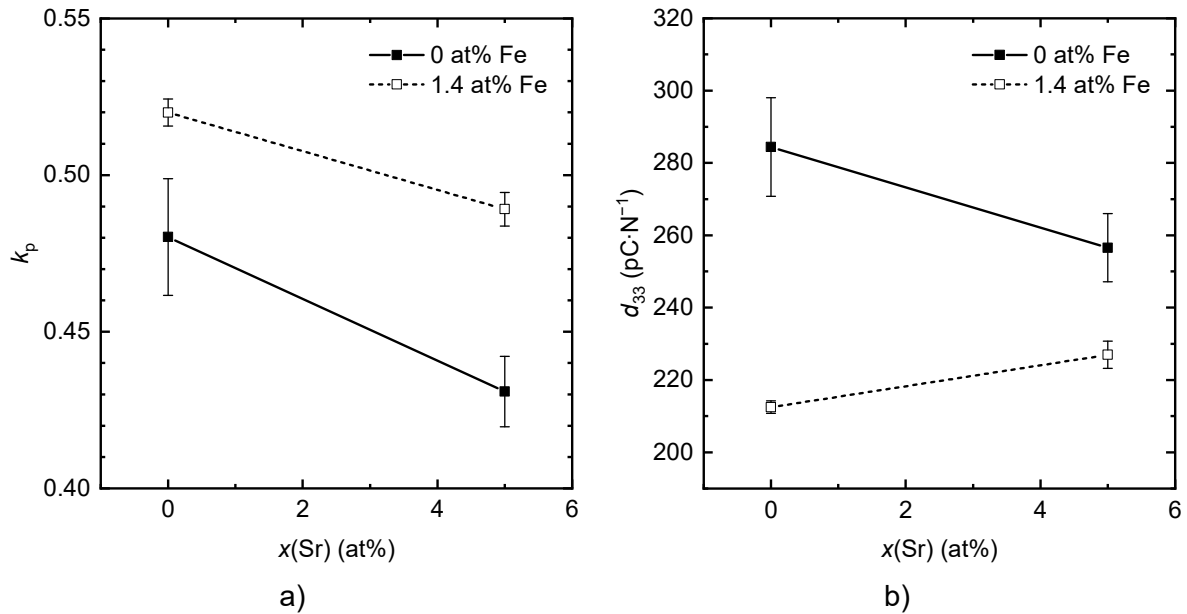


**Figure 7-5 Dependence of a) planar coupling coefficient  $k_p$ , b)  $d_{33}$  coefficient of  $(\text{Pb}_{1-x}\text{Sr}_x)(\text{Zr}_{0.52}\text{Ti}_{0.48})_{1-z}\text{Fe}_z\text{O}_3$  sintered at 1310 °C on Sr content.**

The  $d_{33}$  coefficient as well as  $k_p$  are related to dielectric permittivity and remanent polarisation [27]. The remanent polarisation is expected to decrease with Sr doping, as the MPB shifts away towards higher Zr/Ti ratio [170]. The dependence on permittivity is stronger in the case of  $d_{33}$ , which explains why  $d_{33}$  in Figure 7-5 b) shows a minimal change in the Fe-doped composition and small decrease in the undoped composition as opposed to the decrease  $k_p$ .

The dissipation factors shown in Figure 7-6 a) appear unaffected by sintering temperature, which agrees with previous results [26]. Similarly, it was shown that  $\text{Sr}^{2+}$  addition does not significantly alter the mechanical quality factor [26, 50, 179]. As shown in Figure 7-6 b), Sr doping increased the  $Q_M$  of the Fe-doped sample, which is possibly connected to the decrease

in grain size, rather than the substitution itself. It has been concluded in section 7.1 that  $Q_M$  increases with increasing density and decreasing grain size.

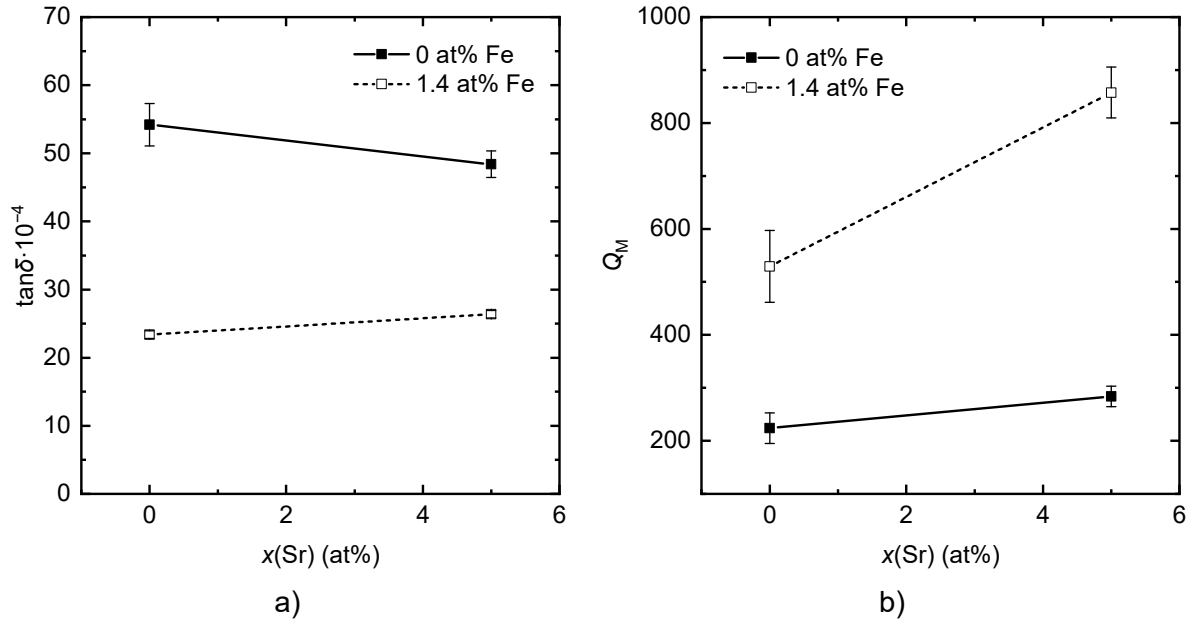


**Figure 7-6** Dependence of a) dissipation factor  $\tan\delta$ , b) mechanical quality factor  $Q_M$  of  $(\text{Pb}_{1-x}\text{Sr}_x)(\text{Zr}_{0.52}\text{Ti}_{0.48})_{1-z}\text{Fe}_z\text{O}_3$  sintered at 1310 °C on Sr content.

### 7.3 Fe content

As described in section 2.5.2, main effects of acceptor doping are a decrease of  $\tan\delta$ ,  $\epsilon_r$ ,  $k_p$  and  $d_{33}$ , and an increase of  $Q_M$ . The relative permittivity showed a rapid initial decrease from 0 at% Fe up to 1.4 at% Fe which then remained constant as the Fe content was raised to 2 at% (Figure 7-7 a)). A similar trend was observed for the dissipation factor as shown in Figure 7-7 b). In this case, the decrease is observed only up to 0.4 at% Fe. Both trends are consistent with the previous study by Weston et al. [80].

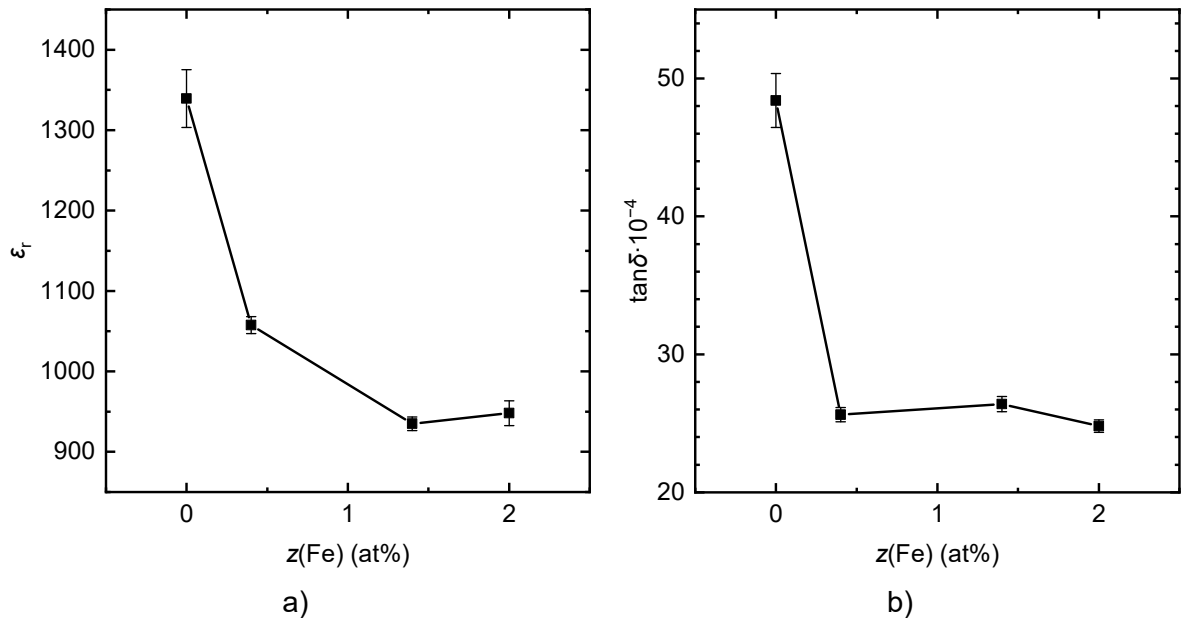


**Figure 7-7 Dependence of a) relative permittivity  $\epsilon_r$ , b) dissipation factor  $\tan\delta$  of  $(\text{Pb}_{0.95}\text{Sr}_{0.05})(\text{Zr}_{0.52}\text{Ti}_{0.48})_{1-z}\text{Fe}_z\text{O}_3$  sintered at 1310 °C on Fe content.**

Figure 7-8 shows that addition of 0.4 at% Fe significantly increased the planar coupling factor while further Fe addition slightly lowered it. Such a significant increase in  $k_p$  is unexpected and disagrees with general acceptor doping effects. Specifically, because  $k_p$  directly scales with the square root of  $\epsilon_r$  [27], which decreases with Fe doping, as shown in Figure 7-7 a). The increase in planar coupling factor could be possibly explained by relative density, which increased with Fe doping. In a study published by Weston et al. [80], Fe-doped PZT (0–5 at%) showed  $k_p$  values between 0.52 and 0.49, slightly decreasing with doping above 0.5 at% Fe. However, the

samples were sintered in an oxygen atmosphere, attaining the same density irrespective of the level of Fe doping. In comparison to these values, the  $k_p$  of the composition with 0 at% Fe in this work appears to show an abnormally low  $k_p$ , rather than the Fe-doped samples showing excessively high values.

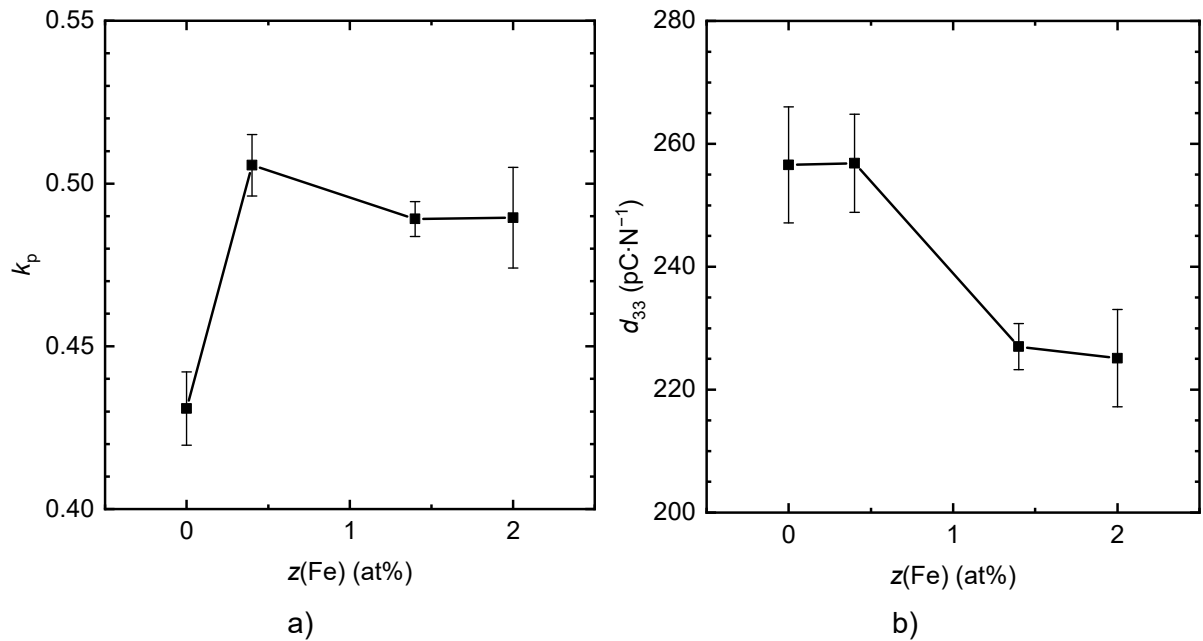


**Figure 7-8 Dependence of a) planar coupling coefficient  $k_p$ , b)  $d_{33}$  coefficient of  $(\text{Pb}_{0.95}\text{Sr}_{0.05})(\text{Zr}_{0.52}\text{Ti}_{0.48})_{1-z}\text{Fe}_z\text{O}_3$  sintered at 1310 °C on Fe content.**

The  $d_{33}$  coefficient (Figure 8-8 b)), which correlates with  $\epsilon_r$  and  $P_r$ , showed no change with a substitution of 0.4 at% Fe. As  $\epsilon_r$  decreased with increased Fe doping and the polarisation-electric field ( $P_E$ - $E$ ) loops shown in Figure 7-9 a) suggest that the same was true for  $P_r$ , the higher density is the likely cause of this behaviour, as suggested in the case of  $k_p$ . The substitution of 1.4 and 2 at% Fe led to decreases in  $d_{33}$ , which agree with the respective trends in relative density (constant),  $\epsilon_r$  (decreases) and  $P_r$  (decreases).

The mechanical quality factor significantly increases with increasing Fe content and reaches a maximum at 1.4 at% Fe as shown in Figure 7-9 b). This response agrees well with general acceptor doping trends [26, 80, 179].

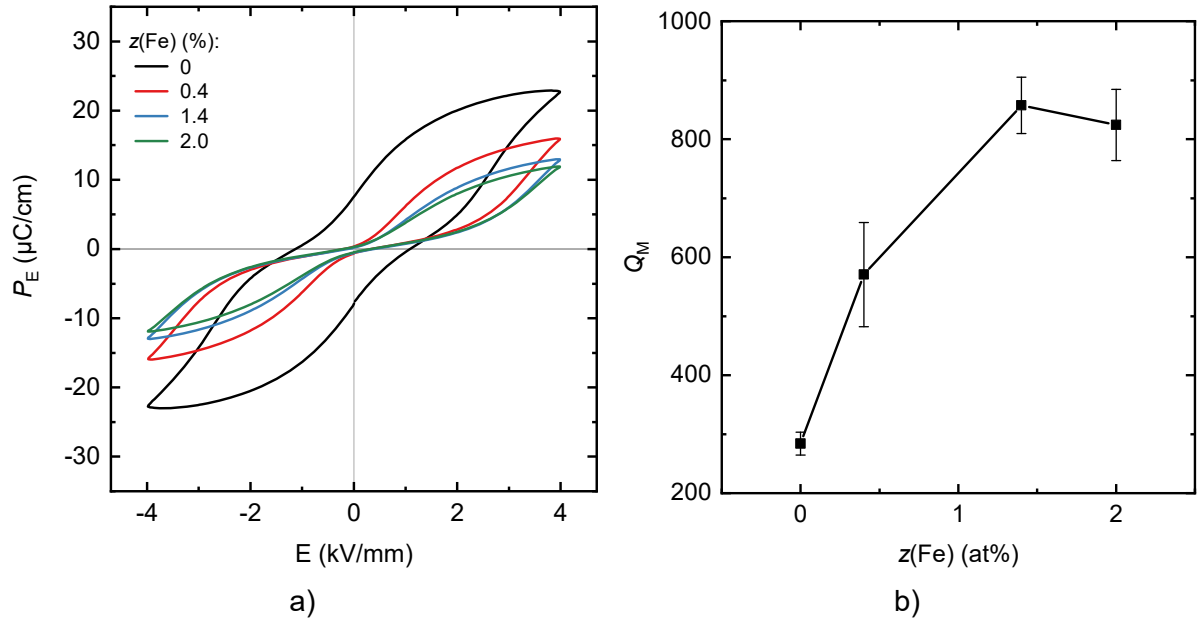


**Figure 7-9 a) Polarisation-electric field ( $P_E$ - $E$ ) loops of  $(\text{Pb}_{0.95}\text{Sr}_{0.05})(\text{Zr}_{0.52}\text{Ti}_{0.48})_{1-z}\text{Fe}_z\text{O}_3$  doped with 0.0–2.0 at% Fe and sintered at 1310 °C; b) dependence of mechanical quality factor  $Q_M$  of  $(\text{Pb}_{0.95}\text{Sr}_{0.05})(\text{Zr}_{0.52}\text{Ti}_{0.48})_{1-z}\text{Fe}_z\text{O}_3$  sintered at 1310 °C on Fe content.**

None of the properties discussed in this section show any significant change as the Fe content is increased from 1.4 to 2.0 at%, which supports the hypothesis that the Fe solubility limit in PZT is reached between 0.4 and 1.4 at%.

## 7.4 Zr/Ti ratio

Maxima of relative permittivity and remanent polarisation do not coincide near the MPB, as illustrated in Figure 7-10, replotted from [26].  $P_r$  usually exhibits a maximum value near the rhombohedral edge of the MPB, while the maximum of  $\epsilon_r$  is located near the tetragonal edge [27]. Maxima of  $k_p$  and  $d_{33}$  are located between the maxima of  $P_r$  and  $\epsilon_r$  due to their correlation. However, because the dependence of  $k_p$  on  $\epsilon_r$  is weaker, the  $k_p$  maximum ends up being located closer to the  $P_r$  maximum. Therefore it would be expected that with increasing  $y$  in  $(\text{Pb}_{1-x}\text{Sr}_x)(\text{Zr}_y\text{Ti}_{1-y})_{1-z}\text{Fe}_z\text{O}_3$ , the maxima of properties appear in the order:  $\epsilon_r$ ,  $d_{33}$ ,  $k_p$ ,  $P_r$ . The maximum unidirectional strain  $S$  is not located exactly at the MPB (equal volume of both phases), but rather on a tetragonal side of it, as was discussed in section 2.5.1.

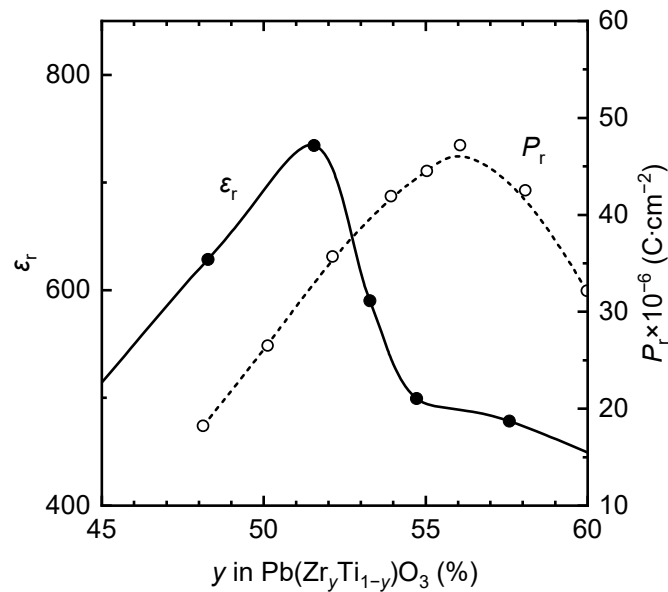


**Figure 7-10** Relative permittivity  $\epsilon_r$  and remanent polarisation  $P_r$  as a function of Zr fraction in PZT replotted from [26].

Plots of  $\epsilon_r$ ,  $k_p$  and  $d_{33}$  as a function of  $y(\text{Zr})$  are shown in Figure 7-11. Maxima of  $\epsilon_r$ ,  $d_{33}$  and  $k_p$  respectively were found at  $y = 52, 53, 53/55$  at% in samples without Fe and  $y = 51, 52/53, 53$  at% in Fe-doped samples. The order of maxima agrees with the correlations described in the previous paragraph. It appears that the MPB is slightly shifted towards lower  $y$  in Fe-doped

samples. This has been previously suggested [80]. However, XRD in this work showed a tetragonal-to-rhombohedral transition between  $y = 53$  and  $55$  at% in both Fe-doped and undoped compositions. It has been shown that the preparation and doping have a severe impact on the micro/nanoscale homogeneity of the material. Excellent high homogeneity can be reached using methods such as hydrothermal synthesis precipitation or a sol-gel method and the sharpness of the peaks in electrical properties increases with homogeneity and shifts the MPB to a higher  $y(\text{Zr})$  [27]. It was hypothesised that Fe doping impedes diffusion, making homogenisation of the material more difficult. Inhomogeneity on a nano/microscale level in Fe-doped samples would explain the less pronounced maxima of  $\epsilon_r$ ,  $k_p$  and  $d_{33}$  as well as the apparent shift of MPB to lower  $y(\text{Zr})$ . Inhomogeneities were observed in TEM specimens in section 6.6, regardless of Fe doping, but the Fe-doped sample contained some extra inter- and intragranular secondary phases, which the undoped sample did not. Inhomogeneity was also used to explain the XRD results presented in section 6.5, which showed an increased amount of rhombohedral content in all Fe-doped samples in the Zr/Ti series.

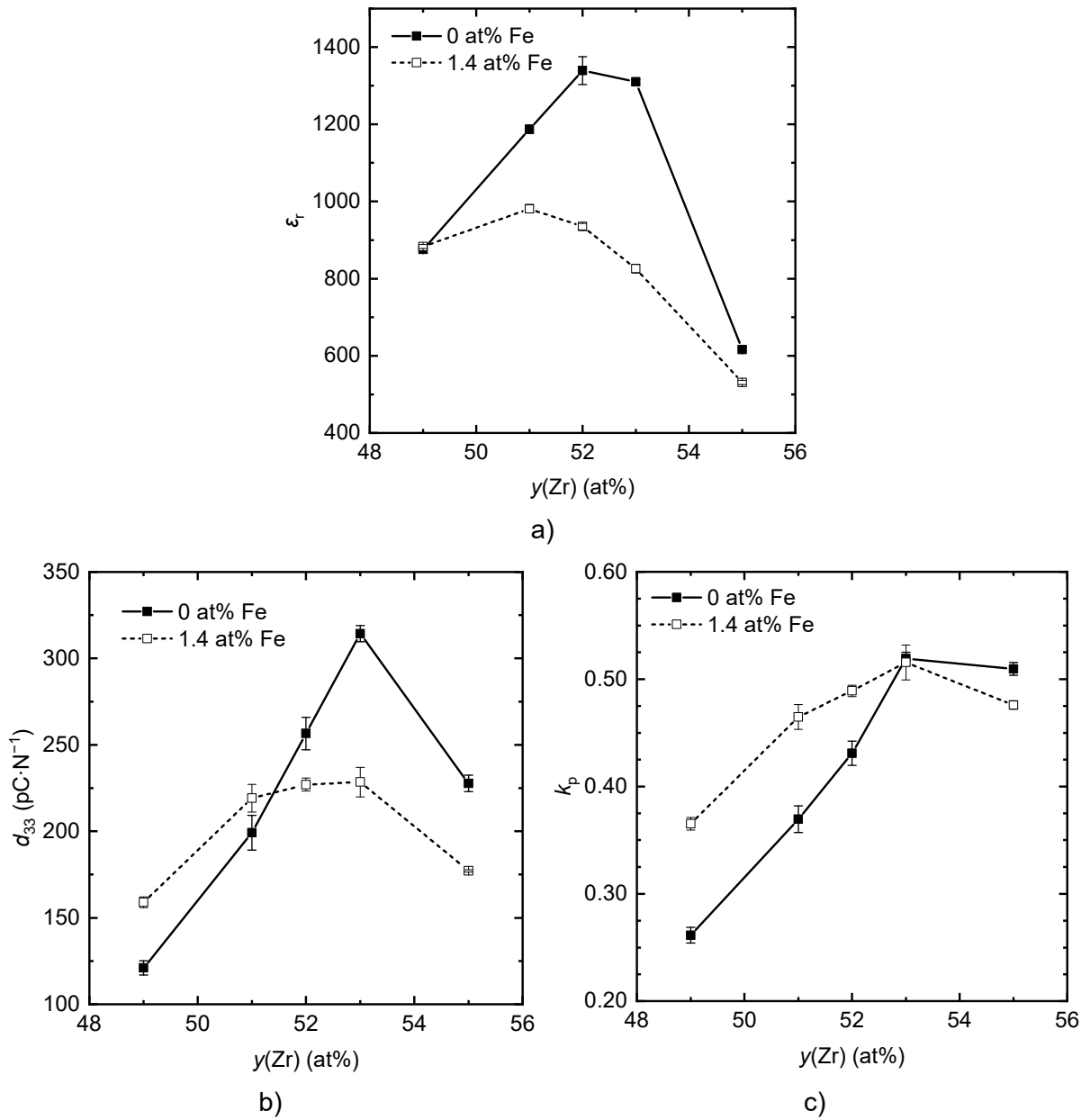
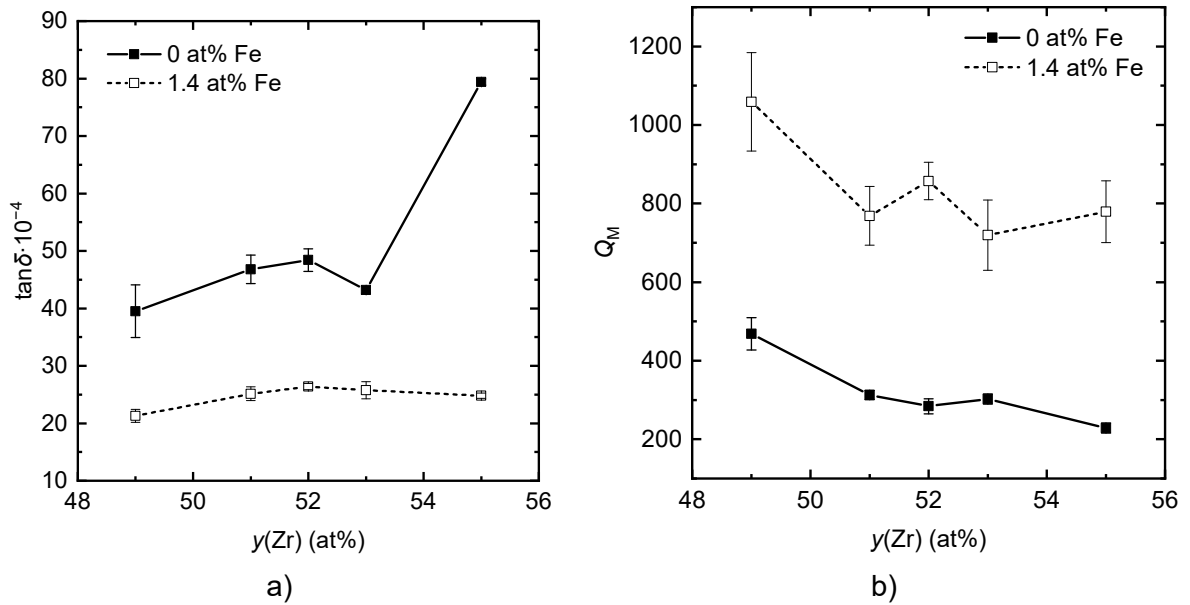


Figure 7-11 Dependence of a) relative permittivity  $\epsilon_r$ , b)  $d_{33}$  coefficient, c) planar coupling coefficient  $k_p$ , of  $(\text{Pb}_{0.95}\text{Sr}_{0.05})(\text{Zr}_y\text{Ti}_{1-y})_{1-z}\text{Fe}_z\text{O}_3$  sintered at 1310 °C on Zr/Ti ratio.

The dissipation factor of samples with no added Fe generally stays constant with increasing  $y$  in  $(\text{Pb}_{1-x}\text{Sr}_x)(\text{Zr}_y\text{Ti}_{1-y})_{1-z}\text{Fe}_z\text{O}_3$  up to  $y = 53$  at% and increases at  $y = 55$  at%, as shown in Figure 7-12 a). Doping with Fe effectively suppresses any changes in  $\tan\delta$  with increasing  $y$ . The mechanical quality factor decreases with increasing  $y$  in all compositions (Figure 7-12 b)). These results agree with previous findings [26, 80].



**Figure 7-12** Dependence of a) dissipation factor  $\tan\delta$ , b) mechanical quality factor  $Q_M$  of  $(\text{Pb}_{0.95}\text{Sr}_{0.05})(\text{Zr}_y\text{Ti}_{1-y})_{1-z}\text{Fe}_z\text{O}_3$  sintered at 1310 °C on Zr/Ti ratio.

## 7.5 Summary

The piezoelectric and dielectric properties of all the compositions improved when the sintering temperature was raised from 1260 to 1310 °C. This was likely due to the increase in relative density.  $d_{33}$  and  $k_p$  showed a further increase when the sintering temperature was raised to 1360 °C, while the  $Q_M$  value was lowered. Increased grain size and domain wall mobility were indicated as the main causes of these effects.

Sr doping showed a low effectiveness in improving  $\epsilon_r$  and  $k_p$  compared to reported values ( $k_p$  even decreased). In other studies, increase in relative density was observed after adding Sr, which played a role in improving electrical properties. It was hypothesised that raw oxide impurities and stoichiometric excess of PbO in this work negated densification effects of Sr as no significant change in density with Sr doping was observed. Only a significant grain size decrease was observed for samples doped with both Fe and Sr.

Addition of Fe induced property changes typical of acceptor doping – decrease in  $\tan\delta$ ,  $\epsilon_r$ ,  $d_{33}$  and increase in  $Q_M$ . Only  $k_p$  increased unexpectedly, which was attributed to the increase in relative density. The solubility limit of Fe was estimated to lie between 0.4 and 1.4 at% Fe as no change in properties was observed between 1.4 and 2.0 at% Fe. This is in contrast with tetragonal cell distortion results from XRD measurements which showed a continuous decrease with Fe content.

Maxima of  $\epsilon_r$ ,  $d_{33}$ ,  $k_p$  in  $(\text{Pb}_{1-x}\text{Sr}_x)(\text{Zr}_y\text{Ti}_{1-y})_{1-z}\text{Fe}_z\text{O}_3$  lay between  $y = 52\text{--}55$  at% in samples with no added Fe and between  $y = 51\text{--}53$  at% in samples doped with 1.4 at% Fe. The apparent shift of MPB to lower  $y$  in Fe-doped compositions could be caused by a decrease in micro-/nanoscale homogeneity revealed by nanoscale homogeneity investigations.

The results demonstrate the complexity of relationships between the electrical properties, chemical composition and microstructure of PZT. For the samples prepared in this work which achieved relative densities of 95–98 %, the chemical composition had the greatest impact on electrical properties, especially Fe doping and Zr/Ti ratio (proximity to MPB). The dielectric and piezoelectric properties of materials produced in this work showed values resembling those of commercially-made hard PZT.

## 8 MECHANICAL PROPERTIES

This chapter presents results of mechanical-property measurements, namely elastic modulus, Vickers hardness, surface roughness, equibiaxial flexural strength and microscale fracture toughness. The results are compared with the previously published dependences of technical ceramics. Equibiaxial strength results in section 8.4 are categorised by factors and discussed in more detail. Comparison with a commercial hard PZT can be found in section 8.4.8. General discussion of the influence of physical properties on the mechanical properties can be found in section 8.4.10.

### 8.1 Elastic modulus

The general influence of microstructure on the mechanical properties of ceramics has been already discussed in section 2.1.2. It is reasonable to assume that the Young's modulus ( $Y$ ) of materials produced in this work should follow the dependence in equation (2-8) shown in section 2.1.2 unless their structure gets significantly affected by compositional changes. To test the hypothesis, the Young's moduli of all the prepared batches were plotted against porosity as shown in Figure 8-1. Batches related to studied factors ( $T_{\text{sint}}$ , Sr content, Zr/Ti ratio, Fe content) are distinguished by symbols and colour, and connected with solid lines. The maximum and the minimum values of each factor are shown next to their respective points. The lines intersect in 2 points, which represent the 2 central batches: 4 ( $(\text{Pb}_{0.95}\text{Sr}_{0.05})(\text{Zr}_{0.52}\text{Ti}_{0.48})\text{O}_3$ ) and 13 ( $(\text{Pb}_{0.95}\text{Sr}_{0.05})(\text{Zr}_{0.52}\text{Ti}_{0.48})_{0.986}\text{Fe}_{0.014}\text{O}_3$ ) sintered at 1310 °C. A linear fit was performed using results from the PSZT batches sintered at different temperatures together with the PSZT batch doped with 0.4 at% Fe (the highest similarity in composition).

The graph shows that most of the points are located near the linear fit, which supports the previous hypothesis. The least square parameters were  $Y_0 = 100.2$  GPa,  $b = 5.64$ . The value of  $b$  is high compared to other studies. Dean and Lopez [19] found  $b$  in the range of 1.55–3.89 for

16 datasets, Biswas [23] studied properties of Nb doped PZT with artificially introduced spherical pores (110–150  $\mu\text{m}$ ) and found a  $b$  value of 2.5 for  $P$  between 0.006 – 0.083. It is likely that the accuracy of the fit in Figure 8-1 is limited due to the small porosity range covered. The character of the porosity is also different than in [23]. Nevertheless, the graph still reveals points significantly deviating from the line, and it is reasonable to assume that compositional effects rather than porosity dominate Young's modulus values of these samples. Individual deviations will be further discussed in the context of their respective series.

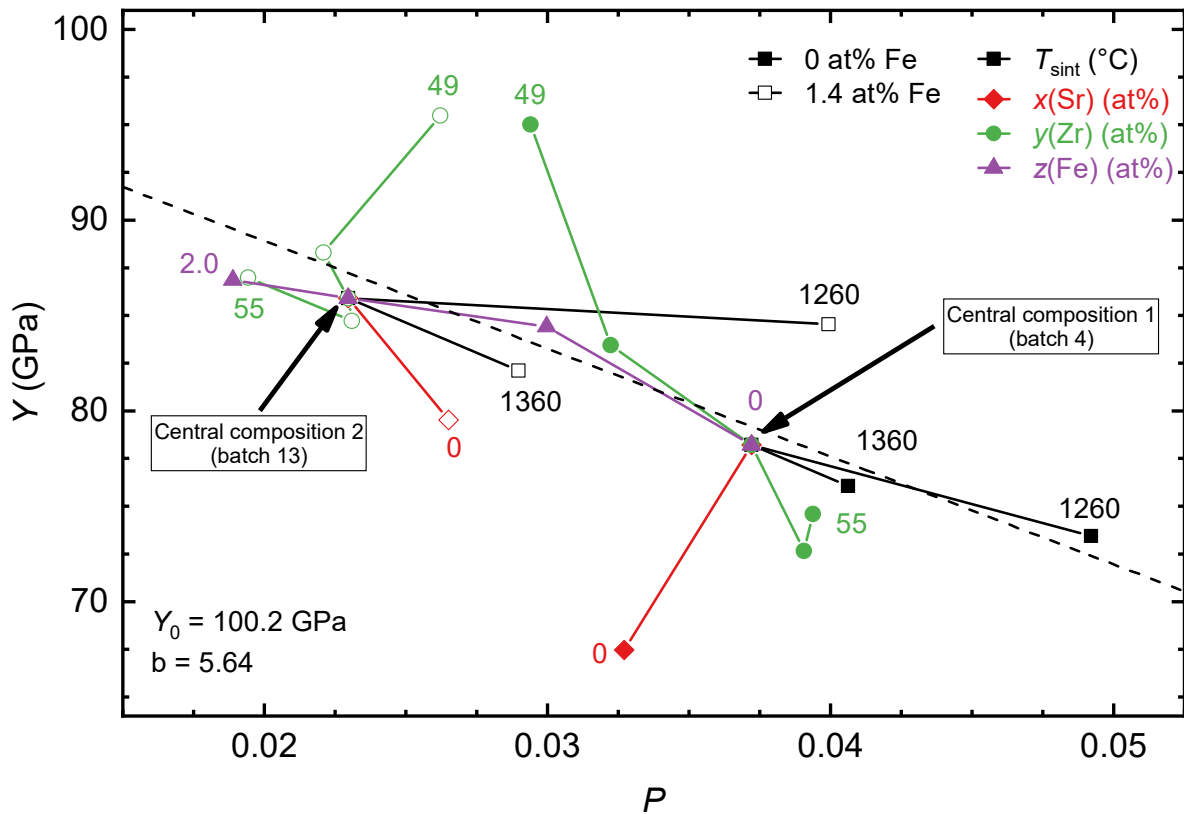


**Figure 8-1** Dependence of Young's modulus  $Y$  on fractional porosity  $P$  of all prepared series. Each series is connected by a solid line from the lowest to the highest value of its respective variable. Fe-doped and undoped series are represented by empty and filled symbols respectively ( $\text{Fe}_z$  series itself has filled triangular symbols). Undoped  $T_{\text{sint}}$  series (batches number 4–6) and a batch doped with 0.4 at% Fe (number 10) were used for the linear fit.

Disregarding the presence of Fe, the  $Y$  of materials sintered at different temperatures should follow the linear porosity dependence. This appears to be valid except for the Fe-doped PSZT samples sintered at 1260 °C, which show significant deviation in Figure 8-1. The relative density measurements of this batch revealed significant sample-to-sample differences, as demonstrated by an exceptionally high standard deviation in Figure 6-2. This was likely related to the binder inhomogeneities introduced during the preparation and their less effective elimination at the lowest sintering temperature. Young's modulus was measured on 4 samples, which could have been in the "denser" portion of the batch (different samples were used for each measurement). The standard deviation of Young's modulus shown in Figure 8-2 a) is also the highest in this batch. It is therefore concluded that deviation from the linear  $Y$ - $P$  dependence of this batch is caused by sample-to-sample density inhomogeneities.

Fe-doped samples from the sintering temperature series follow the linear fit of undoped samples in Figure 8-1, suggesting that the changes in  $Y$  originate from microstructural rather than structural changes. This is not surprising given the low dopant concentration.

The addition of Sr increased the Young's modulus of PZT irrespective of Fe presence, making the ceramic stiffer (see Figure 8-2 b). Both compositions free of Sr show deviations from the linear fit in Figure 8-1. XRD results presented in chapter 6.5 showed that Sr doping does affect the phase content and the degree of tetragonal distortion, however, its effect is less pronounced than the effect of Fe doping, for which samples follow the linear fit of  $Y$  versus  $P$ .

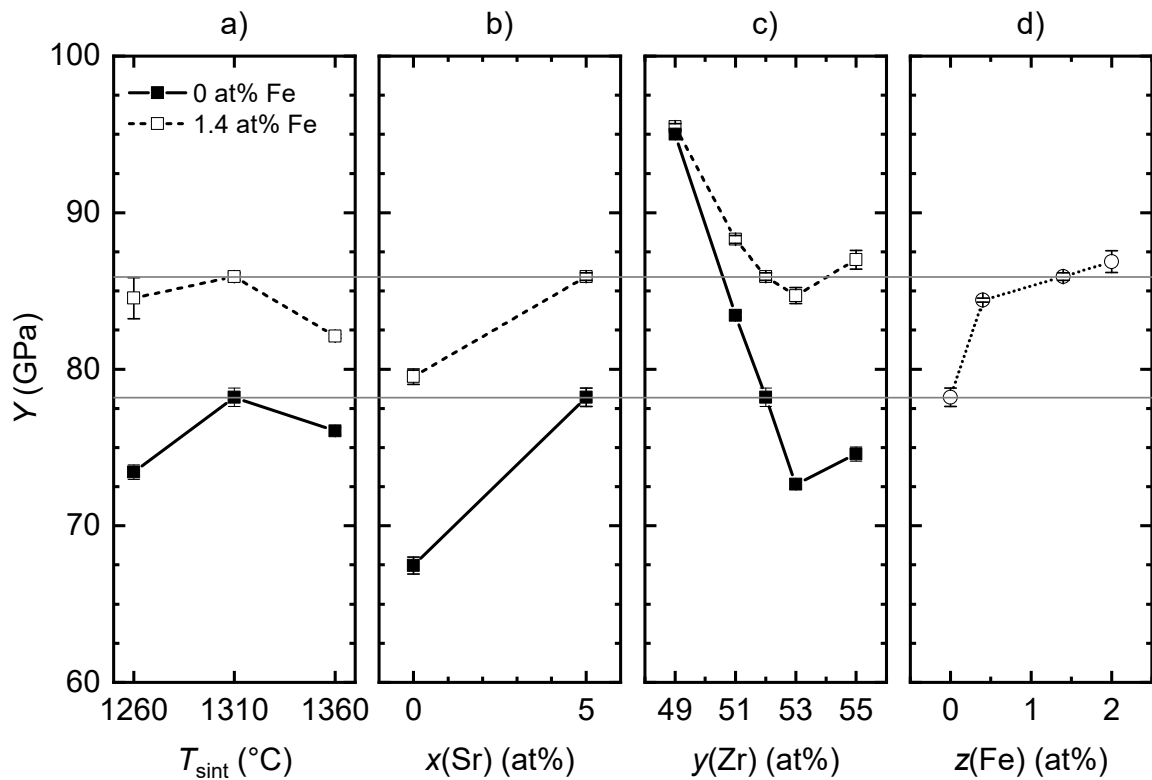


**Figure 8-2** Dependence of dynamic Young's modulus  $Y$  on a) sintering temperature ( $T_{\text{sint}}$ ), b) Sr content, c) Zr/Ti ratio, d) Fe content of  $(\text{Pb}_{1-x}\text{Sr}_x)(\text{Zr}_y\text{Ti}_{1-y})_{1-z}\text{Fe}_z\text{O}_3$ . Grey horizontal lines connect single central compositions, error bars represent SDM,  $T_{\text{sint}} = 1310$  °C if not stated otherwise.

It has been shown that PZT exhibits a minimum in elastic modulus (softening) near the MPB, even at temperatures near 0 K, where all extrinsic contributions to piezoelectric properties are no longer active [181]. Explanation of this behaviour is not trivial, and the current understanding has been summarised in a review by Cordero [48]. In practice, it means that proximity to the MPB influences Young's modulus. This is demonstrated in Figure 8-1, where compositions with  $\text{Zr}/\text{Ti} = 49/51$  significantly deviate from the linear fit. In this work, these compositions have been shown as the farthest ones from the MPB. In Fe-doped samples, the rest of the compositions with  $y$  in  $(\text{Pb}_{0.95}\text{Sr}_{0.05})(\text{Zr}_y\text{Ti}_{1-y})_{0.986}\text{Fe}_{0.014}\text{O}_3$  up to 55 at% lie in proximity to the line. Undoped compositions behave similarly except for the composition with  $y = 53$  at%, which appears somewhat diverged. This batch was shown to be the closest to the MPB, therefore a minimum in Young's modulus would be expected as the softening effect is

at its maximum. The composition with  $y(\text{Zr}) = 55$  at% is located on the rhombohedral side of the boundary, where  $Y$  increases again. This trend is shown in Figure 8-2 c). The reason why only samples containing 49 at% of Zr diverge in Fe-doped compositions is also apparent from the Figure 8-2 and dielectric/piezoelectric property results; The minimum of properties in these batches is significantly less sharp and property values are more similar.

A strong dependence of  $Y$  on the proximity to the MPB might also explain the divergence of pure PZT compositions from the linear fit (compositions with no Sr). Regardless of Fe doping, the presence of Sr shifts the MPB to the rhombohedral side. At certain Zr/Ti ratio, pure PZT samples are closer to the MPB and their  $Y$  should be lower. Again, this effect is more pronounced in samples with no Fe.

In the Fe doping series, the phase content changed when 0.4 at% of dopant was added and then showed no further variation (see Figure 6-22). For this reason, all Fe-doped compositions in this series would be expected to follow a linear dependence of  $Y$  on  $P$ . This seems to be the case in Figure 8-1. Based on the presented results, it is concluded that presence of Fe in PZT increases Young's modulus by increasing relative density, shifting MPB and making the minima in properties near the boundary less pronounced.

The values of  $Y$  obtained in this work have been compared with values reported elsewhere in Table 8-1. Most manufacturers report Young's modulus values calculated from material coefficients of poled piezoceramics described in [132]. Poled materials are anisotropic and yield different values of  $Y$  when measured in short (superscript "E") or open (superscript "D") circuit conditions. This leads to 4 separate important moduli:  $Y_{11}^E$ ,  $Y_{33}^E$ ,  $Y_{11}^D$ ,  $Y_{33}^D$  of which only the first 2 are commonly reported. Young's modulus measured on unpoled material by other methods (denoted as  $Y$ ) lies in the following range [182]:

$$Y^E \leq Y \leq Y^D,$$

$$\frac{2}{3}Y_{11}^E + \frac{1}{3}Y_{33}^E \leq Y \leq \frac{2}{3}Y_{11}^D + \frac{1}{3}Y_{33}^D.$$

Depending on the method of measurement, values of Young's modulus in Table 8-1 are shown either as single values or as ranges. Results from the current work agree well with reported values. Soft PZT values, also included for comparison, are generally lower than values (ranges) of the hard compositions. Assuming all industrially produced compositions are as close to the MPB as possible, soft PZT is expected to show lower  $Y$  values as the soft dopants make the property peak/dip near the MPB taller/deeper.

Table 8-1 Reported values of Young's modulus for various PZT compositions

Source	Method <sup>†</sup>	Composition	Y <sup>‡</sup> (GPa)	
Jaffe [26]	P	(Pb <sub>0.94</sub> Sr <sub>0.06</sub> )(Zr <sub>0.53</sub> Ti <sub>0.47</sub> )O <sub>3</sub>	76–103	
<i>Current work</i>	E	Range of PSZT compositions without Fe	73–95	
Jaffe [26]	P	(Pb <sub>0.94</sub> Sr <sub>0.06</sub> )(Zr <sub>0.53</sub> Ti <sub>0.47</sub> ) <sub>0.976</sub> Nb <sub>0.024</sub> O <sub>3</sub>	58–82	Soft PZT
CeramTec (272)	P		58–93	
Fett and Munz [182]	E	Not specified	65, 68	
Fett and Munz [182]	E	Not specified	87	Hard PZT
CeramTec [183]	P		74–108	
<i>Current work</i>	E	Range of all Fe-doped compositions	80–96	

<sup>†</sup> P = calculated using dielectric/piezoelectric parameters of poled ceramics; E = measured by means of impulse excitation of vibration method in unpoled state

<sup>‡</sup> for method "P", the range of  $Y^E$ – $Y^D$  is reported

## 8.2 Hardness

The dependences of Vickers hardness ( $H_v$ ) on sintering temperature and composition are shown in Figure 8-3. In the majority of the results, the values of the standard deviations exceed the values of absolute changes in  $H_v$ . The relatively high standard deviation values are likely related to the testing method and sample microstructures. As shown in section 6.4, the pore size range is wide. On the scale of the indent square size (40–65  $\mu\text{m}$ ), the porosity can be considered inhomogeneous and the size of the indent will strongly depend on the local porosity. The largest pores and pore clusters were intentionally avoided by the operator. Pores of similar size or somewhat smaller than the indentation, in most cases, obscure corners or deform the square, which then leads to rejection of the respective indent and bias towards lower porosity regions. Local areas of high concentration of pores on the same scale of size as the indent can affect the variability of the indent size and calculated  $H_v$ . Another important source of error is the indent size measurement, performed by the operator. This was discussed earlier in chapter 4.2.2, where the SEM indent size measurement method was shown to obtain consistent results despite the high values of standard deviation.

The dependence of  $H_v$  on sintering temperature (as shown in Figure 8-3 a)) resembles the Young's modulus and porosity trends. As explained in section 2.1.2, hardness is also linearly dependent on porosity in various ceramic materials, given the overall level of porosity is low (up to approx. 10%) [18]. However, unlike Young's modulus, hardness is also affected by grain size according to the Hall-Petch relationship in equation (2-9).

Compositional dependencies (Figure 8-3 b–d) resemble inverted grain size trends. Inhibition of grain growth cause by Fe doping and its combination with Sr is reflected by a significant increase in Vickers hardness (Figure 8-3 b). Changes in hardness appear more pronounced in

batches with lower average grain size (Fe-doped samples), which agrees with the relationship in equation (2-9).

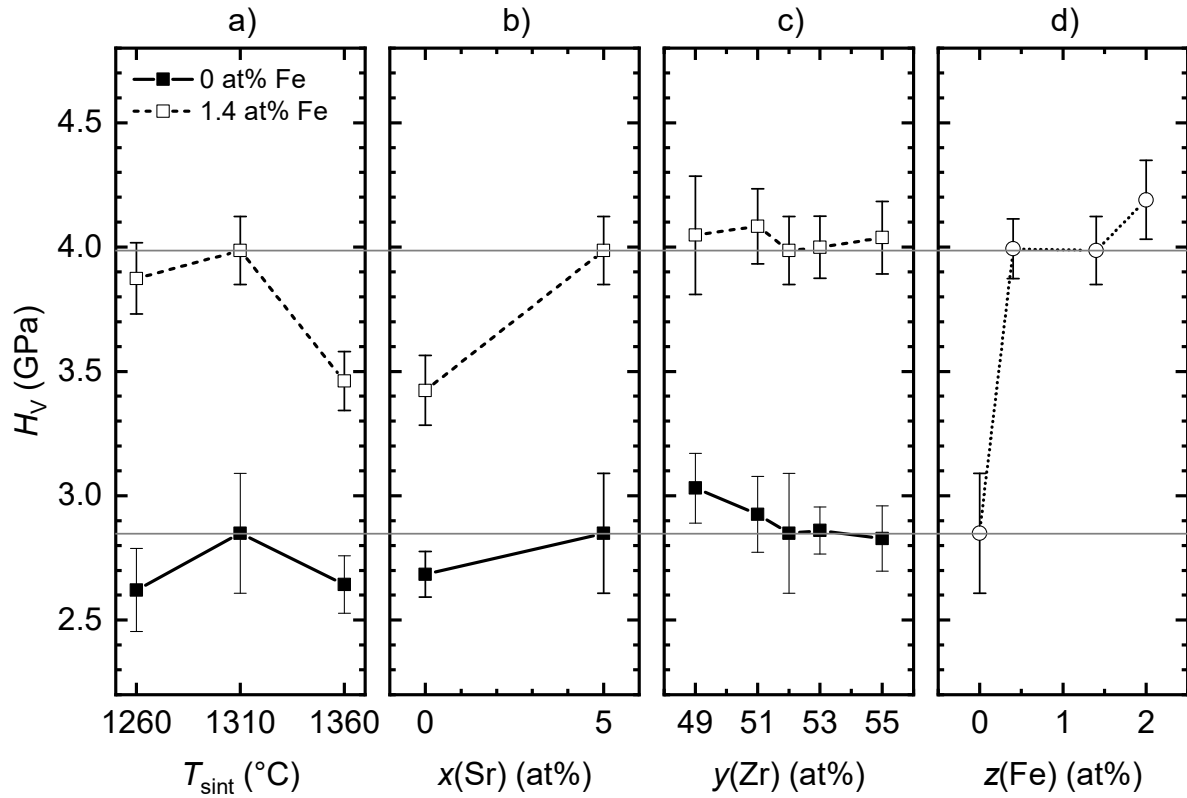


**Figure 8-3** Dependence of Vickers hardness  $H_V$  on a) sintering temperature ( $T_c$ ), b) Sr content, c) Zr/Ti ratio, d) Fe content of  $(\text{Pb}_{1-x}\text{Sr}_x)(\text{Zr}_y\text{Ti}_{1-y})_{1-z}\text{Fe}_z\text{O}_3$ . Grey horizontal lines connect single central compositions, error bars represent SDM,  $T_{\text{sint}} = 1310\text{ }^\circ\text{C}$  if not stated otherwise.

In order to assess any trends in the hardness with grain size, the hardness values need to be first corrected for the difference in porosity of their respective batches. The  $H_V$  of samples of similar average grain size have been plotted against porosity and are shown in Figure 8-4. Two groups of samples (Fe-doped and undoped materials) were fitted with linear regression, reflecting the following relationship [18]:

$$H_V = H_0(1 - bP), \quad (8-1)$$

which is the same as the equation (2-8) for  $Y$ - $P$  dependence presented in section 2.1.2. A different value of  $b$  was found for each group, which suggests that hardness-porosity

dependence changes with grain size.  $H_0$  was calculated for each batch individually and a corrected value of Vickers hardness ( $H_{V,corr}$ ) was obtained for the selected porosity value of  $P = 0.031$  (also shown in Figure 8-4). The value of  $b_1 = 5.40$  was used in all compositions with 0 at% Fe and value of  $b_2 = 2.06$  was used in all Fe-containing compositions.

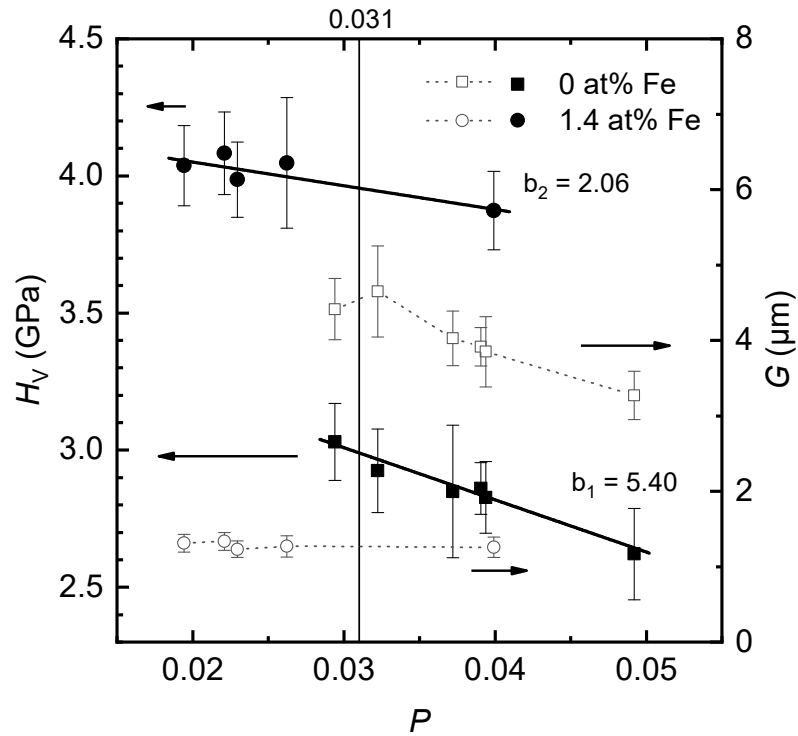


**Figure 8-4 Vickers hardness ( $H_V$ ) of 2 sample groups (see text for details) with similar average grain size ( $G$ ) plotted against their fractional porosity  $P$ . Error bars represent SDM.**

Since values of  $H_{V,corr}$  represent the hardness at a single porosity value, they can be directly plotted against  $1/\sqrt{G_a}$ , and this is shown in Figure 8-5. Corrected hardness results distinctively follow a linear trend, proving the validity of the Hall-Petch dependence in PZT. Notable deviations from a linear porosity dependence were observed in Young's modulus. Hardness does not show any exceptionally large deviations from the linear trend given its standard deviation. The only notable deviation is the batch of undoped samples with 0 at% Sr and Fe (sample 1 in Figure 8-5), which shows lower  $H_{V,corr}$  than the corresponding Sr-containing compositions. The same batch showed a large linear trend deviation of  $Y$ , which supports

a hypothesis that Sr at 5 at% somewhat stiffens and hardens PZT. Stiffening of Ti-rich compositions observed in Figure 8-1 is not reflected in hardness. As Fe-doped compositions follow the linear trend, regardless of acceptor content, it may be concluded that hardening in Fe-doped PZT is caused by grain growth inhibition, rather than incorporation of Fe into the PZT crystal lattice.

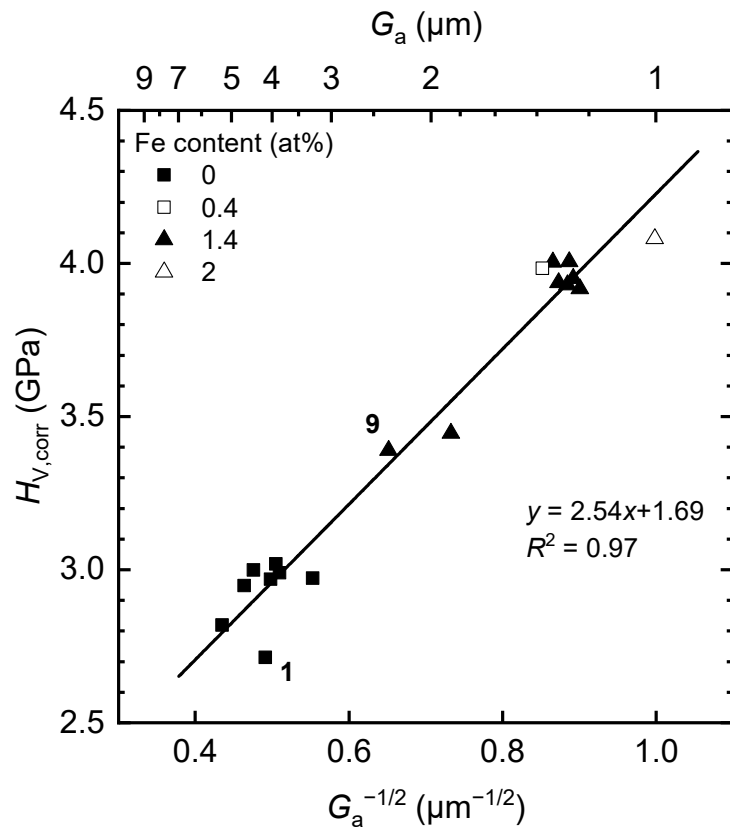


Figure 8-5 Corrected Vickers hardness  $H_V$  plotted against the inverse square root of average grain size  $G_a$ . Samples from batches number 1 and 9 indicate compositions with 0 at% Sr.

### 8.3 Surface roughness

The condition of the surface of a ceramic often plays an important role in a component's strength and reliability as it could contain residual machining or handling damage, which may serve as a fracture origin. When fracture originates from the surface, the strength of the component is controlled by the surface topography, which can be quantified by surface roughness. There are several surface roughness parameters used in practice, each with its pros and cons. 3 parameters were chosen for this work; arithmetical mean roughness value  $R_a$ , mean roughness depth  $R_z$  and maximum valley depth  $R_v$ .  $R_a$  represents the mean value of deviations from the mean line of the profile and is generally lower than  $R_z$ , which represents a mean value of the highest peak-deepest valley distances obtained from 10 sampling lengths [184]. All measured values are summarised in Table 8-2.

Table 8-2 Surface roughness and maximum valley depth of investigated batches of  $(\text{Pb}_{1-x}\text{Sr}_x)(\text{Zr}_y\text{Ti}_{1-y})_{1-z}\text{Fe}_z\text{O}_3$  sintered at 1310 °C unless stated otherwise.

Batch no.	x (Sr)	y (Zr)	z (Fe)	$R_a$	SDA	$R_z$	SDA	$R_v$
	at%			$(\mu\text{m})$		$(\mu\text{m})$		$(\mu\text{m})$
1	0	52		1.5	0.2	7.1	0.9	8.9
2		49		1.5	0.2	7.4	0.8	11.3
3		51		1.5	0.2	7.0	0.7	7.7
4				1.2	0.1	6.0	0.5	7.2
5 <sup>†</sup>	5	52	0	1.1	0.1	5.6	0.5	6.4
6 <sup>‡</sup>				1.0	0.1	5.5	0.4	7.2
7		53		0.9	0.1	4.5	0.7	5.2
8		55		0.8	0.1	4.3	0.4	5.6
10		52		0.4	0.7	0.1	3.7	0.3
9	0	52		0.7	0.1	3.8	0.3	4.5
11		49		1.1	0.1	5.3	0.5	7.7
12		51		1.0	0.1	5.0	0.6	8.6
13				0.8	0.1	4.2	0.3	4.4
14 <sup>†</sup>	5	52	1.4	0.7	0.1	4.0	0.4	4.7
15 <sup>‡</sup>				0.7	0.1	3.9	0.5	5.6
16		53		0.8	0.1	4.2	0.5	4.7
17		55		0.9	0.1	4.5	0.6	5.2
18		52	2.0	0.9	0.1	4.8	0.5	8.4

<sup>†</sup>sintered at 1260 °C

<sup>‡</sup>sintered at 1360 °C

It is evident that despite using the same machining parameters, surface roughness varies significantly for the different batches. To better illustrate this,  $R_z$  has been plotted against sintering temperature and compositional parameters in Figure 8-6.  $R_a$  shows the same trends as  $R_z$ . Its values were only included in Table 8-2 for comparison with other studies as it is a more widely used parameter. Maximum valley depth was included for comparison with fracture

origin sizes, although was not found useful due to a very small investigated portion of the surface and inability of the stylus to enter small cracks.

Surface roughness is related to ceramic wear and machining. Removal of brittle material is a complex process accompanied by elastic deformation, microscale plastic deformation, cracking and chipping [185]. The removal mechanism depends on fracture toughness, grain size, thermal conductivity, grinding wheel velocity, porosity and other factors. It is beyond the scope of this work to fully interpret the differences in surface roughness and additional tests such as scratch hardness would likely be necessary to do this effectively.

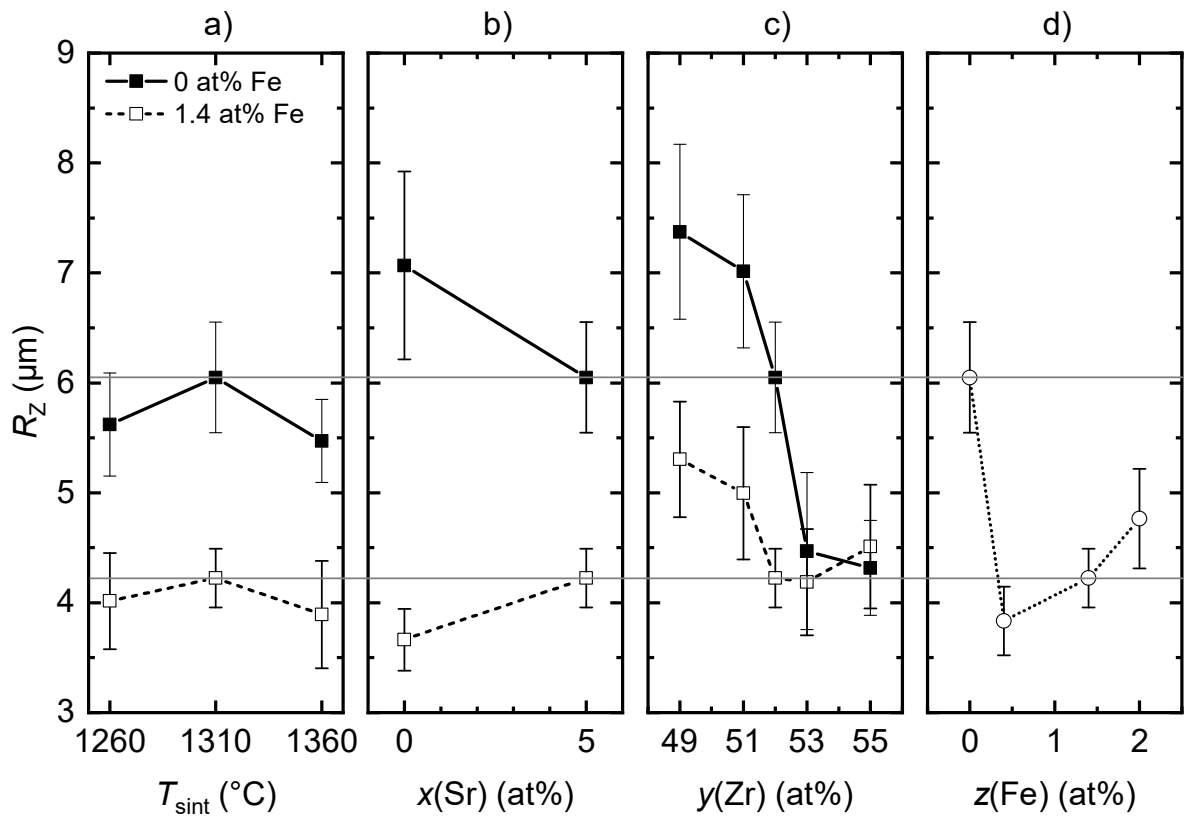


**Figure 8-6** Dependence of mean roughness depth  $R_z$  on a) sintering temperature ( $T_{\text{sint}}$ ), b) Sr content, c) Zr/Ti ratio, d) Fe content of  $(\text{Pb}_{1-x}\text{Sr}_x)(\text{Zr}_y\text{Ti}_{1-y})_{1-z}\text{Fe}_z\text{O}_3$ . Grey horizontal lines connect single central compositions, error bars represent SDM,  $T_{\text{sint}} = 1310$   $^{\circ}\text{C}$  if not stated otherwise.

The plotting of roughness values against various properties revealed an apparent correlation of surface roughness with Young's modulus, which is shown in Figure 8-7. Roughness generally increased with increasing Young's modulus and samples of higher average grain size (3.3–5.3  $\mu\text{m}$ ) showed higher surface roughness than finer-grained batches. Batch 1 (( $\text{Pb}_{0.95}\text{Sr}_{0.05}$ )( $\text{Zr}_{0.52}\text{Ti}_{0.48}$ ) $\text{O}_3$ ) showed a deviation from the general trend; batches 7 and 8 ( $y = 53$  and  $55$  at% in ( $\text{Pb}_{0.95}\text{Sr}_{0.05}$ )( $\text{Zr}_y\text{Ti}_{1-y}$ ) $\text{O}_3$ ) showed unexpectedly low roughness values, on the level of finer-grained samples. This will be revisited in the next section. Roughness values do not accurately represent the depth of surface damage due to the size of stylus and complex crack shapes. It may be expected however, that trends in surface roughness reflect trends in overall surface damage.

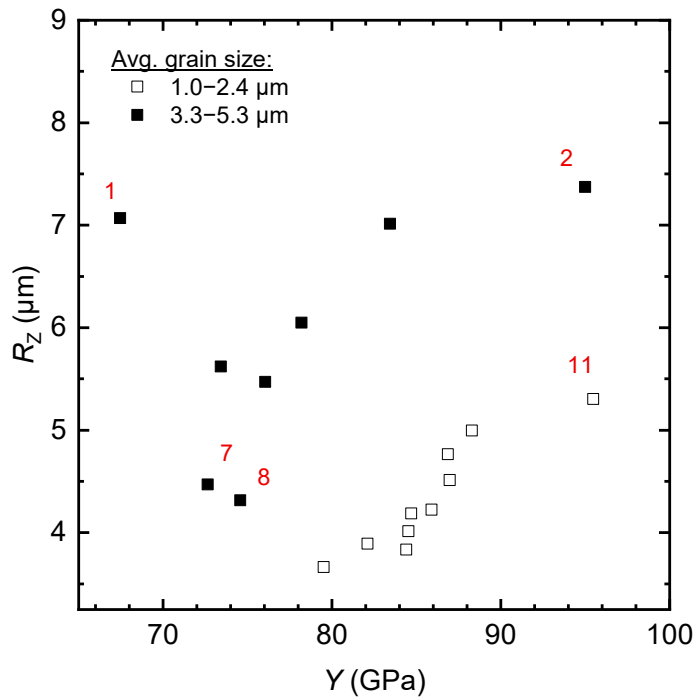


**Figure 8-7 Graph of mean roughness depth  $R_z$  plotted against Young's modulus  $Y$ . Numbered samples correspond to batch numbers in Table 8-2.**

## 8.4 Equibiaxial flexural strength

This section contains results of the main property of interest in this work, the equibiaxial flexural strength, as well as results from other related topics such as ferroelasticity and fractography. Over 800 specimens were tested, and an extensive amount of experimental data was generated. Attempts have been made to convey these results in a logical order and avoid repetition as much as possible. However, the complex relations between the various factors and properties has necessitated plotting some results more than once. When this was done, replotted results were always put in a new context or against a different variable.

Batch numbers rather than compositional descriptions are used in this chapter to improve the flow of the discussion. The full list of batch numbers and their respective labels, compositions and sintering temperatures can be found in Table 5-4 in section 5.2. Descriptions of composition or sintering temperature are still mentioned periodically, and they are usually apparent from the relevant figures.

The section is structured as follows: Section 8.4.1 presents test sequence plots, which assess the randomness and spread of strength data (both are related to the testing method). Section 8.4.2 shows strength histograms, and assesses their skewness, modality and presence of outliers. Section 8.4.3 introduces features found on the fracture surfaces of examined samples which is used in subsequent discussions.

Sections 8.4.4 to 8.4.7 discuss Weibull distribution fits, fractography, strength and reliability results for each factor of interest (sintering temperature, Sr content, Zr/Ti ratio and Fe content). The Weibull fit of strength data was performed in Origin software (Originlab) using the Maximum Likelihood Estimation method. Goodness-of-fit was assessed visually as well as using 2 statistical methods, the modified Kolmogorov-Smirnov (K-S) and Anderson-Darling

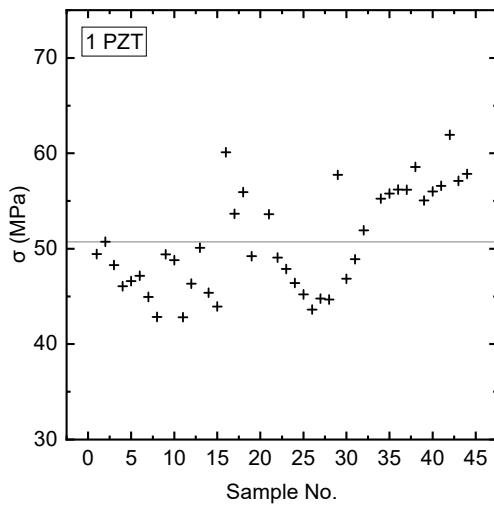
(A-D) tests. Algorithms of these tests are described in the software's online manual [186]. The modified K-S test did not reject Weibull distributions for any dataset ( $p > 0.1$ ). The A-D test, which gives more weight to distribution tails [187], found Weibull distributions unsuitable for some batches ( $p < 0.05$ ).  $p$  values of A-D tests will be reported and discussed in the relevant sections. The use of other statistical methods such as one- or two-way analysis of variance (ANOVA) was considered when evaluating data, but its use was debatable for some results, which did not comply with the assumptions for these methods. Also, using these methods to prove that 2 sets of data are significantly different was already achieved in the same manner with Weibull strength and its 95% confidence intervals (CI). The Weibull probability plots are not shown more than once as the assessment of the fit does not change when compared to other distributions. For this reason, central compositions (batches 4 and 13), which are part of all factor dependencies, have their Weibull distribution fits discussed only in section 8.4.4.

Section 8.4.8 shows strength results of commercial hard PZT material and compares it to the results of the prepared materials. Section 8.4.9 discusses the relevance of ferroelastic effects in this work. Finally, section 8.4.10 attempts to relate all the previously discussed strength results to other mechanical and physical properties studied in this work. It also discusses ways of improving strength and reliability and evaluates the testing method itself.

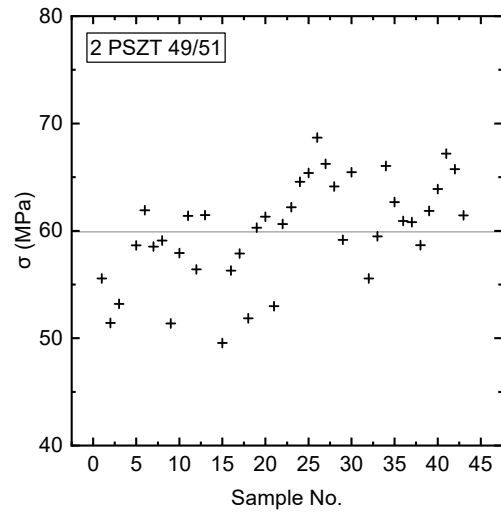
#### 8.4.1 Test sequence plots

Strength results obtained from the testing procedure described in section 4.2.4.2 were plotted against their sample number. Samples within each batch were tested in a sequence from number 1 upwards. The test sequence graphs help to reveal outliers as well as shifts in data location (noticeable shifts in local mean/median with the test number) or variation. Selected graphs are shown in Figure 8-8. Batch 6 in Figure 8-8 e) represents a test sequence with constant location and random scatter. Similar graphs were shown by most batches and can be found in Appendix

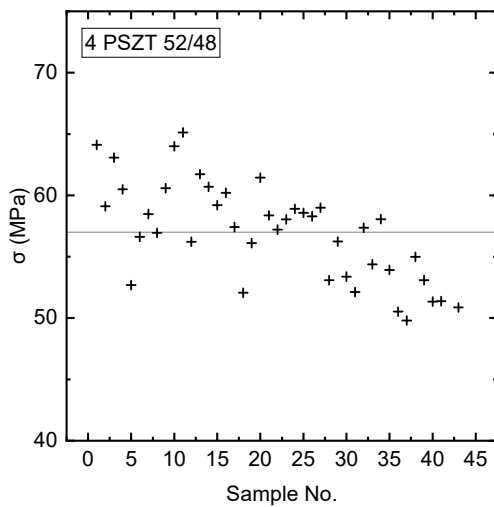
I. The Fe-doped samples showed a tendency for outliers, as illustrated by batch 9 in Figure 8-8 f). Batches 1, 2, 5 (Figure 8-8 a), b), d) respectively) exhibited a location shift from lower to higher strength values, while batch 4 (Figure 8-8 c)) exhibited the opposite behaviour. Any location shifts are clearly undesirable and indicate an issue with the testing method. Great effort has been made to identify all possible sources of bias for this method as described in chapter 4.2.4 and it is not clear what caused these location shifts. A hypothesis was formed after testing 1/3 of the batches.



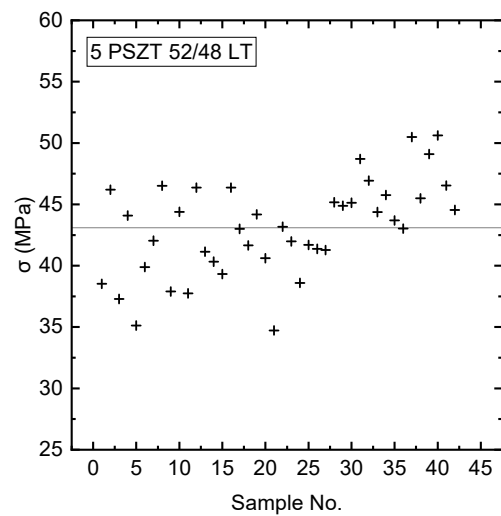
a)



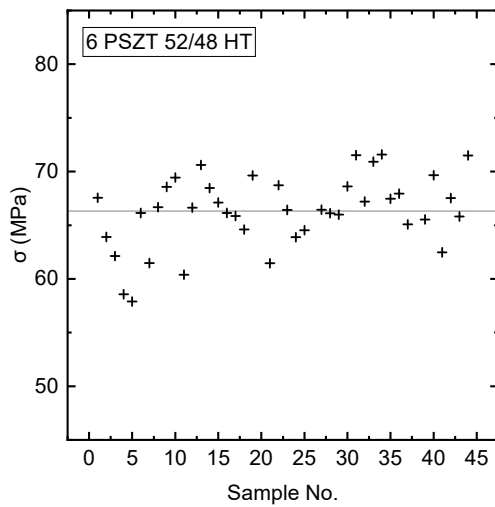
b)



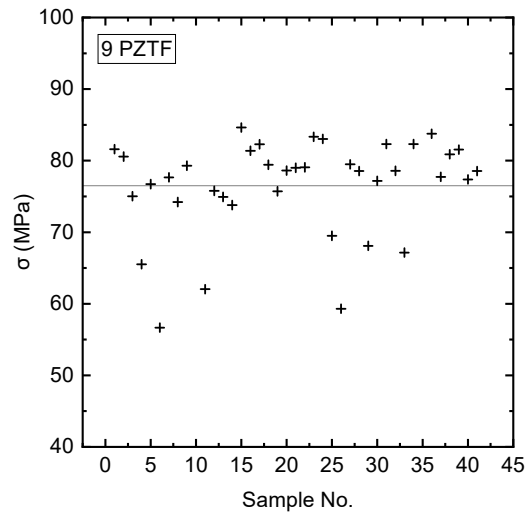
c)



d)



e)



f)

**Figure 8-8 Selected test sequence graphs. Horizontal grey lines represent mean strength values  $\sigma$ . Batches a) 1, b) 2, c) 4, d) 5 show location shifts; e) batch 6 represents a random scatter around the same location; f) batch 9 represents a batch with distinct outliers.**

The load (top) ring of the biaxial test fixture is held by 3 rubber “O” rings and seated on a bearing ball, which should eliminate any effects of non-parallelism of the samples. PTFE tape between the ring and the sample should reduce friction and allow the load ring to “slide” and tilt. However, the friction is not eliminated completely, and the tape is soft and plastic, causing the ring to indent it, which potentially makes it more difficult to slide/tilt further into an optimal position. If the load ring is tilted prior to the test, as illustrated in Figure 8-9 b), it creates a stress concentration in a certain portion of the sample until the correct ring position is reached (Figure 8-9 a). During this interval, the test sample may break at a lower recorded load.

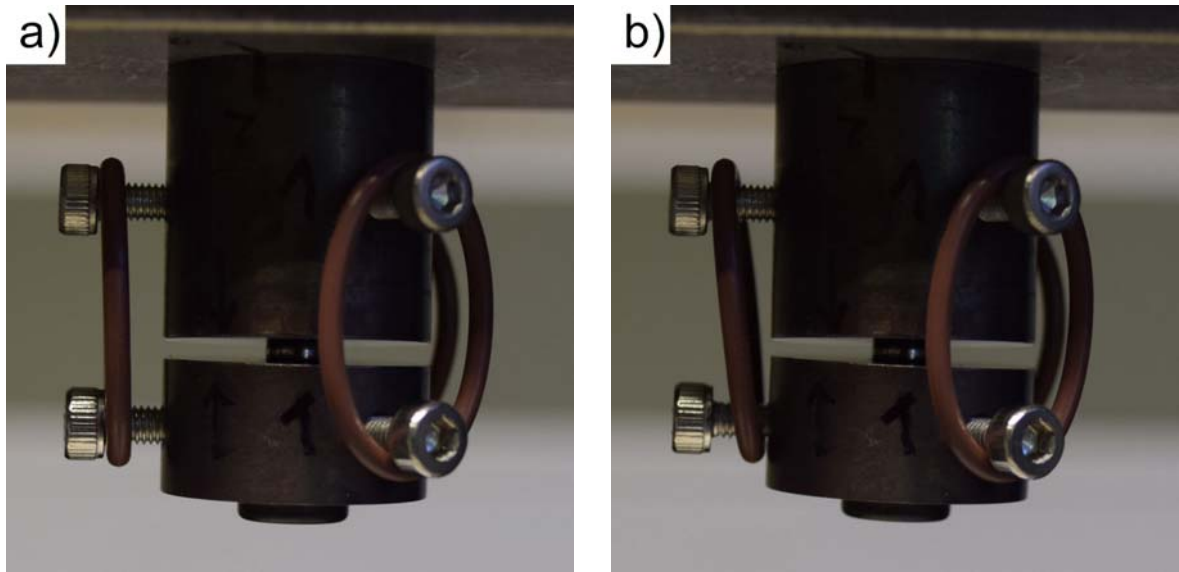


**Figure 8-9 Load ring a) parallel with support ring and with correctly attached rubber bands; b) tilted due to incorrect position of 1 rubber band.**

The load ring was removed, cleaned and checked for damage twice per test of each batch. The load ring can attain a tilt if one of the “O” rings is not positioned correctly. “O” rings can also move spontaneously right after fracture, when the ring tilts naturally with the broken fragments.

Although this hypothesis hasn’t been experimentally proven, the tilt of the load ring was visually checked after each sample when testing the remaining 2/3 of batches. None of the batches past number 5 show strength location shifts (batches were tested in their numbering order). If the hypothesis is correct, the “true” strength of batches 1, 2, 4, 5 should correspond to locations of higher strength in their respective graphs in Figure 8-8. This will be further considered in subsequent discussions. For any future tests, it is recommended to use soft springs instead of “O” rings and custom-made screws with machined location grooves to prevent the springs from spontaneous movement.

### 8.4.2 Histograms

To assess skewness, modality and the presence of outliers, the strength data of each batch were plotted in the form of histograms. Each dataset was divided into 6 bins of equal size, the bin size was dependent on the range of strength values. Each histogram was overlaid with a Weibull distribution curve to identify any potential deviations. An example of a histogram showing unimodal and slightly left skewed distribution is represented by batch number 8 in Figure 8-10. Only results deviating from this exemplary histogram will be discussed in the following paragraphs, the remaining histograms can be found in Appendix II.

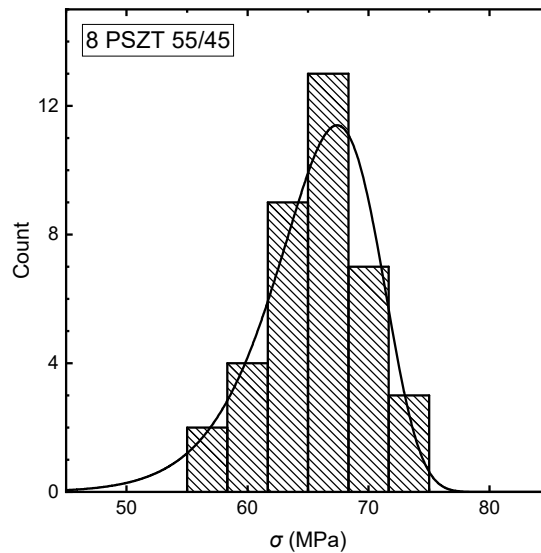


**Figure 8-10 Histogram of measured strength data of batch number 8 representing unimodal and slightly left skewed distribution. Histogram is overlaid by a Weibull distribution curve.**

Data from batches 1 and 3 are shown in Figure 8-11 a) and b) respectively and exhibit multimodal distributions. The test sequence graph of batch 1 revealed a location change, which is the likely cause of this behaviour. On the other hand, the test sequence graph of batch 3 did not show any location or variation shifts. More information will be gained from the Weibull distribution graphs and fractography presented and discussed later.

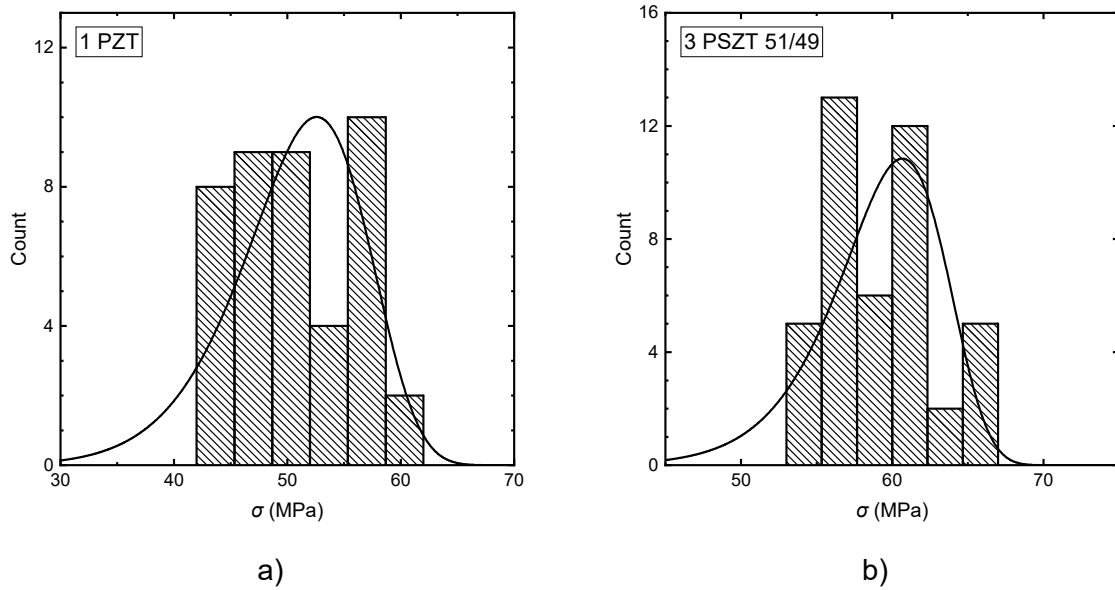
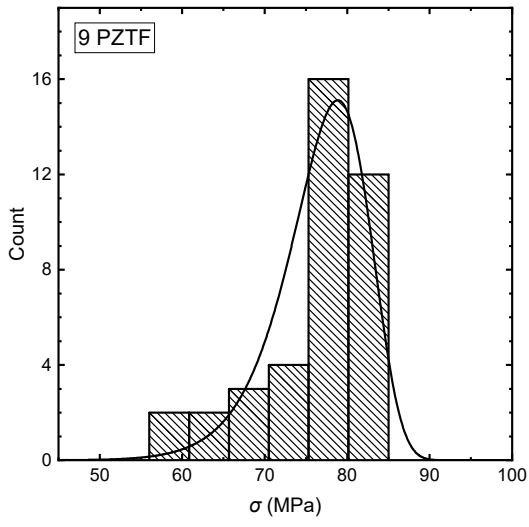
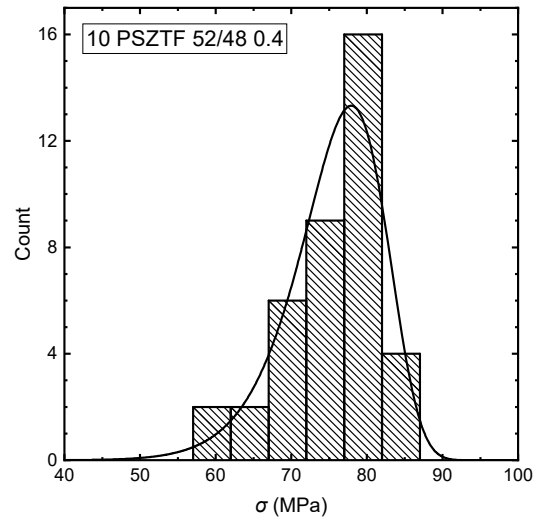


**Figure 8-11 Histograms of measured strength data of batches a) 1 and b) 3 showing multimodal distributions.**

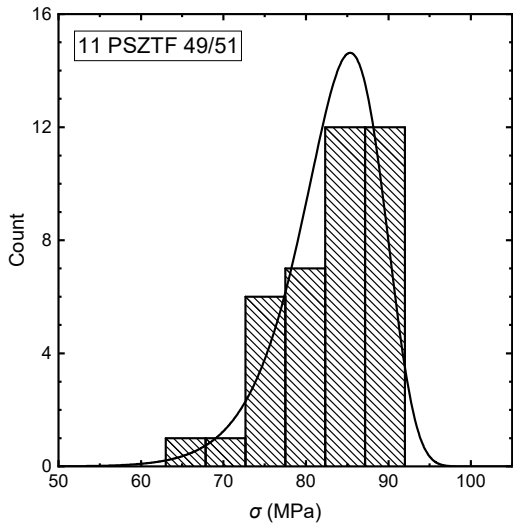
Most of the strength datasets exhibited left skewed distributions. In several cases, left skewed portions of histograms exceeded the frequency expected by a Weibull distribution. These batches are shown in Figure 8-12. The lowest strength data making up these portions of histograms can possibly be part of a different defect population. Again, more information will be gained from the Weibull distribution graphs, box plots and fractography presented and discussed below.



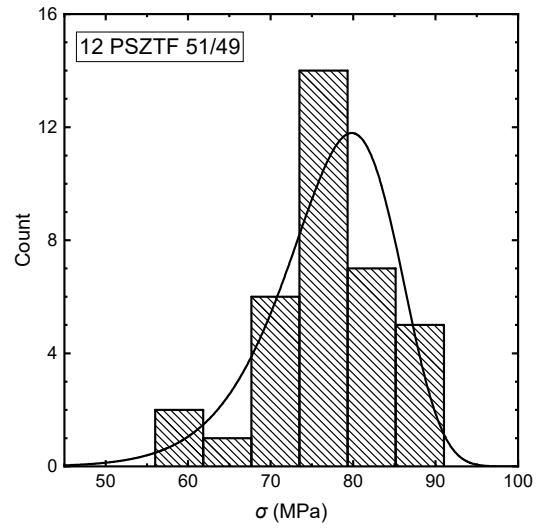
a)



b)



c)



d)

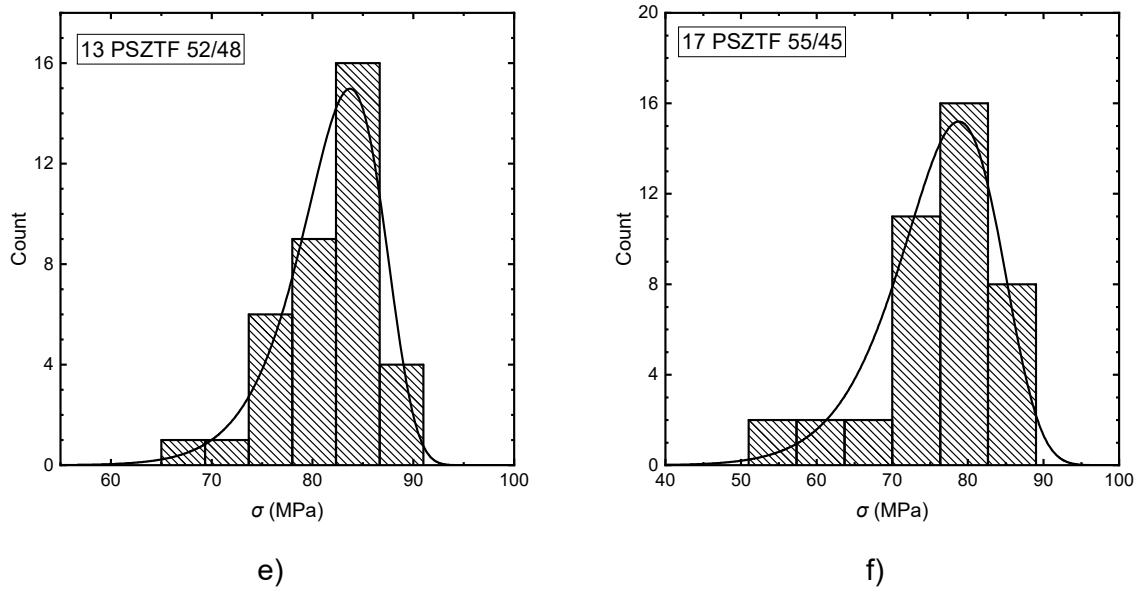


**Figure 8-12 Histograms of batch a) 9, b) 10, c) 11, d) 12, e) 13, f) 17, which exhibited excessively left skewed distributions of measured strength (relative to expected Weibull distributions).**

#### 8.4.3 Fractography

The fractographic practice and methods used in this work were described in section 4.2.4.3. This section provides an overview of the features found on the fracture surfaces of the samples tested in the biaxial test fixture, general remarks about the examination and limitations of the findings.

Each tested sample was first viewed at low magnifications with an optical microscope. In most cases, the location of the fracture origin could be successfully identified after examining crack branching patterns and features on the primary fracture plane. General features to be observed near the fracture origin are illustrated in Figure 8-13. In the case of PZT, the mist and mirror regions were not formed in most cases due to porosity and the relatively low strength of the material. Only hackle lines emanating outwards from the origin were present. Locating the origin was difficult in samples with higher porosity and where the fracture was not purely transgranular, as hackle lines were obscured by the roughness of the fracture surface.

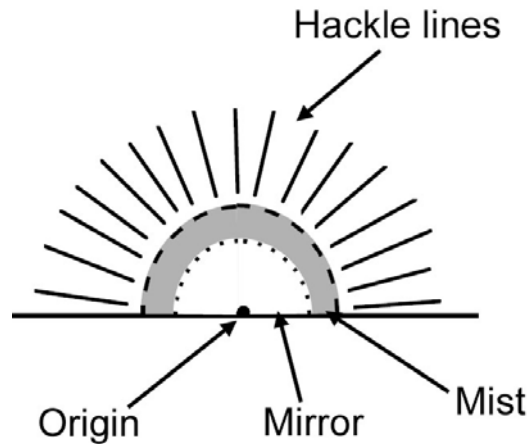


**Figure 8-13 General features near the fracture origin (reproduced from [120]).**

The identity of the fracture origin and its size could only be recognised using an SEM and not by optical microscopy, except for samples containing significant scratches on the surface, such as the one shown in Figure 8-14. If a significant scratch was present, it acted as a fracture origin and was followed by the primary plane of fracture (or a portion of it). Significant scratches were classified as handling damage and samples fractured from this origin were removed from the population as handling damage does not represent intrinsic material flaws or the typical machining damage. However, these rejected samples are still included in the tables of fracture origin investigation results.



**Figure 8-14 Example of a surface scratch acting as a fracture origin. The primary fracture plane clearly follows a portion of the scratch.**

Table 8-3 List of fracture origin identities

Fracture origin identity	Abbreviation	Flaw type <sup>†</sup>	Description
Agglomerate	A	Vol	cluster of grains, particles, platelets or whiskers
Pore	P	Vol	Discrete cavity or void
Porous region	PR	Vol	3-dimensional zone of (micro)porosity
Porous seam	PS	Vol	2-dimensional area of (micro)porosity
Handling damage	HD	Sur	Scratches, chips, cracks
Machining damage	MD	Sur	Scratches, chips, cracks created during machining process
Unidentified origin	?		

<sup>†</sup>Vol = volume, Sur = surface

A list of fracture identities found in this study is summarised in Table 8-3. Examples of all identities are shown in Figure 8-15 and Figure 8-16. Samples from the majority of batches showed a transgranular mode of fracture, represented in Figure 8-15 a), d) and Figure 8-16 a–d). In these cases, the fracture surfaces were smooth, hackle lines clearly visible and the fracture origin was easy to find. Samples from batches not containing Fe (with the exception of batch 6) showed a prevalent intergranular mode of fracture mixed with varying degree of transgranular

fracture. Examples of this fracture mode are shown in Figure 8-15 b) and c). Rough surface and the appearance of well-defined grain boundaries are typical for this mode. The roughness and higher porosity make finding the origin location more difficult. In several cases, the fracture origin could not be successfully identified.

Porosity was found to be one of the main origins of fracture. The following rules were followed when classifying porous origins: When a single pore or cavity was considered 3-dimensional, the origin was classified as a “pore” (Figure 8-15 a). Single and flat pores and cavities were classified as “porous seams” (Figure 8-15 b). Multiple connected smaller pores were classified as a “porous region”. An example is shown in Figure 8-15 c), where the surface shows signs of machining damage. A random porous seam, which probably did not influence the fracture, is also located nearby. Figure 8-15 d) shows an agglomerate – a cluster of grains surrounded by porosity.

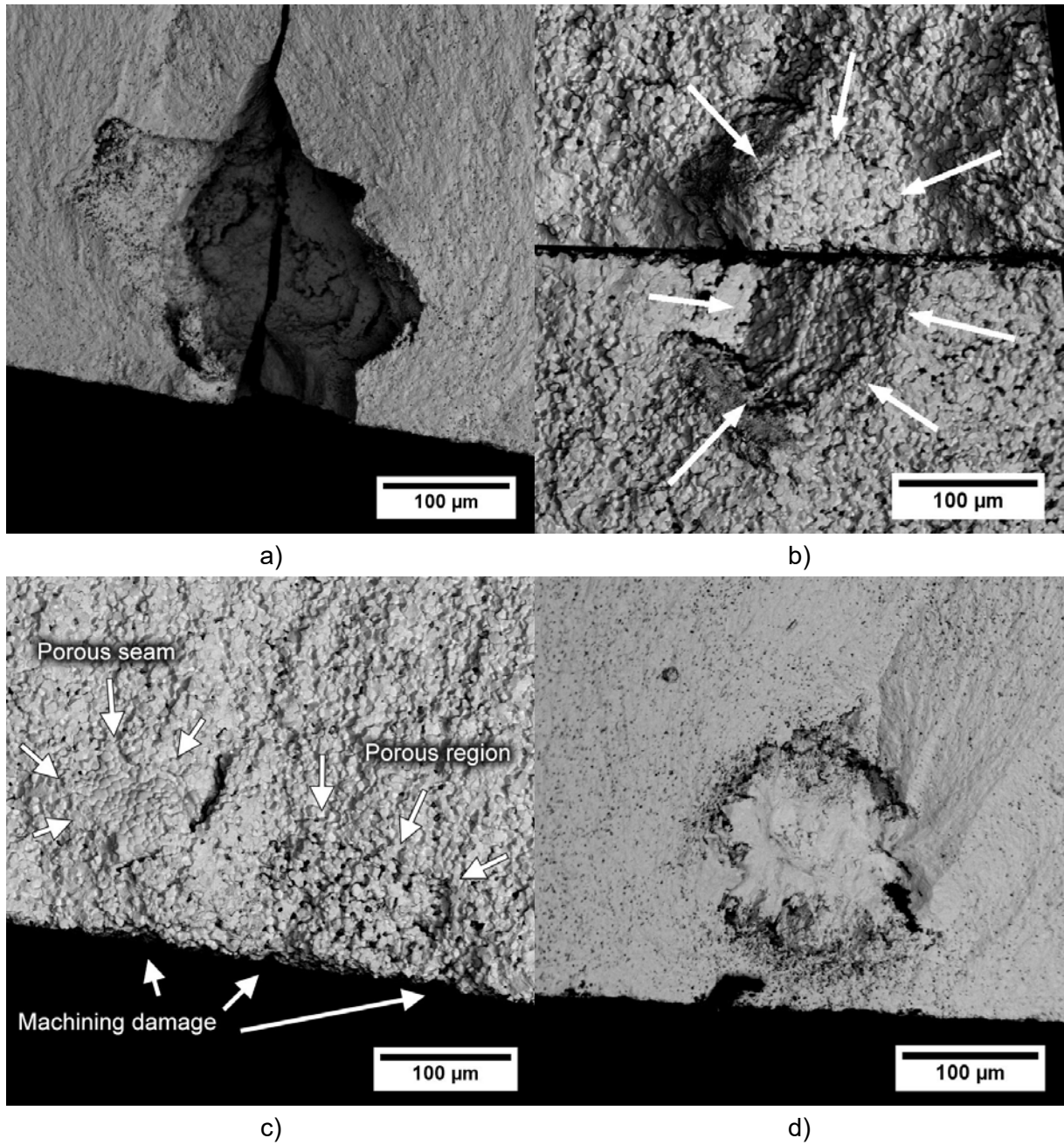


**Figure 8-15 SEM micrographs of various forms of porosity acting as a fracture origin: a) pore (3-dimensional feature), b) porous seam (2-dimensional feature), c) porous region acting as a fracture origin mixed with machining damage, d) agglomerate.**

Surface damage induced by the standard industrial machining process was the second most common fracture origin. Machining damage as a flaw is usually elongated, hackle lines do not have common focus point and chips are often present as machining induces formation of cracks [120]. Typical machining damage is shown in Figure 8-16 a). Porous regions get naturally more

damaged by machining. When machining damage was found directly in/by a porous region/pore, the latter was considered as the fracture origin. For example, the fracture origins in Figure 8-15 c) and Figure 8-16 c) were classified as porous region and porous seam respectively. In some cases, a porous region was present near a damaged surface, but its involvement was unclear, as illustrated in Figure 8-16 b). Machining damage was considered as the fracture origin in this case. The micrograph in Figure 8-16 d) shows an area near the fracture origin. The upper half does not reveal the fracture origin and the lower half has a significant portion chipped off. In this case, the fracture origin could not be identified as the chip, which is quite sizeable, may have contained an origin other than the observed machining damage. The fracture origin was also often not found in more porous samples showing intergranular fracture.

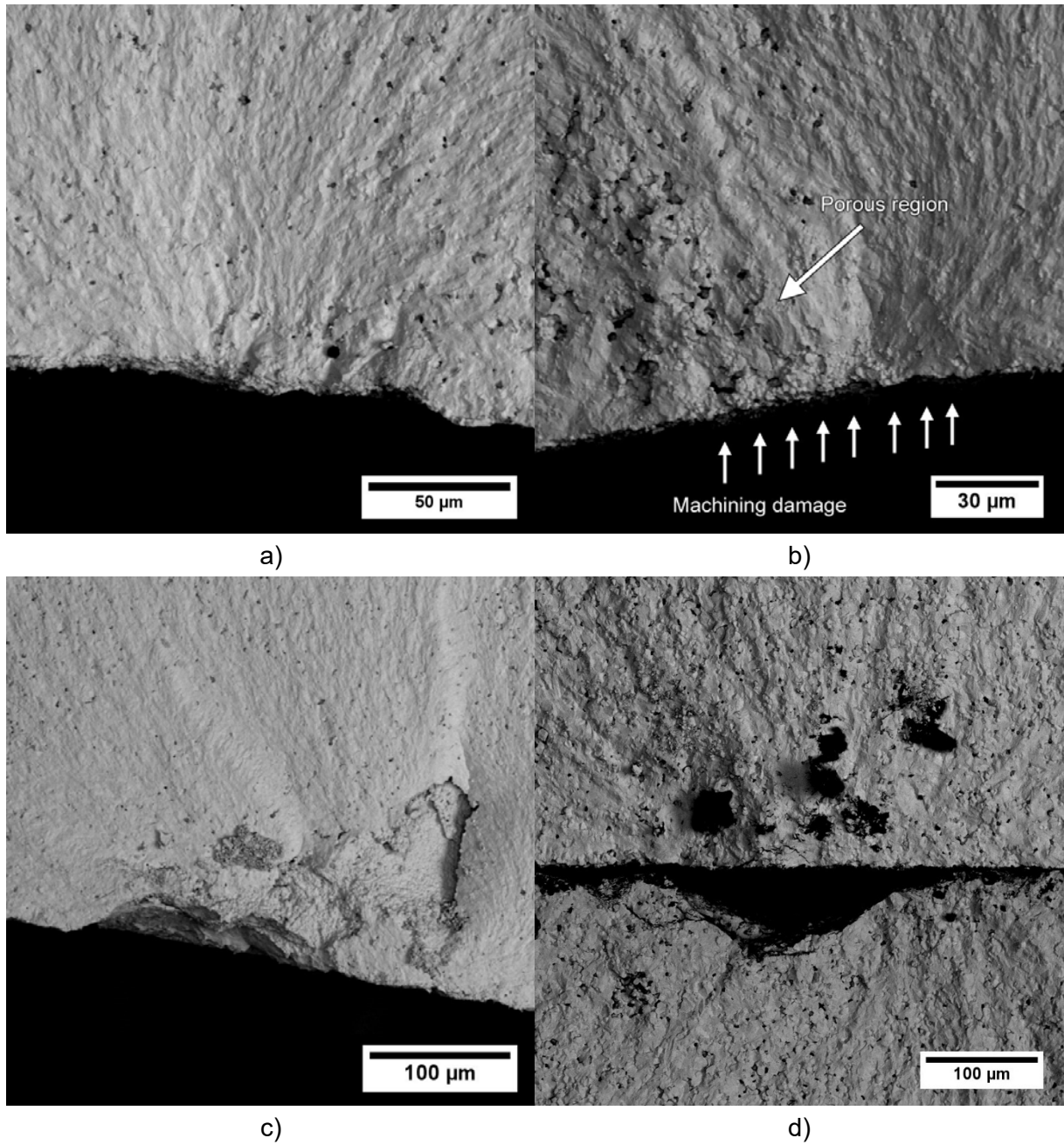


**Figure 8-16 SEM micrographs of fracture origins with different forms of surface damage: a) regular machining damage with no extra features, b) machining damage with an adjacent porous region, c) porous seam which likely caused chipping after fracture, d) unknown origin, possibly located in the missing piece. Dark spots on the upper half are organic contamination.**

Microstructural flaws in as-sintered pieces are either part of the material's surface or volume (denoted as "flaw type" in Table 8-3). When a ceramic piece is machined, volume-type flaws such as porosity can be found on the surface. Whenever the flaw location is discussed in this work, it refers to its position relative to the machined surface. With a few exceptions, mentioned

at the appropriate places, all fracture initiating flaws in this work were located on the tensile surface of tested samples and not in the volume.

The approximate sizes of the fracture origins were measured from the micrographs as the longest distance between the origin edges on a single line, also known as the Feret diameter. An example is shown in Figure 8-17. All size measurements should be interpreted with caution, as origin shapes were usually not simple, equidistant or fully visible. Size was not estimated for poorly defined origins such as some machining damage or porous regions in porous samples.

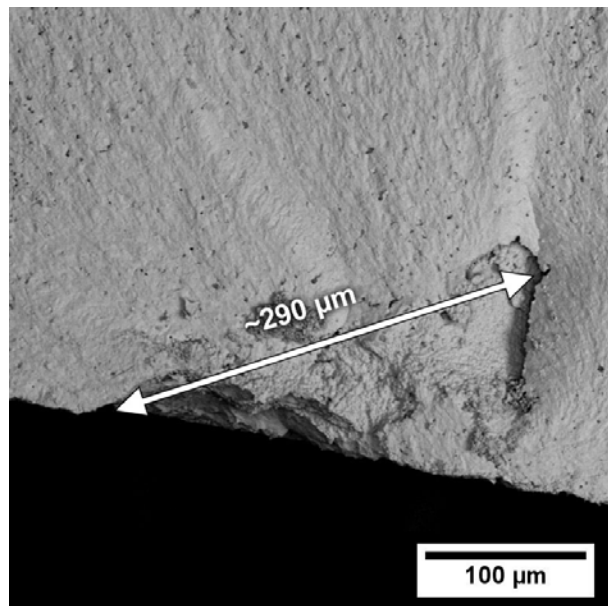
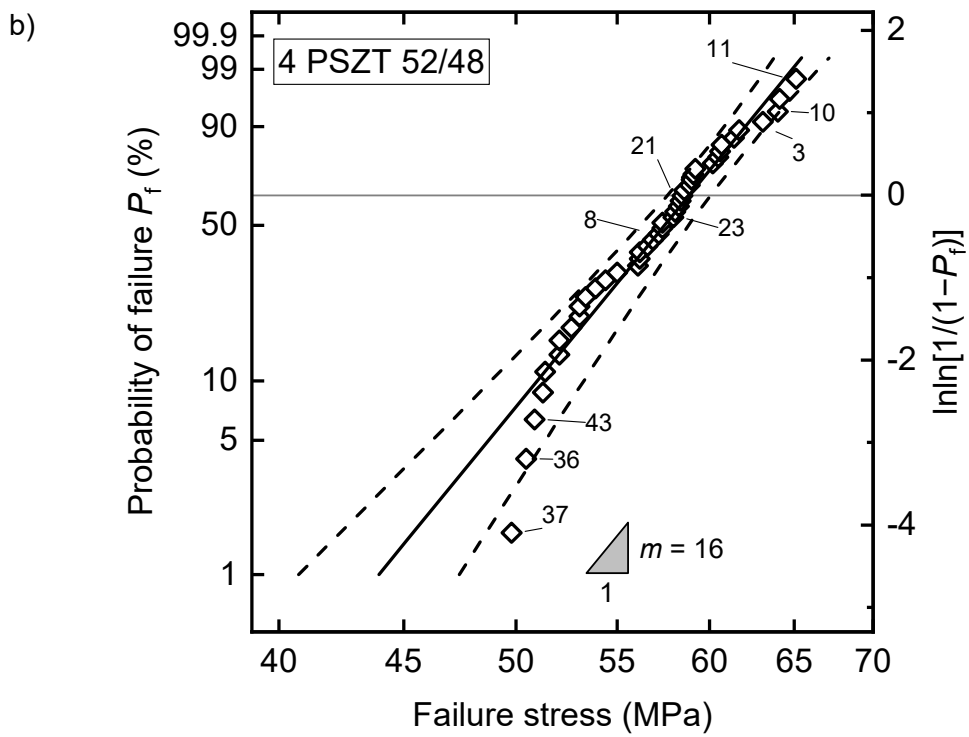
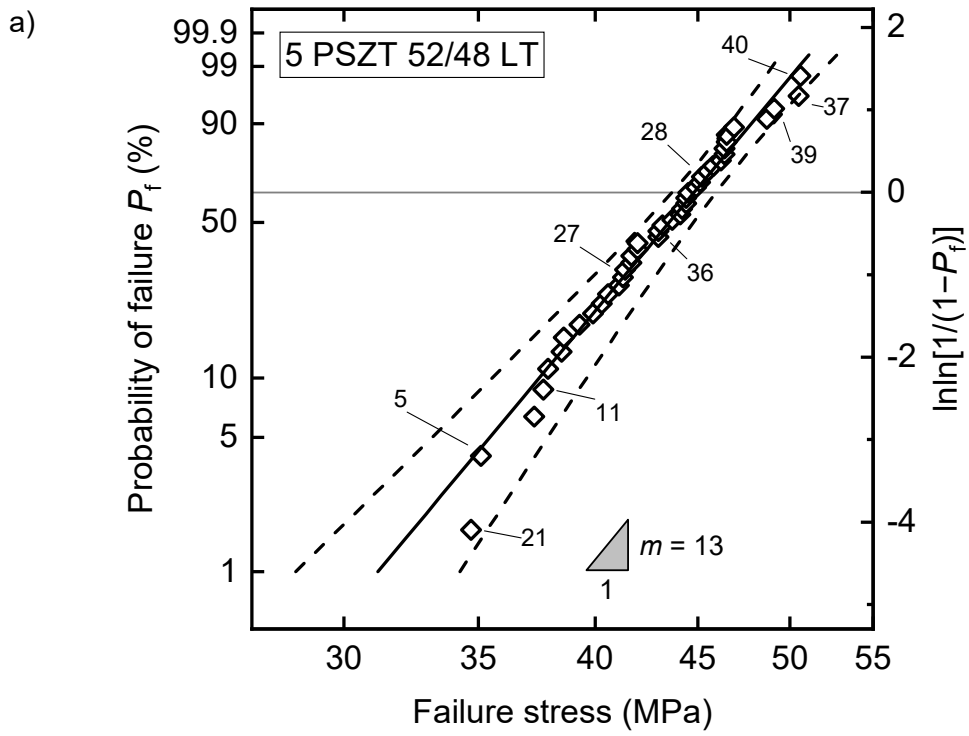


**Figure 8-17 Example of a fracture origin size measurement.**

#### 8.4.4 Sintering temperature dependence

##### 8.4.4.1 Probability distributions and fractography (0 at% Fe)

Probability plots containing the Weibull distribution fits of the biaxial strengths of  $(\text{Pb}_{0.95}\text{Sr}_{0.05})(\text{Zr}_{0.52}\text{Ti}_{0.48})\text{O}_3$  (0 at% Fe) samples sintered at different temperatures are shown in Figure 8-18. Data from all 3 batches seem to fit the distribution well as supported by the A-D test ( $p \geq 0.25$ ). Data from batch number 4 ( $T_{\text{sint}} = 1310 \text{ }^\circ\text{C}$ ) deviate from the fit at lower failure stresses. It is important to distinguish if the data show a left or right deviation relative to the predicted Weibull line. A left side deviation signifies data from samples which failed at a lower stress than statistically predicted and indicates the possible presence of a second flaw population with a lower  $m$  value (Weibull modulus/slope). An example of a material with 2 competing flaw populations is shown in Figure 8-19 a). The weakest flaw is always the source of failure, therefore for low strengths, the material will fail from flaws contained in the population with a lower  $m$  value, whereas for high strengths failure will be from flaws in the population with a high  $m$  value. When a right-side deviation is observed, as in the case of batch 4, it means that specimens with the lowest strength failed at higher stresses than predicted by the Weibull distribution. Such behaviour was discovered in several batches and will be discussed in the following paragraphs.



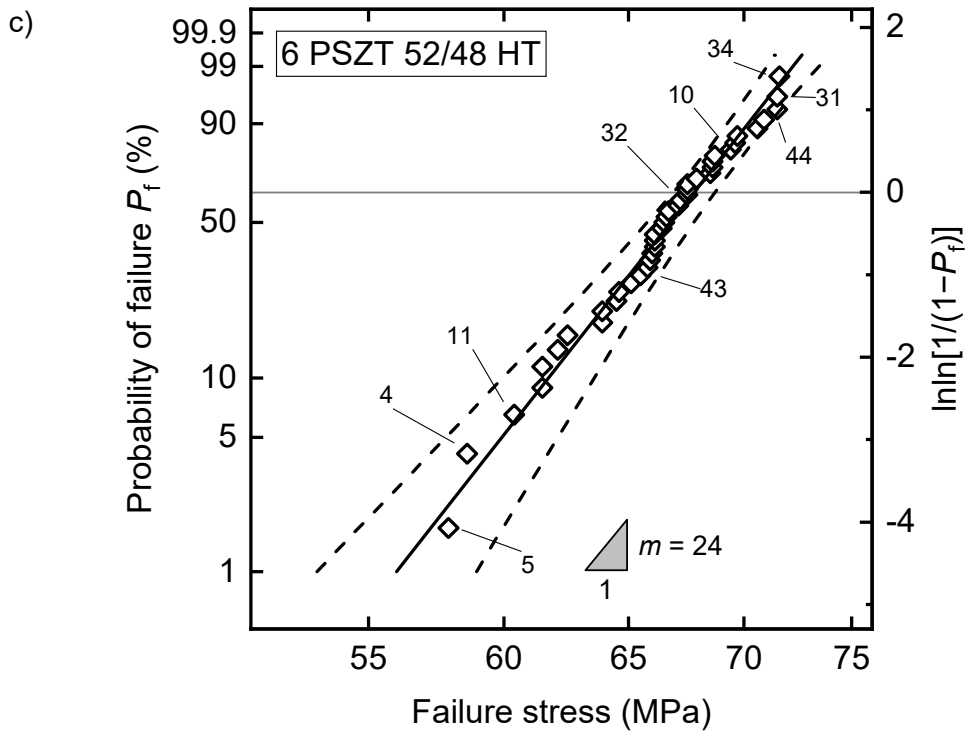


**Figure 8-18 Probability plots with Weibull distribution fits of  $(\text{Pb}_{0.95}\text{Sr}_{0.05})(\text{Zr}_{0.52}\text{Ti}_{0.48})\text{O}_3$  sintered at a) 1260 °C, b) 1310 °C, c) 1360 °C. Dashed lines represent 95% CI, marked samples had their fracture surface examined using SEM.**

**Table 8-4 Results of A-D tests and fracture origin investigations of  $(\text{Pb}_{0.95}\text{Sr}_{0.05})(\text{Zr}_{0.52}\text{Ti}_{0.48})\text{O}_3$  sintered at different temperatures.**

<b>5 PSZT 52/48 LT</b> ( $T_{\text{sint}} = 1260 \text{ °C}$ )			<b>4 PSZT 52/48</b> ( $T_{\text{sint}} = 1310 \text{ °C}$ )			<b>6 PSZT 52/48 HT</b> ( $T_{\text{sint}} = 1360 \text{ °C}$ )		
<b>Mode: intergranular</b>			<b>Mode: intergranular</b>			<b>Mode: transgranular</b>		
$p(\text{A-D})^\dagger \geq 0.25$			$p(\text{A-D})^\dagger \geq 0.25$			$p(\text{A-D})^\dagger \geq 0.25$		
Sample no.	Identity	Approx. size ( $\mu\text{m}$ )	Sample no.	Identity	Approx. size ( $\mu\text{m}$ )	Sample no.	Identity	Approx. size ( $\mu\text{m}$ )
21	?	?	37	PR	?	5	PS	?
5	PR	?	36	PR	?	4	P	400–500
11	PR	?	43	PR	?	11	PS	400
27	?	?	8	PS	100	43	PR	100–200
36	?	?	23	PR	?	32	PR	?
28	PR	100	21	PR	?	10	PR	100–150
39	?	?	3	PR	50–100	44	PR	150–200
37	PR	?	10	PR	100	31	PR	150–200
40	PR	100	11	PR	100	34	PR	50–100

Key: A = agglomerate, P = pore, PR = porous region, PS = porous seam, HD = handling damage, MD = machining damage, ? = unknown

$\dagger p$  value of Anderson-Darling goodness-of-fit test

The presence of a second flaw population with higher  $m$  value failing at lower stress would be theoretically possible under certain conditions. However, fractography of 9 specimens from batch 4 showed that the fracture origins of weakest samples did not significantly differ from the rest, making the presence of a second flaw population unlikely.

It is possible that the presence of a second flaw population cannot be recognised from the fit due to limits of the applicability of the Weibull distribution to small datasets, which was discussed in detail by Danzer et al. [13]. Small datasets reveal only a portion of the entire critical flaw populations (the grey area in Figure 8-19 a) and different flaw populations may be active in samples of different volumes. The 40 specimens per batch used in this work are more than that recommended by the ASTM C1499-15 standard, however, it still may not be enough to reveal competing flaw populations, especially if they have similar Weibull parameters. Sample volume is not an issue in this work as the goal is to only compare similar-sized specimens.

Other reason for a right-side deviation at low strengths can be the presence of R-curve behaviour (increasing or decreasing fracture toughness with crack length described as “rising” or “falling” R-curve respectively). If material exhibits a rising R-curve, larger cracks may fail at higher applied stress intensity factors [14]. PZT is known to exhibit rising R-curve behaviour [188], however, the available flexural strength data from previous work fitted to Weibull distributions do not show significant right-side deviations [87, 89, 90, 189-191].

Danzer et al. [13] suggested that internal stresses in the specimens can also cause presence of a threshold stress for failure. If that was the case, it would be expected to see this effect in the majority of batches as they all underwent the same treatment. On the contrary, a right-side deviation was only found in batches 1, 3, 4, 7 and 14.

The last explanation is that some of the right-deviating flaw populations simply show a better fit to the three-parameter Weibull distribution, which was originally suggested by Weibull and which is also used in practice [192]. The three-parameter Weibull distribution introduces a threshold stress  $\sigma_u$ , below which the failure does not occur:

$$P = 1 - \exp \left[ - \left( \frac{\sigma - \sigma_u}{\sigma_0} \right)^m \right]. \quad (8-2)$$

The fit of batch 4 strength data to the three-parameter Weibull distribution is shown in Figure 8-19 b). The fit is better, but not perfect, which can be possibly related to the issue with testing procedure and decreasing trend of strength with test number discussed in chapter 8.4.1. In the rest of this work, Weibull distributions will refer to the 2-parameter version unless specified otherwise.

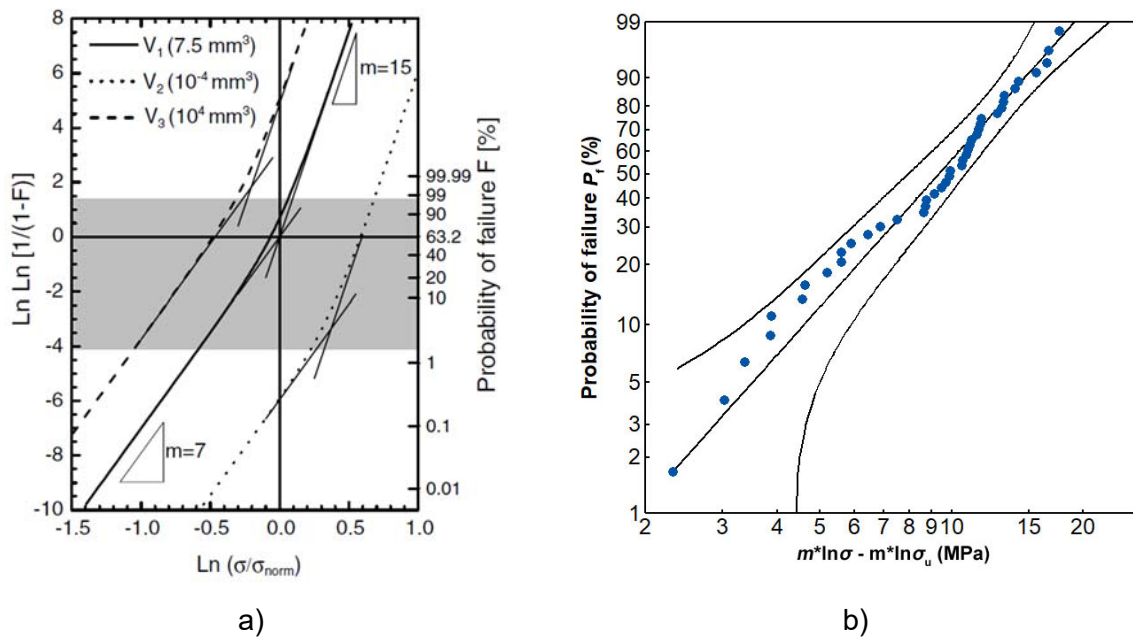


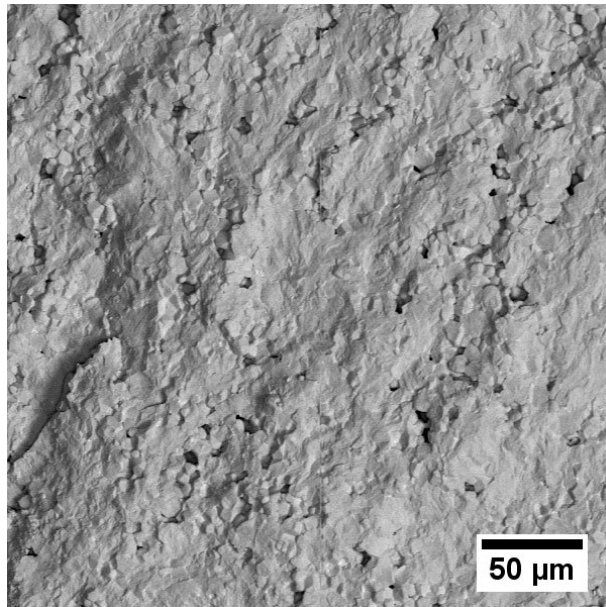
**Figure 8-19 a) Failure stress probability (signified as F instead of  $P_f$  in this figure) distribution of a model material containing both volume ( $m = 15$ ) and surface ( $m = 7$ ) defects. Grey area illustrates the portion of the distribution revealed by testing 30 specimens,  $V_1$ – $V_3$  show specimen volume. Graph reproduced from an article by Danzer et al. [13]; b) Fit of  $(\text{Pb}_{0.95}\text{Sr}_{0.05})(\text{Zr}_{0.52}\text{Ti}_{0.48})\text{O}_3$  (batch 4) to a 3-parameter Weibull distribution.**

The fracture mode was mainly identified as intergranular in batches 5 and 4 ( $T_{\text{sint}} = 1260\text{ }^{\circ}\text{C}$ ,  $1310\text{ }^{\circ}\text{C}$  respectively) and changed to transgranular in batch 6 sintered at  $1360\text{ }^{\circ}\text{C}$ . This is reflected in the micrographs shown in Figure 8-20. An increase in grain size with sintering temperature and a higher porosity in batch 5 are also evident. Porosity was the prevalent fracture origin in all these batches. The results presented in Table 8-4 suggest that batch 6 ( $T_{\text{sint}} = 1360\text{ }^{\circ}\text{C}$ ) contained larger defects than the other 2 batches. Pore size generally increases with grain size and it has been shown in section 6.4 that the fraction of larger-sized porosity increased at  $1360\text{ }^{\circ}\text{C}$ . It should be noted that the size of most flaws in batches 4 and 5 could not be estimated due to the intergranular fracture mode and high level of porosity.



a) 5 PSZT 52/48 LT (1260 °C)

b) 4 PSZT 52/48 (1310 °C)

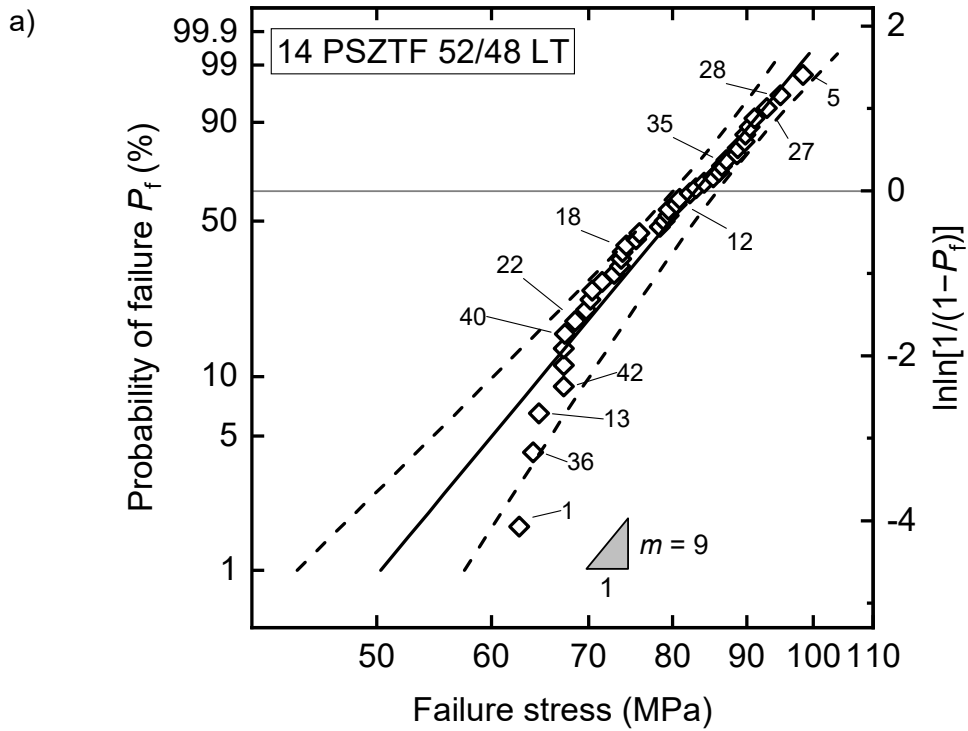


c) 6 PSZT 52/48 HT (1360 °C)

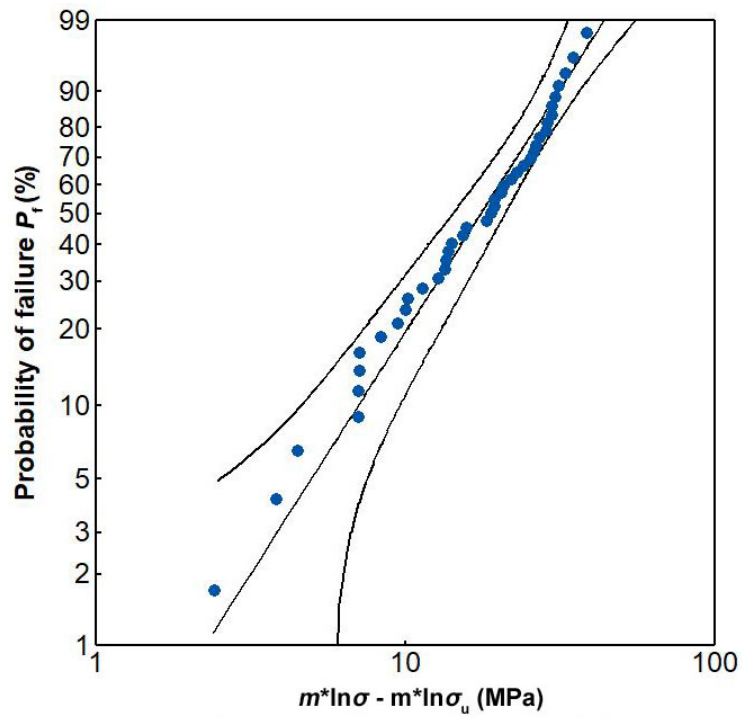
**Figure 8-20 Representative SEM fracture surface micrographs of batches a) 5, b) 4, c) 6.**

#### 8.4.4.2 Probability distributions and fractography (1.4 at% Fe)

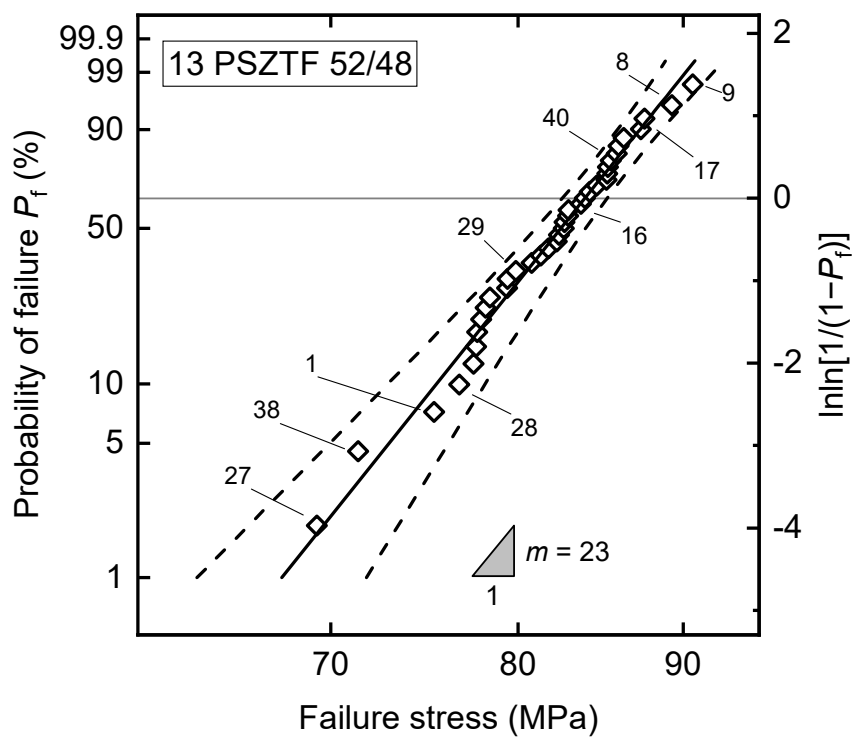
Failure probability plots of samples from batches 13–15 ( $(\text{Pb}_{0.95}\text{Sr}_{0.05})(\text{Zr}_{0.52}\text{Ti}_{0.48})_{0.986}\text{Fe}_{0.014}\text{O}_3$  sintered at different temperatures) are shown in Figure 8-21. Batches 13 and 15 show a good fit to the Weibull distribution, while batch 14 deviates from it at low fracture strengths. Deviation of batch 14 is similar to the deviation of batch 4 (Figure 8-18 b)) and the 3-parameter Weibull distribution provides a better fit as shown in Figure 8-21 b). The A-D test did not reject the Weibull distribution for any of the three batches ( $p > 0.05$ ).



b)



c)



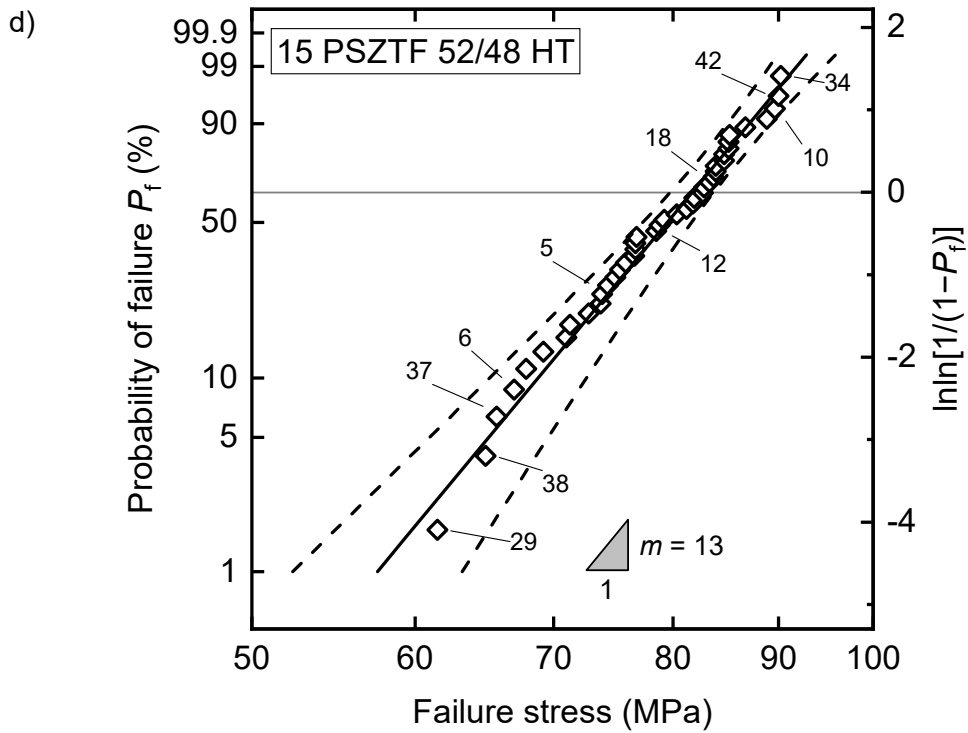


**Figure 8-21 Probability plots with 2-parameter Weibull distribution fits of  $(\text{Pb}_{0.95}\text{Sr}_{0.05})(\text{Zr}_{0.52}\text{Ti}_{0.48})_{0.986}\text{Fe}_{0.014}\text{O}_3$  sintered at a) 1260 °C, c) 1310 °C, d) 1360 °C. Dashed lines represent 95% CI, marked samples had their fracture surface examined using SEM; b) 3-parameter Weibull distribution fit of batch 14 sintered at 1260 °C.**

Table 8-5 Results of A-D tests and fracture origin investigations of  $(\text{Pb}_{0.95}\text{Sr}_{0.05})(\text{Zr}_{0.52}\text{Ti}_{0.48})_{0.986}\text{Fe}_{0.014}\text{O}_3$  sintered at different temperatures.

<b>14 PSZTF 52/48 LT</b> ( $T_{\text{sint}} = 1260\text{ }^{\circ}\text{C}$ ) Mode: transgranular $p(\text{A-D})^{\dagger} = 0.18$			<b>13 PSZTF 52/48</b> ( $T_{\text{sint}} = 1310\text{ }^{\circ}\text{C}$ ) Mode: transgranular $p(\text{A-D})^{\dagger} \geq 0.25$			<b>15 PSZTF 52/48 HT</b> ( $T_{\text{sint}} = 1360\text{ }^{\circ}\text{C}$ ) Mode: transgranular $p(\text{A-D})^{\dagger} \geq 0.25$		
Sample no.	Identity	Approx. size ( $\mu\text{m}$ )	Sample no.	Identity	Approx. size ( $\mu\text{m}$ )	Sample no.	Identity	Approx. size ( $\mu\text{m}$ )
1	P	280	3	HD		29	PR	140
36	PR	250	27	PS	280	38	PR	260
13	A (V) <sup>‡</sup>	150–170	38	MD	?	37	PR	240
42	PR	200	1	MD	100–130	6	PS	100–200
40	PR (V) <sup>‡</sup>	430	28	MD	?	5	PR (V) <sup>‡</sup>	140
22	PR	220	29	MD	?	12	PR	120–220
18	PS	150	16	MD	150	18	?	?
12	?	?	40	PS	100	10	A (V) <sup>‡</sup>	220
35	MD	80–120	17	MD	?	42	PR	?
27	MD	80	8	MD	?	34	MD	?
28	MD	100	9	MD	?			
5	MD	?						

Key: A = agglomerate, P = pore, PR = porous region, PS = porous seam, HD = handling damage, MD = machining damage, ? = unknown

<sup>†</sup>p value of Anderson-Darling goodness-of-fit test

<sup>‡</sup>flaw located within the volume of the sample and not on the surface

A transgranular fracture mode was dominant in all 3 batches. Batch 14, sintered at the lowest temperature of 1260 °C, had both porosity and machining damage acting as critical flaws. Surface and intrinsic volume flaws often form 2 distinct flaw populations and are distinguishable on Weibull plots. No multiple flaw populations can be recognised in Figure 8-21 a), which may imply that these 2 populations are similar in their Weibull parameters and can be only distinguished by a full fractographical analysis, which was not done in this work.

Batch 13 failed primarily from machining damage. This can be linked to a decrease in porosity after the sintering temperature was raised to 1310 °C. Sintering at 1360 °C increased grain size as well as the fraction of larger pores. This led to a change of fracture origin back to porosity

as larger pores and their clusters became more severe flaws than the machining damage. This agrees with the observed changes in pore size distributions presented in section 6.4.

#### 8.4.4.3 Weibull strength and reliability

Figure 8-22 shows boxplots of the strength data of samples from batches 4, 5, 6, 13, 14 and 15 discussed in the previous sections. It can be seen that except for batch 6, all the strength results were within the  $1.5 \times$  interquartile range. Batch 6 exhibits 2 outliers. Neither fractography nor the Weibull fit revealed any significant difference in these specimens from the rest of the population. Batch 14 shows a significantly wider distribution than any other batch.

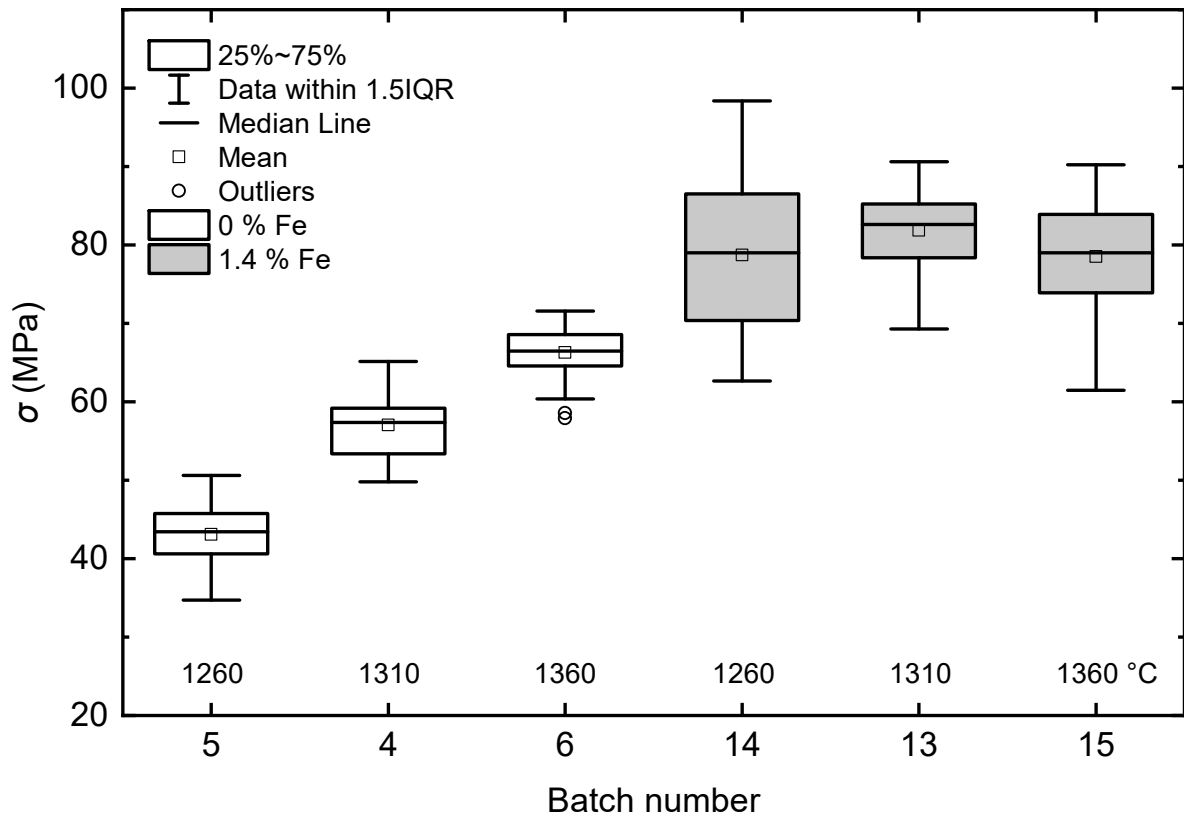


**Figure 8-22 Strength box plots of all batches in the sintering temperature series.**

$(\text{Pb}_{0.95}\text{Sr}_{0.05})(\text{Zr}_{0.52}\text{Ti}_{0.48})\text{O}_3$  (batches 4–6) clearly shows an increasing trend in strength with increasing sintering temperature. The same conclusion can be drawn from the plot of Weibull scale factors presented in Figure 8-23.

The increase in strength of PSZT from 44.8 to 58.9 MPa for samples sintered at 1260 °C and 1310 °C can be attributed to the 1% decrease in porosity and 5 GPa increase in Young's modulus in line with their general dependencies [193]. The sizes of the fracture origins are not defined well enough to draw conclusions based on their size. Biswas [23] introduced spherical pores to PZT by burning out spherical beads of organic material. His experiments showed that strength of PZT decreased with increasing overall porosity despite all the fracture origins being of a similar size. This suggests that batch number 4 would show higher strength values even if failure-causing porous regions of batches 5 and 4 were of a similar size. The grain size increased with increasing sintering temperature, however, it is likely not responsible for any strength changes since the average values of grain size are significantly lower than the fracture origin size. It has been shown that in cases where pore size significantly exceeds the grain size, the strength of ceramics is less sensitive to the latter [24].

Increasing the sintering temperature to 1360 °C further increased the strength of PSZT to 67.8 MPa. The change was accompanied with a slight increase (<0.5 %) in porosity and increase in average grain size from 4 to 5 µm. The fracture origin size either increased or was at least on a similar scale to batch 4. Neither hardness nor elastic modulus showed a significant variation. The only observation possibly explaining this behaviour was the change in fracture mode from inter- to transgranular, which will be discussed in the general discussion in section 8.4.10.

For Fe-doped batches 14, 13 and 15, increasing the sintering temperature did not significantly affect the Weibull strength, as shown in Figure 8-23. An increase from 1260 to 1310 °C did not affect the grain size, and only increased density by approximately 1–2 % (batch 14 showed a high standard deviation). According to the previous discussion, an increase in density should result in an increase in strength, but this was not observed. In fact, the strongest specimens from batch 14 (sintered at 1260 °C) showed a higher strength than specimens from batch 13 (sintered

at 1310 °C) as is apparent from Figure 8-22. It is possible that the strongest specimens from batch 14 had their surface less damaged by machining, however that is difficult to prove as the fracture origin of strongest samples from batch 13 could not be determined and both batches show similar roughness values.

An increase in sintering temperature to 1360 °C results in a 1% decrease in relative density, an increase in grain size of 0.7 μm and an increase in the average pore size. This is reflected in the dominant fracture origin shifting from machining damage to porosity. Due to an apparent increase in fracture origin size, batch 15 would be expected to exhibit lower Weibull strength than batch 13, but this was not observed. It may be concluded, therefore, that the strength dependence on microstructural properties is different when Fe is present and appears to be relatively insensitive to sintering temperature within the range used in this work.

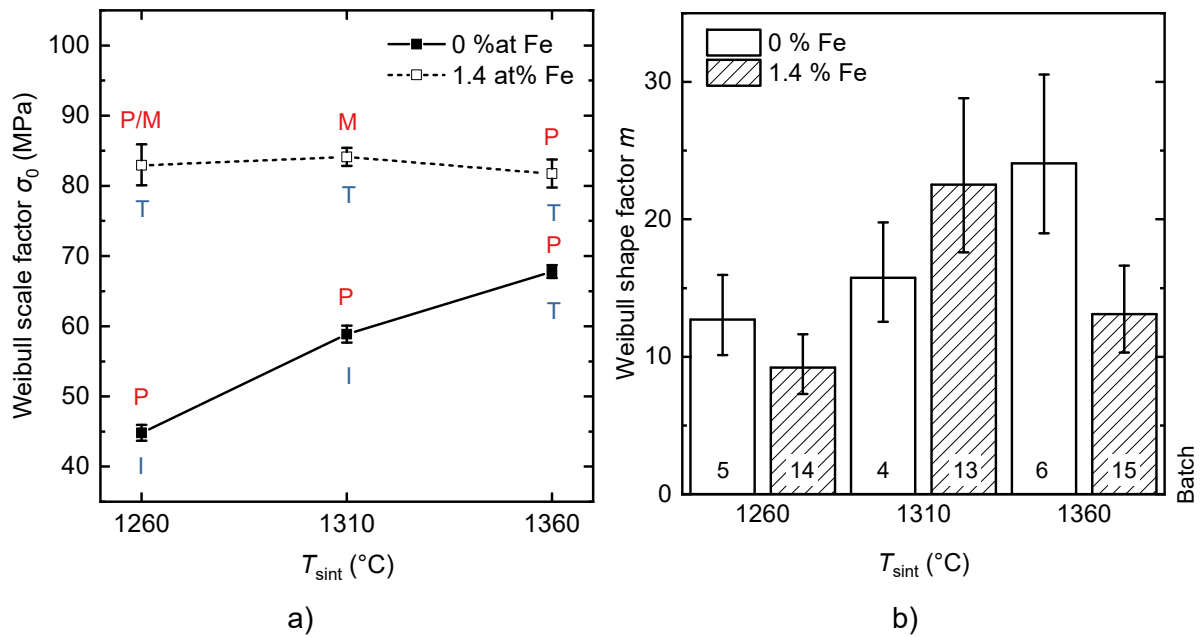


**Figure 8-23 Plots of Weibull a) scale and b) shape factors of all batches in the sintering temperature series. Error bars represent 95% CI. Notes above the data points indicate the prevalent fracture origin: M = machining damage, P = porosity; notes below data points indicate prevalent mode of fracture: I = intergranular, T = transgranular.**

The Weibull modulus increased with increasing temperature from 13 to 24 in batches without Fe. Porosity is the dominant fracture origin in these materials and the width of the pore size distribution would be expected to narrow its range with increasing sintering temperature, making the material more reliable. It should be noted that the Weibull moduli exhibit much wider 95% confidence intervals than the Weibull strengths. The upper/lower limits of Weibull moduli are generally  $\pm 2-6$  relative to their average value, which should be kept in mind in the subsequent discussions. The exact values of 95 % CI are not reported in the text as they would impede the flow of the discussion.

In the case of Fe-doped compositions, the dominant flaw population changes at each selected sintering temperature. The size range of critical flaws narrows and changes to machining damage when the sintering temperature is raised from 1260 to 1310 °C as part of the porosity is reduced. Increasing the sintering temperature to 1360 °C, creates a new population of larger pores which becomes the dominant fracture origin and widens the size range of critical flaws. This would explain why the value of  $m = 23$  of batch 13 sintered at 1310 °C is higher than that of batches 14 (9) and 15 (13) sintered at 1260 and 1360 °C respectively.

## 8.4.5 Strontium doping dependence

### 8.4.5.1 Probability distributions and fractography

The Weibull fits of the biaxial flexural strengths of  $\text{Pb}(\text{Zr}_{0.52}\text{Ti}_{0.48})\text{O}_3$  and  $\text{Pb}(\text{Zr}_{0.52}\text{Ti}_{0.48})_{0.986}\text{Fe}_{0.014}\text{O}_3$  (batches 1 and 9 with 0 % Sr) are shown in Figure 8-24. The data from batch 1 deviate from the 2-parameter Weibull distribution in a similar fashion to batches 4 and 14 discussed in the previous section, where the 3-parameter version provided a better fit. In this case, the 2-parameter version was even rejected by the A-D test ( $p < 0.01$ ). It is also apparent that the medium strength data between samples 3 and 18 do not follow the distribution, suggesting the presence of multiple flaw populations or a different effect. The test sequence graph of batch 1 samples (see Figure 8-8 a) in section 8.4.1) as well as the fracture origin data in Table 8-6 suggest that testing issues, rather than multiple flaw populations, are responsible.

Batch 9 also deviates from the 2-parameter Weibull fit, significantly enough to be rejected by the A-D test ( $p = 0.02$ ). However, the deviation is left-sided for the weakest samples, strongly suggesting the presence of a second flaw population. This was supported by fractography (see Table 8-6), which showed that the weakest samples failed from porosity, whereas the strongest samples were limited by machining damage.

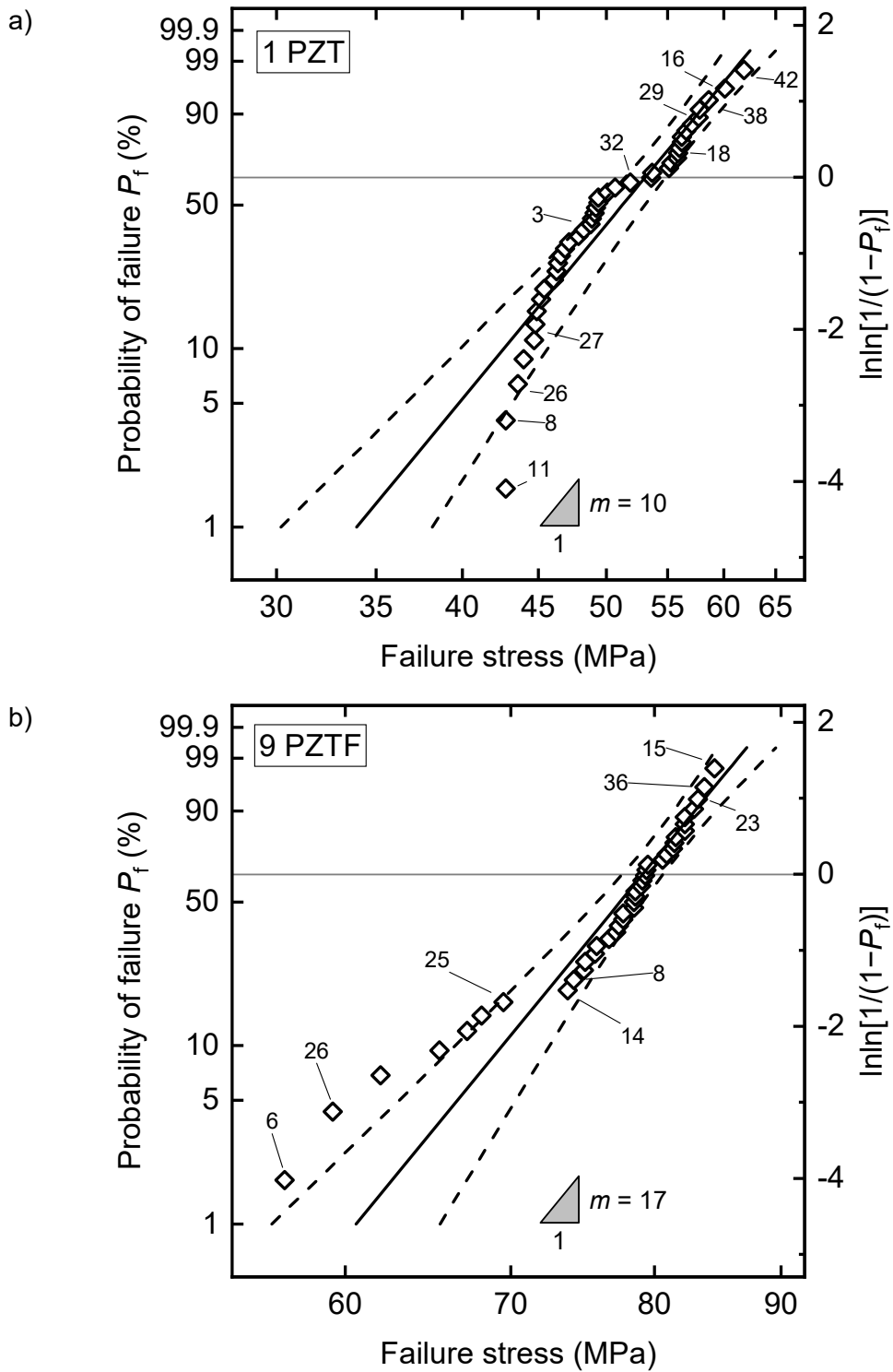


**Figure 8-24 Probability plots with Weibull distribution fits of a)  $\text{Pb}(\text{Zr}_{0.52}\text{Ti}_{0.48})\text{O}_3$  and b)  $\text{Pb}(\text{Zr}_{0.52}\text{Ti}_{0.48})_{0.986}\text{Fe}_{0.014}\text{O}_3$  sintered at 1310 °C. Dashed lines represent 95% CI, marked samples had their fracture surface examined using SEM.**

Table 8-6 Results of A-D tests and fracture origin investigations of  $\text{Pb}(\text{Zr}_{0.52}\text{Ti}_{0.48})\text{O}_3$  doped with 0/5 % Sr and 0.0/1.4 % Fe.

<b>1 PZT</b> <b>x(Sr) = 0 at%</b> <b>Mode: intergranular</b> <b>p(A-D)<sup>†</sup> &lt; 0.01</b>			<b>4 PSZT 52/48</b> <b>x(Sr) = 5 at%</b> <b>Mode: intergranular</b> <b>p(A-D)<sup>†</sup> ≥ 0.25</b>			<b>9 PZTF</b> <b>x(Sr) = 0 at%</b> <b>Mode: transgranular</b> <b>p(A-D)<sup>†</sup> = 0.018</b>			<b>13 PSZTF 52/48</b> <b>x(Sr) = 5 at%</b> <b>Mode: transgranular</b> <b>p(A-D)<sup>†</sup> ≥ 0.25</b>		
Sample no.	Identity	Approx. size (μm)	Sample no.	Identity	Approx. size (μm)	Sample no.	Identity	Approx. size (μm)	Sample no.	Identity	Approx. size (μm)
20	HD		37	PR	?	6	P	340	3	HD	
11	PR	150	36	PR	?	26	PR	350	27	PS	280
8	PR	?	43	PR	?	25	P	100–150	38	MD	?
26	PR	?	8	PS	100	14	PR	100–150	1	MD	100–130
27	P	100	23	PR	?	8	PR	100–150	28	MD	?
3	?	?	21	PR	?	23	MD	30	29	MD	?
32	?	?	3	PR	50–100	36	MD	?	16	MD	170
38	P	100	10	PR	100	15	?	?	40	PS	100
16	?	?	11	PR	100				17	MD	?
42	PS	100							8	MD	?
									9	MD	?

Key: A = agglomerate, P = pore, PR = porous region, PS = porous seam, HD = handling damage, MD = machining damage, ? = unknown

<sup>†</sup>p value of Anderson-Darling goodness-of-fit test

Batches 1 and 4 (0 at% Fe) exhibited intergranular fracture modes. Porosity was the dominant flaw irrespective of Sr doping. The flaw size of the strongest samples was approximately 100 μm in both batches. Box plots presented in Figure 8-25 show that the distribution width of batch 1 is greater and neither batch has any outliers present. Both Fe-doped batches exhibited a transgranular fracture mode.

#### 8.4.5.2 Weibull strength and reliability

The box plot of batch 9 presented in Figure 8-25 reveals the presence of several outliers, which supports the hypothesis that multiple flaw populations are active. In batch 13, machining damage was found as the fracture origin even in the weakest samples. Pore clusters in batch 9 are readily visible on a polished surface shown in Figure 6-9 c) in section 6.4, whereas there are no such features visible in samples from batch 13 (Figure 6-9 d)).

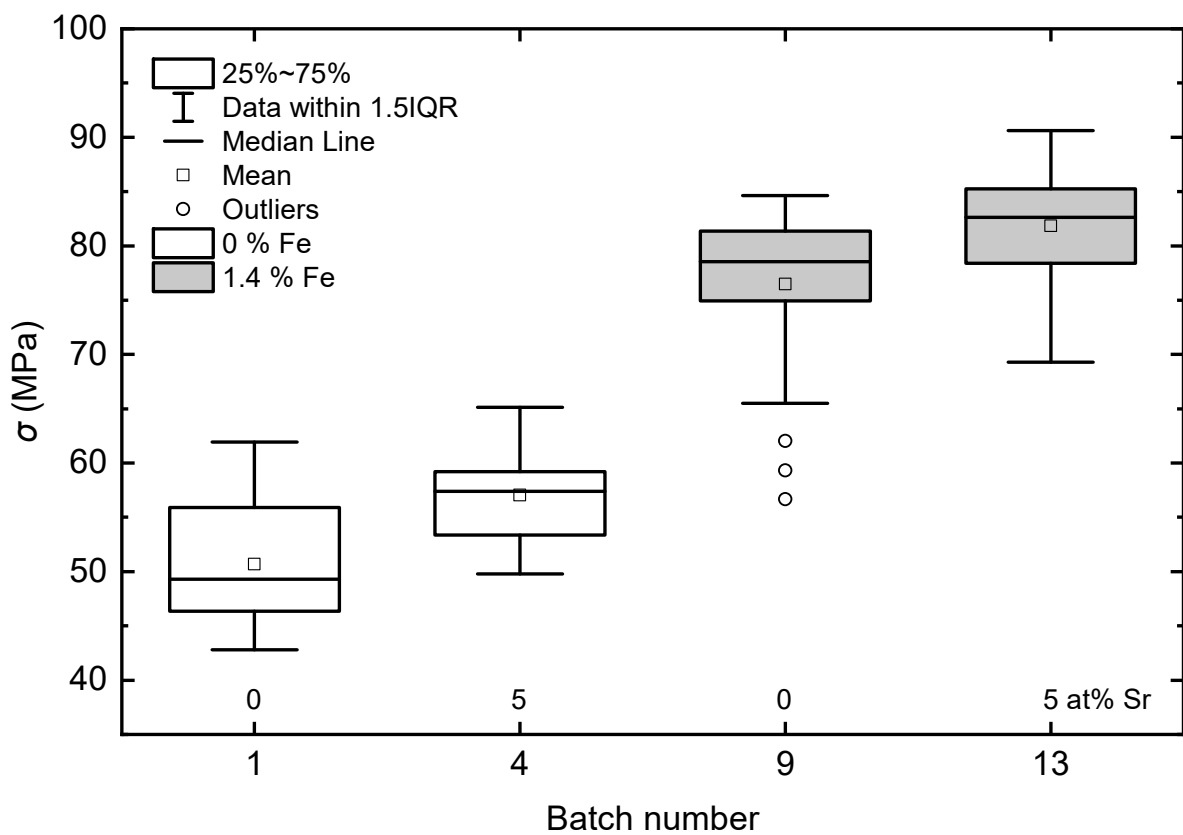
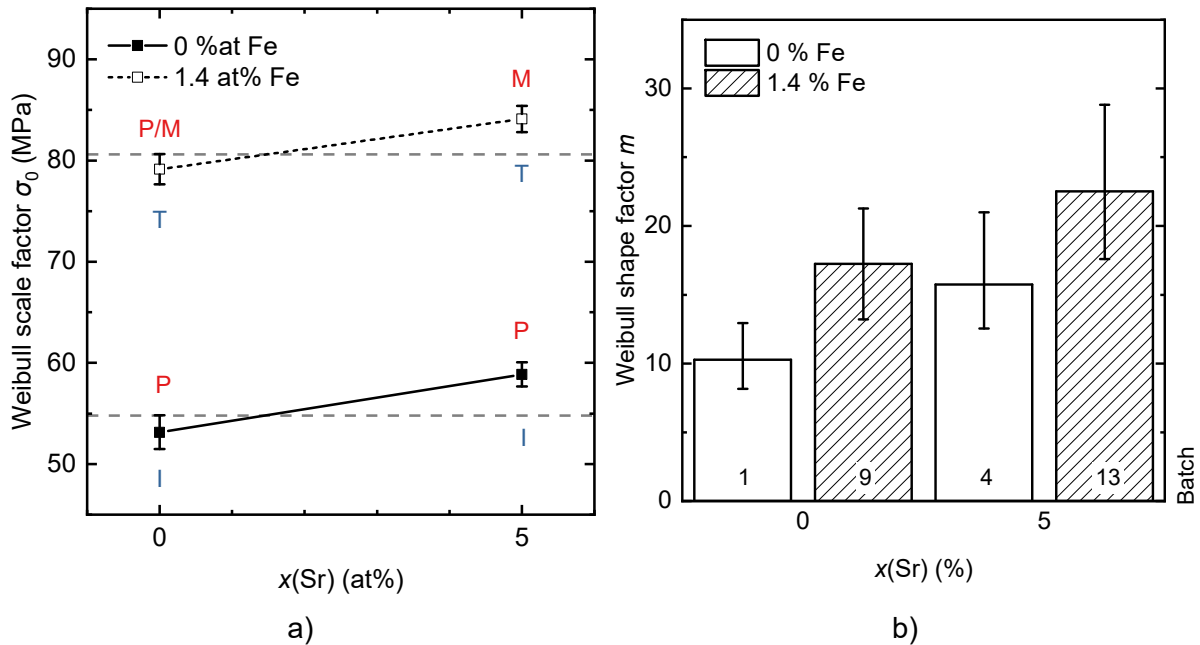


Figure 8-25 Strength box plots of all batches in the Sr/Fe doping series.

As shown in Figure 8-26, Sr increased the strength of  $(\text{Pb}_{1-x}\text{Sr}_x)(\text{Zr}_{0.52}\text{Ti}_{0.48})_{1-z}\text{Fe}_z\text{O}_3$  (based on 95% CI) irrespective of Fe doping. In the case of Fe-doped samples (batch 9 and 13), the increase from 79.1 to 84.1 MPa is supported by two important microstructural changes, namely a decrease in average grain size by 1  $\mu\text{m}$  and shift of average pore size to lower values, decreasing the presence of pore clusters.

In samples with 0 % Fe (batch 1 and 4), doping with Sr increased the Weibull strength from 53.1 to 58.9 MPa, but did not significantly affect the relative density, grain size or pore size distribution. The elastic modulus increased by 11 GPa, which was ascribed to the effects of the proximity to the MPB in section 8.1. According to equation (2-2), an increase in  $Y$  should increase the strength by increasing the fracture toughness (assuming that fracture energy increases or stays constant). The effect of  $Y$  on the strength should be more notable in the Zr/Ti series as its range of  $Y$  values is wider.



**Figure 8-26** Plots of Weibull a) scale and b) shape factors of all batches in the Sr/Fe doping series. Error bars represent 95% CI. Notes above the data points indicate the prevalent fracture origin: M = machining damage, P = porosity; notes below data points indicate prevalent mode of fracture: I = intergranular, T = transgranular.

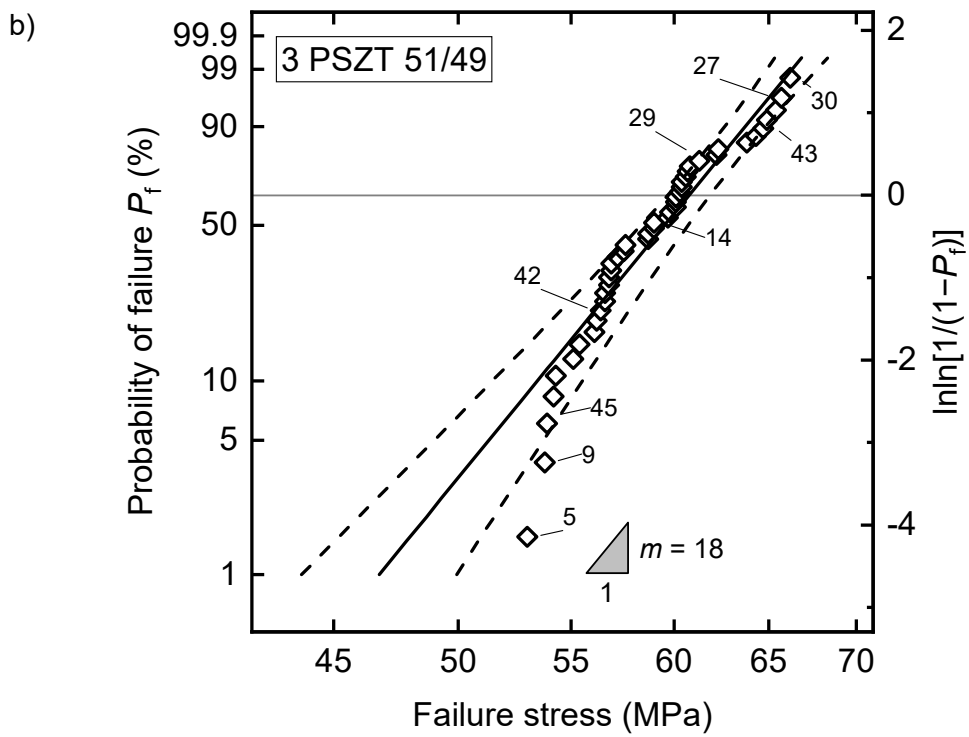
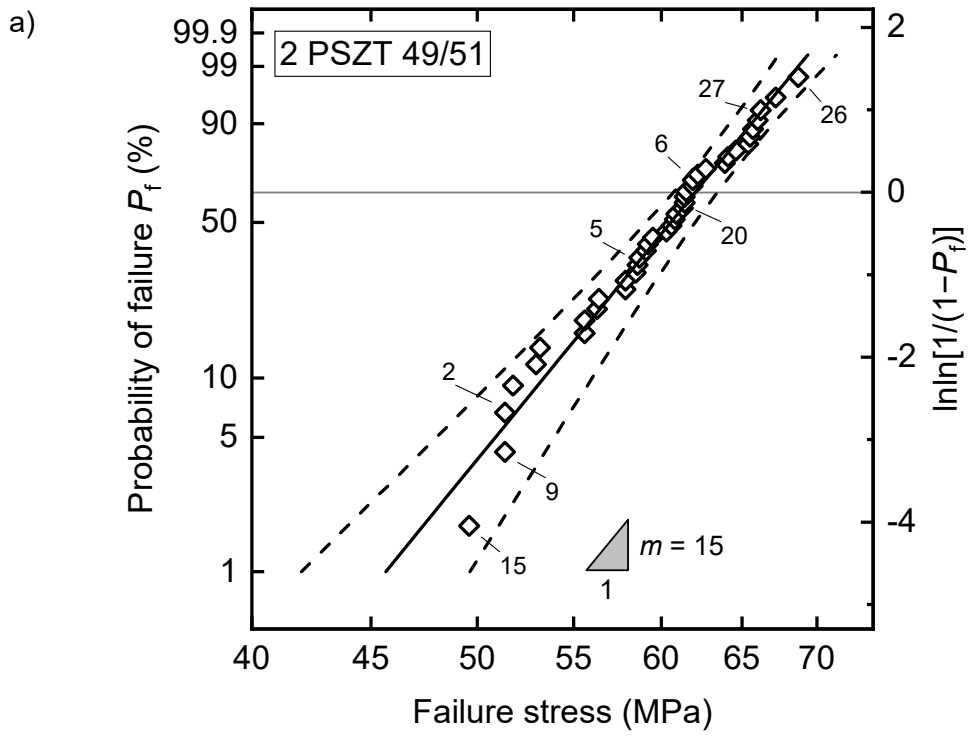
Batch 1 exhibited the lowest Weibull modulus of 10, as shown in Figure 8-26. This is likely connected to the strength testing issues discussed previously. Both batches 1 and 4 showed higher porosity and pores as the fracture origin compared to batch 13 ( $m = 23$ ), which mostly failed from machining damage. Batch 9 showed a lower Weibull modulus of 17 likely due to the presence of two active flaw populations.

## 8.4.6 Zr/Ti ratio dependence

### 8.4.6.1 Probability distributions and fractography (0 at% Fe)

Weibull distribution fits of the biaxial strength of samples of  $(\text{Pb}_{0.95}\text{Sr}_{0.05})(\text{Zr}_y\text{Ti}_{1-y})\text{O}_3$  (0 at% Fe) with varying  $y$  (batches 2, 3, 7 and 8) are shown in Figure 8-27. The fit of batch 4 with  $y = 52$  at% has been discussed in section 8.4.4.1 above. The results of fracture origin investigations and A-D tests are presented in Table 8-7. A Weibull distribution was found unsuitable for batch 3 ( $p < 0.01$ ). This batch along with batch 7 exhibited a right-side deviation at low strengths. The causes and implications of this behaviour have already been discussed in section 8.4.4. Additionally, data from batch 3 do not follow the distribution well at medium strengths. It is possible that multiple active populations are present, however, knowledge gained from the testing sequences rather suggests an influence of the testing issues with batches 1–4 discussed in section 8.4.1.

The dominant fracture mode was intergranular in compositions with  $y \leq 52$  at% and transgranular for  $y \geq 53$  at%. This is illustrated by the micrographs in Figure 8-28. The same transition was already observed in batch 6 ( $T_{\text{sint}} = 1360$  °C) from the sintering temperature series and will be further discussed in the general discussion in section 8.4.10. Porosity dominated all compositions as a fracture origin. The approximate size of the fracture origin appears to be on a similar scale for all batches.



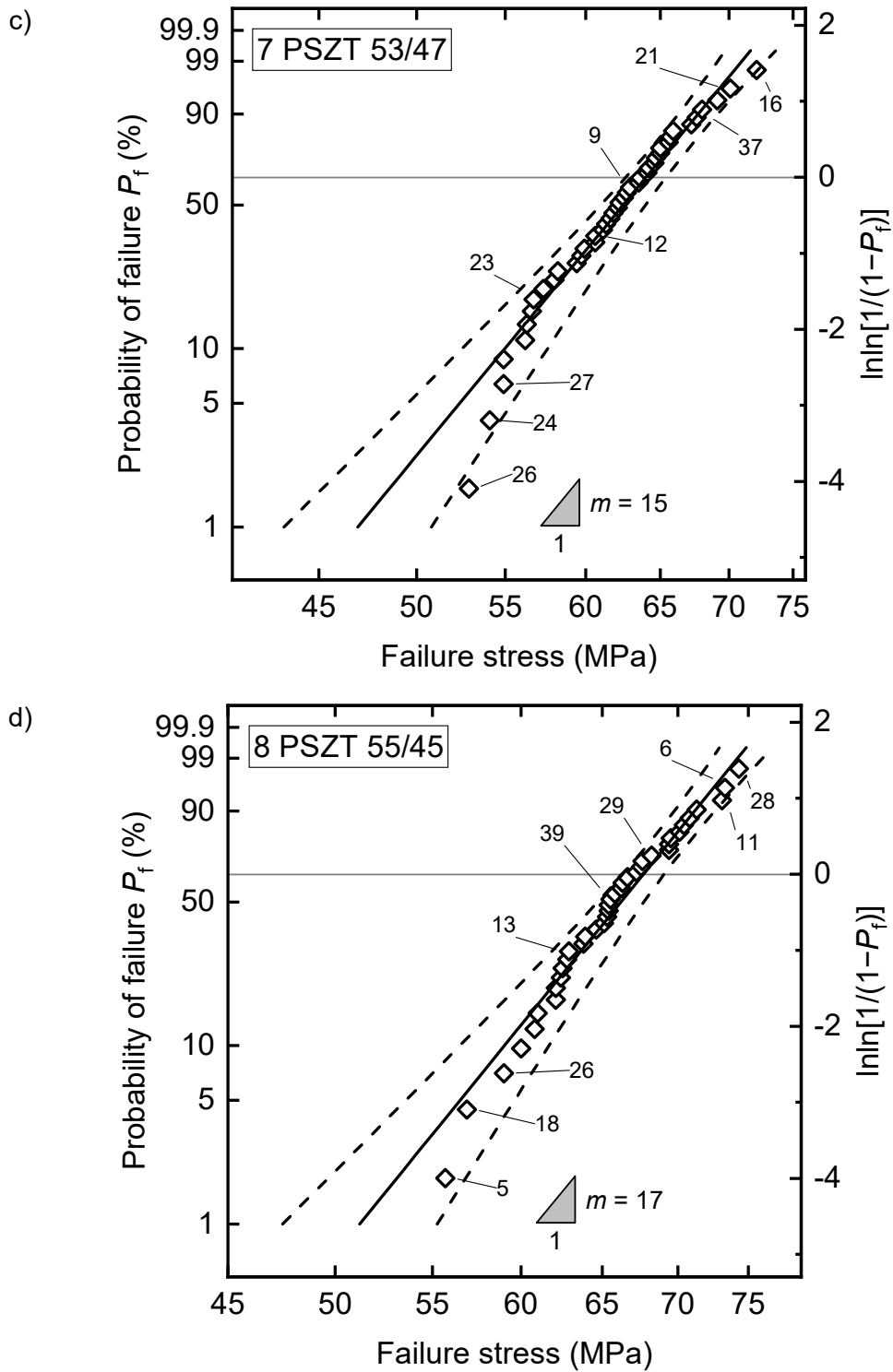
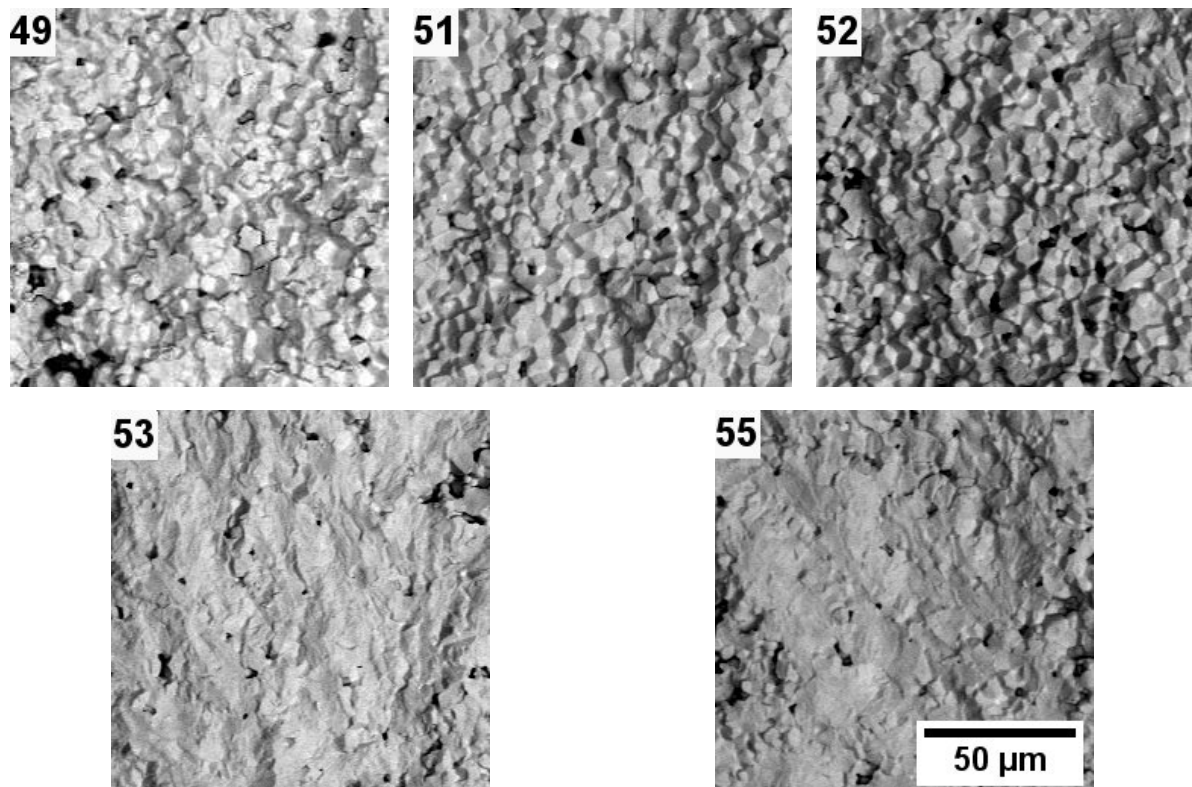


Figure 8-27 Probability plots with Weibull distribution fits of  $(\text{Pb}_{0.95}\text{Sr}_{0.05})(\text{Zr}_y\text{Ti}_{1-y})\text{O}_3$  sintered at  $1310^\circ\text{C}$ .  $y =$  a) 0.49, b) 0.51, c) 0.53, d) 0.55. Dashed lines represent 95% CI, marked samples had their fracture surface examined using SEM.

Table 8-7 Results of A-D tests and fracture origin investigations of  $(\text{Pb}_{0.95}\text{Sr}_{0.05})(\text{Zr}_y\text{Ti}_{1-y})\text{O}_3$  with  $y = 49\text{--}55$  at%.

2 PSZT 49/51 $y(\text{Zr}) = 49$ at%			3 PSZT 51/49 $y(\text{Zr}) = 51$ at%			4 PSZT 52/48 $y(\text{Zr}) = 52$ at%			7 PSZT 53/47 $y(\text{Zr}) = 53$ at%			8 PSZT 55/45 $y(\text{Zr}) = 55$ at%		
Mode: intergranular $p(\text{A-D})^\dagger \geq 0.25$			Mode: intergranular $p(\text{A-D})^\dagger < 0.01$			Mode: intergranular $p(\text{A-D})^\dagger \geq 0.25$			Mode: transgranular $p(\text{A-D})^\dagger \geq 0.25$			Mode: transgranular $p(\text{A-D})^\dagger \geq 0.25$		
Sample no.	Identity	Approx. size ( $\mu\text{m}$ )	Sample no.	Identity	Approx. size ( $\mu\text{m}$ )	Sample no.	Identity	Approx. size ( $\mu\text{m}$ )	Sample no.	Identity	Approx. size ( $\mu\text{m}$ )	Sample no.	Identity	Approx. size ( $\mu\text{m}$ )
15	PR	300	5	PR	?	37	PR	?	26	PR	200	5	PS	?
9	PR	200	9	PR	200	36	PR	?	24	PS	?	18	PR	300
2	PR	?	45	PS	150	43	PR	?	27	PR	160	26	PR	250
5	?	?	42	PR	?	8	PS	100	23	PS	?	13	PR	250
20	PS	100	14	PR	50-100	23	PR	?	12	PR	140	39	PR	?
6	PR	100	29	PR	100	21	PR	?	9	PR	105	29	?	?
27	?	?	43	PR	100	3	PR	50-100	37	PR	100	11	PR	150-200
26	?	?	27	?	?	10	PR	100	21	PR	100-110	6	PR	150
31	P	50-100	30	MD	80	11	PR	100	16	PR	85-145	28	PR	100

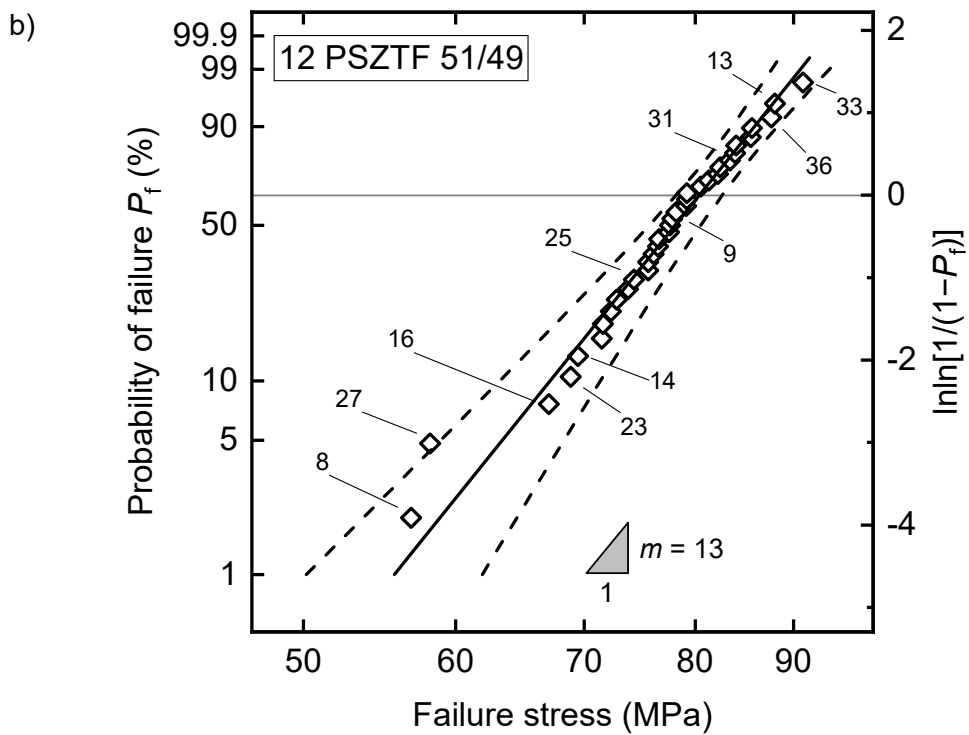
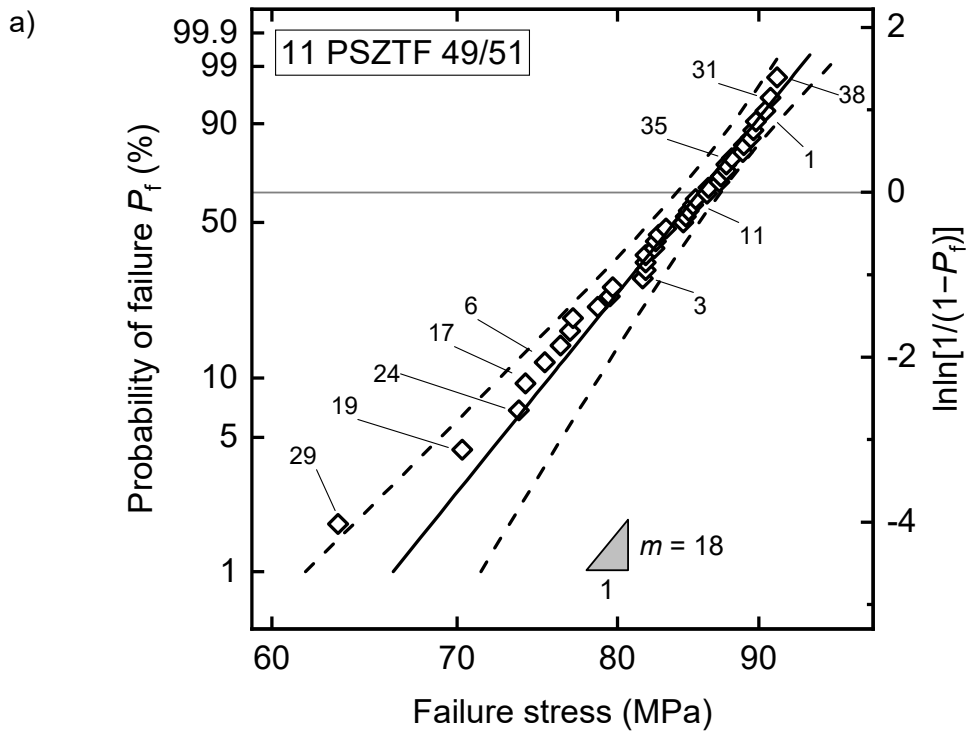
Key: A = agglomerate, P = pore, PR = porous region, PS = porous seam, HD = handling damage, MD = machining damage, ? = unknown  
 $\dagger p$  value of Anderson-Darling goodness-of-fit test



**Figure 8-28** Micrographs of fracture surfaces of  $(\text{Pb}_{0.95}\text{Sr}_{0.05})(\text{Zr}_y\text{Ti}_{1-y})\text{O}_3$  samples with varying  $y$  (stated in at% in the top left corner). Fracture mode changes from intergranular to transgranular at  $y = 53$  and  $55$  at%.

#### 8.4.6.2 Probability distributions and fractography (1.4 at% Fe)

All Fe-doped batches from the Zr/Ti series (batches 11, 12, 16 and 17) showed a good fit to a Weibull distribution, as shown in Figure 8-29 and confirmed by the A-D tests (Table 8-8). Deviation of some of the weakest samples is visible in batches 11, 12 and 17. These deviations are all left-sided, meaning that they failed at lower stresses than predicted by their respective Weibull distributions. The fracture mode was transgranular in all batches. As shown in Table 8-8, the dominant fracture origin was machining damage for  $(\text{Pb}_{0.95}\text{Sr}_{0.05})(\text{Zr}_y\text{Ti}_{1-y})_{0.986}\text{Fe}_{0.014}\text{O}_3$  batches with  $y \geq 52$  at%. A significant number of pore clusters initiating fracture was found in batches 11 and 12. This agrees with the porosity observations discussed in section 6.4. The sizes of the fracture origins are difficult to compare as machining damage was impossible to reliably estimate in most cases.



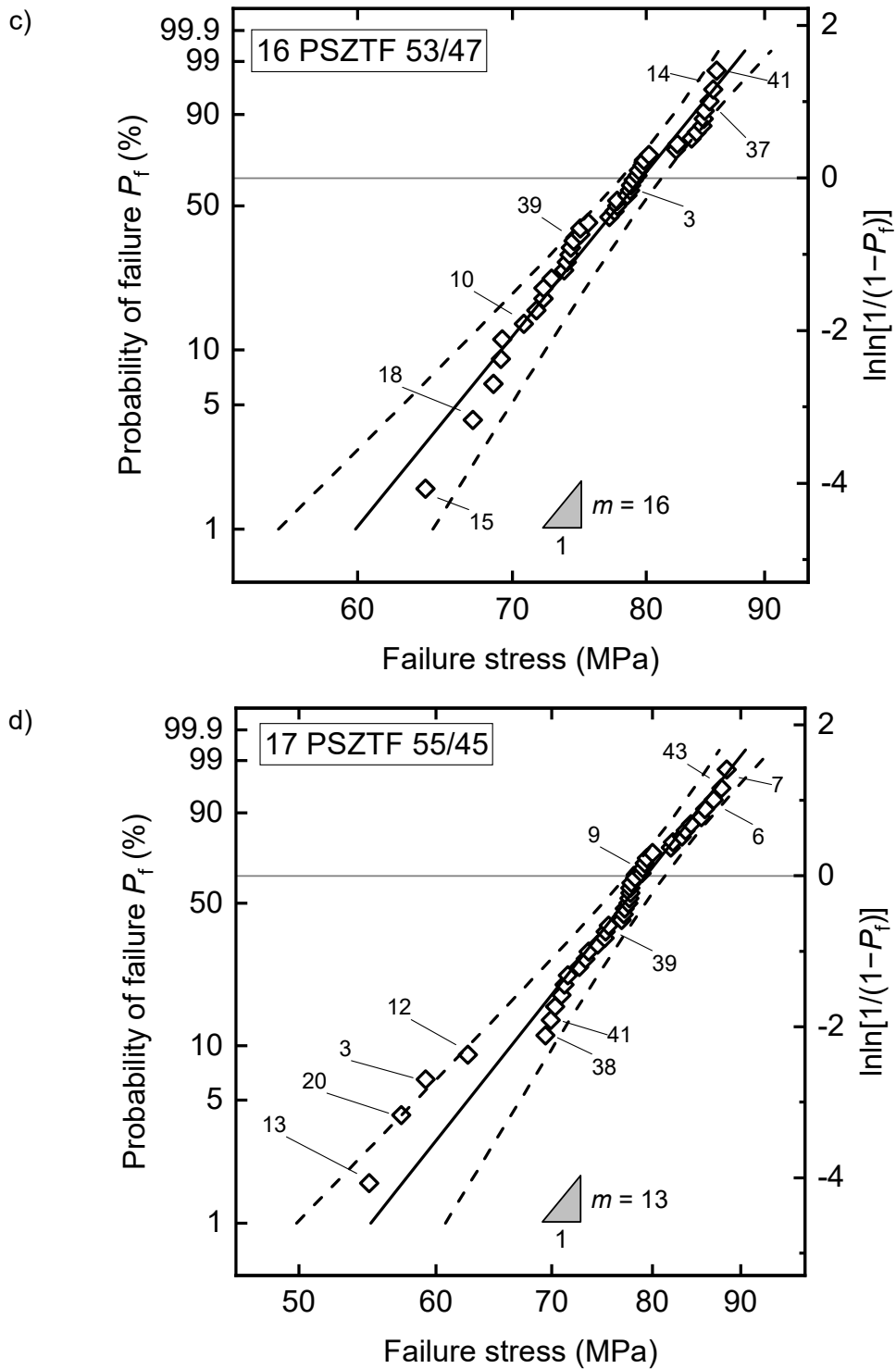


Figure 8-29 Probability plots with Weibull distribution fits of  $(\text{Pb}_{0.95}\text{Sr}_{0.05})(\text{Zr}_y\text{Ti}_{1-y})_{0.986}\text{Fe}_{0.014}\text{O}_3$  sintered at 1310 °C.  $y =$  a) 0.49, b) 0.51, c) 0.53, d) 0.55. Dashed lines represent 95% CI, marked samples had their fracture surface examined using SEM.

Table 8-8 Results of A-D tests and fracture origin investigations of  $(\text{Pb}_{0.95}\text{Sr}_{0.05})(\text{Zr}_y\text{Ti}_{1-y})_{0.986}\text{Fe}_{0.014}\text{O}_3$  with  $y = 49\text{--}55$  at%.

11 PSZTF 49/51 $y(\text{Zr}) = 49$ at%			12 PSZTF 51/49 $y(\text{Zr}) = 51$ at%			13 PSZTF 52/48 $y(\text{Zr}) = 52$ at%			16 PSZTF 53/47 $y(\text{Zr}) = 53$ at%			17 PSZTF 55/45 $y(\text{Zr}) = 55$ at%		
Mode: transgranular $p(\text{A-D})^\dagger \geq 0.25$			Mode: transgranular $p(\text{A-D})^\dagger \geq 0.25$			Mode: transgranular $p(\text{A-D})^\dagger \geq 0.25$			Mode: transgranular $p(\text{A-D})^\dagger \geq 0.25$			Mode: transgranular $p(\text{A-D})^\dagger \geq 0.25$		
Sample no.	Identity	Approx. size ( $\mu\text{m}$ )	Sample no.	Identity	Approx. size ( $\mu\text{m}$ )	Sample no.	Identity	Approx. size ( $\mu\text{m}$ )	Sample no.	Identity	Approx. size ( $\mu\text{m}$ )	Sample no.	Identity	Approx. size ( $\mu\text{m}$ )
40	HD		17	HD		3	HD		23	HD		21	HD	
29	PR	230	8	A	280	27	PS	280	15	P	200	13	PR	>180
19	PS	230	27	P	>280	38	MD	?	18	MD	?	20	PS	240
24	PR	230	16	MD	?	1	MD	100–130	10	MD	130	3	PS	140
17	PS	170	23	PR	220	28	MD	?	39	MD	?	12	?	?
6	PS	140	14	PS	150	29	MD	?	3	MD	?	38	PS	130
3	PR	160	25	MD	?	16	MD	170	37	MD	?	41	MD	70
11	PR	120–220	9	PR	130	40	PS	100	14	MD	?	39	MD	80
35	MD	?	31	MD	60	17	MD	?	41	MD	30–80	9	MD	?
1	MD	?	36	PR (V) <sup>‡</sup>	110	8	MD	?				6	MD	?
31	MD	?	13	MD	50	9	MD	?				43	MD	?
38	PS	90	33	PS	110							7	MD	50

Key: A = agglomerate, P = pore, PR = porous region, PS = porous seam, HD = handling damage, MD = machining damage, ? = unknown

<sup>†</sup> $p$  value of Anderson-Darling goodness-of-fit test

<sup>‡</sup>flaw located within the volume of the sample and not on the surface

#### 8.4.6.3 Weibull strength and reliability

Figure 8-30 shows box plots of all the compositions in the Zr/Ti series. All batches containing Fe are located at higher strength values than those containing no Fe. Distribution widths vary between 15–25 MPa except from batch 17, which shows a distribution width of 35 MPa. Outliers were detected in batches 11, 12 and 17, which correspond to deviations from the Weibull distribution discussed earlier. The outlier in batch 11, sample 29, failed from a large porous region shown in Figure 8-31 a), which is similar to the fracture origin in sample 24 from the same batch (not an outlier) shown in Figure 8-31 b). While there is a difference in shape and size, it cannot be concluded that sample 29 differs from the rest of the population in any significant way. 2 Outliers in batch 12 were identified as an agglomerate and an exceptionally large pore, both considered as extreme manifestations of the preparation method. Fractography of batch 17 and its deviation from the Weibull distribution shown in Figure 8-29 d) suggest that 2 distinct fracture populations are present. The weakest samples had porosity as their fracture origins, whereas machining damage initiated fracture at higher loads. The presence of outliers in the Fe-doped batches was likely caused by the binder incorporation process. Extreme flaws related to binder mixing are more likely to become outliers in Fe-doped compositions as they are on a much larger scale than the natural porosity.

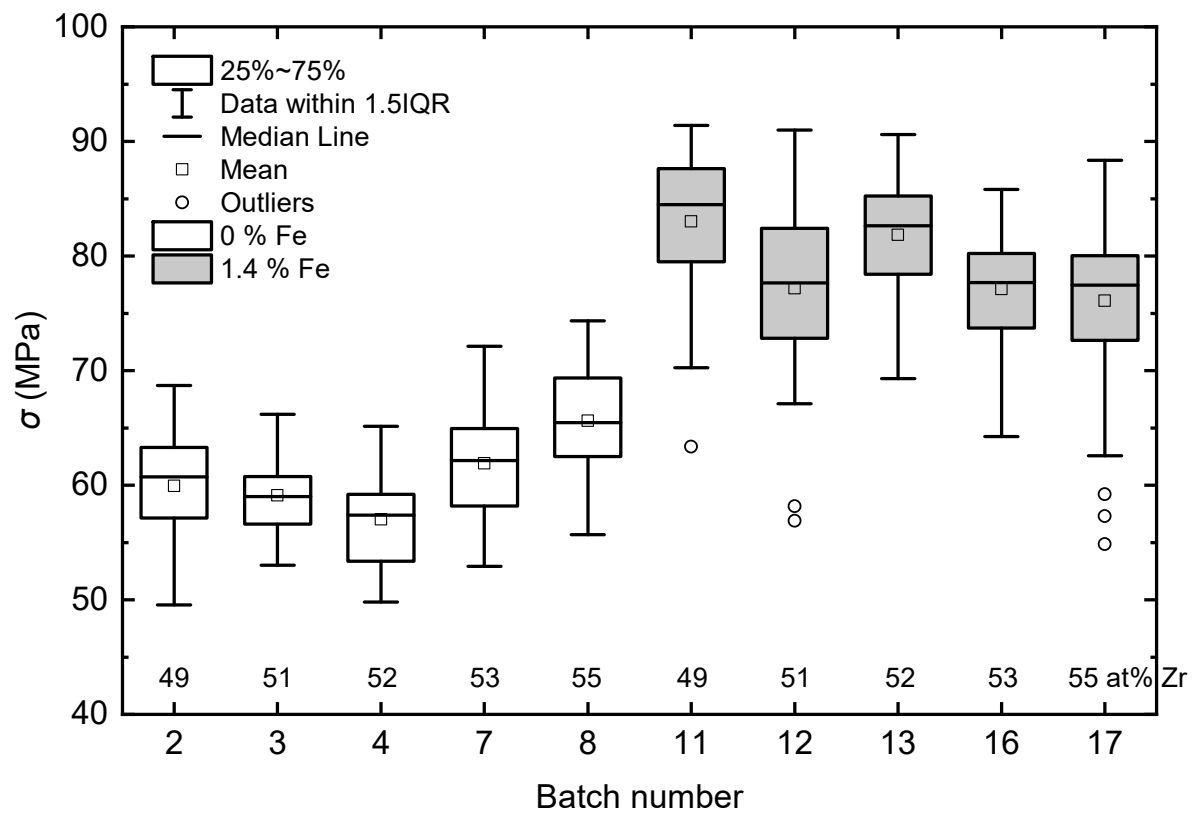


Figure 8-30 Strength box plots of all batches in Sr/Fe doping series.

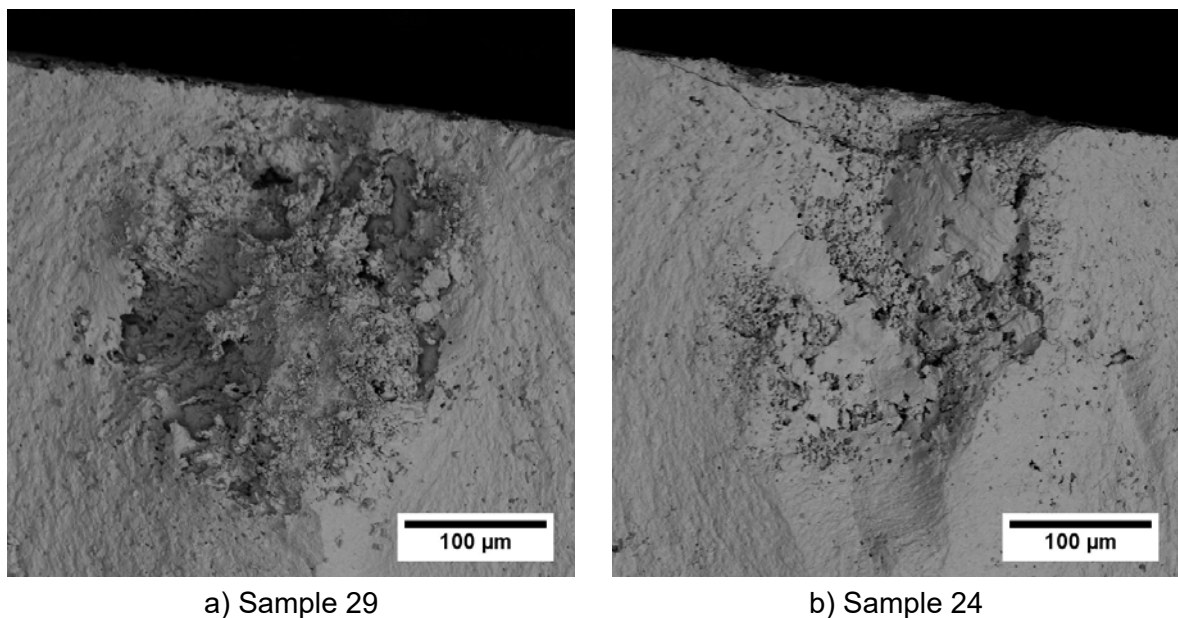


Figure 8-31 SEM micrographs of fracture origins of samples a) 29 and b) 24 from batch 11.

The Weibull strengths and moduli of the compositions with varying Zr/Ti ratios are plotted in Figure 8-32 a). The Fe-doped compositions exhibited higher Weibull strengths. Within this series,  $(\text{Pb}_{0.95}\text{Sr}_{0.05})(\text{Zr}_y\text{Ti}_{1-y})_{0.986}\text{Fe}_{0.014}\text{O}_3$  with  $y = 49$  and  $52$  at% (batches 11 and 13) were statistically stronger (85.6 and 84.1 MPa respectively) than the remaining batches (79.3–80.4 MPa), according to 95% CI. Microstructural investigations did not show any features that might be responsible for this conclusion. The relative density changes by  $< 1\%$ , elastic modulus decreases between  $y = 49$ – $52$  at%, grain size and hardness do not show any variation. Porosity investigations, fractography and surface roughness results suggested that batches 11 and 12 should have exhibited lower strength as they showed higher surface roughness and contained significantly more pore clusters which could have acted as fracture origins. As this was not the case, the differences in strength are more likely connected to the inaccuracies of the testing method and surface damage extremities not reflected in the average surface roughness. The difference in Young's modulus of  $\approx 10$  GPa between  $y = 49$ – $53$  at% does not seem to be reflected in the Weibull strength dependency.

Compositions not containing Fe showed Weibull strength decrease from 62.1 to 58.9 MPa with increasing  $y$  in  $(\text{Pb}_{0.95}\text{Sr}_{0.05})(\text{Zr}_y\text{Ti}_{1-y})\text{O}_3$  up to 52 at% and then an increase beyond this value, as shown in Figure 8-32 a). Batch 8 with  $y = 55$  at% exhibited the statistically highest strength of 67.7 MPa (95% CI). Grain size and relative density variations were within the standard deviation. Porosity investigations discussed in section 6.4 revealed that batches 7 and 8 contained finer porosity of more homogeneous appearance than batches 2–4. However, based on fractography results, the fracture origin size was not lower in batches 7 and 8, suggesting that despite the change in pore size distribution, extreme flaws of a similar size could be found in all these compositions. Another factor might be the change from inter- to transgranular fracture mode observed in batches 7 and 8. PSZT sintered at 1360 °C (batch 6), and discussed

in section 8.4.4.1, also exhibited this fracture mode transition, however, its roughness did not significantly differ from PSZT sintered at 1310 °C (batch 4). Both the surface roughness and fracture mode change might be responsible for the strength increase, the former being less likely since all discussed batches failed primarily from porosity and not machining damage. Machining damage around pore clusters would not be expected to change, unless it was affected by the fracture mode change. Reasons for the fracture mode change will be discussed in detail in section 8.4.10. The decrease of Young's modulus by  $\approx 20$  GPa between the  $y$  values of 49–53 at% does not seem to be reflected in the Weibull strength dependence. This signifies that either the behaviour of the material deviates from the LEFM or that another factor increases the fracture energy.

Another factor to consider is the uncertainty connected with testing issues of batches 1–4. If the hypothesis identifying the issues of the jig described in chapter 8.4.1 is valid, these batches would be expected to show somewhat higher Weibull strength values. However, only weaker samples from the population would be expected to break at higher strength and the maximum strength value of entire population would not change. As shown in Figure 8-30, batches 7 and 8 have their entire distributions located at higher strength, suggesting that fixing the issues with the jig would not change the conclusions drawn in the previous paragraph. Lastly, domain switching may affect the strength of PZT. This phenomenon will be discussed in section 8.4.9.

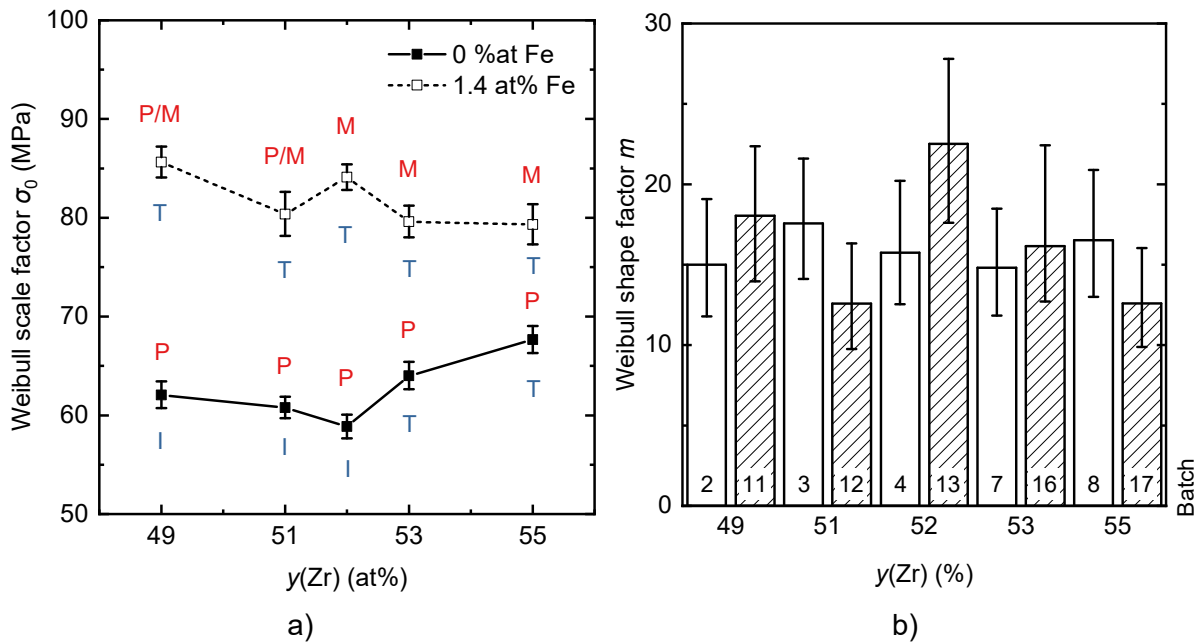


**Figure 8-32** Plots of Weibull a) scale and b) shape factors of all batches in the Zr/Ti series. Error bars represent 95% CI. Notes above the data points indicate the prevalent fracture origin: M = machining damage, P = porosity; notes below data points indicate prevalent mode of fracture: I = intergranular, T = transgranular.

The Weibull moduli of batches from the Zr/Ti series shown in Figure 8-32 b) do not exhibit any apparent trend and range from 12 to 23. The moduli do not seem to be affected by the presence of Fe. Batches 12 and 17 (Fe-doped PSZT with 51 and 55 % Zr) were the batches with the lowest  $m$  value of 13 due to the presence of outliers as the Weibull modulus is sensitive to them. Removing the outliers from the data increases the  $m$  value of batches 12 and 17 to approximately 15. The highest reliability ( $m = 23$ ) was shown by batch 13. The reason is not clear.

## 8.4.7 Iron doping dependence

### 8.4.7.1 Probability distributions and fractography

Weibull distribution fits of strength data from batches containing 0.4 and 2.0 % Fe (batches 10 and 18) are shown in Figure 8-33. The Weibull fits of batches with 0 and 1.4 % (batches 4 and 13) Fe were presented in Figure 8-18 b) and Figure 8-21 c) and discussed in section 8.4.4. The data fit the distribution well ( $p > 0.05$  according to the A-D test) and there are no obvious deviations at lower strengths. Batch 10 showed a deviation between samples 1 and 17 corresponding to an abnormally high population in this strength range. It can signify a presence of multiple flaw populations, however, only porosity was found as an origin of fracture (see Table 8-9). Batch 18 contains “gaps” in the population near the centre of the distribution for an unknown reason. While fractography suggests the presence of multiple flaw distributions, it is unlikely that they would be responsible for such behaviour.

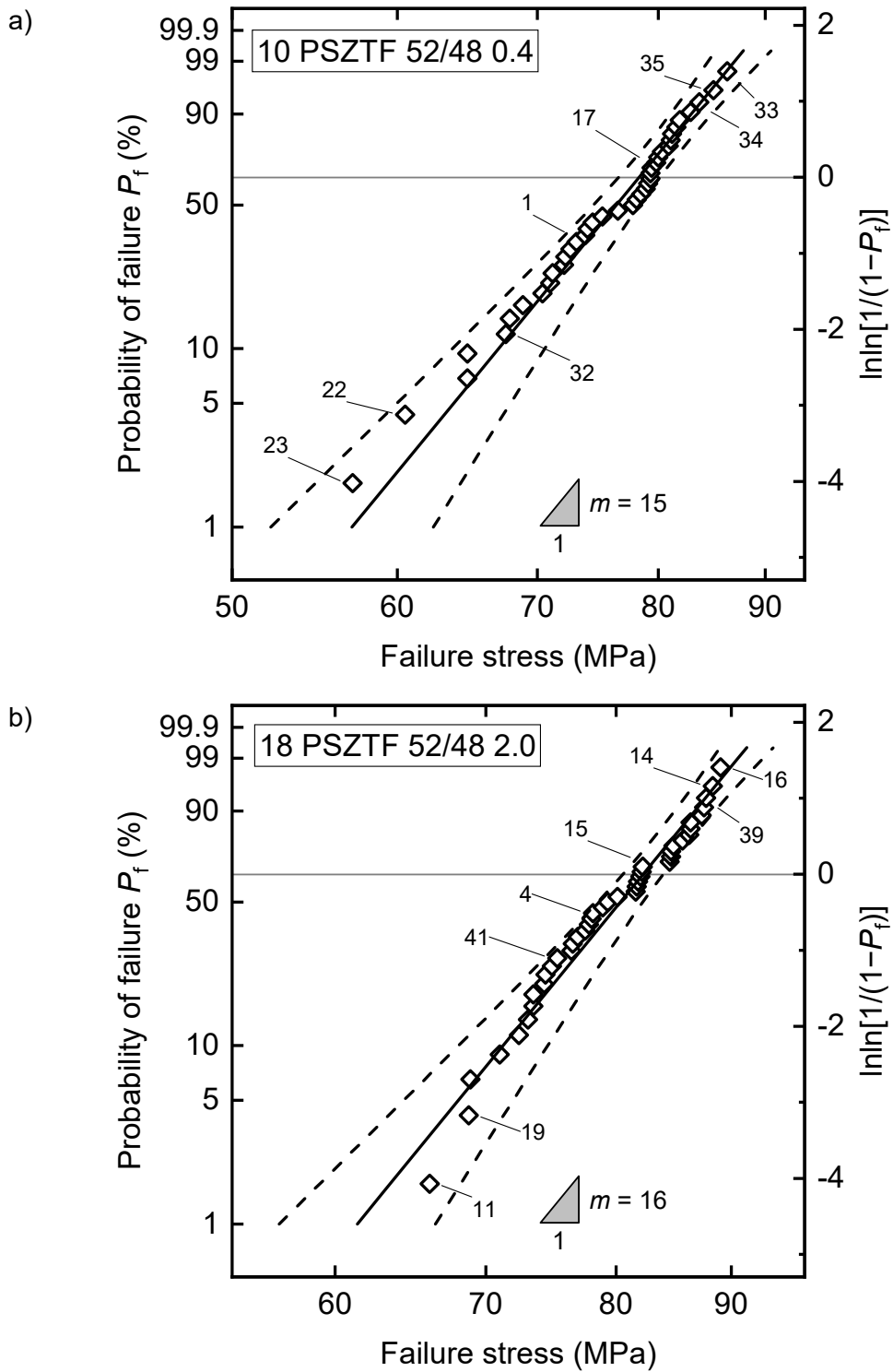


Figure 8-33 Probability plots with Weibull distribution fits of  $(\text{Pb}_{0.95}\text{Sr}_{0.05})(\text{Zr}_{0.52}\text{Ti}_{0.48})_{1-z}\text{Fe}_z\text{O}_3$  doped with a) 0.4 and b) 2.0 % Fe. Dashed lines represent 95% CI, marked samples had their fracture surface examined using SEM

Table 8-9 Results of A-D tests and fracture origin investigations of  $(\text{Pb}_{0.95}\text{Sr}_{0.05})(\text{Zr}_{0.52}\text{Ti}_{0.48})\text{O}_3$  doped with 0.4 and 2.0 % Fe.

<b>4 PSZT 52/48</b> <b>z(Fe) = 0 at%</b> <b>Mode: intergranular</b> <b><math>p(\text{A-D})^\dagger \geq 0.25</math></b>			<b>10 PSZTF 0.4</b> <b>z(Fe) = 0.4 at%</b> <b>Mode: transgranular</b> <b><math>p(\text{A-D})^\dagger \geq 0.25</math></b>			<b>13 PSZTF 1.4</b> <b>z(Fe) = 1.4 at%</b> <b>Mode: transgranular</b> <b><math>p(\text{A-D})^\dagger \geq 0.25</math></b>			<b>18 PSZTF 2.0</b> <b>z(Fe) = 2.0 at%</b> <b>Mode: transgranular</b> <b><math>p(\text{A-D})^\dagger = 0.21</math></b>		
Sample no.	Identity	Approx. size ( $\mu\text{m}$ )	Sample no.	Identity	Approx. size ( $\mu\text{m}$ )	Sample no.	Identity	Approx. size ( $\mu\text{m}$ )	Sample no.	Identity	Approx. size ( $\mu\text{m}$ )
37	PR	?	8	HD		3	HD		21	HD	
36	PR	?	23	PS	200	27	PS	280	11	PR	130
43	PR	?	22	PS (V) <sup>‡</sup>	400	38	MD	?	19	MD	?
8	PS	100	32	PR	100	1	MD	100–130	41	MD	?
23	PR	?	1	PS	200	28	MD	?	4	MD	?
21	PR	?	17	PR	150	29	MD	?	15	PS	100
3	PR	50–100	34	PR	150	16	MD	170	39	PS	30
10	PR	100	35	PR	150–200	40	PS	100	14	MD	?
11	PR	100	33	PR	50–100	17	MD	?	16	PR	<130
						8	MD	?			
						9	MD	?			

Key: A = agglomerate, P = pore, PR = porous region, PS = porous seam, HD = handling damage, MD = machining damage, ? = unknown

<sup>†</sup>p value of Anderson-Darling goodness-of-fit test

<sup>‡</sup>flaw located within the volume of the sample and not on the surface

The  $(\text{Pb}_{0.95}\text{Sr}_{0.05})(\text{Zr}_{0.52}\text{Ti}_{0.48})_{1-z}\text{Fe}_z\text{O}_3$  exhibited a fracture mode change from inter- to transgranular when doped with Fe. The dominant fracture origin is porosity in batches 4 and 10, machining damage in batch 13 and a combination of both in batch 18. This is consistent with porosity observations discussed in section 6.4. The sizes of the fracture origins of discussed batches (4, 10, 13 and 18) are most likely on a similar scale, as suggested by the results in Table 8-9.

#### 8.4.7.2 Weibull strength and reliability

The strength box plots shown in Figure 8-34 revealed a single outlier in batch 10. Its fracture origin was identified as a porous seam but does not significantly differ in nature or size from the other fracture origins also identified as porous seams in this batch. It was found that samples 1, 22 and 23 failed from volume located porous seams, as illustrated in micrographs in Figure 8-35. The Weibull fit of data from batch 10 presented in Figure 8-33 shows signs of multiple active flaw populations. It is possible that volume and surface located flaws are part of 2 separate populations. Batch 4 (0 at% Fe) showed the narrowest distribution (15 MPa), while batch 10 showed the widest distribution (29 MPa). A varying dominant fracture origin may be responsible for the differences.

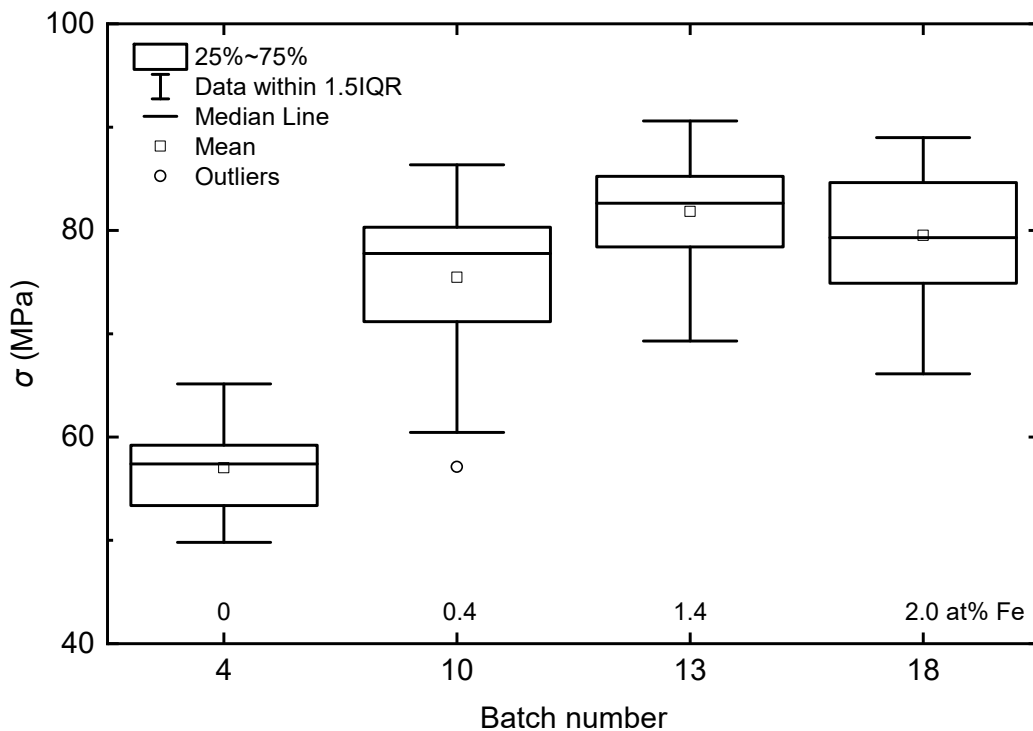
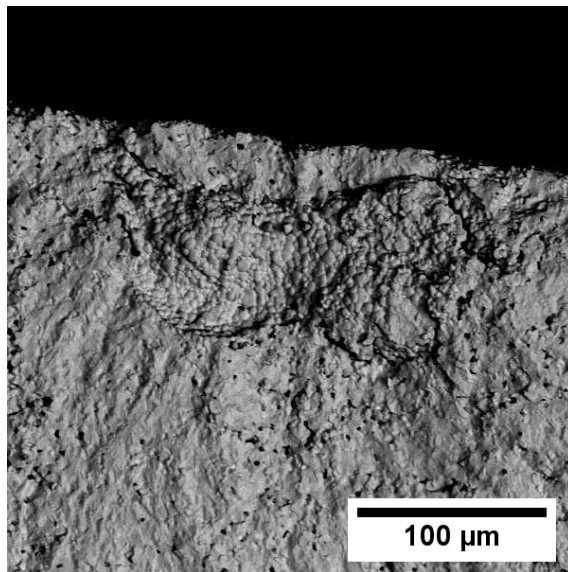
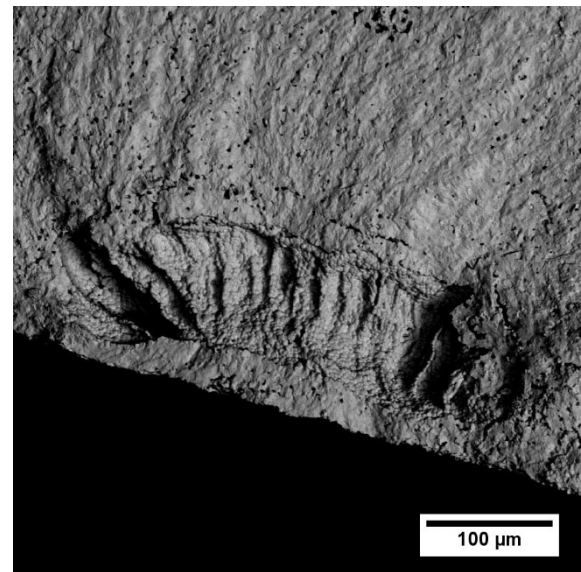


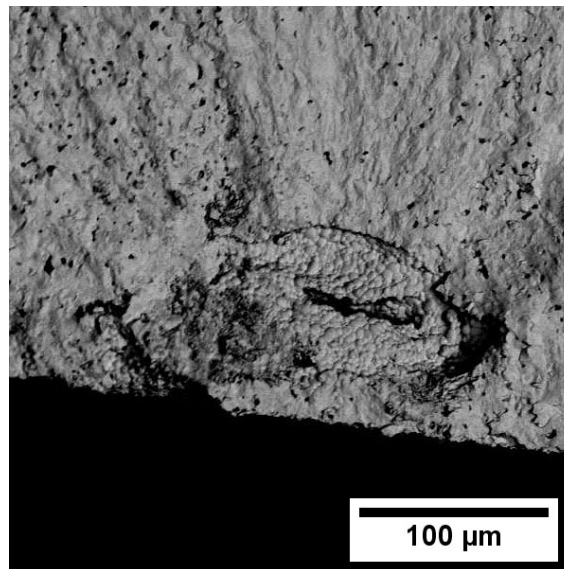
Figure 8-34 Strength box plots of all batches in the Fe doping series.



Sample 23



Sample 22



Sample 1

**Figure 8-35 Volume located fracture origins in samples from batch 10.**

The distribution location of batch 4 with 0 at% Fe is at a lower strength than those of the Fe-doped batches, as is apparent from Figure 8-34. A similar conclusion can be drawn from the graph of Weibull strength presented in Figure 8-36 a). Doping with 0.4 at% Fe increases strength from 58.9 to 78.3 MPa. An additional increase in strength to 84.1 MPa is observed when the Fe content is increased to 1.4 at%. Doping with 2.0 % Fe does not have any further effect according to the 95% CI. It can be concluded that doping the

$(\text{Pb}_{0.95}\text{Sr}_{0.05})(\text{Zr}_{0.52}\text{Ti}_{0.48})_{1-z}\text{Fe}_z\text{O}_3$  with Fe increases its strength. The role of microstructural and other factors will be discussed in section 8.4.10.

The Weibull shape factor (Figure 8-36 b) did not show any consistent correlation with Fe doping. Batch 13 exhibited a larger  $m$  value (23) than other batches (15–16). The reason for this phenomenon is not clear. Fractography of the full dataset would likely help to answer this question. The modulus of batch 13 was unusually high even compared to the  $(\text{Pb}_{0.95}\text{Sr}_{0.05})(\text{Zr}_y\text{Ti}_{1-y})_{0.986}\text{Fe}_{0.014}\text{O}_3$  compositions with varying Zr content.

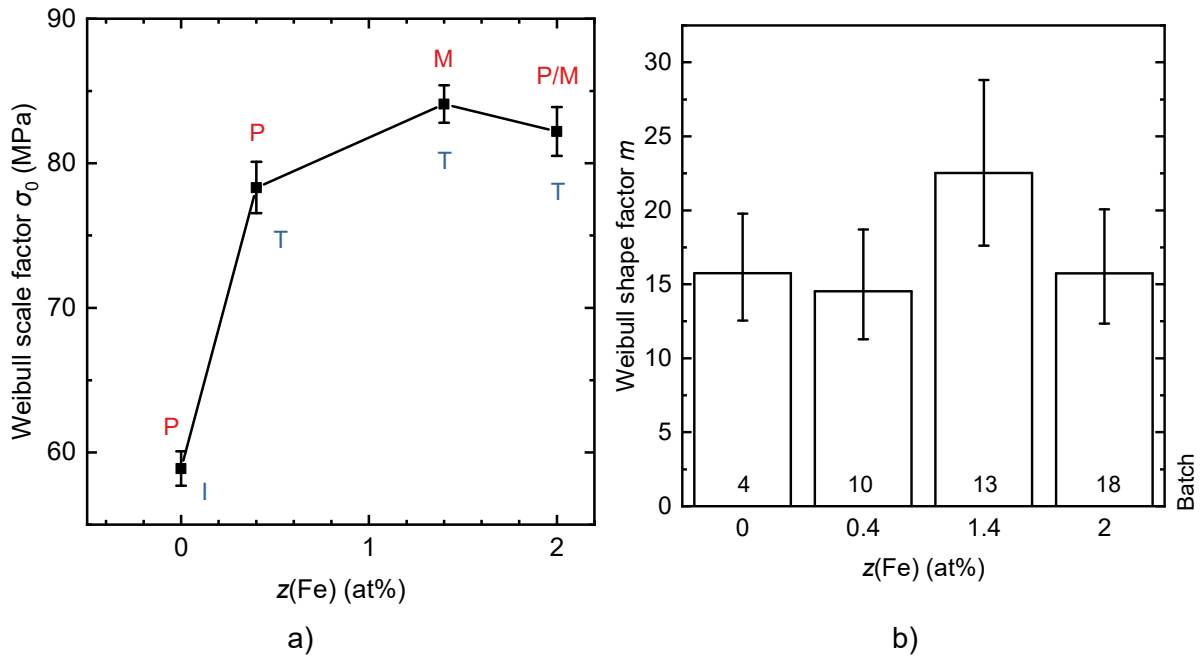


**Figure 8-36** Plots of Weibull a) scale and b) shape factors of all batches in the Fe doping series. Error bars represent 95% CI. Notes above the data points indicate the prevalent fracture origin: M = machining damage, P = porosity; notes below data points indicate prevalent mode of fracture: I = intergranular, T = transgranular.

#### 8.4.8 Commercial material

All materials in this work were processed in small batches using laboratory techniques, different from large scale industrial processing. The most notable difference was in binder mixing, which was done in a low-moisture state using a spatula and sieve instead of spray drying, which is generally used for large batches (> 50 kg). It is therefore desirable to compare batches made in this work with a commercial material to be able to make industrially applicable conclusions.

##### *8.4.8.1 Physical and mechanical properties excluding strength*

The commercial material of choice was NCE81 produced by CTS Corp. It is a hard PZT material that has similar piezoelectric properties to those of the Fe-doped compositions in this work. The material was received as a binder-containing powder, which was then processed in the same way as other batches in this work, including surface finishing. For convenience, the commercial material will be labelled as “CTS”.

The physical and mechanical properties of the commercial samples are listed in Table 8-10. The ranges of property values compiled from all the Fe-doped composition sintered at 1310 °C (including batch 9 with 0 at% Sr) are also shown for comparison. The grain size, relative density, elastic modulus and Vickers hardness of the CTS samples are all well within the range of the compositions prepared in this work. The surface roughness value of 5.6  $\mu\text{m}$  corresponds to the highest  $R_z$  value found in the Fe-doped compositions (batch 11).

Table 8-10 Comparison of physical properties of commercial hard PZT (CTS) and Fe-doped compositions prepared in this work.

	<b>CTS<sup>†</sup></b>	<b>Fe-doped compositions<sup>‡</sup></b>
$G_a$ ( $\mu\text{m}$ )	1.3 (0.2)	1.0–2.4
$\rho_{\text{rel}}$ (%)	97.4 (0.1)	97.0–98.1
$Y$ (GPa)	85.9 (0.6)	79.5–95.5
$H_v$ (GPa)	4.0 (0.1)	3.4–4.2
$R_z$ ( $\mu\text{m}$ )	5.6 (0.6)	3.7–5.3

<sup>†</sup>values in brackets represent SDM.

<sup>‡</sup>Values combined from all Fe-doped batches 9–18, excluding 14 and 15, which were sintered at different temperatures.

The pore size distribution of the CTS samples is plotted in Figure 8-37 along with data from batches from the Fe doping series. Corresponding surface micrographs are shown in Figure 8-38. The distribution of pore sizes in the CTS batch is similar to that of the undoped PSZT, except for pores with a Feret diameter below 8  $\mu\text{m}$ , where the CTS samples show significantly fewer pores. Compared to the Fe-doped compositions, the CTS material shows a higher percentage of larger pores and less finer porosity. In contrast to the prepared compositions, no pore clusters were found in the commercial samples. Visual observations also suggested that the CTS samples contained less large non-equiaxiated pores. These described differences in porosity are most likely related to the method of binder mixing.

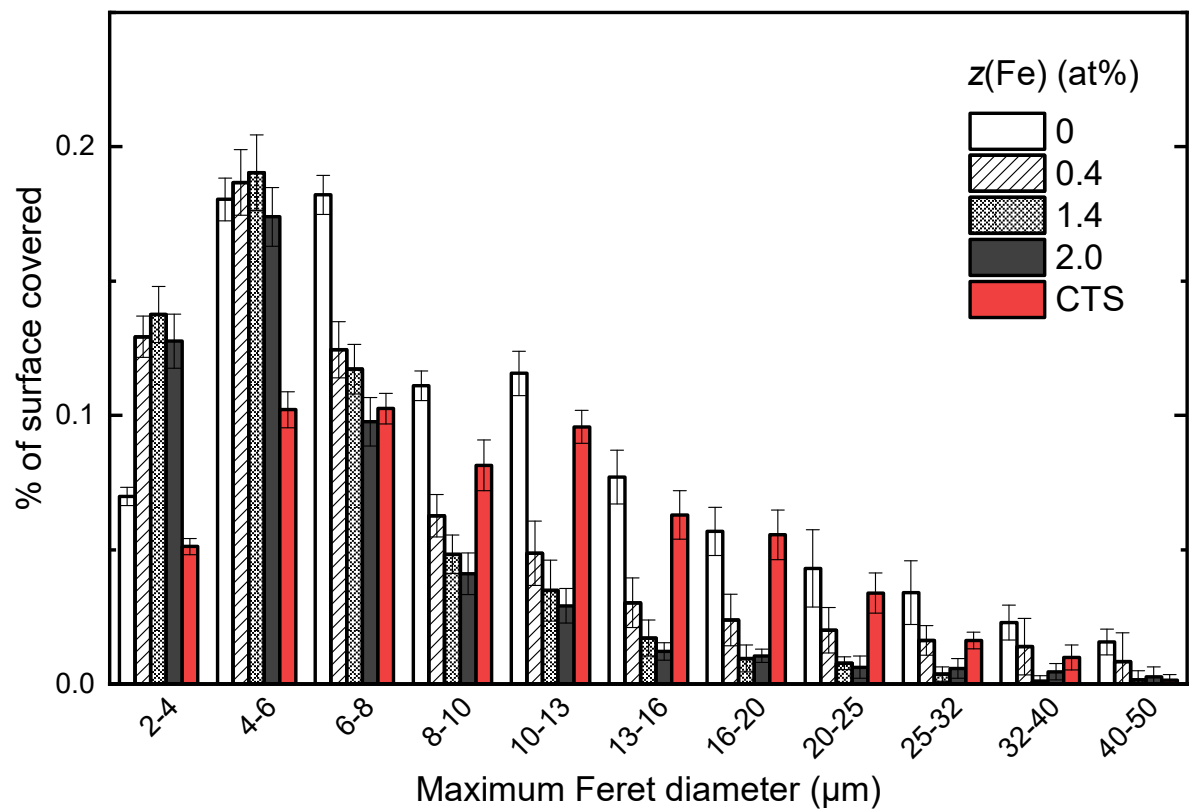
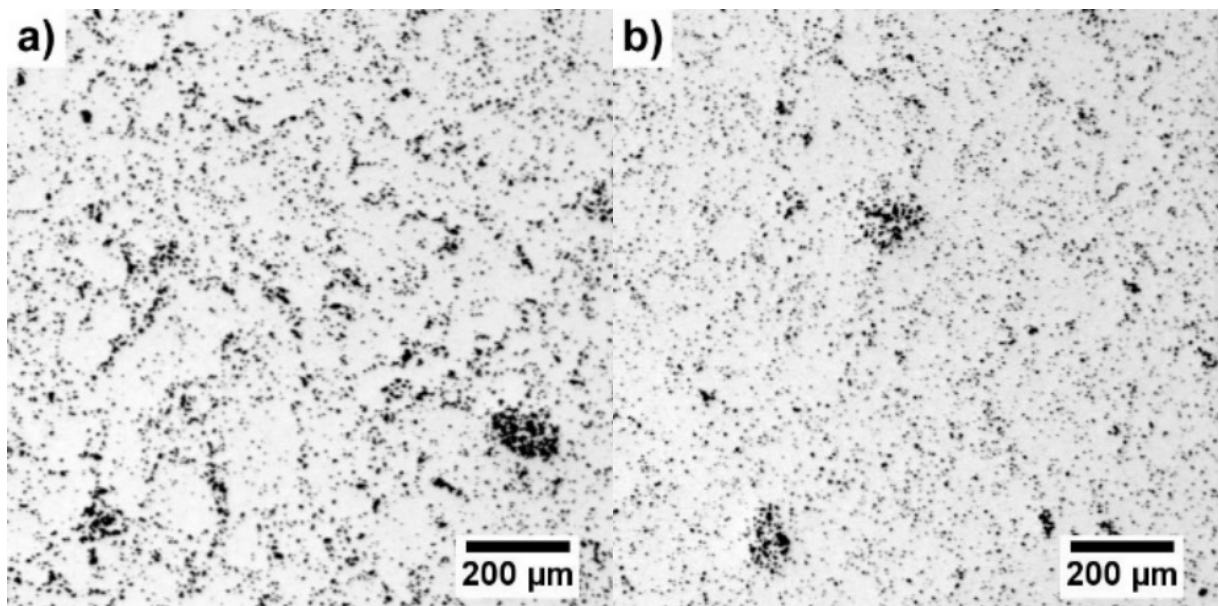


Figure 8-37 The percentage of surface area covered by pores of certain maximum Feret diameter in a commercial PZT (CTS) compared to  $(\text{Pb}_{0.95}\text{Sr}_{0.05})(\text{Zr}_{0.52}\text{Ti}_{0.48})_{1-z}\text{Fe}_z\text{O}_3$  doped with varying Fe content prepared in this work.



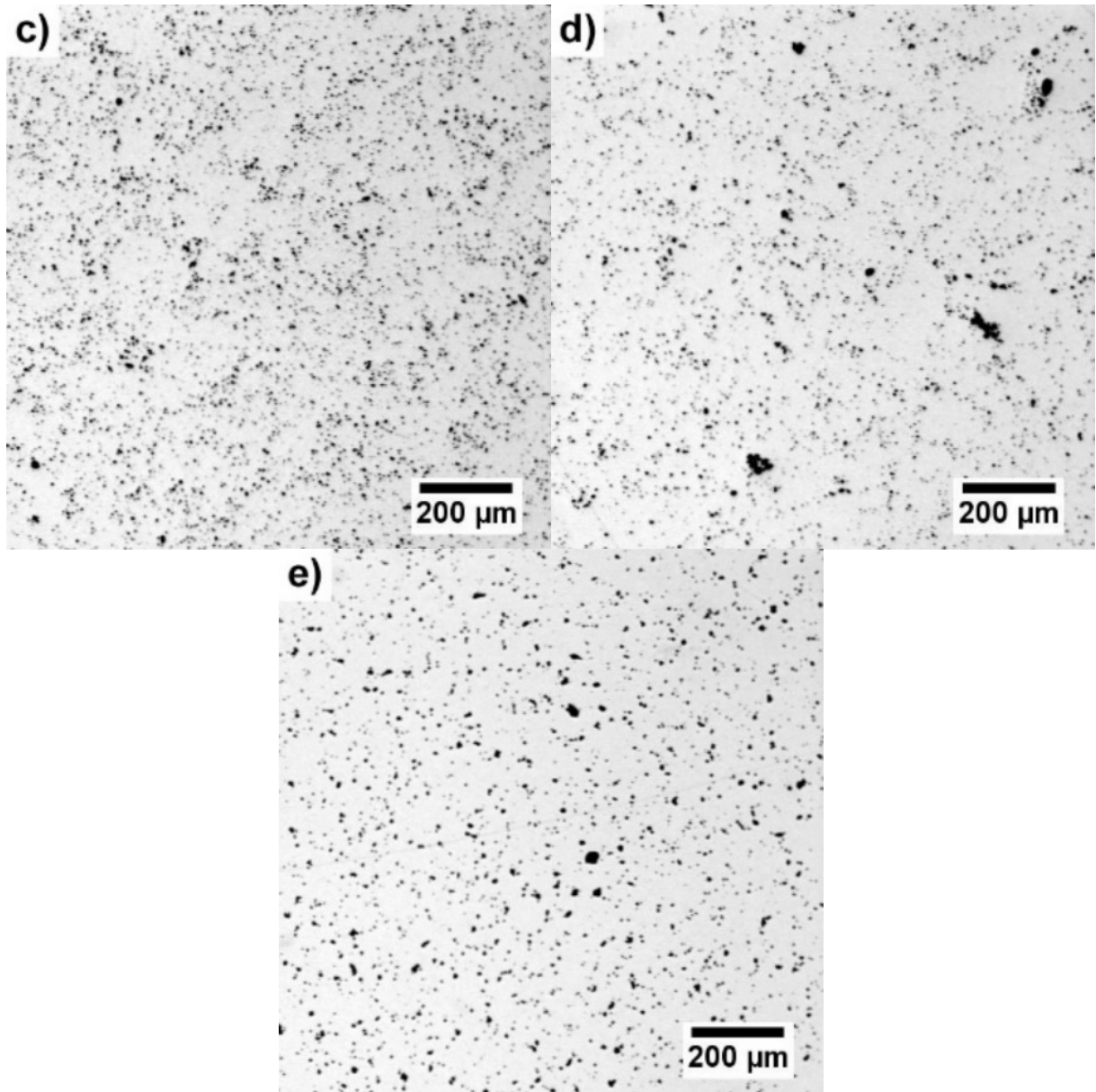
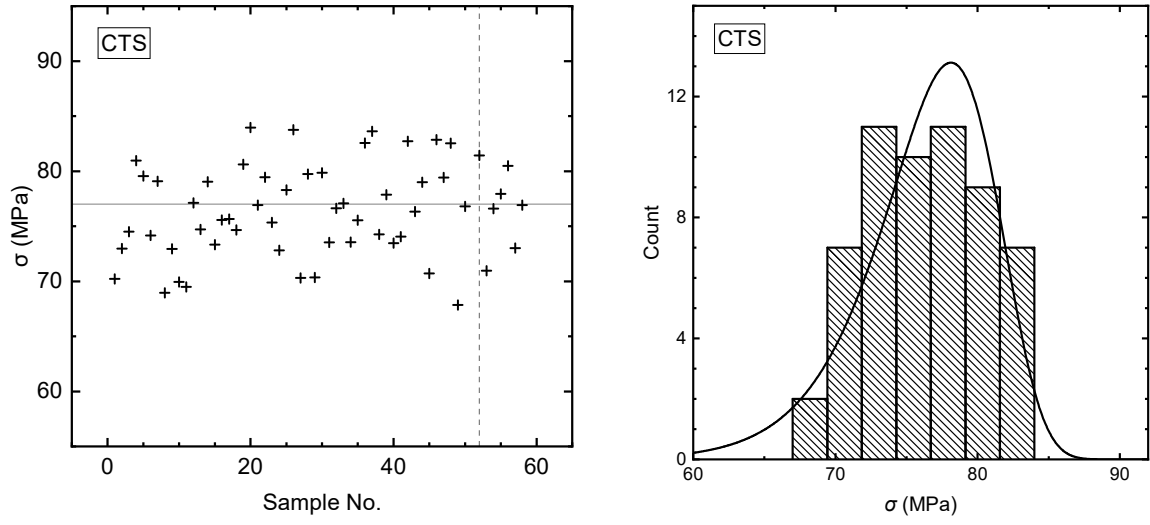


Figure 8-38 Optical micrographs of polished surfaces of  $(\text{Pb}_{0.95}\text{Sr}_{0.05})(\text{Zr}_{0.52}\text{Ti}_{0.48})_{1-z}\text{Fe}_z\text{O}_3$  doped with  $z =$  a) 0.000, b) 0.004, c) 0.014, d) 0.020 compared with commercial material in e).

#### 8.4.8.2 Strength

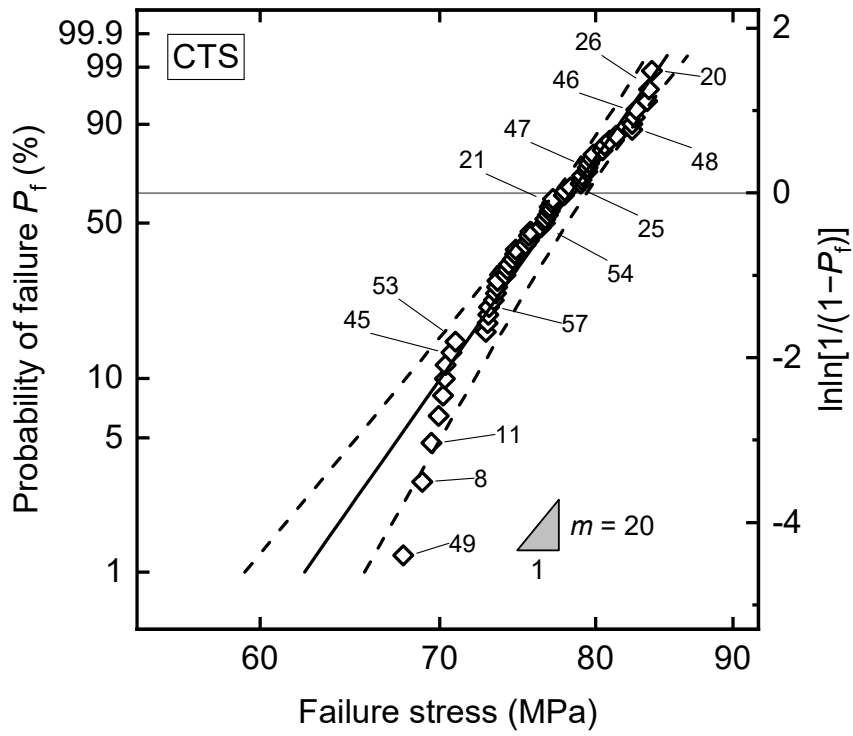
Graphs relating to biaxial flexural strength testing of the CTS samples are shown in Figure 8-39. Significantly more samples were made of the commercial material than of the prepared batches for trial testing purposes. A total of 58 samples were strength-tested. 52 were tested as an initial batch, prior to any of the prepared batches, and 6 samples were tested as the last batch to see if there were any significant differences in location of the scatter. As seen in Figure 8-39 a), the location did not significantly change, the scatter appears random and without any obvious outliers.

The histogram in Figure 8-39 b) reveals an unexpectedly high presence of weaker samples compared to the predicted distribution. This may suggest the presence of multiple flaw populations. The Weibull fit in the failure probability plot (Figure 8-39 c)) also suggests a similar point. However, this phenomenon may also be influenced by the testing issues found in batches 1–4, even though no discrepancies were found in the test sequence plot of the CTS samples. Except for the weakest samples, the dataset exhibits a good fit to a Weibull distribution. The Weibull distribution was not rejected even for the uncensored dataset with  $p(A-D) = 0.12$ .



a)

b)



c)

Figure 8-39 a) Test sequence plot, b) histogram and c) probability plot with Weibull distribution fit of strength results of commercial PZT. The vertical dashed line in the test sequence plot separates 2 datasets tested before/after testing prepared compositions, the horizontal solid line represents the mean strength value. Dashed lines in the probability plot represent 95% CI, marked samples had their fracture surface examined using SEM.

Table 8-11 Results of A-D tests and fracture origin investigations of commercial PZT samples.

<b>CTS</b>								
<b>Number of specimens: 58</b>								
<b>Mode: transgranular</b>								
<b><math>p(A-D)^{\dagger} = 0.12</math></b>								
Sample no.	Identity	Approx. size ( $\mu\text{m}$ )	Sample no.	Identity	Approx. size ( $\mu\text{m}$ )	Sample no.	Identity	Approx. size ( $\mu\text{m}$ )
49	MD	90	57	MD	?	48	?	?
8	MD	?	54	MD	80	46	MD	60
11	MD	?	21	P	60	26	MD	?
45	?	?	25	MD	70	20	MD	?
53	?	?	47	MD	60			

Key: A = agglomerate, P = pore, PR = porous region, PS = porous seam, HD = handling damage, MD = machining damage, ? = unknown

<sup>†</sup>p value of Anderson-Darling goodness-of-fit test

The fracture origin investigations, summarised in Table 8-11, show that the dominant fracture origin was machining damage. This agrees well with the porosity results. In the prepared batches, the weakest samples failed mostly from clusters of pores, porous seams or irregularly shaped large pores. Observations showed no presence of such features in the commercial material; therefore, the strength is limited by the second most prevalent fracture origin – machining damage. Since CTS samples showed similar physical properties to the Fe-doped batches, it would be expected to show a similar strength as both were mostly limited by machining damage. This was the case, as illustrated in Figure 8-40, where the strength distribution of CTS samples in the form of a box plot lies well within the strength range of the Fe-doped sample batches. The exact values are summarised in Table 8-12. The width of the CTS distribution (16 MPa) was lower than of any other batch in the box plot, as would be expected from the batch with a more homogeneous microstructure, free of extreme volume-type defects.

Since extreme porous defects were not found on a polished surface of the commercial material, surface polishing would be expected to increase its strength. To verify this, a set of 10 samples was polished to 1 $\mu$ m finish and tested in the same manner as other samples. The set, labelled as CTS-P, is included in Figure 8-40 and clearly shows a strength increase of the whole population. Another effect of polishing is an increase in distribution width from 16 to 21 MPa.

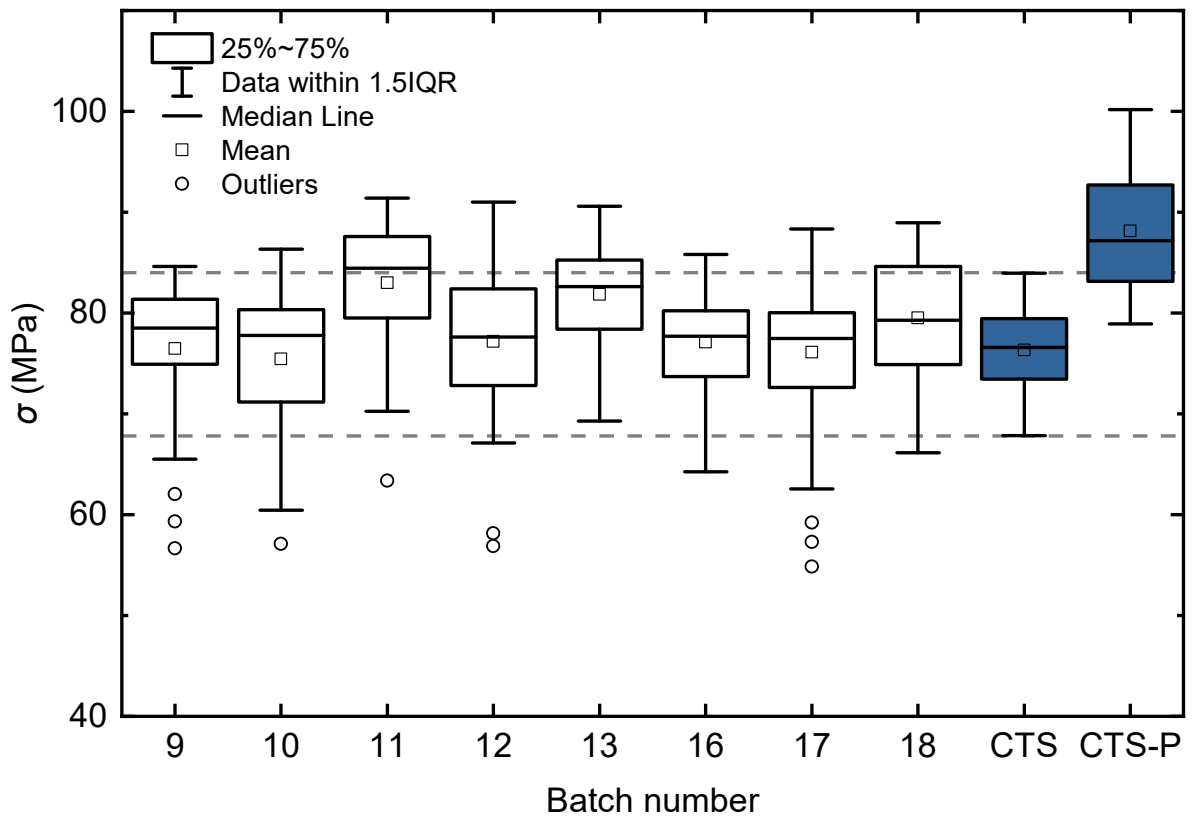


Figure 8-40 Strength box plots of all Fe-doped batches sintered at 1310 °C, commercial PZT (CTS) and polished commercial PZT (CTS-P).

Table 8-12 Comparison of mechanical properties of commercial hard PZT (CTS) and Fe-doped compositions prepared in this work.

	CTS	CTS-P <sup>†</sup>	Fe-doped compositions <sup>‡</sup>
$\sigma_{\min}-\sigma_{\max}$	67.8–84.0	78.9–100.2	54.9–91.4
$\sigma_0$ [95% CI] (MPa)	78.3 [77.3, 79.4]	91.3 [86.6, 96.3]	78.3–85.6
$m$ [95% CI]	20.2 [16.5, 24.6]	13.7 [8.2, 23.1]	12.6–22.5

<sup>†</sup>surface polished to 1 $\mu$ m finish

<sup>‡</sup>Values combined from all Fe-doped batches 9–18, excluding 14 and 15, which were sintered at different temperatures.

The Weibull strength of the CTS commercial PZT (78.3 MPa) was on par with that of batch 10 (0.4 % Fe), the weakest Fe-doped composition. Polishing increased the Weibull strength to 91.3 MPa, the highest value recorded. Table 8-12 shows that Weibull modulus of CTS decreased with polishing from 20 to 14. Both values are within the range of the prepared compositions.

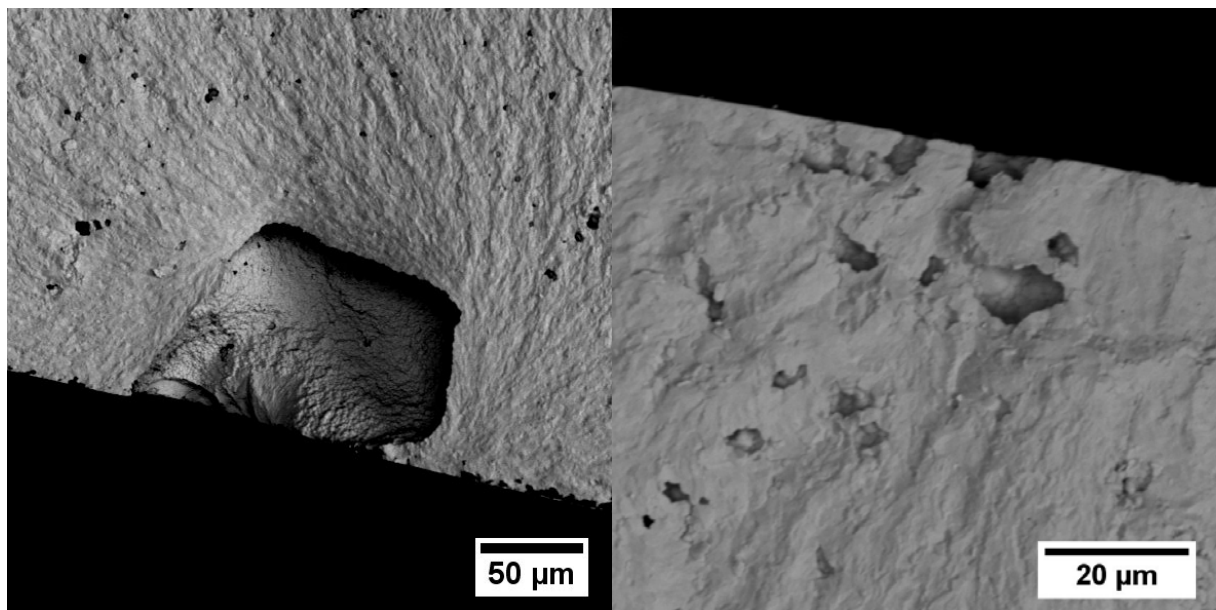
Table 8-13 summarizes the fracture origin investigations of CTS-P. The majority of specimens exhibited porosity as their dominant flaw population. 2 samples were removed from the strength population as their fracture origins were located outside of the load ring area. One of these samples, number 9, failed from a pore shown in Figure 8-41, which was the largest defect found. It suggests that even commercial material contains extreme porous flaws, but they are less frequent. Other fracture origins were on a smaller size scale compared to the origins found in the prepared batches, which is consistent with the measured increase in strength. While many of the critical defects were easily identified, such as porous region in sample 6, some remained unclear, for example, samples 1 and 4 shown in Figure 8-41. Sample 1 showed a sharp object inside its fracture mirror, which could possibly be a large grain, but it also has a pore right next to it. The fracture might have originated from either flaw or from both. Sample 4 exhibited a semi-circular area near the surface with visibly sharp grain boundaries. Because the boundaries

are sharp, it is probably not a pore. Possible explanations include grain pull-out during the polishing process or remnants of the original machining damage as the sample thickness removed by polishing might have been too small.

Table 8-13 Results of fracture origin investigations of polished commercial PZT samples.

<b>CTS-P</b>								
<b>Number of specimens: 10</b>								
<b>Mode: transgranular</b>								
No.	Identity	Approx. size (μm)	No.	Identity	Approx. size (μm)	No.	Identity	Approx. size (μm)
4	?	20	7	PR	?	2 <sup>†</sup>	?	12
9 <sup>†</sup>	P	135	3	PR	?	10	PS (V)	> 8
8	PR	17	6	PR	?			
1	?	20	5	P	12			

<sup>†</sup>failed from flaw located outside the load ring area; removed from strength results



No.9

No. 6

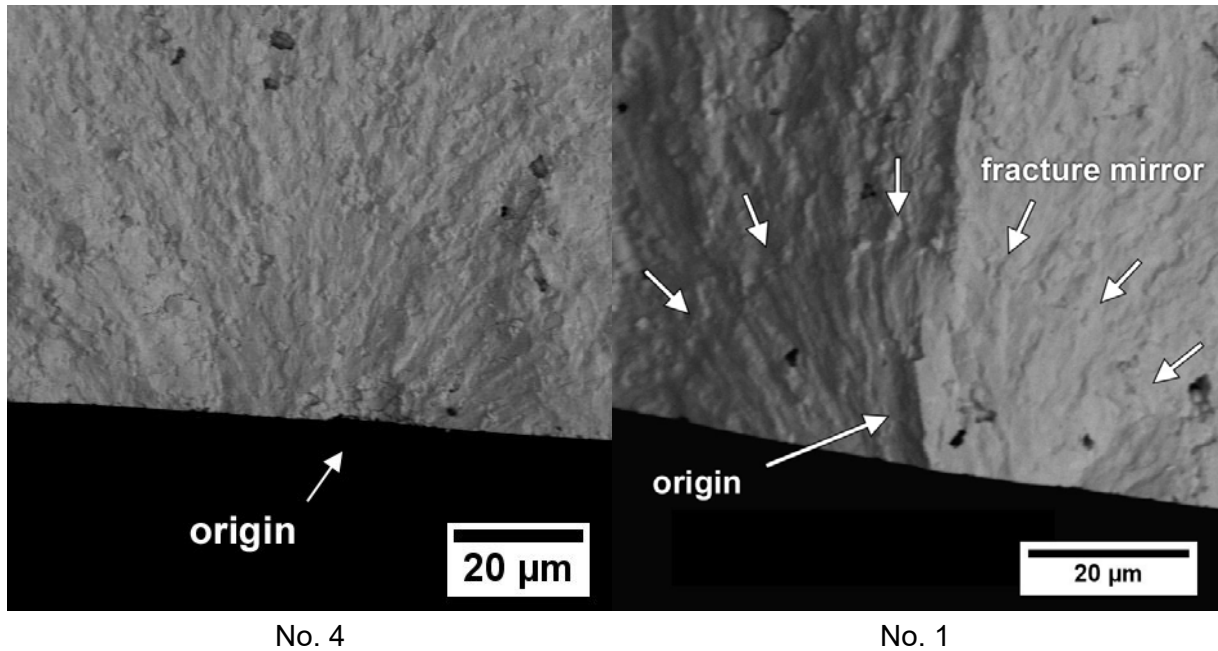


**Figure 8-41** Examples of fracture origins found in CTS-P (samples number 1, 4, 6 and 9).

The reliability of both commercial batches (as machined and polished) is likely connected to their critical defects. The unpolished batch of CTS samples showed an  $m$  value of 20 similar to laboratory prepared samples as they both exhibited similar machining damage as the dominant flaw population. Polishing increased the strength overall, but the critical flaws in the weakest samples were still on a strength level consistent with machining damage, while the strongest samples showed values as high as 100 MPa, widening the strength range and decreasing reliability.

#### 8.4.9 Ferroelastic effects

The phenomenon of stress-induced domain reorientation absorbing the energy of the opening crack and thus increasing the measured strength of a ferroelectric (or ferroelastic) material was introduced in section 2.4. This becomes an issue when multiple materials of different susceptibility to domain switching are compared, as their strengths might not be affected in the same manner. The PZT-based materials investigated in this work contained various concentrations of  $\text{Fe}_2\text{O}_3$ , which makes the material ferroelastically hard and less susceptible to domain switching at room temperature compared to undoped material. It is therefore important to address whether domain switching may have had an impact on the strength results and their interpretation presented here. Estimation of the ferroelastic contributions to strength is a complicated task. Fett et al. [194] separated the elastic and plastic contributions to the strain of soft PZT loaded in 4-point bend configuration using 2 pairs of strain gauges, one on the compressive face of the sample and the other on the tensile side. The true stress on the tensile side of the specimen was calculated using the procedure described by Nadai in [195], as opposed to the commonly used stress computed from equations based on the LEFM. In a follow-up paper [196], Fett et al. concluded that ferroelastic switching accounted for 20 % of the elastically calculated strength of unpoled soft PZT (fracture strength around 60 MPa).

Unfortunately, the fixture design and sample size used in this work did not permit the use of strain gauges. In addition, equibiaxial loading conditions are more complex than the uniaxial conditions in 4-point bend. Therefore, in this work, other methods have been used to estimate the ferroelastic contributions to the data measured, and the strengths presented.

Figure 8-42 shows boundary loading curves, which represent boundaries of an area where loading curves of other specimens were located. The graph compares linearly elastic material,  $\text{Al}_2\text{O}_3$ , with all the PZT-based batches prepared in this work. Significant non-linearity can be

observed, which was primarily caused by the rubber and PTFE tape used to minimise friction between the sample and the fixture. It can be assumed that this effect is approximately constant for all materials. There is no apparent deviation of PZT-based samples from alumina.

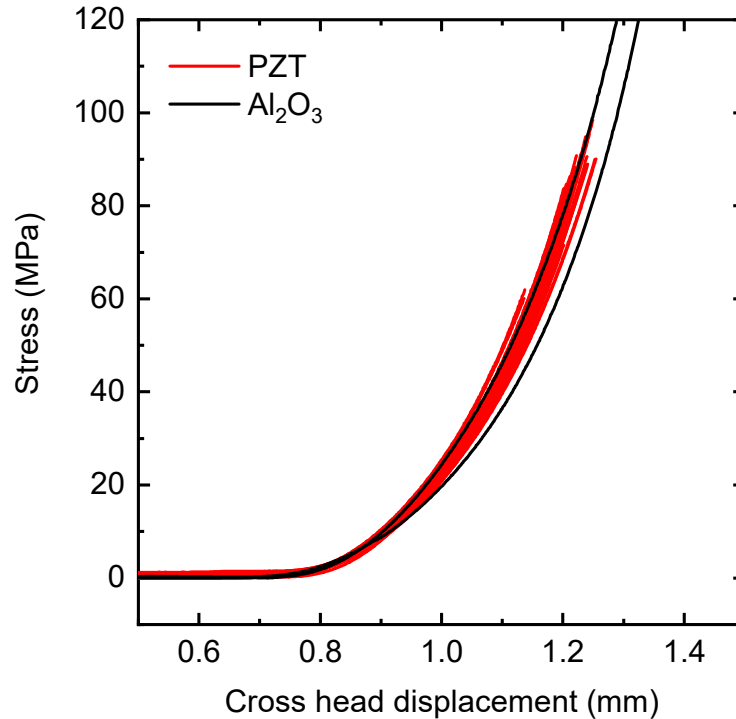
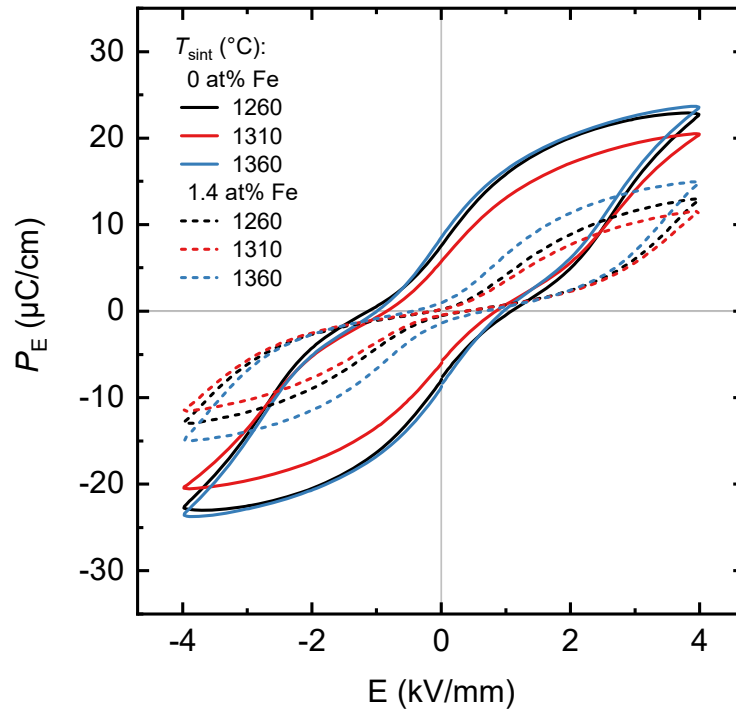


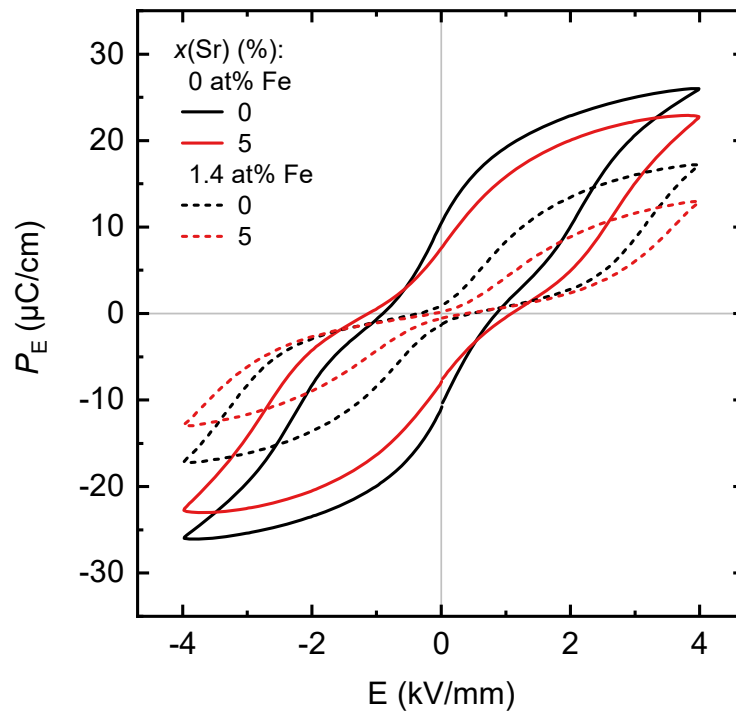
**Figure 8-42 Boundary loading curves of Al<sub>2</sub>O<sub>3</sub> and all prepared batches (boundary curves were 2 curves between which all other loading curves were located).**

Ferroelectric domains can be switched by either electric field or stress. Polarisation-electric field ( $P_E$ - $E$ ) and current-electric field ( $I_E$ - $E$ ) hysteresis loop measurements should therefore provide a tool for comparing the susceptibility to domain reorientation between the materials of interest.  $P_E$ - $E$  loops of the prepared materials grouped by the factors of interest are shown in Figure 8-43.  $P_E$ - $E$  loops of PZT doped with varying Fe concentration were already presented in section 7.3, Figure 7-9 a). All materials exhibited “pinched” loops typical for hard-doped materials, which was explained in section 2.5.2. The piezoelectric response increases as the Zr/Ti ratio approaches and passes the MPB. The maximum remanent polarisation ( $P_r$ ) has not

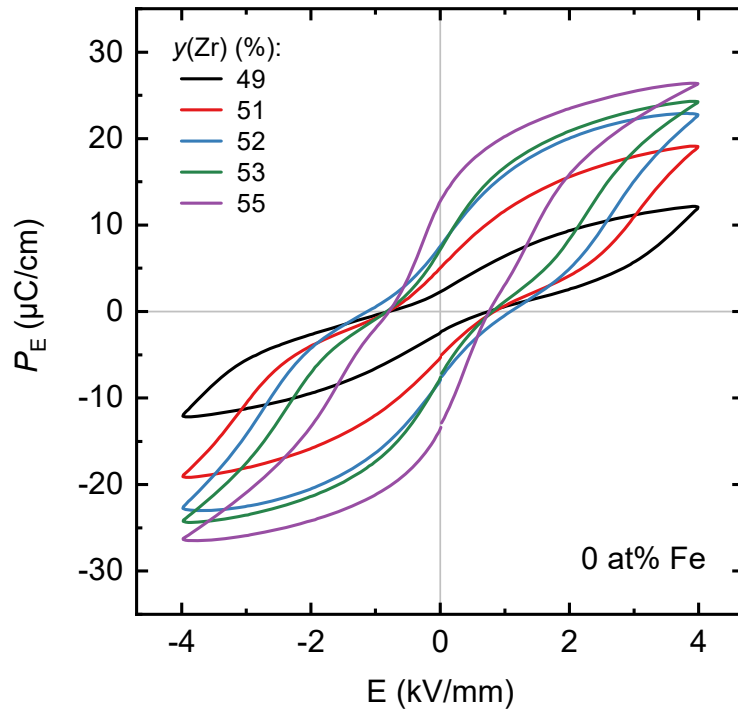
been observed in the current range of Zr/Ti ratios. This agrees with previously reported data and has been discussed in section 7.4.



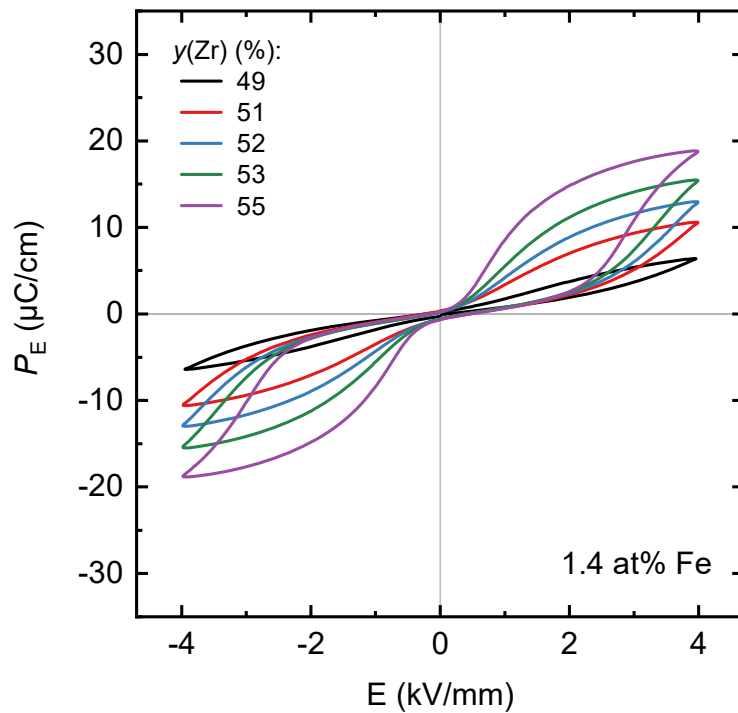
a)



b)



c)



d)

**Figure 8-43**  $P_E$ - $E$  loops of prepared  $(\text{Pb}_{1-x}\text{Sr}_x)(\text{Zr}_y\text{Ti}_{1-y})_{1-z}\text{Fe}_z\text{O}_3$  samples grouped by the following factors: a) sintering temperature and Fe doping, b) Sr doping and Fe doping, c) Zr/Ti ratio ( $z = 0.0$  at%), d) Zr/Ti ratio ( $z = 1.4$  at%) .

Schäufele and Härdtl [31] have shown that the coercive stress ( $\sigma_c$ ) correlates with the coercive field ( $E_c$ ) in a roughly linear fashion. This is illustrated in Figure 8-44, which contains data from their experiments. The onset of switching can be estimated as approximately 30 MPa lower than the coercive stress based on the visual examination of 2 loading curves presented in the paper (load at which curves diverged from linearity).

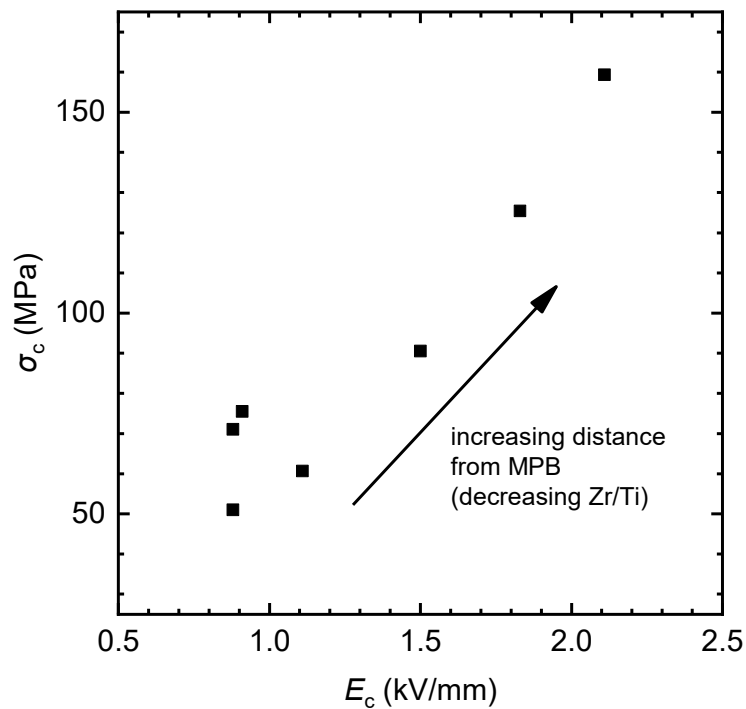


**Figure 8-44 Plot of coercive stress versus coercive field for soft PZT (replotted from [31])**

The coercive field of each batch in this work was determined from their respective  $I_E$ - $E$  hysteresis loops. The dependence of coercive field on composition and sintering temperature is shown in Figure 8-45. As expected, the coercive field generally increased with increasing distance from the MPB and increasing Fe content. The “hardening” effect of Sr agrees with XRD observations, which showed that the MPB shifts towards higher  $y$  in  $(\text{Pb}_{1-x}\text{Sr}_x)(\text{Zr}_y\text{Ti}_{1-y})_{(1-z)}\text{Fe}_z\text{O}_3$  (discussed in section 7.2). The lowest coercive field of  $\approx 1.5$  kV/mm was exhibited by batch 8 with  $z(\text{Fe}) = 0$  at% and  $y(\text{Zr}) = 55$  at%. This corresponds to a coercive stress of 90 MPa and onset of domain switching of roughly 60 MPa, according to [31].

Since the Weibull strength of this batch was 68 MPa, it cannot be ruled out that domain switching did not affect this result. Batches 7 and 8 with  $y = 53$  and  $55$  at% respectively showed an increase in strength while the strength of compositions up to  $y = 52$  at% monotonously decreased. Batch 7 exhibited a coercive field of  $\approx 2.3$  kV/mm, which corresponds to the onset of switching above 100 MPa. This is well above its achieved Weibull strength of 64 MPa. Seo et al. [197] found an increase in toughness when the Zr/Ti ratio was  $\geq 53/47$  in soft PZT, which corresponds to the strength increase found in this work. They concluded that the increase was caused by higher domain switchability (lower coercive stress) on the Zr-rich side of the MPB, which was tied to lower lattice distortion. Additional measurements would be necessary to see if that was the case in this work.

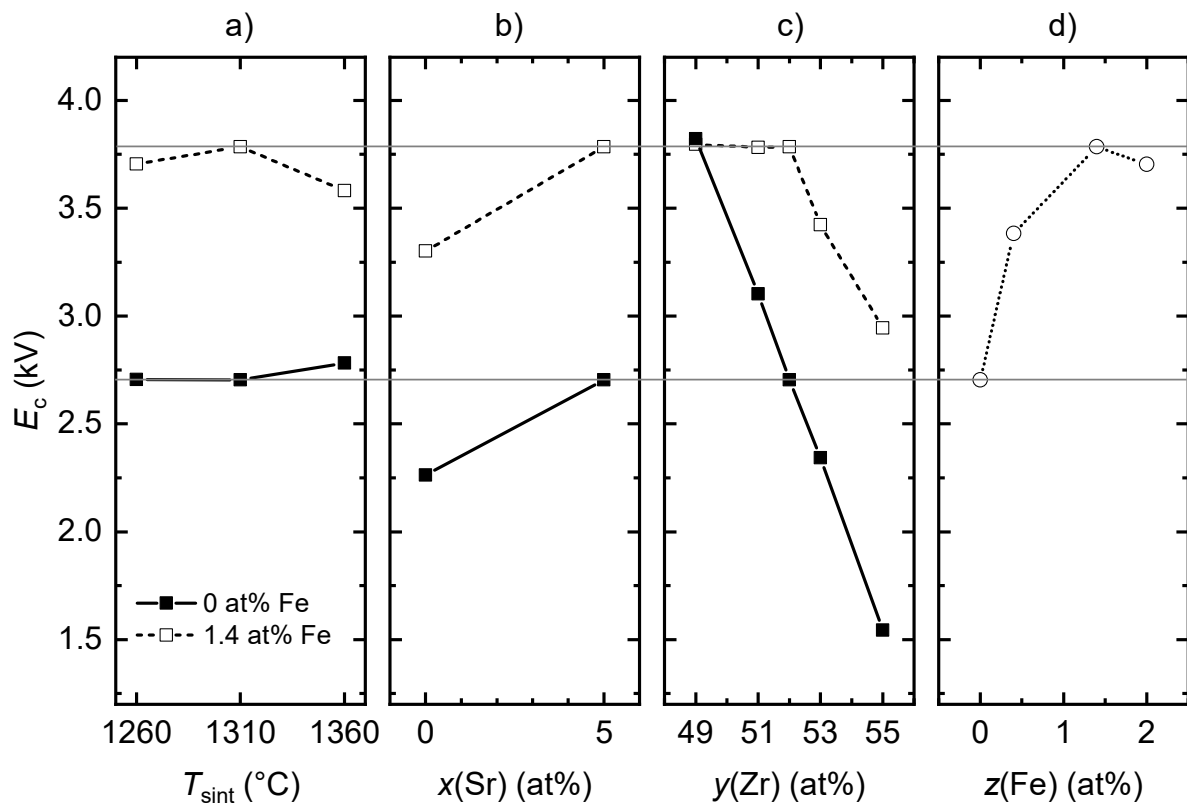


**Figure 8-45** Dependence of coercive field on a) sintering temperature ( $T_{\text{sint}}$ ), b) Sr content, c) Zr/Ti ratio, d) Fe content of  $(\text{Pb}_{1-x}\text{Sr}_x)(\text{Zr}_y\text{Ti}_{1-y})_{1-z}\text{Fe}_z\text{O}_3$ . Grey horizontal lines connect single central compositions,  $T_{\text{sint}} = 1310$  °C if not stated otherwise.

The last aspect to discuss is the number of directions from which domains can be theoretically switched by different loading conditions. When a bar is loaded in 3- or 4-point bend, randomly oriented domains on the tensile side switch to a single axis, as illustrated in Figure 8-46 a). Equibiaxial loading induces domain switching to a plane (see Figure 8-46 b)), therefore less domains are switched than in the 3 or 4-point bend. This means that the strength obtained from equibiaxial flexural test should be somewhat less affected by domain switching, than in 3- or 4- point bend.

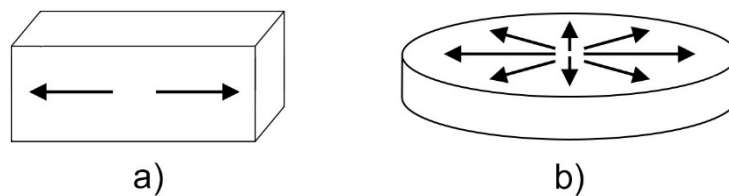


**Figure 8-46 Possible directions of polarisation in samples loaded in a) 3- or 4- point flexure, b) equibiaxial flexure (loading directions are not shown).**

In conclusion it is considered that domain switching most likely did not significantly affect the strength results presented here, except for the Zr-rich compositions of PZT with 0 at% Fe in which the results are inconclusive.

### 8.4.10 General discussion

In this section, the strength results from all batches are compared and discussed together in the context of the individual processing/compositional factors. Figure 8-47 shows the dependence of the Weibull strength of all batches on their respective factors. All Fe-doped compositions exhibited higher strength than other compositions, regardless of the processing conditions. They also showed transgranular fracture modes and their strengths were mostly limited by machining damage, except for batch 15, sintered at 1360 °C, and batch 10, doped with 0.4 at% Fe. A mixture of machining damage and porosity as competing flaw distributions are the most probable reasons why the majority of acceptor-doped compositions exhibit wider 95% confidence intervals.

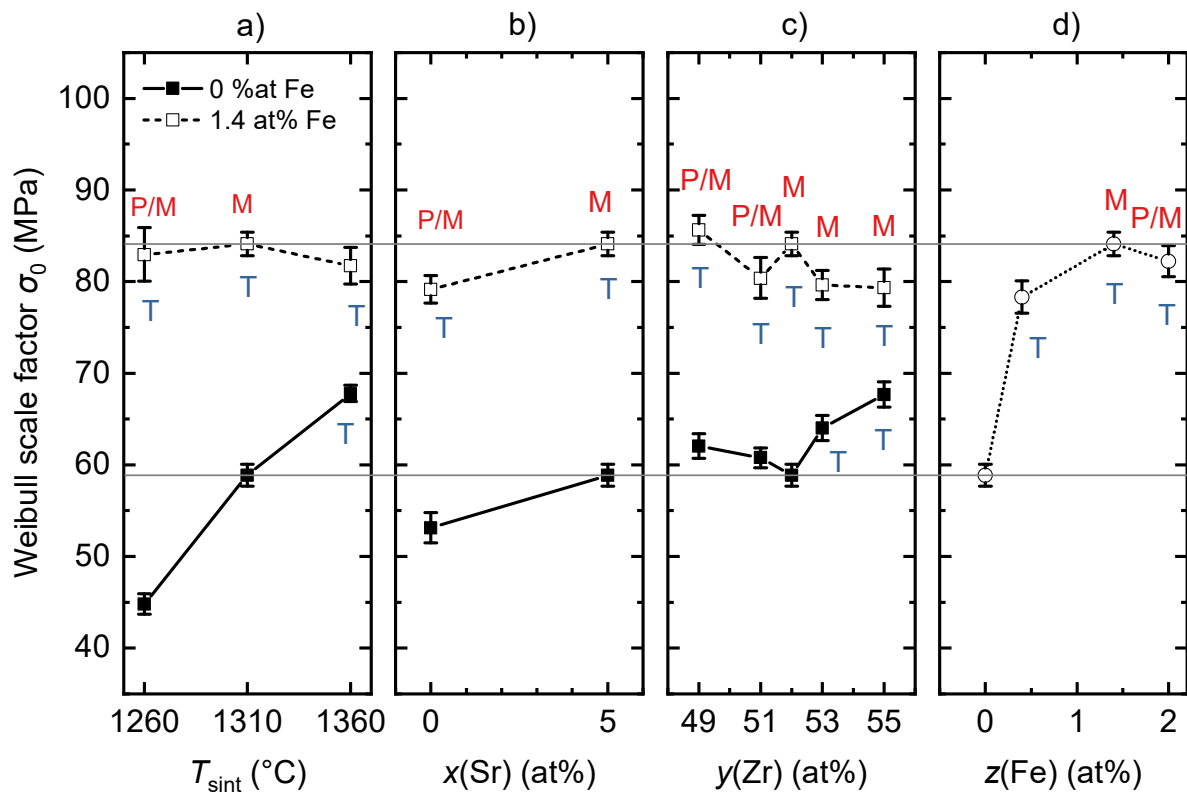


**Figure 8-47** Dependence of Weibull strength on a) sintering temperature ( $T_{\text{sint}}$ ), b) Sr content, c) Zr/Ti ratio, d) Fe content of  $(\text{Pb}_{1-x}\text{Sr}_x)(\text{Zr}_y\text{Ti}_{1-y})_{1-z}\text{Fe}_z\text{O}_3$ . Grey horizontal lines connect single central compositions. Error bars represent 95% CI. T = transgranular fracture mode; fracture origin: P – porosity, M – machining damage. Batches with porosity as dominant fracture origin and/or intergranular fracture were left unmarked.

A scatterplot of Weibull strengths versus porosity is shown in Figure 8-48. Results show a general decreasing trend of strengths with increasing porosity, however, additional conclusions can be made when the batches are separated based on Fe content. The strength of Fe-doped compositions appears disjointed from the undoped batches and unaffected by density as batch 14 ((Pb<sub>0.95</sub>Sr<sub>0.05</sub>)(Zr<sub>0.52</sub>Ti<sub>0.48</sub>)<sub>0.986</sub>Fe<sub>0.014</sub>O<sub>3</sub> sintered at 1260 °C) shows similar strength as the other Fe-doped compositions despite exhibiting significantly higher porosity. Separation of the data into distinct populations would be expected since there is an overall difference in most properties and dominant fracture origin identity. It should be noted that compositions with 0.4 and 2.0 at% Fe (batches 10 and 18) do not stand out from the rest of the Fe-doped compositions.

Compositions with no acceptor doping (0 at% Fe) do not show an overall trend. Batches 6, 7 and 8 exhibit higher strength than the rest of the undoped compositions. A common feature of these batches is the transgranular fracture mode, as indicated by the grey dashed ellipse in Figure 8-48. Batch 1 shows lower strengths than other batches of similar porosity, which may possibly be related its lack of Sr doping. If batches 1, 6, 7 and 8 discussed above are disregarded, the remaining results show a roughly linearly decreasing trend in strength with increasing porosity for the samples with 0 at% Fe. This would be expected since similarly sized fracture origins were found in all these materials. For the same reasons, a similar trend would be expected in Fe-doped compositions, however the results indicate that the strength of the Fe-doped materials is approximately independent of porosity up to a value of 4 %.

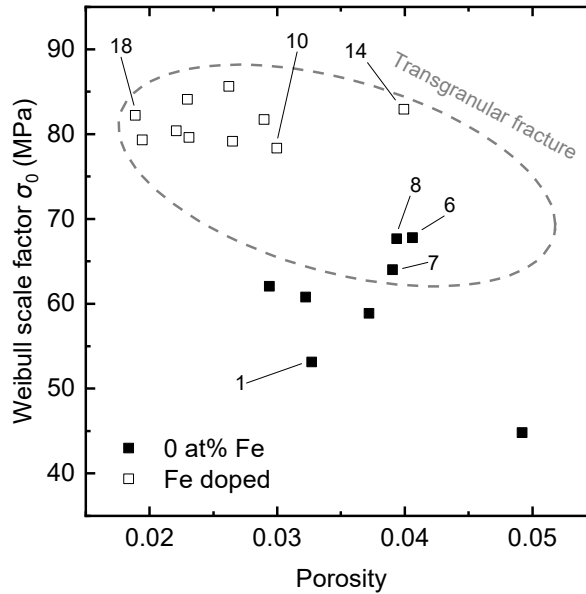


**Figure 8-48 Dependence of Weibull strength  $\sigma_0$  on porosity of  $(\text{Pb}_{1-x}\text{Sr}_x)(\text{Zr}_y\text{Ti}_{1-y})_{1-2}\text{Fe}_2\text{O}_3$  (only batches discussed in the text are labelled).**

Both strength and Young's modulus are affected by porosity, and similarities in  $Y$ - $P$  and  $\sigma$ - $P$  dependences are often observed in linearly elastic ceramics [198]. Therefore, the strength of a ceramic material would be expected to increase with increasing Young's modulus. In section 8.1 it was demonstrated that the Young's modulus of PZT is additionally affected by the presence of Sr, and the proximity to the MPB. This means that if both porosity and proximity to the MPB affect the strength of compositions prepared in this work, the  $\sigma_0$ - $Y$  dependence should show a general trend. This does not appear to be the case, as shown in Figure 8-49. Disregarding batches 6, 7 and 8, which showed transgranular fracture mode, the Weibull strengths of the remaining compositions with 0 at% Fe do not show a consistent trend with increasing  $Y$ . The strength of Fe-doped materials seems randomly scattered within a 15 GPa range and is generally higher than the strength of undoped compositions with similar  $Y$ . This means that the changes in  $Y$  are not responsible for the higher strength of the Fe-doped compositions.

An increasing trend in the  $\sigma$ - $Y$  dependence can be found when only the batches exhibiting transgranular fracture mode are considered. However, it is not clear why the batches with intergranular fracture mode would not exhibit a similar dependence.

Based on equation (2-2) both Young's modulus and fracture energy affect the fracture toughness (and strength). It is possible that the changes in the fracture energy, which were not measured in this work, are responsible for the strength differences between Fe-doped and undoped series and the lack of a general  $\sigma_0$ - $Y$  trend. Microscale fracture toughness measurements presented in section 8.4.10 give some indication whether this is true.

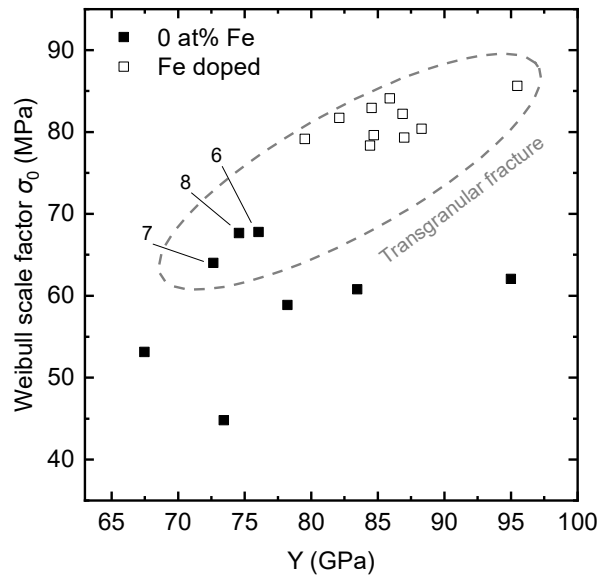


**Figure 8-49 Dependence of Weibull strength  $\sigma_0$  on Young's modulus  $Y$  (only batches discussed in the text are labelled).**

Figure 8-50 shows the dependence of Weibull strength on surface roughness. Samples with higher surface roughness exhibited lower strength. However, the roughness itself may not be responsible for this phenomenon. In case of batches with 0 at% Fe (batches 1–8), the dominant fracture origin was porosity, therefore, the roughness would not be expected to influence the strength unless it interacted with porosity and weakened (or enlarged) any existing defects. Batches 7 and 8 exhibited the lowest surface roughness values as reported in section 8.3.

Fracture surface observations revealed that this was likely due to a dominant transgranular fracture mode, which created smoother surfaces. In the case of Fe-doped samples, which failed predominantly due to machining-induced surface damage, roughness would be expected to affect strength. This was not the case, as apparent from Figure 8-50, where it can be seen that the average surface roughness varied between 3.7–5.3  $\mu\text{m}$  and did not cause any significant change in strength. There are two possible reasons for this behaviour: First, in most of these batches, machining damage was the dominant but not exclusive origin of fracture and porosity may have influenced the strength. Second, the average roughness value may not correlate with the extreme manifestations of machining damage. It is therefore concluded that surface roughness did not correlate with Weibull strength in this work.

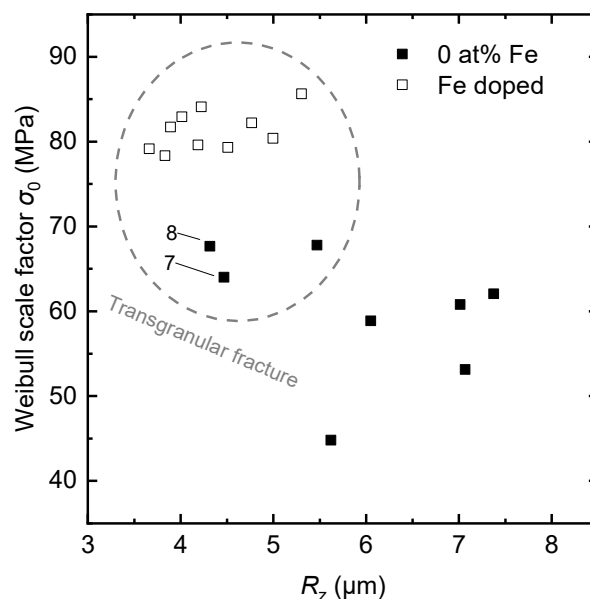


**Figure 8-50 Dependence of Weibull strength  $\sigma_0$  on surface roughness  $R_z$  (only batches discussed in the text are labelled).**

Figure 8-51 shows the dependence of the Weibull strength on the average grain size. As in the previous cases, the data appear to form 2 distinct populations. Fe-doped batches do not show any strength variation with increasing grain size. Batches not doped with Fe and which exhibit an average grain size  $\approx 4 \mu\text{m}$  show strength variations of approximately 15 MPa. Batch 6,

sintered at 1360 °C, exhibited a similar strength as batches 7 and 8 despite having a larger average grain size of 5.3 μm. Batch 5, sintered at 1260 °C, exhibited the lowest strength, which is likely the effect of its low density rather than its smaller grain size. The strength increase with increasing grain size, observed when the sintering temperature of  $(\text{Pb}_{0.95}\text{Sr}_{0.05})(\text{Zr}_{0.52}\text{Ti}_{0.48})\text{O}_3$  was increased from 1310 °C (batch 4) to 1360 °C (batch 6), can be possibly explained by a change in fracture energy. Rice et al. [199] demonstrated that fracture energy exhibits a maximum at a certain grain size for some non-cubic materials (PZT was not studied). However, the study by Zhang and Raj [200] reported no significant change in fracture toughness (which directly scales with fracture energy) for PZT with an average grain size between 1–5 μm. Change in grain size distribution presents another possible explanation. Meschke et al. [201] showed that fracture toughness of  $\text{BaTiO}_3$  increased with increasing fraction of large grains in fine-grained matrix. Figure 8-52 shows etched surfaces of batches 4 and 6 sintered at 1310 °C and 1360 °C respectively. However, it does not suggest that any of presented microstructures exhibit a bimodal grain size distribution. It is therefore concluded that the grain size was most likely not responsible for strength variations of PZT-based materials in this work.

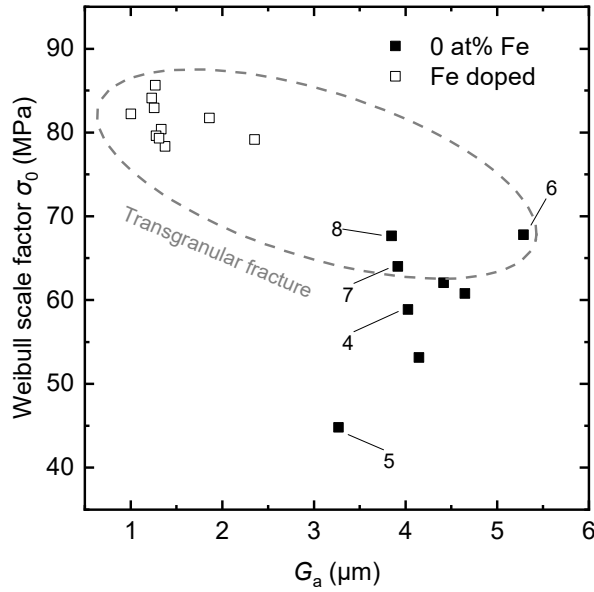


Figure 8-51 Dependence of Weibull strength  $\sigma_0$  on average grain size  $G_a$  (only batches discussed in the text are labelled).

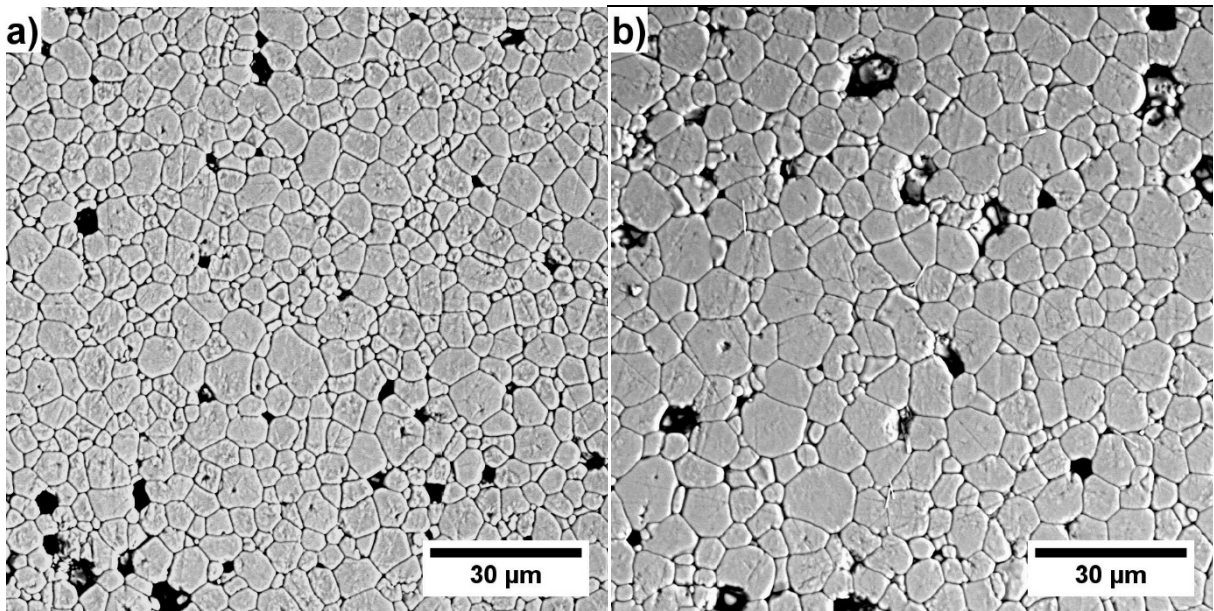
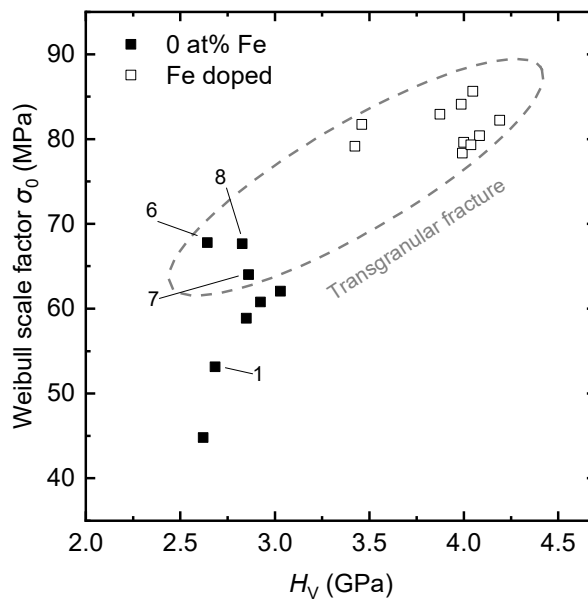


Figure 8-52 SEM micrographs of thermally etched surface of  $(\text{Pb}_{0.95}\text{Sr}_{0.05})(\text{Zr}_{0.52}\text{Ti}_{0.48})\text{O}_3$  sintered at a) 1310 °C (batch 4) and b) 1360 °C (batch 6).

The final observed property is Vickers hardness  $H_V$ , shown in relation to Weibull strength in Figure 8-53. The overall shape of data suggests that increasing values of Vickers hardness correlate with increasing strength. Hardness-strength correlations are not uncommon, [202] however, there are several reasons why this was probably not the case in the present study. It

was shown in section 8.2 that hardness follows the Hall-Petch relationship with grain size and is also affected, to a lesser degree, by porosity. On the other hand, Weibull strength showed only a possible correlation with porosity in the case of materials with 0 at% Fe. Taking this into consideration, Fe-doped materials would not be expected to show any correlation with increasing hardness. Figure 8-53 shows that the Weibull strengths of Fe-doped compositions were indeed independent of hardness. In the case of compositions with 0 at% Fe, it might be expected that there would be an increase of strength with increasing hardness, as both properties increase when the porosity decreases. Batches 1 (PZT with 0 at% Sr), 6 (PSZT sintered at 1360 °C), 7 and 8 (PSZT with  $y(\text{Zr}) = 53$  and 55 at% respectively, showing transgranular fracture) would be expected to deviate from this trend, as they did in the  $\sigma_0$ -Porosity scatterplot in Figure 8-48. The plot presented in Figure 8-53 is rather inconclusive as the strength variation is much higher than the variation in hardness. Based on the standard deviations, which can be found in Figure 8-3, a conclusion may be drawn, that there is a strength increase at a constant value of Vickers hardness, therefore the hardness does not correlate with the Weibull strength.



**Figure 8-53 Dependence of Weibull strength  $\sigma_0$  on Vickers hardness  $H_v$  (only batches discussed in the text are labelled).**

The discussion in the paragraphs above has indicated that none of the measured physical and microstructural properties significantly correlated with the Weibull strength, except for porosity, which affected the strength of compositions with 0 at% Fe, and Young's modulus, which appeared to correlate with the Weibull strength of batches exhibiting transgranular fracture mode. It is unclear, which factors are responsible for the observed strength increase in Fe-doped compositions and the abnormally high strength of batches 6, 7 and 8. One property, which has not been discussed so far, is the fracture mode. Transgranular fracture was a common feature of all batches with Weibull strength of 64 MPa and above and may be correlated with the increase in strength.

It has been shown in numerical models [102, 103] and experimentally [97, 101], that PZT exhibits an increasing degree of intergranular fracture with decreasing grain size. Kim et al. [101] found 90% intergranular fracture in pure  $\text{Pb}(\text{Zr}_{0.5}\text{Ti}_{0.5})\text{O}_3$  with  $G_a = 10 \mu\text{m}$  and 90 % transgranular fracture when  $G_a = 17.5 \mu\text{m}$ . The average grain sizes of all samples in this work were below  $10 \mu\text{m}$ , suggesting that solely intergranular fracture should be present, while the opposite was observed.

Some studies of the fracture modes of Pb-based piezoelectric materials have suggested the grain boundary strengthening/weakening effects of certain dopants. Rui-fang et al. [104], who modified complex Pb-based perovskite systems, reported a transition to transgranular fracture and grain boundary strengthening with ZnO/SnO<sub>2</sub> doping. When WO<sub>3</sub> (a donor dopant) was added to commercial acceptor-doped PZT, the fracture mode changed from trans- to intergranular, which was attributed to a grain boundary weakening effect of the dopant. Favaretto et al. [203] reached the same conclusions after doping  $(\text{Pb}_{0.9}\text{La}_{0.1})(\text{Zr}_{0.65}\text{Ti}_{0.35})\text{O}_3$  with WO<sub>3</sub>.

Guillon et al. [85, 95] studied the mechanical properties of 4 commercial PZT materials, two of which were acceptor-doped and the other two donor-doped. While only one of the acceptor-doped PZT materials exhibited a higher tensile strength than the rest, both hard compositions showed transgranular fracture, whereas the soft PZT compositions fractured intergranularly. The fracture toughness of the hard compositions was found to be significantly higher (1.59, 1.92 MPa·m<sup>1/2</sup>) than the soft compositions (0.86, 0.93 MPa·m<sup>1/2</sup>). The authors concluded that donor dopants segregated at the grain boundaries and made them weaker, however, this was only a speculation not supported by experimental evidence. Another aspect making the interpretation of results in this paper very difficult is the variability in the physical and microstructural properties of individual materials. The average grain size varied between 2.5–4.8 μm, *Y* between 43–69 GPa and each material had a different Zr/Ti ratio and Sr content. Strengthening of the grain boundaries in Fe-doped PZT is one of the possible explanations for the increased strength of the compositions in this work. In (Pb<sub>0.95</sub>Sr<sub>0.05</sub>)(Zr<sub>0.52</sub>Ti<sub>0.48</sub>)<sub>0.98</sub>Fe<sub>0.02</sub>O<sub>3</sub>, discussed in the nanoscale observations in section 6.6, the dopant was concentrated in grain boundaries and in triple junctions. While the Fe ion is clearly part of the segregated secondary phase in the triple junctions, it is unclear whether it creates a secondary phase along the grain boundaries or is incorporated into the perovskite structure. Hase et al. [204] observed an increase in strength and change from inter- to transgranular fracture in PZT doped with MnO<sub>2</sub> (acceptor dopant) only when the material was sintered above 1100 °C, which was indicated as the temperature when Mn<sup>2+</sup> diffuses into the PZT crystal lattice. This may suggest that Fe<sup>3+</sup> in the grain boundaries is incorporated within the crystal structure of the surrounding grains.

The fracture toughness and strength of ceramics can be increased by introducing a reinforcing secondary phase and creating a ceramic matrix composite. Strengthening/toughening mechanisms are based on the dissipation of energy of a propagating crack and include matrix-

reinforcement debonding, crack deflection, matrix microcracking and transformation toughening [17]. The first two mechanisms were found present in Ag-PZT composites [205]. Energy consuming transformation of ZrO<sub>2</sub> from its tetragonal to monoclinic form has also been proven effective toughening mechanism for PZT [206]. In both cases however, an increase in strength has not related to a change in fracture mode.

It is possible that the Fe-rich secondary phase present in the triple junctions in (Pb<sub>0.95</sub>Sr<sub>0.05</sub>)(Zr<sub>0.52</sub>Ti<sub>0.48</sub>)<sub>0.98</sub>Fe<sub>0.02</sub>O<sub>3</sub> (2 at% Fe) acted as a reinforcement via one of the mechanisms mentioned above. However, if the secondary phase was acting as a reinforcement, it would suggest Fe segregation in all Fe-doped samples, regardless of its concentration, since the strength did not significantly vary with Fe content.

Another factor influencing fracture mode is the character of the porosity. Intergranular pores and their increasing size enhance intergranular fracture because cracks generally follow a path of minimum solid area [18]. Conversely, intragranular pores enhance transgranular fracture. Microscopic observations of polished and/or etched sections did not show the presence of transgranular pores in any batch. The TEM study discussed in section 6.6 revealed intragranular Pb-rich particles near grain boundaries, however, it is not clear whether these particles could promote transgranular fracture. It could be argued that if the particles promoted transgranular fracture and made the grains weaker, it would not lead to the overall increase in strength. Garg and Agrawal [94] prepared Pb(Zr<sub>0.535</sub>Ti<sub>0.465</sub>)O<sub>3</sub> with under- and overstoichiometric amounts of PbO (0.5 and 1.5 wt% excess). The material exhibited an increase in strength as well as fracture toughness and transition from intergranular to transgranular fracture when a Pb excess was used. Pb deficient PZT showed an increase in strength, but no change in fracture mode. The authors speculated that transgranular fracture and an improvement in strength were consequences of

the density improvement induced by a Pb excess. Pb deficiency created ZrO<sub>2</sub> secondary phase particles, which could enhance  $K_{IC}$  by the strengthening mechanisms mentioned earlier.

Kim and Kim [99] reported an increase in fracture toughness in transparent La (donor) doped PZT after heat treating their specimens in air, which curved grain boundaries and changed the fracture mode from intergranular to transgranular. No similar looking boundaries were found in this work, therefore, this reinforcing mechanism is likely not responsible.

To the author's knowledge, no change of fracture mode has been previously associated with Zr/Ti ratio or sintering temperature. It is difficult to speculate the reason for the fracture mode changes observed in this work as most of the previously listed mechanisms could be responsible. There was a noticeable change in pore size distribution with Zr/Ti ratio and sintering temperature. The latter also somewhat affected grain size distribution, as was illustrated earlier in Figure 8-52. The average grain size of 5.3  $\mu\text{m}$  of (Pb<sub>0.95</sub>Sr<sub>0.05</sub>)(Zr<sub>0.52</sub>Ti<sub>0.48</sub>)O<sub>3</sub> sintered at 1360 °C (batch 6) does not reflect the maximum and minimum grain size. In fact, the largest grains exhibit Feret diameters above 10  $\mu\text{m}$ , possibly making the sizes themselves responsible for the fracture mode change, although, Kim et al. [101] previously reported 95% intergranular fracture mode for PZT with an average grain size of 10  $\mu\text{m}$ . A high sintering temperature or increasing Zr/Ti ratio might have led to changes in local stoichiometry near the grain boundaries or formation of PbZrO<sub>3</sub> particles in case of the Zr/Ti dependence. Unfortunately, it was out of the scope of this work to study grain boundary composition of these batches.

Table 8-14 quantifies absolute changes in Weibull strength and other measured properties. Changes larger than 2 $\times$  their average standard deviation are highlighted in blue colour. The table shows that the highest change in strength was induced by Fe doping (24 MPa). Polishing commercial hard PZT specimens led to a further increase by 7 MPa. The second highest change

in strength (23 MPa) was achieved by controlling the sintering temperature. However, this applies only to Fe free PZT. The Sr content and Zr/Ti ratio are the least effective factors for controlling strength, with only 2–9 MPa variation. Based on these results, doping and finer surface finish should be used to increase the strength of PZT. As Fe<sub>2</sub>O<sub>3</sub> strongly affects the dielectric and piezoelectric properties, it would be valuable to find a different dopant, which would maintain similar strengthening effect but not drastically change the piezoelectric properties. The strength of doped materials can be further improved by eliminating abnormally large pores and porous regions. This will also increase the reliability of the material.

Table 8-14 Relative change of Weibull strength, physical and mechanical properties with composition of (Pb<sub>1-x</sub>Sr<sub>x</sub>)(Zr<sub>y</sub>Ti<sub>1-y</sub>)<sub>(1-z)</sub>Fe<sub>z</sub>O<sub>3</sub> and processing conditions. Blue cells indicate that the value is >2× SDM.

		z(Fe)	x(Sr)		Sintering temperature		y(Zr)		2×Avg. SD <sup>†</sup>
Range		0–2 at%	0–5 at%		1260–1360 °C		49–55 at%		
Fe content (at%)			0	1.4	0	1.4	0	1.4	
Strength range (MPa)		59–83	53–59	79–84	45–46	82–83	59–68	79–85	3
<b>Absolute change</b>	W. Strength (MPa)	24	6	5	23	2	9	6	3
	Rel. density (%)	1.8	0.5	0.4	1.2	1.7	1.0	0.7	0.4
	Grain size (µm)	3.0	0.1	1.1	2.0	0.6	0.8	0.1	0.6
	Elastic modulus (GPa)	9	11	6	5	4	22	11	1
	V. hardness (GPa)	1.3	0.2	0.0	0.2	0.5	0.2	0.1	0.4
	Surf. roughness (µm)	2.2	1.0	0.6	0.6	0.3	3.1	1.1	1.0

<sup>†</sup>except for Weibull strength, which has 2×95% confidence interval instead

The reliability (Weibull shape factor) of the ceramics prepared in this work did not show any significant trends and measured values were between 10–23. The lowest values were found in the most porous samples and when large number of pore clusters were present. These features are most likely not present in industrially made ceramics. A reduction in the Weibull shape factor was found when industrially made samples were polished, suggesting that a wide range

of porosity was present. Eliminating the largest pores would likely increase the reliability as these were identified as the weakest flaws.

The testing method exhibited possible issues manifested as non-random test sequences and a tendency for fracture to occur directly below the load ring. Friction and misalignment were identified as likely causes, but further testing would be required to get a definite answer. Apart from the first 4 batches tested, results were consistent, and the method successfully revealed differences in strength between certain materials. The method can be recommended for periodic tests of strength. Combined with fractography, it can give valuable information about the weakest flaws in the material. The cylindrical shaped samples are easier and cheaper to produce than the specimens required for 3- or 4-point bend test configurations. The size and equibiaxial nature of the stress distribution make the method less viable for experiments involving ferroelasticity and domain switching. On the other hand, it inherently induces less domain switching than uniaxial flexural or tensile tests.

## 8.5 Microscale fracture toughness

The possibility of grain boundary strength enhancement induced by Fe<sub>2</sub>O<sub>3</sub> doping was proposed in the previous section as an explanation for the dependence of strength on dopant concentration. Since strength depends on fracture origin size, fracture toughness measurements can help to confirm the validity of the hypothesis. In order to investigate this, some preliminary measurements were performed on micrometre-scale cantilevers prepared by the techniques described in section 4.2.5. Because the sample preparation, testing and fracture surface observations were very time consuming, only 3 cantilevers from batches 4 and 18 containing 0 and 2 at% Fe respectively were prepared and tested. When terms “doped” or “undoped” compositions are used in this section, they refer solely to Fe<sub>2</sub>O<sub>3</sub> doping.

The results of the  $K_{IC}$  measurements are shown in Figure 8-54. The fracture toughness of the undoped composition exhibited values between 0.41–0.56 MPa·m<sup>0.5</sup>, while for the doped composition  $K_{IC}$  was 0.59–0.70 MPa·m<sup>0.5</sup>. ‘Average’  $K_{IC}$  values of 0.50 and 0.64 MPa·m<sup>0.5</sup> for undoped and doped compositions respectively suggest that the presence of Fe increases fracture toughness. As the cross-section of cantilevers was approximately 0.4×1 μm, results were not affected by multiple grain boundaries or porosity. The stress intensity factor of PZT has been previously reported to be between 0.7–1.9 MPa·m<sup>0.5</sup> [77, 85, 92, 98, 197, 200, 207, 208]. Values found in this work are lower, which is probably due to the absence of multiple grain boundaries and porosity, which consume some of the energy of crack opening. Multiple factors may have been responsible for the relatively large scatter of results, namely grain boundary misorientations, imperfect shape of the pre-notch or differences in local inhomogeneities near the fracture path.

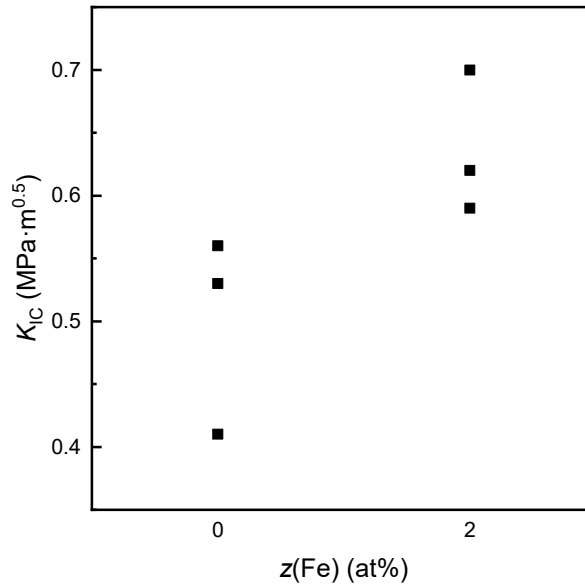


**Figure 8-54 Scatter of fracture toughness results of  $(\text{Pb}_{0.95}\text{Sr}_{0.05})(\text{Zr}_{0.52}\text{Ti}_{0.48})_{1-z}\text{Fe}_z\text{O}_3$  doped with  $z = 0$  and  $2$  at%.**

Cantilevers were prepared with a goal of having a straight grain boundary parallel with the loading direction near the cantilever base. A defined pre-notch was then made along the boundary to increase the local stress and induce grain boundary fracture. This was successful for undoped samples, however, none of the doped samples fractured along the grain boundary and rather formed a separate transgranular crack next to it. Examples of this behaviour are shown in Figure 8-55, where a) shows curved fracture along the grain boundary and b) shows a straight crack initiated and propagated within the grain. This behaviour supports the theory that  $\text{Fe}^{3+}$  enhances grain boundary strength.

Based on the fracture toughness results, it appears that the nature of interfaces between grains plays an important role in the crack initiation/propagation and the strength of PZT. The TEM studies presented in section 6.6 did not reveal any secondary phases at the grain boundaries of the sample with no  $\text{Fe}^{3+}$ , but it is possible that a thin Pb-rich amorphous layer was still present between the grain boundaries on a smaller scale (1–4 nm). Such layers were previously reported by Hammer and Hoffmann [74] and Tan and Shang [73]. The nature of these layers or their

presence would be expected to change with sintering conditions and composition, which in turn could be responsible for the fracture mode changes observed in this work. The study of the effect of processing and composition on the grain boundary interfaces and the fracture mode is a possible topic for future work.

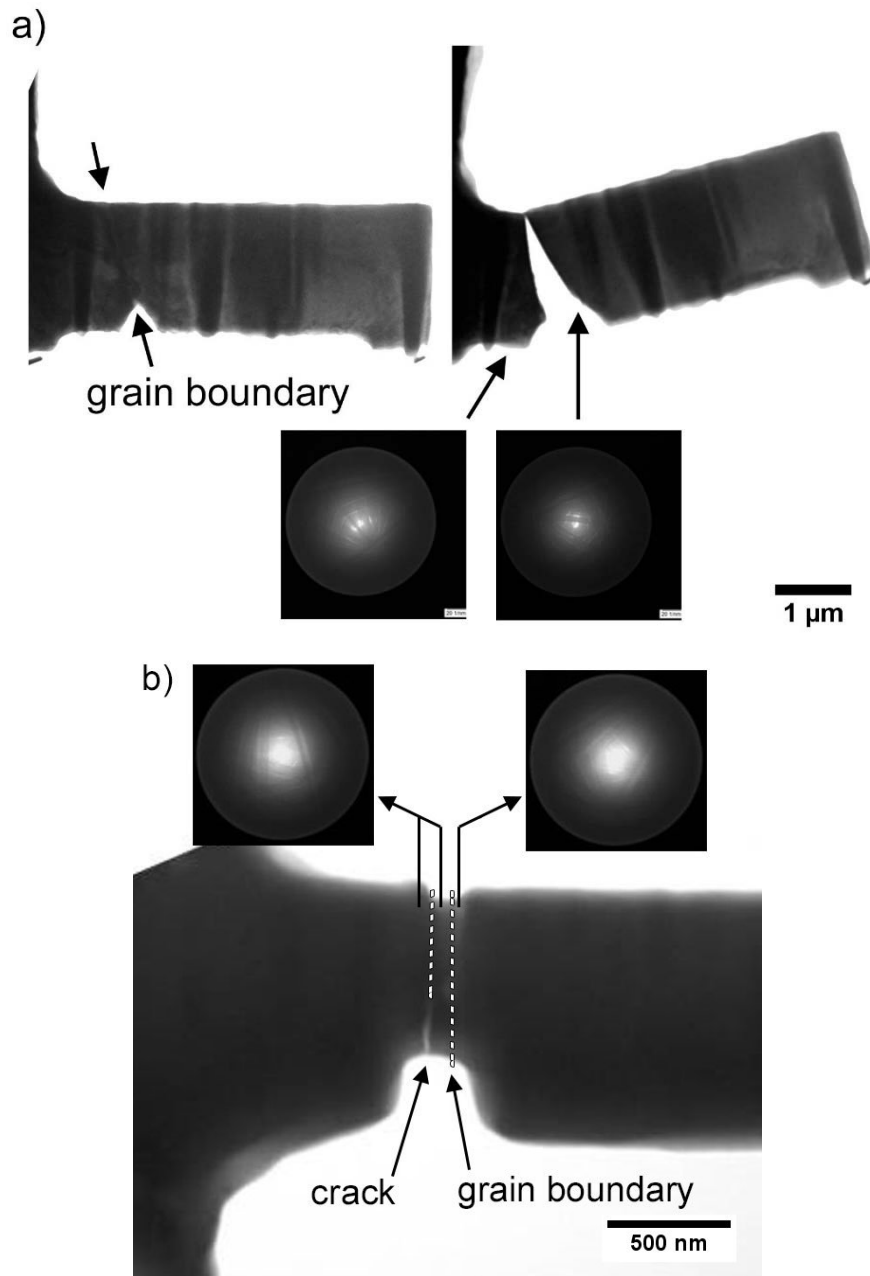


**Figure 8-55 a) cantilever of  $(\text{Pb}_{0.95}\text{Sr}_{0.05})(\text{Zr}_{0.52}\text{Ti}_{0.48})\text{O}_3$  (batch 4) before and after testing, Kikuchi lines confirm the presence of 2 distinct grains, fracture is intergranular; b) cantilever of  $(\text{Pb}_{0.95}\text{Sr}_{0.05})(\text{Zr}_{0.52}\text{Ti}_{0.48})_{0.98}\text{Fe}_{0.02}\text{O}_3$  (batch 18) after fracture, Kikuchi lines show 2 distinct grains, but the crack did not follow the grain boundary.**

## 8.6 Summary

This section summarises the most important results and conclusions of chapter 8, which presented and discussed the mechanical properties of the full range of prepared materials.

Elastic modulus exhibited a linear dependence on porosity. Several compositions showed deviation from this trend due to softening near the MPB. Values agreed well with previously published results.

Vickers hardness was shown to follow the Hall-Petch relationship with grain size, after correcting for porosity. The proximity of the composition to the MPB or Fe content did not have a noticeable effect on  $H_v$ , suggesting that microstructural changes (mainly grain growth inhibition) induced by the presence of Fe were responsible rather than intrinsic material changes related to the incorporation of  $\text{Fe}^{3+}$  into the crystal lattice of PZT.

Samples with a composition of  $(\text{Pb}_{0.95}\text{Sr}_{0.05})(\text{Zr}_{0.52}\text{Ti}_{0.48})\text{O}_3$  showed a continuous increase in strength with increasing sintering temperature from 1260 °C to 1360 °C. The initial increase was explained by an increase in relative density. The second increase was unexpected as it was accompanied by an increase in grain size and porosity. The fracture mode changed from inter- to transgranular for samples sintered at 1360 °C, which was later found to be a common feature of the compositions exhibiting the highest strengths. Explanation of this phenomenon is unclear, several strength-enhancing mechanisms may be responsible and further study is necessary. Domain switching did not influence the strength in this case. It was hypothesised that the phenomenon might be related to a change in the nature of the grain boundaries (presence of secondary phases and their composition). Distribution of the Weibull strength narrowed with increasing sintering temperature, making the material more reliable. Since the fracture origin

was exclusively porosity, this enhancement was likely affected by the width and homogeneity of the pore size distribution.

Increasing the sintering temperature for  $(\text{Pb}_{0.95}\text{Sr}_{0.05})(\text{Zr}_{0.52}\text{Ti}_{0.48})_{0.986}\text{Fe}_{0.014}\text{O}_3$  induced a similar change in porosity as for the undoped compositions but did not significantly affect the strength. A transgranular fracture mode was dominant for all these batches. The fracture origin changed with increasing sintering temperature from mixed porosity/machining damage to machining damage and then back to porosity at the highest temperature. Based on nanoscale studies and fracture toughness results, it was concluded, that Fe strengthened the grain boundaries, and this changed the fracture behaviour of the material, making its strength less sensitive to microstructural factors. A decrease in porosity improved the reliability (Weibull modulus) of the Fe-doped materials, most probably by decreasing the size of the largest pore clusters.

The presence of Sr in the compositions increased the Weibull strength, but the change did not correlate with any of the studied properties, except for the elastic modulus. The change in elastic modulus was explained by the shift of the MPB. Both batches exhibited non-random test sequences, which was attributed to testing issues. Introducing Sr to Fe-doped PZT noticeably decreased the presence and/or size of pore clusters, as shown by the Weibull probability plots and fracture origin investigations. Based on the observed effects of Sr on the microstructure of  $(\text{Pb}_{1-x}\text{Sr}_x)(\text{Zr}_{0.52}\text{Ti}_{0.48})_{0.986}\text{Fe}_{0.014}\text{O}_3$ , it was hypothesised that pore coalescence and densification are further affected when Fe and Sr are combined. The strength of Fe-doped materials increased with Sr doping, which was likely due to the removal of the largest pore clusters. The Weibull modulus did not significantly change with Sr doping.

Increasing the  $y$  in  $(\text{Pb}_{0.95}\text{Sr}_{0.05})(\text{Zr}_y\text{Ti}_{1-y})\text{O}_3$  up to 52 at% (approaching the MPB) resulted in a continuous strength decrease, which correlated with a decrease in relative density. When  $y$

exceeded 52 at%, the strength started increasing again. This change did not correlate with any other measured property except for fracture mode, which changed from inter- to transgranular. It is not clear what caused this transition, a change in the nature of the grain boundaries was proposed earlier as a possible mechanism. The two stronger Zr-rich compositions showed noticeable deviations from the rest of the population in scatterplots of strength against other physical and mechanical properties. They also exhibited lower surface roughness, likely due to the transgranular fracture and more homogeneous porosity. Roughness probably did not affect strength in this case, as the fracture origin was mostly porosity. Ferroelastic contributions might have increased the strength of the two Zr-rich compositions, but the available results were inconclusive.

$(\text{Pb}_{0.95}\text{Sr}_{0.05})(\text{Zr}_y\text{Ti}_{1-y})_{0.986}\text{Fe}_{0.014}\text{O}_3$  did not exhibit any significant strength trends with varying Zr/Ti ratio. Relative density slightly increased from Ti- to Zr-rich compositions, opposite to the undoped compositions. Ti-rich compositions with  $y = 49$  and  $51$  at% exhibited higher surface roughness, possibly due to a higher Young's modulus and an increased frequency of pore clusters. Pores and pore clusters were the strength limiting flaws in the Zr/Ti series, whereas machining damage was the fracture origin of the strongest specimens. The Weibull modulus was not significantly affected by Zr/Ti ratio regardless of the presence of Fe.

Fe doping was found to be the most important strength-influencing factor. The strength increased for compositions up to 1.4 at% Fe. All other observed properties were also significantly affected by Fe doping, but none of them showed any correlation with the strength variation. The influence of the studied factors on the strength of Fe-doped PZT was much lower than for materials without Fe, which is potentially one of the reasons why no correlations were found. The loss of sensitivity to the studied factors and the overall increase in strength was attributed to a doping-induced change of fracture mode from an inter- to transgranular.

Nanoscale observations found increased concentrations of Fe at grain boundaries and triple junctions in PSZT doped with 2 at% Fe. Other Fe concentrations were not studied. It is unclear if  $\text{Fe}^{3+}$  at grain boundaries enters the crystal lattice or forms a secondary phase. Bicrystal fracture toughness results showed higher average values when Fe was present, supporting the possibility of grain boundary strengthening. The strength limiting flaws in Fe-doped materials were identified as pore clusters, introduced by the manual binder mixing method. Commercial material also contained porous flaws, but on a smaller scale. Weibull modulus did not improve with Fe doping, likely due to both porosity and machining damage acting as critical flaws and widening the strength distribution.

Control of sintering temperature (relative density) and doping with elements to strengthen the grain boundaries were suggested as the most effective ways of improving the strength of PZT. The upper strength limit can be further raised by improving the surface finish, and the lower strength limit can be raised by optimising the binder incorporation process. The latter should also increase reliability.

Based on the results of the physical and mechanical properties, the compositions prepared in this work showed a good resemblance to a commercial hard PZT. Therefore, the conclusions should be applicable in a commercial environment.

The developed equibiaxial flexural strength test was recommended for use on PZT. The apparatus exhibited some issues even after optimisation, but their possible source was identified, and improvements were suggested. With these, the jig should work well for quick and relatively inexpensive strength tests for comparison purposes and quality check. Coupled with fractography, the method yields valuable information about weakest flaws and the nature of the fracture. The jig design used in this work does not permit use of electric field or strain gauges.

While this would be possible with certain alterations, the biaxial stress configuration would make it difficult to separate elastic and plastic contributions. Uniaxial tests would likely be more suitable in this case.

## 9 CONCLUSIONS

This chapter summarises the progress made towards the objectives of this work which were set out in Chapter 3, and details the main conclusions that can be made.

18 batches each of 70–80 PZT-based specimens were fabricated using a conventional powder processing route and industrial processing parameters. The method was optimised to obtain samples of pure perovskite phase, desired stoichiometry and as homogeneous porosity as possible. Some pore clusters were found on polished cross sections as a result of the binder mixing method and pore transport during sintering, which may have influenced some of the results, but note has been made where this is the case. The following compositional and processing factors were studied with the overall composition  $(\text{Pb}_{1-x}\text{Sr}_x)(\text{Zr}_y\text{Ti}_{1-y})_{1-z}\text{Fe}_z\text{O}_3$ : acceptor  $\text{Fe}^{3+}$  doping ( $z = 0.4, 1.4$  and  $2.0$  at%), isovalent  $\text{Sr}^{2+}$  doping ( $x = 0$  and  $5$  at%), Zr/Ti ratio ( $y = 49$ – $55$  at%, values near the MPB) and sintering temperature ( $1260, 1310$  and  $1360$  °C).

The effect of the studied variables on the dielectric and piezoelectric properties mostly agreed with literature. One of the exceptions was  $\text{Sr}^{2+}$  doping, which unexpectedly resulted in only a minor increase in relative permittivity from 1200 to 1340 (for  $z = 0$  at%) and from 690 to 940 (for  $z = 1.4$  at%) and a decrease in coupling coefficient from 0.50 to 0.45 (for  $z = 0$  at%) and from 0.55 to 0.51 (for  $z = 1.4$  at%). This was attributed to the presence of impurities in the raw oxides and their combined effect with  $\text{Sr}^{2+}$  on the microstructure. An unexpected increase in  $k_p$  was observed with Fe doping, but its absolute values were similar to previously published results. It was concluded that the low density of the samples without  $\text{Fe}^{3+}$  was likely responsible for their low  $k_p$ . The MPB was widened with the presence of  $\text{Fe}^{3+}$  likely due to compositional inhomogeneities on the nanoscale level. The Zr/Ti ratio of maximum properties also shifted towards the Ti-rich region in  $\text{Fe}^{3+}$  doped specimens.

An equibiaxial flexural strength test fixture was designed and successfully optimised to yield consistent and reliable results according to the available standards and literature. The method was validated by testing commercial alumina samples and comparing their strength values with previously published data. Issues with non-random test sequences were found in some batches. The source of these issues was identified, but not confirmed experimentally. Additional design improvements were suggested. The test was found well suited for the comparison and quality control purposes, and able to reveal even minor strength differences of roughly 5 MPa or more in strength using an easily fabricated cylindrical sample geometry. The current design does not allow the application of an electric field or attachment of strain gauges.

#### **The effect of selected variables on the physical properties and microstructure:**

##### a) $\text{Fe}^{3+}$ doping

The presence of  $\text{Fe}^{3+}$  significantly inhibited grain growth. Average grain size dropped from 4.0 to 1.4  $\mu\text{m}$  at 0.4 at% doping and continued to slightly decrease to 1.0  $\mu\text{m}$  at  $x = 2.0$  at%. These values were all close to the average particle size of their respective starting powders. As all the powders were milled using the same conditions, it is apparent that  $\text{Fe}^{3+}$  inhibits particle growth during calcination. The relative density showed almost a linear increase from 96 to 98 % with increasing  $\text{Fe}^{3+}$  content, suggesting that  $\text{Fe}^{3+}$  does not negatively affect densification, possibly even enhances it. The density increase correlates with a decrease in grain size up to 0.4 at%  $\text{Fe}^{3+}$ . The reason for the continued density increase at higher  $\text{Fe}^{3+}$  doping levels is unclear. Nanoscale observations revealed Fe segregation in samples with 2 at% of  $\text{Fe}^{3+}$ , which confirms that the solubility limit of  $\text{Fe}^{3+}$  in the PZT lattice was exceeded. Specimens containing lower  $\text{Fe}^{3+}$  doping levels were not investigated.

b) Sintering temperature

Increasing sintering temperature from 1260 to 1360 °C increased the average grain size from 3.3 to 5.3  $\mu\text{m}$  for (for  $z = 0$  at%) and from 1.3 to 1.9  $\mu\text{m}$  (for  $z = 0$  at%). The relative density exhibited a maximum value of 96.3 % (for  $z = 0$  at%) and 97.7 % (for  $z = 1.4$  at%) at 1310 °C, above which the density decreased due to formation of larger stable pores.

c) Presence of  $\text{Sr}^{2+}$

The presence of  $\text{Sr}^{2+}$  decreased the grain size of compositions doped with  $\text{Fe}^{3+}$  (by  $\approx 1$   $\mu\text{m}$ ), but not of pure PZT, which suggested some degree of dopant interaction. Investigation of polished sections revealed that 5 at% of  $\text{Sr}^{2+}$  induced the formation of stable larger pores in pure PZT, which lowered density. In acceptor (Fe) doped PZT,  $\text{Sr}^{2+}$  prevented the formation of pore clusters, which increased the density. XRD revealed an increase in the tetragonal phase, which was likely connected with the previously reported MPB shift due to  $\text{Sr}^{2+}$  substitution into the crystal lattice of PZT.

d) Zr/Ti ratio

Increasing the fraction of Zr in Zr/Ti from 49 to 55 at% led to a small increase in density from 97.4 to 98.1 % (for  $z = 1.4$  at%), and a small decrease in relative density from 97.1 to 96.1 % (for  $z = 0$  at%). The density decrease was attributed to the fact that  $\text{PbZrO}_3$  has a higher melting point than  $\text{PbTiO}_3$  and decreases the sinterability of PZT. This was supported by an observed grain size decrease of 0.8  $\mu\text{m}$ . It was hypothesised that when  $\text{Fe}^{3+}$  is present, grain growth is already inhibited, and densification is not further affected by the fraction of  $\text{PbZrO}_3$ , as in the previous case.

### **The effect of the physical and microstructural changes on mechanical properties:**

The elastic moduli of prepared materials exhibited a linear dependence on porosity with some notable deviations due to softening effects around the MPB. Vickers hardness exhibited a Hall-Petch dependence on grain size with no obvious deviations.

#### a) Fe<sup>3+</sup> doping

The Weibull strength increased from 59 to 78 MPa with 0.4 at% Fe<sup>3+</sup> and to 84 MPa with 1.4 at% Fe<sup>3+</sup> respectively, which was the highest strength change recorded in this work. None of the studied physical, microstructural or mechanical properties significantly correlated with this strength increase. A hypothesis was formed that Fe<sup>3+</sup> strengthened the grain boundaries, which led to the overall increase in strength. This was supported by the change of fracture mode from inter- to transgranular and an increase in fracture toughness observed between specimens with 0 and 2 at% of Fe<sup>3+</sup>. The fracture origins of the strongest specimens were, in most cases, machining damage introduced by conventional grinding, indicating that a finer surface finish should increase the overall strength. The weakest specimens exhibited pore clusters or large pores as their origins of fracture. Eliminating such defects would likely lead to a narrower strength distribution and increase in reliability (Weibull modulus). The Weibull moduli of the materials ranged between values of 15 and 23 with no obvious correlation with the Fe<sup>3+</sup> doping.

#### b) Sintering temperature

The Weibull strength of (Pb<sub>0.95</sub>Sr<sub>0.05</sub>)(Zr<sub>0.52</sub>Ti<sub>0.48</sub>)O<sub>3</sub> showed a continuous increase in strength from 45 to 68 MPa as the sintering temperature was increased from 1260 to 1360 °C. The former was related to an increase in relative density and Young's modulus at 1310 °C and a change in fracture mode from inter- to transgranular at 1360 °C. The reason for the fracture mode change was unclear, but a hypothesis was formed that the change might be related to a

potential presence/absence and composition of a thin Pb-rich grain boundary film. Fe<sup>3+</sup>-doped PZT did not show any strength variation with the sintering temperature. It was hypothesised that this strength insensitivity to sintering temperature was related to transgranular fracture mode. An improvement in reliability was generally observed for samples sintered at higher sintering temperatures as the width of pore size distribution decreased, with the exception of the  $z = 1.4$  at% composition sintered at 1360 °C. The Weibull modulus increased from 13 to 24 as the sintering temperature was increased from 1260 to 1360 °C (for  $z = 0$  at%) and from 9 to 23 as the sintering temperature was increased from 1260 to 1310 °C (for  $z = 1.4$  at%).

c) Presence of Sr<sup>2+</sup>

The Weibull strength was increased from 79.1 to 84.1 MPa for Fe<sup>3+</sup> doped PZT, which was attributed to the elimination of the largest pore clusters. The presence of Sr<sup>2+</sup> increased the strength of pure PZT from 53.1 to 58.9 MPa. The increase correlated only with the increase in Young's modulus from 67.5 to 78.2 GPa.

d) Zr/Ti ratio

The Weibull strength did not vary with Zr/Ti ratio in Fe<sup>3+</sup> doped compositions. When the dopant was not present, Weibull strength exhibited a minimum of 58.9 MPa at Zr/Ti = 52/48. An initial strength decrease with decreasing Zr content correlated with a decrease in density, but the strength increase observed in Zr-rich compositions ( $y = 53$  and  $55$  at%) did not correlate with any other measured property, except for a change in fracture mode from inter- to transgranular and a change in their pore size distribution. Both compositions were the closest to MPB, which implied they were the most susceptible to stress-induced domain switching. Measurements of the coercive fields to investigate whether ferroelastic switching affected the measured strengths

were inconclusive. A similar hypothesis explaining the fracture mode change can be made as for the case observed in the sintering temperature dependence.

A batch of commercial hard PZT material showed similarities to the materials fabricated in this work in terms of their physical and mechanical properties. The most notable difference was the absence of pore clusters in the commercial material, which was attributed to the different methods of binder incorporation into the calcined powder. The maximum strength of the commercial material was 78 MPa, and was limited by machining damage, similar to the case of prepared samples. Polishing to a 1 $\mu$ m surface finish increased the Weibull strength by 13 MPa. Pores and pore clusters were found as the weakest defects, but their size was lower than in the case of prepared specimens. It was concluded that prepared specimens showed a good representation of commercial PZT and knowledge gained in this work should be applicable in industrial conditions.

Thus, this project has involved a systematic and comprehensive study of four variables on the microstructural, structural, physical, functional and mechanical properties of hard PZT compositions, representing a significant addition to previous reports. In particular, through the careful control of PbO loss and processing parameters, it was possible to observe the effects of selected factors on the physical properties and microstructure of PZT and make direct comparisons. The characterisation included the usual physical properties as well as rarely reported properties such as pore size distribution, grain boundary fracture toughness, an estimate of ferroelastic contributions and identification of the fracture origin of several samples from each batch. Cross comparing all results, it was possible to identify grain boundary strengthening as the most significant strength increasing feature, which should prove helpful in finding the focus of future studies. The results and developed strength test can be used in a commercial environment to further optimise the strength and reliability of PZT-based materials.

## 10 FUTURE WORK

This work has identified acceptor doping as having a key role in improving the strength of PZT. The improvement was attributed to grain boundary strengthening by  $\text{Fe}^{3+}$ , but the underlying mechanism and atomic structure near the grain boundaries is still unclear. Further study of the grain boundary structure when  $\text{Fe}^{3+}$  or other dopants are present could lead to a better understanding of this phenomenon and help discover other ways of improving strength. The nature of the grain boundaries can be studied by TEM using Fresnel imaging and diffuse dark-field imaging [73], by a high-resolution TEM, and/or by an analytical scanning TEM [74]. Finding donor dopants that exhibit a similar effect on grain boundaries as  $\text{Fe}^{3+}$  is of particular interest, since  $\text{Fe}^{3+}$  cannot be universally used for this purpose, as it drastically changes the dielectric and piezoelectric properties. Donor dopants were previously found to cause grain growth inhibition by disrupting defect equilibria [27], likely in a similar manner to acceptor dopants. However, their fracture mode (if reported) remained intergranular. A paper published by Pferner et al. [6] can be listed as an example of this behaviour.

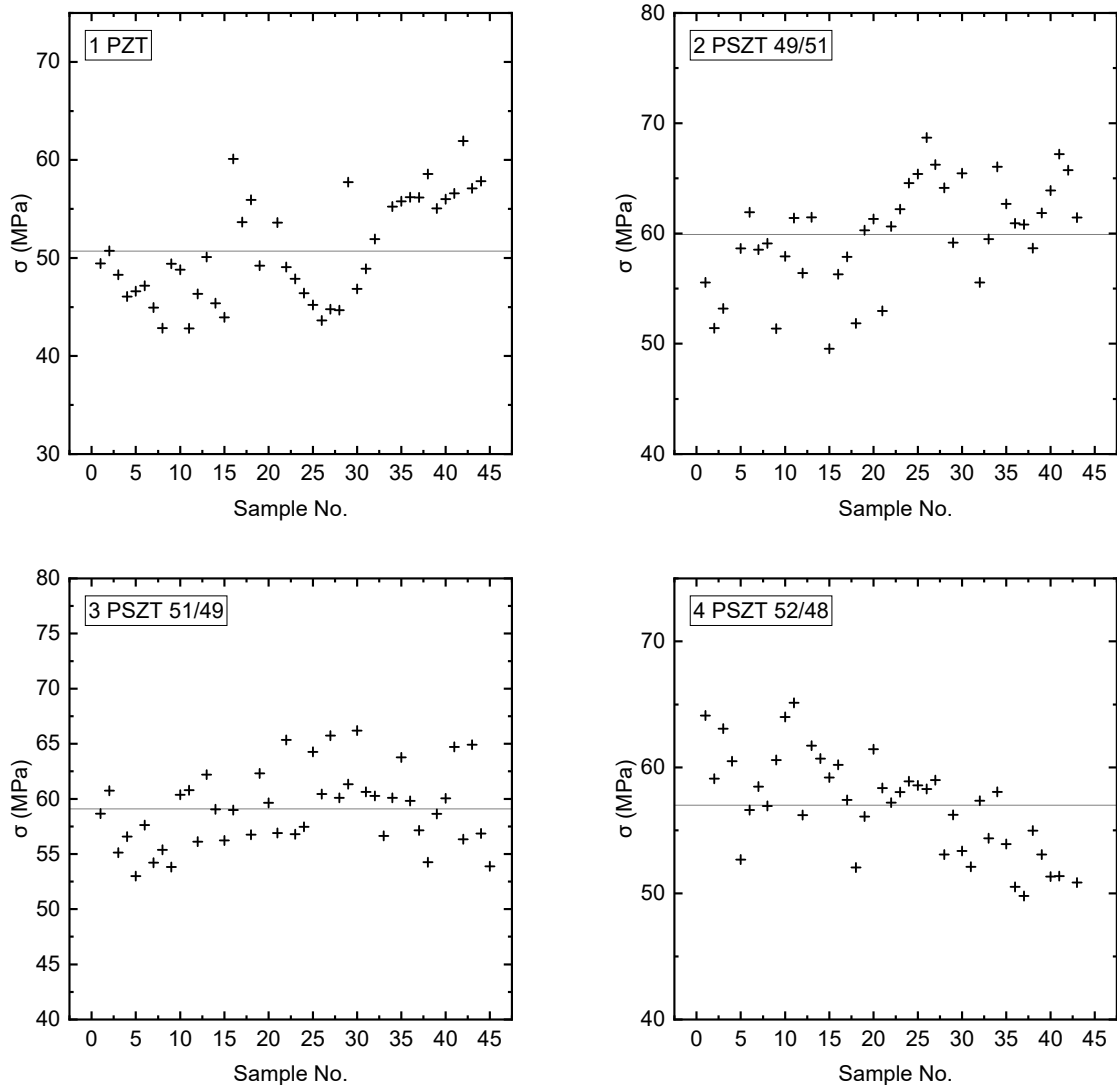
The change in fracture mode and increase in strength that was observed in  $(\text{Pb}_{0.95}\text{Sr}_{0.05})(\text{Zr}_{0.52}\text{Ti}_{0.48})\text{O}_3$  sintered at 1360 °C could not be explained by any of the physical, microstructural or physical properties studied in this work. Further study, particularly of the atomic structure and local compositional homogeneity near the grain boundaries could help in identifying possible causes for this behaviour. The same applies to Zr-rich PSZT, which exhibited a similar transition at a Zr fraction of 53 at% and above. Additionally, the strength of Zr-rich compositions was suspected to be influenced by ferroelastic switching. Strength testing of bars made of materials from Zr/Ti rich series in 3- or 4- point bend with strain gauges attached would confirm if this was the case.

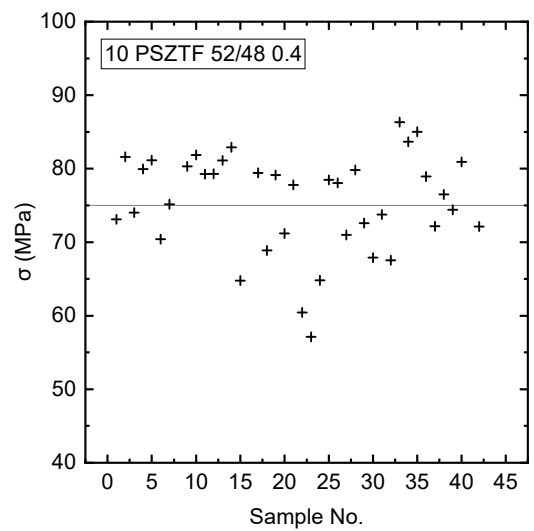
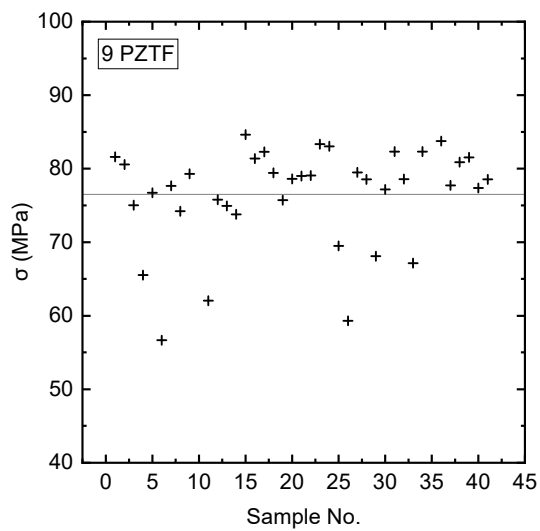
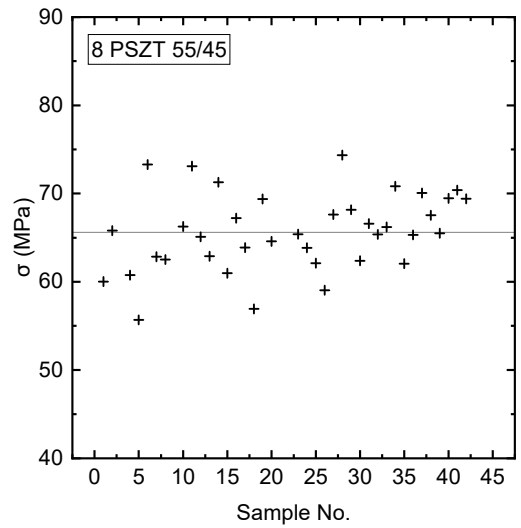
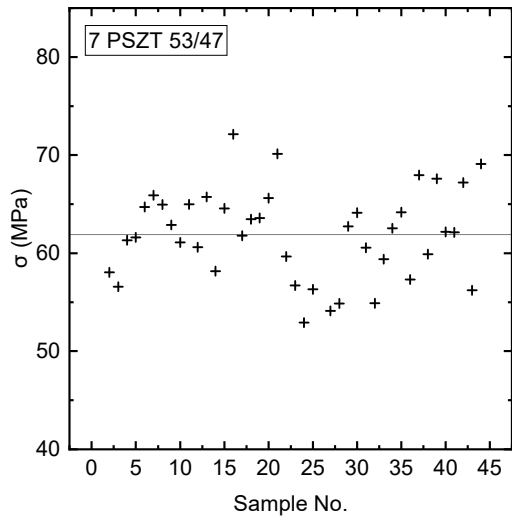
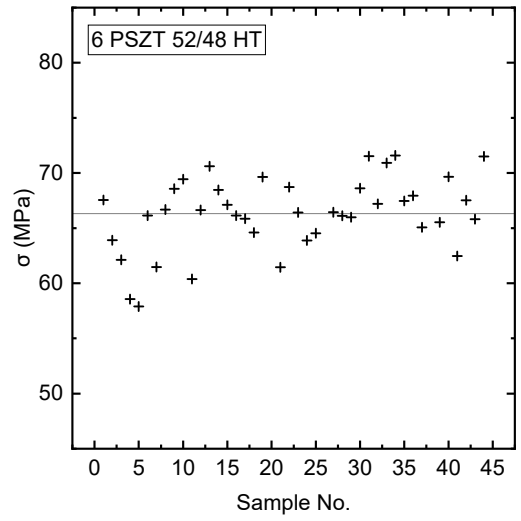
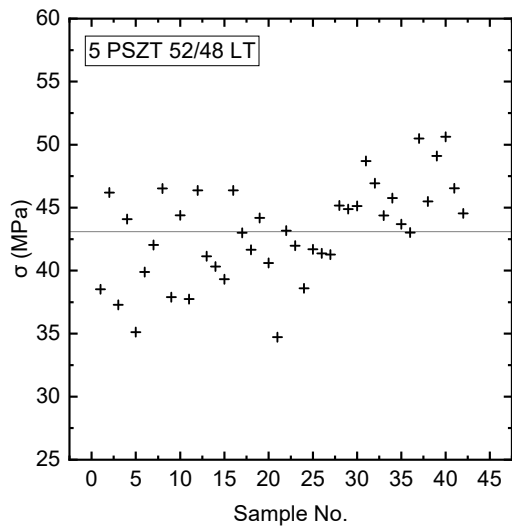
Observations of fracture origins in this work suggested that further optimisation of binder mixing technique would benefit the strength and reliability of both laboratory- and commercially-made PZT ceramics. Another point of focus should be machining optimisation. Results showed that polishing can increase the maximum strength by at least 10 MPa. In practice, the goal will likely be a compromise between low roughness and cost of the machining.

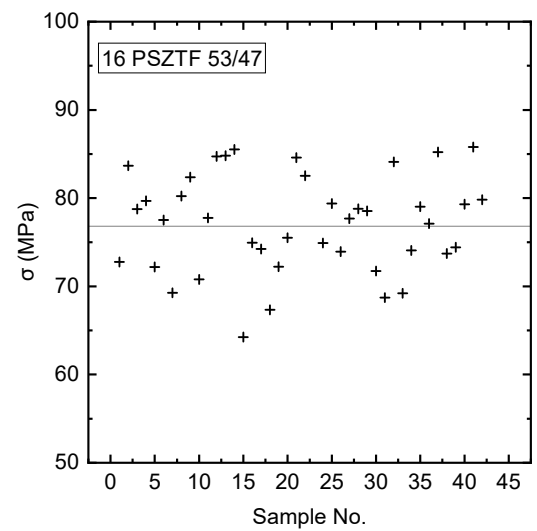
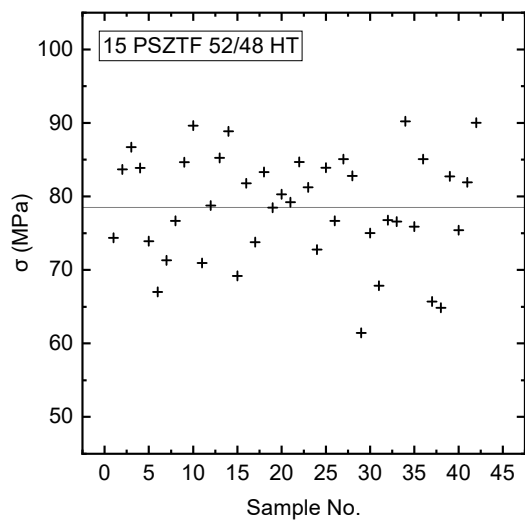
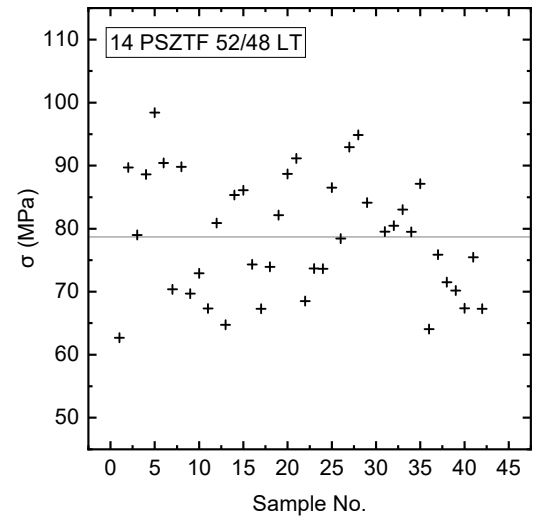
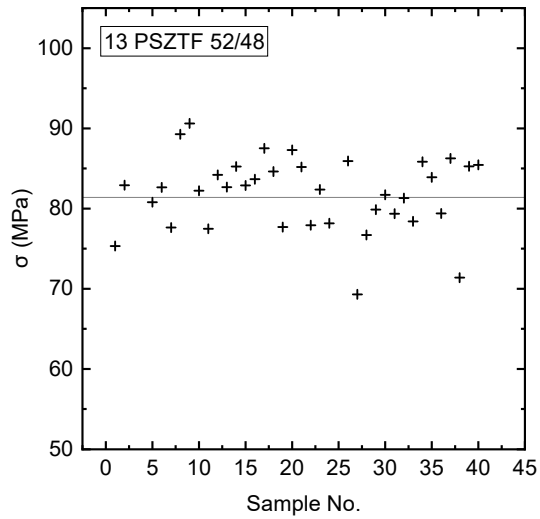
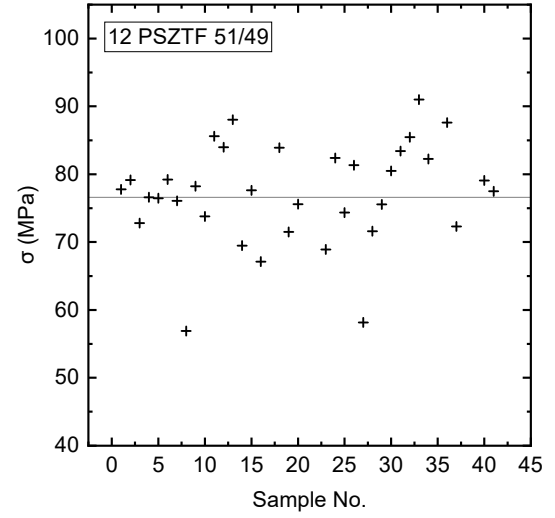
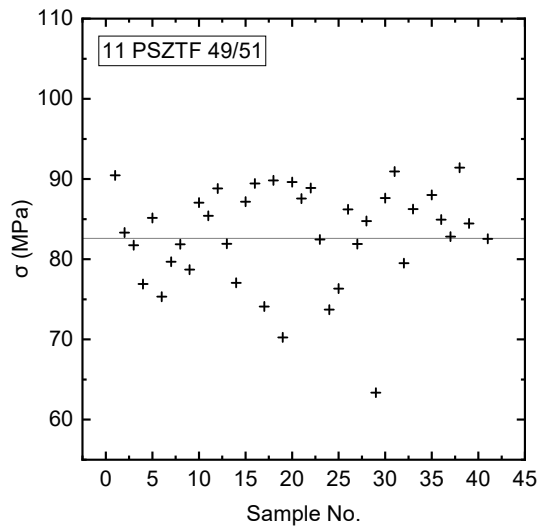
Several batches showed non-random strength test sequences, which indicated issues with the equibiaxial flexural strength test fixture. The use of metal springs instead of rubber “O” rings and a more defined attachment of the load ring to the upper portion of the fixture was suggested as the way of solving these issues. Additional tests are required to confirm this hypothesis and ensure the consistency of this strength measurement method.

## APPENDIX I. STRENGTH TEST SEQUENCE PLOTS

The plots in Figure A1 - 1 below show the strength results obtained from the testing procedure described in section 4.2.4.2. The strength of each sample was plotted against its sample number, which corresponds with the sequence in which they were tested. Batch numbers, compositions and labels are listed in section 5.2 (Table 5-4). Evaluation of these graphs is described in section 8.4.1.







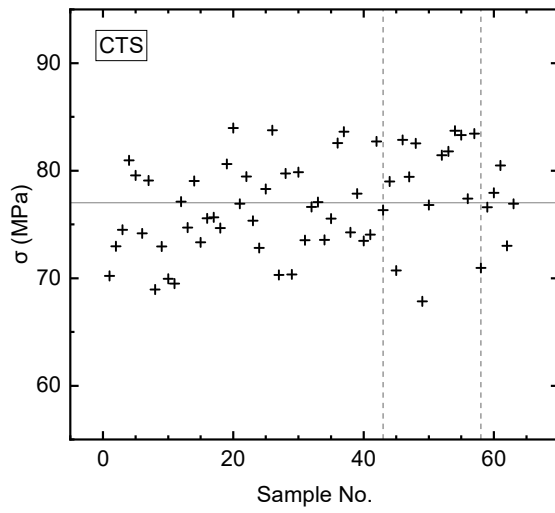
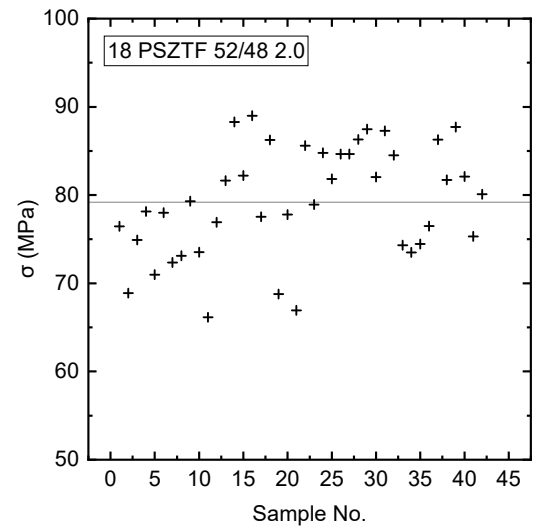
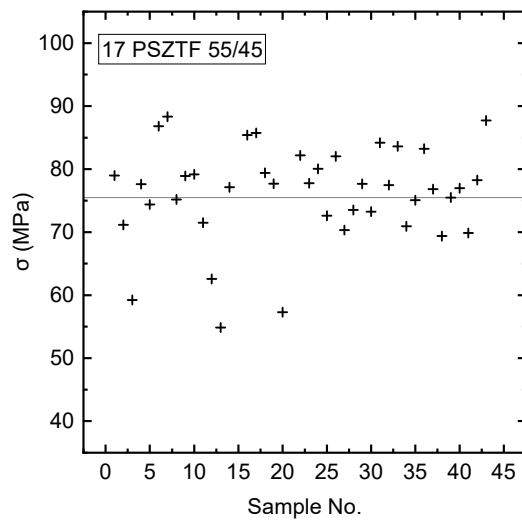
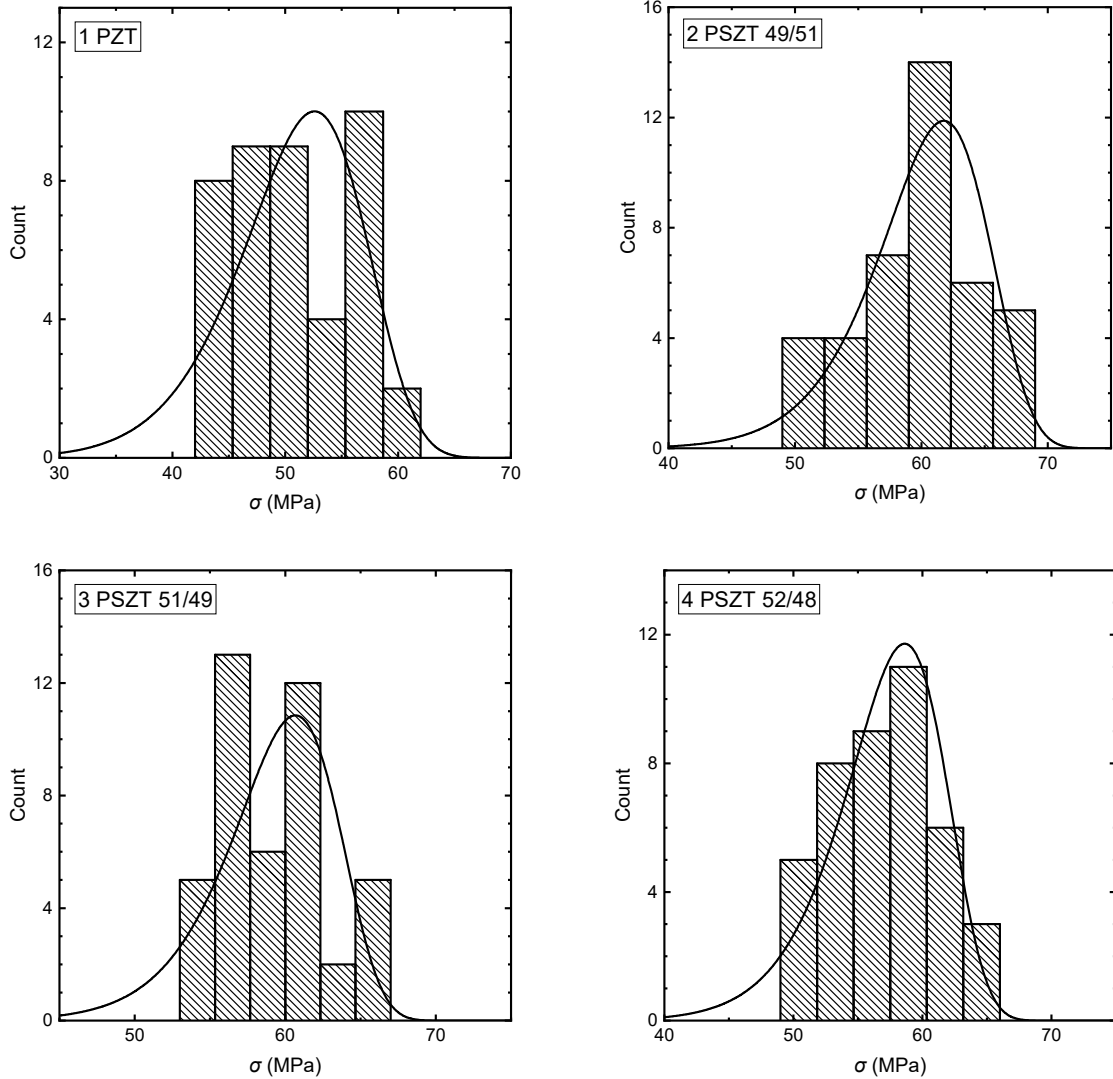
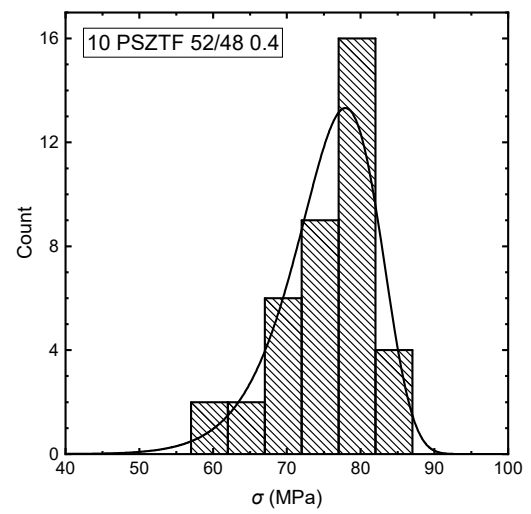
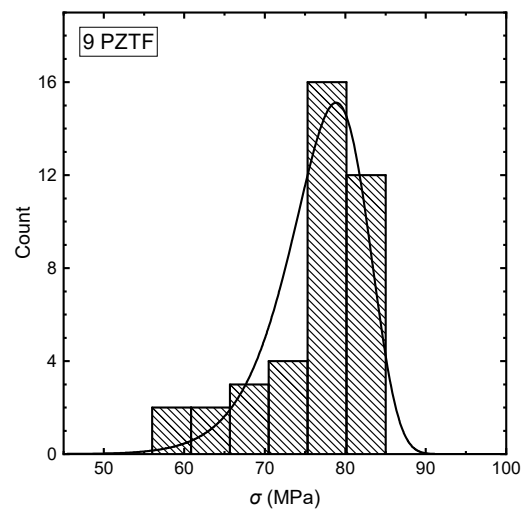
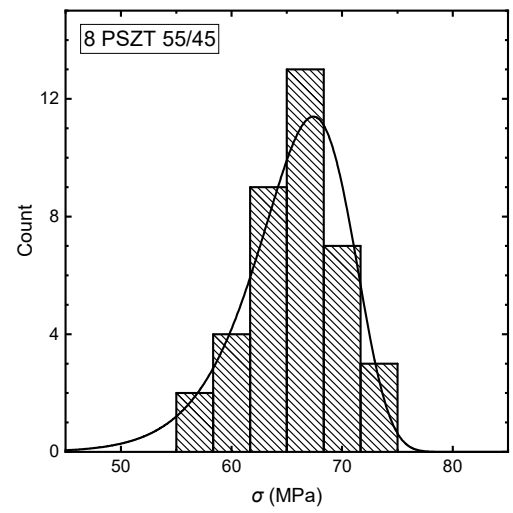
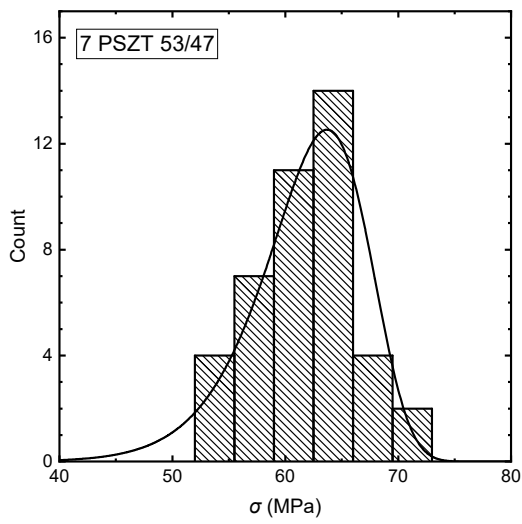
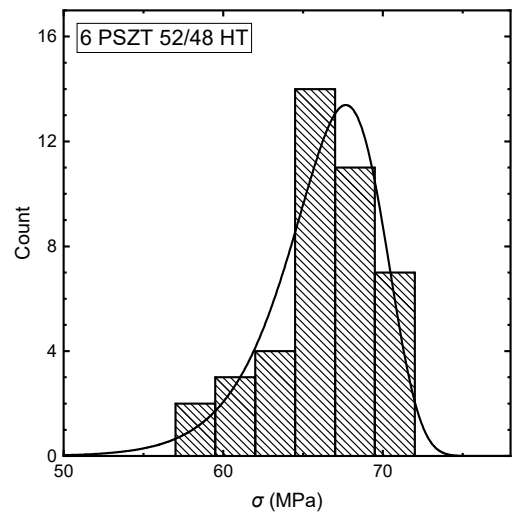
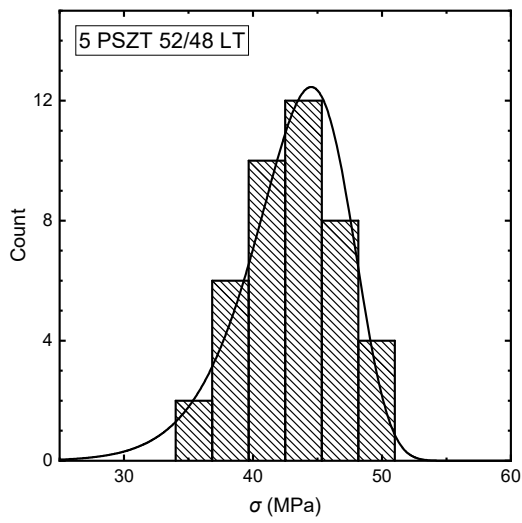


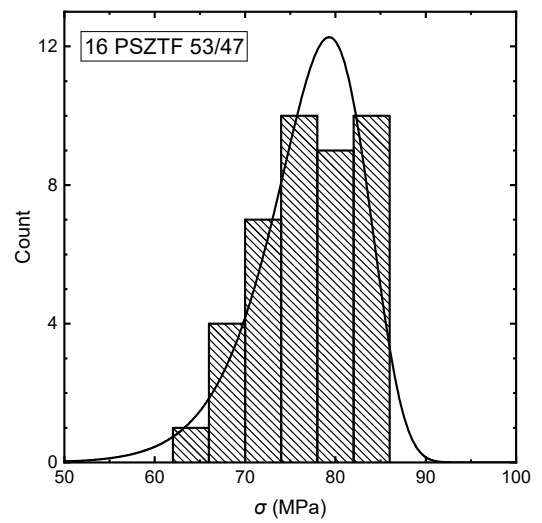
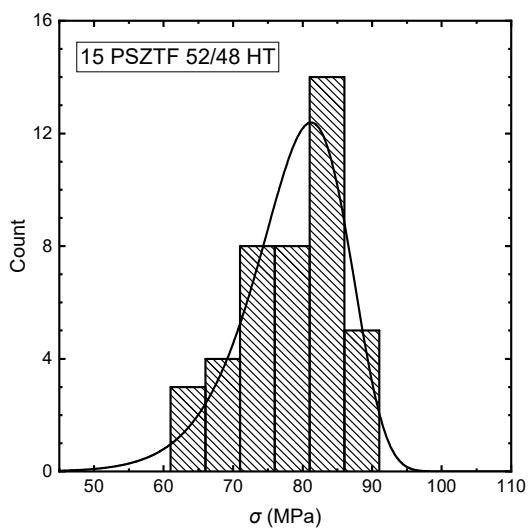
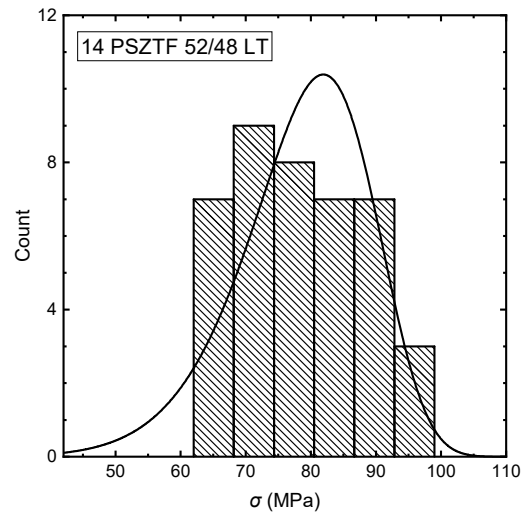
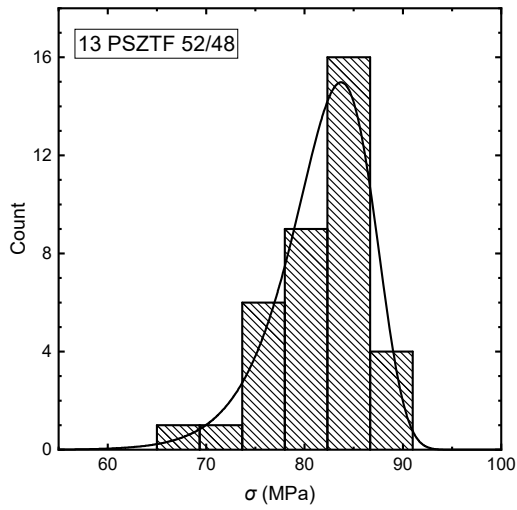
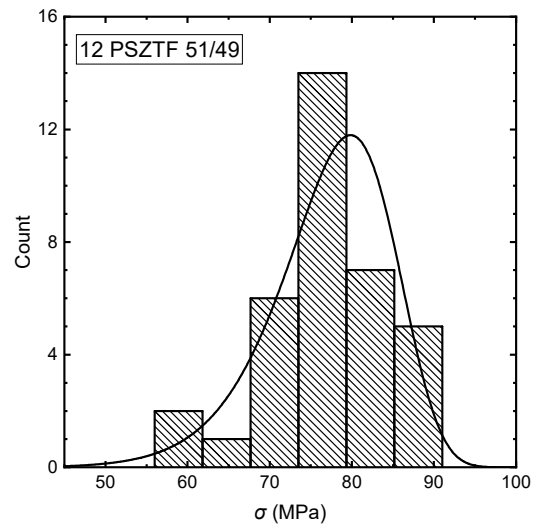
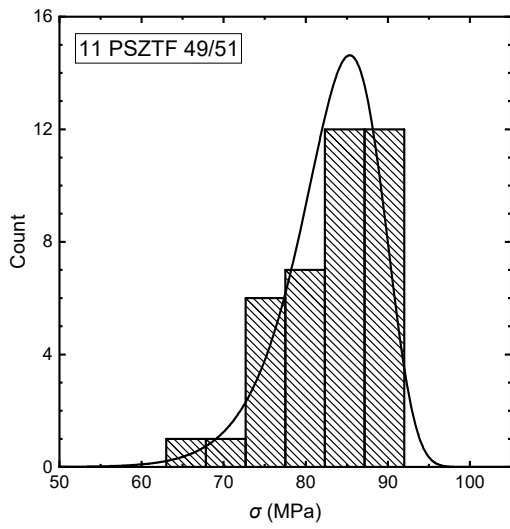
Figure A1 - 1 Test sequence plots. Horizontal grey lines represent mean strength values  $\sigma$ .

## APPENDIX II. STRENGTH HISTOGRAMS

The graphs below in Figure A2 - 1 show histograms of the strength data for each batch. Batch numbers, compositions and labels are listed in section 5.2 (Table 5-4). Binning and evaluation are described in section 8.4.2. The histograms are overlaid by a Weibull distribution curve.







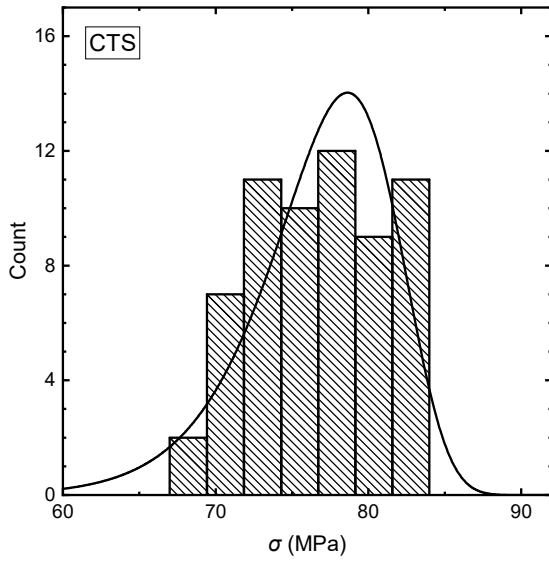
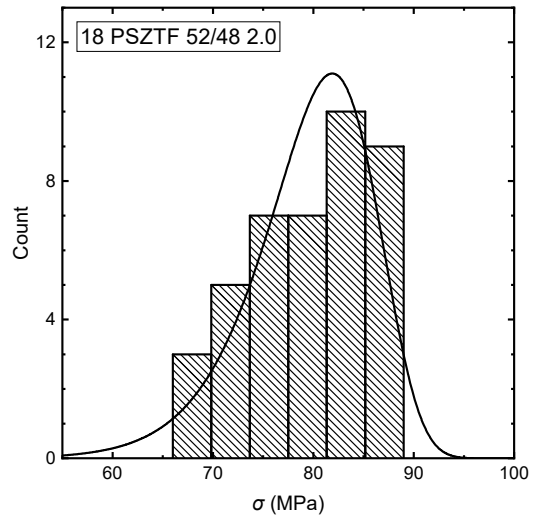
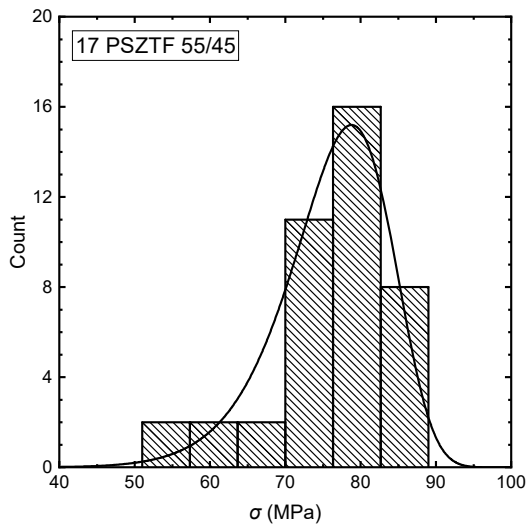


Figure A2 - 1 Strength histograms overlaid by Weibull distribution curves.

## LIST OF REFERENCES

- [1] J. A. Salem and A. Singh, "Polynomial expressions for estimating elastic constants from the resonance of circular plates," *Materials Science and Engineering: A*, vol. 422, pp. 292-297, 2006/04/25/ 2006.
- [2] T. P. Abraham, "Expanding Markets for Piezoelectrics," *Ceramic Industry*, vol. 164, pp. 12-16, 21. 4. 2014.
- [3] A. J. Moulson, "Electroceramics : materials, properties, applications / A.J. Moulson," 2nd ed. ed. Chichester: Wiley, 2003.
- [4] G. A. Schneider, "Influence of Electric Field and Mechanical Stresses on the Fracture of Ferroelectrics," *Annual Review of Materials Research*, vol. 37, pp. 491-538, 2007.
- [5] N. Ichinose and M. Kimura, "Preparation and Properties of Lead Zirconate-Titanate Piezoelectric Ceramics Using Ultrafine Particles," *Japanese Journal of Applied Physics*, vol. 30, p. 2220, 1991.
- [6] R. A. Pferner, G. Thurn, and F. Aldinger, "Mechanical properties of PZT ceramics with tailored microstructure," *Materials Chemistry and Physics*, vol. 61, pp. 24-30, 9/30/ 1999.
- [7] S. Goljahi and C. S. Lynch, "Effects of electric field on the fracture toughness ( $K_{IC}$ ) of ceramic PZT," *Smart Materials and Structures*, vol. 22, p. 094014, 2013.
- [8] Y. Chen, S. Xie, Q. Wang, L. Fu, R. Nie, and J. Zhu, "Correlation between microstructural evolutions and electrical/mechanical behaviors in Nb/Ce co-doped  $Pb(Zr_{0.52}Ti_{0.48})O_3$  ceramics at different sintering temperatures," *Materials Research Bulletin*, vol. 94, pp. 174-182, 2017.
- [9] Ö. Vardar, I. Finnie, D. R. Biswas, and R. M. Fulrath, "Effect of spherical pores on the strength of a polycrystalline ceramic," *International Journal of Fracture*, vol. 13, pp. 215-223, April 01 1977.
- [10] S. Somiya, "Handbook of Advanced Ceramics - Materials, Applications, Processing, and Properties (2nd Edition)," ed: Elsevier, 2013.
- [11] C.-L. Huang, B.-H. Chen, and L. Wu, "Variability of impurity doping in the modified  $Pb(Zr,Ti)O_3$  ceramics of type  $ABO_3$ ," *Solid State Communications*, vol. 130, pp. 19-23, 04/01 2004.
- [12] W. Weibull, "A Statistical Theory of the Strength of Materials," Stockholm 1939.
- [13] R. Danzer, P. Supancic, J. Pascual, and T. Lube, "Fracture statistics of ceramics – Weibull statistics and deviations from Weibull statistics," *Engineering Fracture Mechanics*, vol. 74, pp. 2919-2932, 2007/12/01/ 2007.
- [14] D. Munz and T. Fett, *Ceramics: mechanical properties, failure behaviour, materials selection*. New York: Springer-Verlag Berlin Heidelberg, 1999.
- [15] "ASTM C1683-10, Standard Practice for Size Scaling of Tensile Strengths Using Weibull Statistics for Advanced Ceramics," ed. West Conshohocken, PA: ASTM International, 2015.

- [16] "ASTM C1499-15, Standard Test Method for Monotonic Equibiaxial Flexural Strength of Advanced Ceramics at Ambient Temperature," ed. West Conshohocken, PA: ASTM International, 2015.
- [17] W. E. Lee, "Ceramic microstructures : property control by processing / William E. Lee and W. Mark Rainforth," W. M. Rainforth, Ed., ed. London: London : Chapman & Hall, 1994.
- [18] R. W. Rice, *Porosity of ceramics*. New York: Marcel Dekker, Inc., 1998.
- [19] E. A. Dean and J. A. Lopez, "Empirical Dependence of Elastic Moduli on Porosity for Ceramic Materials," *Journal of the American Ceramic Society*, vol. 66, pp. 366-370, 1983.
- [20] R. W. Rice, C. C. Wu, and F. Boichelt, "Hardness–Grain-Size Relations in Ceramics," *Journal of the American Ceramic Society*, vol. 77, pp. 2539-2553, 1994.
- [21] R. W. Rice, "Microstructural dependence of fracture energy and toughness of ceramics and ceramic composites versus that of their tensile strengths at 22 °C," *Journal of Materials Science*, vol. 31, pp. 4503-4519, January 01 1996.
- [22] B. Lawn, *Fracture of Brittle Solids*, 2 ed. Cambridge: Cambridge University Press, 1993.
- [23] D. R. Biswas, "Influence of porosity on the mechanical properties of lead zirconate-titanate ceramics," Ph. D., Lawrence Berkley National Laboratory, University of California, 1976.
- [24] R. W. RICE, "Ceramic tensile strength-grain size relations: grain sizes, slopes, and branch intersections," *Journal of Materials Science*, vol. 32, pp. 1673-1692, April 01 1997.
- [25] J. C. Curie, P., "Développement par compression de l'électricité polaire dans les cristaux hémihédres à faces inclinées.," *Bulletin de la Societe de Minerologique de France*, vol. 3, pp. 90-93, 1880.
- [26] B. Jaffe, "Piezoelectric ceramics," W. R. Cook and H. H. Jaffé, Eds., ed. London: Academic Press, 1971.
- [27] W. Heywang, K. Lubitz, and W. Wersing, "Piezoelectricity : evolution and future of a technology," ed. Berlin: Springer, 2008.
- [28] G. H. Haertling, "Ferroelectric Ceramics: History and Technology," *Journal of the American Ceramic Society*, vol. 82, pp. 797-818, 1999.
- [29] N. Setter, *Piezoelectric Materials in Devices: Extended Reviews on Current and Emerging Piezoelectric Materials, Technology, and Applications*: N. Setter, 2002.
- [30] E. C. F. Standardization, "EN 50324-1 Piezoelectric properties of ceramic materials and components," in *Part 1: Terms and definitions*, ed. Brussels: CEN-CENELEC Management Centre, 2002.
- [31] A. B. Schäufele and K. Heinz Härdtl, "Ferroelastic Properties of Lead Zirconate Titanate Ceramics," *Journal of the American Ceramic Society*, vol. 79, pp. 2637-2640, 1996.

- [32] A. Hizebry, M. Saâdaoui, H. Elattaoui, J. Chevalier, and G. Fantozzi, "R-curve and subcritical crack growth in lead zirconate titanate ceramics," *Materials Science and Engineering: A*, vol. 499, pp. 368-373, 2009/01/15/ 2009.
- [33] D. Fang and J. Liu, *Fracture Mechanics of Piezoelectric and Ferroelectric Solids*. Berlin, Heidelberg: Springer Berlin Heidelberg: Berlin, Heidelberg, 2013.
- [34] Y. Xu, "Ferroelectric materials and their applications," ed. Amsterdam, London: North-Holland, 1991.
- [35] V. M. Goldschmidt, "Die Gesetze der Krystallochemie," *Naturwissenschaften*, vol. 14, pp. 477-485, May 01 1926.
- [36] R. Shannon, "Revised effective ionic radii and systematic studies of interatomic distances in halides and chalcogenides," *Acta Crystallographica Section A*, vol. 32, pp. 751-767, 1976.
- [37] V. R. Cooper, I. Grinberg, N. R. Martin, and A. M. Rappe, "Local Structure of PZT," *AIP Conference Proceedings*, vol. 626, pp. 26-35, 2002.
- [38] D. I. Woodward, J. Knudsen, and I. M. Reaney, "Review of crystal and domain structures in the  $\text{PbZr}_x\text{Ti}_{1-x}\text{O}_3$  solid solution," *Physical Review B*, vol. 72, p. 104110, 09/20/ 2005.
- [39] N. Zhang, H. Yokota, A. M. Glazer, Z. Ren, D. A. Keen, D. S. Keeble, *et al.*, "The missing boundary in the phase diagram of  $\text{PbZr}_{1-x}\text{Ti}_x\text{O}_3$ ," *Nat Commun*, vol. 5, 10/24 2014.
- [40] J. Liu, W. Chen, B. Wang, and Y. Zheng, "Theoretical Methods of Domain Structures in Ultrathin Ferroelectric Films: A Review," *Materials*, vol. 7, pp. 6502-6568, 2014.
- [41] G. A. Rossetti, A. G. Khachatryan, G. Akcay, and Y. Ni, "Ferroelectric solid solutions with morphotropic boundaries: Vanishing polarization anisotropy, adaptive, polar glass, and two-phase states," *Journal of Applied Physics*, vol. 103, p. 114113, 2008.
- [42] B. Noheda, D. E. Cox, G. Shirane, J. A. Gonzalo, L. E. Cross, and S.-E. Park, "A monoclinic ferroelectric phase in the  $\text{Pb}(\text{Zr}_{1-x}\text{Ti}_x)\text{O}_3$  solid solution," *Applied Physics Letters*, vol. 74, pp. 2059-2061, 1999.
- [43] O. Hudak, "Monoclinic phase in PZT: order parameter and phase transition from Tetragonal Phase," *Phase Transitions*, vol. 81, pp. 1073-1079, 2008/11/01 2008.
- [44] D. Damjanovic, "Contributions to the Piezoelectric Effect in Ferroelectric Single Crystals and Ceramics," *Journal of the American Ceramic Society*, vol. 88, pp. 2663-2676, 2005.
- [45] M. Hinterstein, M. Hoelzel, J. Rouquette, J. Haines, J. Glaum, H. Kungl, *et al.*, "Interplay of strain mechanisms in morphotropic piezoceramics," *Acta Materialia*, vol. 94, pp. 319-327, 8/1/ 2015.
- [46] M. Hinterstein, J. Rouquette, J. Haines, P. Papet, M. Knapp, J. Glaum, *et al.*, "Structural Description of the Macroscopic Piezo- and Ferroelectric Properties of Lead Zirconate Titanate," *Physical Review Letters*, vol. 107, p. 077602, 08/09/ 2011.
- [47] X. Lu, L. Zheng, H. Li, and W. Cao, "Theoretical study on phase coexistence in ferroelectric solid solutions near the tricritical point," *Journal of Applied Physics*, vol. 117, p. 134101, 2015.

- [48] F. Cordero, "Elastic Properties and Enhanced Piezoelectric Response at Morphotropic Phase Boundaries," *Materials*, vol. 8, p. 5452, 2015.
- [49] M. J. Hoffmann and H. Kungl, "High strain lead-based perovskite ferroelectrics," *Current Opinion in Solid State and Materials Science*, vol. 8, pp. 51-57, 2004/01/01/2004.
- [50] F. Kulcsar, "Electromechanical Properties of Lead Titanate Zirconate Ceramics with Lead Partially Replaced by Calcium or Strontium," *Journal of the American Ceramic Society*, vol. 42, pp. 49-51, 1959.
- [51] C. A. Randall, N. Kim, J.-P. Kucera, W. Cao, and T. R. Shrout, "Intrinsic and Extrinsic Size Effects in Fine-Grained Morphotropic-Phase-Boundary Lead Zirconate Titanate Ceramics," *Journal of the American Ceramic Society*, vol. 81, pp. 677-688, 1998.
- [52] A. G. Luchaninov, A. V. Shil'nikov, and L. A. Shuvalov, "Domain reorientations and piezoeffect in PZT ceramics," *Ferroelectrics*, vol. 208-209, pp. 385-394, 1998/04/01 1998.
- [53] D. M. Marincel, H. Zhang, S. Jesse, A. Belianinov, M. B. Okatan, S. V. Kalinin, *et al.*, "Domain Wall Motion Across Various Grain Boundaries in Ferroelectric Thin Films," *Journal of the American Ceramic Society*, vol. 98, pp. 1848-1857, 2015.
- [54] Y. Wu and J. Hou, "Intrinsic electromechanical properties of ferroelectric ceramics with the coexistence of tetragonal and rhombohedral phases near the morphotropic phase boundary," *Journal of Applied Physics*, vol. 116, p. 114104, 2014.
- [55] D. M. Marincel, H. R. Zhang, J. Britson, A. Belianinov, S. Jesse, S. V. Kalinin, *et al.*, "Domain pinning near a single-grain boundary in tetragonal and rhombohedral lead zirconate titanate films," *Physical Review B*, vol. 91, p. 134113, 04/27/ 2015.
- [56] D. Damjanovic, "Hysteresis in piezoelectric and ferroelectric materials." vol. Volume III, G. Bertotti and I. Mayergoyz, Eds., ed: Academic Press, pp. 337-465-337-465.
- [57] R.-A. Eichel, H. Meštrić, H. Kungl, and M. J. Hoffmann, "Multifrequency electron paramagnetic resonance analysis of polycrystalline gadolinium-doped  $\text{PbTiO}_3$ —Charge compensation and site of incorporation," *Applied Physics Letters*, vol. 88, p. 122506, 2006.
- [58] P. Jakes, E. Erdem, R.-A. Eichel, L. Jin, and D. Damjanovic, "Position of defects with respect to domain walls in  $\text{Fe}^{3+}$ -doped  $\text{Pb}[\text{Zr}_{0.52}\text{Ti}_{0.48}]\text{O}_3$  piezoelectric ceramics," *Applied Physics Letters*, vol. 98, p. 072907, 2011.
- [59] T. M. Kamel and G. de With, "Poling of hard ferroelectric PZT ceramics," *Journal of the European Ceramic Society*, vol. 28, pp. 1827-1838, // 2008.
- [60] U. Robels and G. Arlt, "Domain wall clamping in ferroelectrics by orientation of defects," *Journal of Applied Physics*, vol. 73, pp. 3454-3460, 1993.
- [61] B. M. Fraygola, A. Chandrasekanar, D. Bahati, U. Salazar, A. Biancoli, N. Marzari, *et al.*, "Piezoelectric softening by Nb substitution in  $(\text{Ba,Pb})\text{ZrO}_3$  ceramics," *Journal of the American Ceramic Society*, vol. 100, pp. 1885-1895, 2017.
- [62] L. Jin, V. Porokhonsky, and D. Damjanovic, "Domain wall contributions in  $\text{Pb}(\text{Zr,Ti})\text{O}_3$  ceramics at morphotropic phase boundary: A study of dielectric dispersion," *Applied Physics Letters*, vol. 96, p. 242902, 2010.

- [63] L. Jin, Z. He, and D. Damjanovic, "Nanodomains in Fe<sup>+3</sup>-doped lead zirconate titanate ceramics at the morphotropic phase boundary do not correlate with high properties," *Applied Physics Letters*, vol. 95, p. 012905, 2009.
- [64] W. Cao and C. A. Randall, "Grain size and domain size relations in bulk ceramic ferroelectric materials," *Journal of Physics and Chemistry of Solids*, vol. 57, pp. 1499-1505, 1996/10/01/ 1996.
- [65] Q. Tan, J.-F. Li, and D. Viehland, "Ferroelectric behaviours dominated by mobile and randomly quenched impurities in modified lead zirconatetitanate ceramics," *Philosophical Magazine B*, vol. 76, pp. 59-74, 1997/07/01 1997.
- [66] H. Thomann, "Piezoelectric mechanisms in lead zirconate-titanate," *Z. Angew. Phys.*, vol. 20, pp. 554-559, 1966.
- [67] Y. Matsuo and H. Sasaki, "Formation of Lead Zirconate-Lead Titanate Solid Solutions," *Journal of the American Ceramic Society*, vol. 48, pp. 289-291, 1965.
- [68] C. Boudaren, A. Mousser, and L. Chuc, "PZT formation in the presence of dopants," *Ceramics International*, vol. 23, pp. 279-282, 1997/01/01 1997.
- [69] B. V. Hiremath, A. I. Kingon, and J. V. Biggers, "Reaction Sequence in the Formation of Lead Zirconate-Lead Titanate Solid Solution: Role of Raw Materials," *Journal of the American Ceramic Society*, vol. 66, pp. 790-793, 1983.
- [70] S. S. Chandratreya, R. M. Fulrath, and J. A. Pask, "Reaction Mechanisms in the Formation of PZT Solid Solutions," *Journal of the American Ceramic Society*, vol. 64, pp. 422-425, 1981.
- [71] D. L. Hankey and J. V. Diggers, "Solid - State Reactions in the System PbO - TiO<sub>2</sub> - ZrO<sub>2</sub>," *Journal of the American Ceramic Society*, vol. 64, pp. C - 172-C - 173, 1981.
- [72] J.-R. Soh, H. M. Lee, and H.-S. Kwon, "Thermodynamic evaluation and phase diagram of PbO-TiO<sub>2</sub> system," *Calphad*, vol. 18, pp. 237-244, 1994/07/01/ 1994.
- [73] X. Tan and J. K. Shang, "In-situ transmission electron microscopy study of electric-field-induced grain-boundary cracking in lead zirconate titanate," *Philosophical Magazine A*, vol. 82, pp. 1463-1478, 2002/05/01 2002.
- [74] M. Hammer and M. J. Hoffmann, "Sintering Model for Mixed-Oxide-Derived Lead Zirconate Titanate Ceramics," *Journal of the American Ceramic Society*, vol. 81, pp. 3277-3284, 1998.
- [75] M. N. Rahaman, "Ceramic processing," ed. Boca Raton, Fla., London: CRC/Taylor & Francis, 2007.
- [76] A. I. Kingon and J. B. Clark, "Sintering of PZT Ceramics: II, Effect of PbO Content on Densification Kinetics," *Journal of the American Ceramic Society*, vol. 66, pp. 256-260, 1983.
- [77] W.-P. Tai and S.-H. Kim, "The effect of poling treatment and crystal structure of PZT on fracture toughness and fatigue resistance," *Journal of Materials Science*, vol. 38, pp. 1787-1792, April 01 2003.

- [78] M. J. Hoffmann, M. Hammer, A. Endriss, and D. C. Lupascu, "Correlation between microstructure, strain behavior, and acoustic emission of soft PZT ceramics," *Acta Materialia*, vol. 49, pp. 1301-1310, 2001/04/19/ 2001.
- [79] M. D. Durruthy, L. Fuentes, M. Hernández, and H. Camacho, "Influence of the niobium dopant concentration on the  $\text{Pb}(\text{Zr}_{0.54}\text{Ti}_{0.46})\text{O}_3$  ceramics sintering and final properties," *Journal of Materials Science*, vol. 35, pp. 2311-2317, May 01 2000.
- [80] T. B. Weston, A. H. Webster, and V. M. McNamara, "Lead Zirconate - Lead Titanate Piezoelectric Ceramics with Iron Oxide Additions," *Journal of the American Ceramic Society*, vol. 52, pp. 253-257, 1969.
- [81] R. B. Atkin and R. M. Fulrath, "Point Defects and Sintering of Lead Zirconate-Titanate," *Journal of the American Ceramic Society*, vol. 54, pp. 265-270, 1971.
- [82] X. Huang, "Sintering kinetics and properties of highly pure lead zirconate titanate ceramics," PhD Dissertation, Fakultät für Biologie, Chemie und Geowissenschaften, Universität Bayreuth, Würzburg, 2009.
- [83] J.-C. M'Peko, A. G. Peixoto, E. Jiménez, and L. M. Gaggero-Sager, "Electrical Properties of Nb-Doped PZT 65/35 Ceramics: Influence of Nb and Excess  $\text{PbO}$ ," *Journal of Electroceramics*, vol. 15, pp. 167-176, November 01 2005.
- [84] H. Camacho, M. E. Fuentes, and L. Fuentes, "Effects of interface properties on densification in a grain compact during sintering," *Journal of Materials Science*, vol. 38, pp. 3269-3278, August 01 2003.
- [85] O. Guillon, F. Thiebaud, D. Perreux, C. Courtois, P. Champagne, A. Leriche, *et al.*, "New considerations about the fracture mode of PZT ceramics," *Journal of the European Ceramic Society*, vol. 25, pp. 2421-2424, // 2005.
- [86] B. Malič, M. Kosec, and G. Dražič, " $\text{Pb}(\text{Zr},\text{Ti})\text{O}_3$  based ceramics prepared by solution processing," *Journal of the European Ceramic Society*, vol. 24, pp. 475-478, 2004/01/01/ 2004.
- [87] H. Wang, H.-T. Lin, and A. A. Wereszczak, "Strength Properties of Poled Lead Zirconate Titanate Subjected to Biaxial Flexural Loading in High Electric Field," *Journal of the American Ceramic Society*, vol. 93, pp. 2843-2849, 2010.
- [88] Z. Kewei, Z. Fan Wen, W. Hong, and L. Hua-Tay, "Strength properties of aged poled lead zirconate titanate subjected to electromechanical loadings," *Smart Materials and Structures*, vol. 21, p. 119601, 2012.
- [89] T. Hang, J. Glaum, T. Phung, and M. Hoffman, "Investigation of Partial Discharge and Fracture Strength in Piezoelectric Ceramics," *Journal of the American Ceramic Society*, vol. 97, pp. 1905-1911, 2014.
- [90] H. Wang and A. A. Wereszczak, "Effects of electric field and biaxial flexure on the failure of poled lead zirconate titanate," *Ultrasonics, Ferroelectrics, and Frequency Control, IEEE Transactions on*, vol. 55, pp. 2559-2570, 2008.
- [91] W. Zuoyi, J. Qing, S. W. Grady, and K. R. Angela, "Processing flaws in PZT transducer rings," *Smart Materials and Structures*, vol. 7, p. 867, 1998.
- [92] T. Miyoshi and H. Funakubo, "Effect of Grain Size on Mechanical Properties of Full-Dense  $\text{Pb}(\text{Zr},\text{Ti})\text{O}_3$  Ceramics," *Japanese Journal of Applied Physics*, vol. 49, 2010.

- [93] M. G. Cain, M. Stewart, M. G. Gee, M. National Physical Laboratory . Centre for Materials, and Technology, "Mechanical and electric strength measurements for piezoelectric ceramics : technical measurement notes," ed: National Physical Laboratory.Great Britain, Centre for Materials Measurement and Technology, 1998, p. 23 p. : ill. ; 30 cm.
- [94] A. Garg and D. C. Agrawal, "Effect of net PbO content on mechanical and electromechanical properties of lead zirconate titanate ceramics," *Materials Science and Engineering: B*, vol. 60, pp. 46-50, 5/31/ 1999.
- [95] O. Guillon, F. Thiebaud, and D. Perreux, "Tensile fracture of soft and hard PZT," *International Journal of Fracture*, vol. 117, pp. 235-246, 2002.
- [96] D. R. Biswas and R. M. Fulrath, "Effect of surface treatments on strength of PZT polycrystalline ceramics," *Journal of Materials Science*, vol. 14, pp. 2721-2725, November 01 1979.
- [97] S.-J. Yoon, J. H. Moon, and H.-J. Kim, "Piezoelectric and mechanical properties of  $\text{Pb}(\text{Zr}_{0.52}\text{Ti}_{0.48})\text{O}_3\text{-Pb}(\text{Y}_{2/3}\text{W}_{1/3})\text{O}_3$  (PZT-PYW) ceramics," *Journal of Materials Science*, vol. 32, pp. 779-782, 1997/02/01 1997.
- [98] T. Karastamatis, D. C. Lupascu, S. L. dos Santos e Lucato, J. Rödel, and C. S. Lynch, "R-curves of lead zirconate titanate (PZT)," *Journal of the European Ceramic Society*, vol. 23, pp. 1401-1408, 2003/08/01/ 2003.
- [99] J.-J. Kim and D.-Y. Kim, "Change in the Fracture Mode of PLZT Ceramics by Chemically Induced Grain-Boundary Migration," *Journal of the American Ceramic Society*, vol. 71, pp. C - 228-C - 229, 1988.
- [100] A. Garg and T. C. Goel, "Mechanical and electrical properties of PZT ceramics (Zr:Ti=0.40:0.60) related to  $\text{Nd}_{3+}$  Addition," *Materials Science and Engineering: B*, vol. 60, pp. 128-132, 1999/06/15/ 1999.
- [101] S.-B. Kim, D.-Y. Kim, J.-J. Kim, and S.-H. Cho, "Effect of Grain Size and Poling on the Fracture Mode of Lead Zirconate Titanate Ceramics," *Journal of the American Ceramic Society*, vol. 73, pp. 161-163, 1990.
- [102] C. V. Verhoosel and M. A. Gutiérrez, "Modelling inter- and transgranular fracture in piezoelectric polycrystals," *Engineering Fracture Mechanics*, vol. 76, pp. 742-760, 2009/04/01/ 2009.
- [103] A. Abdollahi and I. Arias, "Numerical simulation of intergranular and transgranular crack propagation in ferroelectric polycrystals," *International Journal of Fracture*, vol. 174, pp. 3-15, March 01 2012.
- [104] R.-f. Yue, W.-z. He, F.-f. An, J. Yu, and G.-c. Chen, "Preparation of PZT-based piezoceramics with transgranular fracture mode," *Ceramics International*, vol. 38, pp. S225-S228, 2012/01/01/ 2012.
- [105] E. R. Nielsen, E. Ringgaard, and M. Kosec, "Liquid-phase sintering of  $\text{Pb}(\text{Zr,Ti})\text{O}_3$  using  $\text{PbO-WO}_3$  additive," *Journal of the European Ceramic Society*, vol. 22, pp. 1847-1855, 2002/10/01/ 2002.

- [106] T. Watanabe and S. Tsurekawa, "The control of brittleness and development of desirable mechanical properties in polycrystalline systems by grain boundary engineering," *Acta Materialia*, vol. 47, pp. 4171-4185, 1999/11/01/ 1999.
- [107] M. Wojdyr, "Fityk: a general-purpose peak fitting program," *Journal of Applied Crystallography*, vol. 43, pp. 1126-1128, 2010.
- [108] W. S. Rasband, "ImageJ," ed. Bethesda, Maryland, USA: U. S. National Institutes of Health, 1997-2016.
- [109] L. Wojnar, "Image analysis : applications in materials engineering," ed. Boca Raton, London: CRC Press, 1999.
- [110] E. C. f. Standardization, "EN ISO 13383-1 Fine ceramics (advanced ceramics, advanced technical ceramics) - Microstructural characterization," in *Part 1: Determination of grain size and size distribution*, ed. Brussels: CEN-CENELEC Management Centre, 2016, p. 23.
- [111] "ASTM C1327-15, Standard Test Method for Vickers Indentation Hardness of Advanced Ceramics, ASTM International," ed. West Conshohocken, PA: ASTM International, 2015.
- [112] E. C. F. Standardization, "EN 843-4 Advanced technical ceramics - Mechanical properties of monolithic ceramics at room temperature," in *Part 4: Vickers, Knoop and Rockwell superficial hardness*, ed. Brussels: CEN-CENELEC Management Centre, 2005.
- [113] "ASTM C1259-1, Standard Test Method for Dynamic Young's Modulus, Shear Modulus, and Poisson's Ratio for Advanced Ceramics by Impulse Excitation of Vibration," ed. West Conshohocken, PA: ASTM International, 2015.
- [114] G. Martinček, "The determination of poisson's ratio and the dynamic modulus of elasticity from the frequencies of natural vibration in thick circular plates," *Journal of Sound and Vibration*, vol. 2, pp. 116-127, 1965/04/01/ 1965.
- [115] R. Morrell, N. J. McCormick, J. Bevan, M. Lodeiro, and J. Margetson, "Biaxial disc flexure – modulus and strength testing," vol. 98, ed, 1998, pp. 234-240.
- [116] R. Morrell. (1998, Biaxial flexural strength testing of ceramic materials. *National good measurement practice guide (12)*, 52.
- [117] D. Shetty, A. R. Rosenfield, P. McGuire, G. K. Bansal, and W. H. Duckworth, *Biaxial Flexure Test for Ceramics* vol. 59:12, 1980.
- [118] M. E. Manley, T. Ertürk, C. Vaucamps, and D. Gailus, "Four Point and Biaxial Flexure Strength of PZT Ceramics: A Probabilistic Approach," in *Proceedings of the 18th Annual Conference on Composites and Advanced Ceramic Materials—B: Ceramic Engineering and Science Proceedings*, ed: John Wiley & Sons, Inc., 2008, pp. 885-894.
- [119] CTS, "Piezoelectric Polycrystalline (PZT) Components and Wafers," ed: CTS Corporation, 2017.
- [120] R. Morrell. (1999, Fractography of Brittle Materials. *National good measurement practice guide (15)*, 86.
- [121] G. D. Quinn, *Fractography of Ceramics and Glasses* vol. 960-16. Washington: U.S. Government Printing Office, 2016.

- [122] "ASTM C1322-15, Standard Practice for Fractography and Characterization of Fracture Origins in Advanced Ceramics," ed. West Conshohocken, PA: ASTM International, 2015.
- [123] A. A. Wereszczak, J. J. Swab, and R. H. Kraft, "Effects of Machining on the Uniaxial and Equibiaxial Flexure Strength of CAP3 AD-995 Al<sub>2</sub>O<sub>3</sub>," U.S. Army Research Laboratory, Aberdeen Proving Ground 2005.
- [124] CoorsTek, "Advanced Alumina brochure," ed, 2016.
- [125] S. B. Batdorf, "Some approximate treatments of fracture statistics for polyaxial tension," *International Journal of Fracture*, vol. 13, pp. 5-11, February 01 1977.
- [126] N. A. Weil and I. M. Daniel, "Analysis of Fracture Probabilities in Nonuniformly Stressed Brittle Materials," *Journal of the American Ceramic Society*, vol. 47, pp. 268-274, 1964.
- [127] K. Breder, T. Andersson, and K. Schölin, "Fracture Strength of  $\alpha$ - and  $\beta$ -SiAlON Measured by Biaxial and Four-Point Bending," *Journal of the American Ceramic Society*, vol. 73, pp. 2128-2130, 1990.
- [128] J. Lamon, "Statistical Approaches to Failure for Ceramic Reliability Assessment," *Journal of the American Ceramic Society*, vol. 71, pp. 106-112, 1988.
- [129] N. N. Nemeth, L. M. Powers, L. A. Janosik, and J. P. Gyekenyesi, "CARES/LIFE Ceramics Analysis and Reliability Evaluation of Structures Life Prediction Program," NASA 2003.
- [130] M. N. Giovan and G. Sines, "Biaxial and Uniaxial Data for Statistical Comparisons of a Ceramic's Strength," *Journal of the American Ceramic Society*, vol. 62, pp. 510-515, 1979.
- [131] W. Cao, A. Kundu, Z. Yu, M. P. Harmer, and R. P. Vinci, "Direct correlations between fracture toughness and grain boundary segregation behavior in ytterbium-doped magnesium aluminate spinel," *Scripta Materialia*, vol. 69, pp. 81-84, 2013/07/01/ 2013.
- [132] E. C. F. Standardization, "EN 50324-2 Piezoelectric properties of ceramic materials and components," in *Part 2: Methods of measurement - Low power*, ed. Brussels: CEN-CENELEC Management Centre, 2002.
- [133] M. G. Cain and M. Stewart. (2001, Piezoelectric Resonance. *Measurement good practice guide (33)*, 35.
- [134] M. Stewart, W. Battrick, and M. Cain. (2001, Measuring Piezoelectric d<sub>33</sub> coefficients using the Direct Method. *Measurement good practice guide (44)*, 30.
- [135] N. J. Porch, "The net-shape ceramic processing of novel piezoelectric devices for macro actuation applications / by Nicola Jane Porch," Birmingham, 2005.
- [136] D. A. Northrop, "Vaporization of Lead Zirconate-Lead Titanate Materials," *Journal of the American Ceramic Society*, vol. 50, pp. 441-445, 1967.
- [137] D. A. Northrop, "Vaporization of Lead Zirconate-Lead Titanate Materials: II, Hot-Pressed compositions at Near Theoretical Density," *Journal of the American Ceramic Society*, vol. 51, pp. 357-361, 1968.

- [138] R. L. Moon and R. M. Fulrath, "Vaporization and Surface Phases in the Lead Zirconate-Lead Titanate System," *Journal of the American Ceramic Society*, vol. 52, pp. 565-566, 1969.
- [139] R. L. Holman and R. M. Fulrath, "Intrinsic nonstoichiometry in the lead zirconate - lead titanate system determined by Knudsen effusion," *Journal of Applied Physics*, vol. 44, pp. 5227-5236, 1973.
- [140] C.-C. Chung, "Microstructural Evolution in Lead Zirconate Titanate (PZT) Piezoelectric Ceramics," Doctor of Philosophy Doctoral Dissertation, University of Connecticut, 2014.
- [141] C. Slouka, T. Kainz, E. Navickas, G. Walch, H. Hutter, K. Reichmann, *et al.*, "The Effect of Acceptor and Donor Doping on Oxygen Vacancy Concentrations in Lead Zirconate Titanate (PZT)," *Materials*, vol. 9, p. 945, 2016.
- [142] K. H. Härdtl and H. Rau, "PbO vapour pressure in the  $\text{Pb}(\text{Ti}_{1-x})\text{O}_3$  system," *Solid State Communications*, vol. 7, pp. 41-45, 1969/01/01 1969.
- [143] A. I. Kingon and J. B. Clark, "Sintering of PZT Ceramics: I, Atmosphere Control," *Journal of the American Ceramic Society*, vol. 66, pp. 253-256, 1983.
- [144] M. Safar, T. W. Button, and M. Zabcik, "Control of PbO loss during sintering of PZT: Laboratory vs industry," in *2017 Joint IEEE International Symposium on the Applications of Ferroelectric (ISAF)/International Workshop on Acoustic Transduction Materials and Devices (IWATMD)/Piezoresponse Force Microscopy (PFM)*, 2017, pp. 83-88.
- [145] D. B. Marshall, A. G. Evans, B. T. K. Yakub, J. W. Tien, and G. S. Kino, "The Nature of Machining Damage in Brittle Materials," *Proceedings of the Royal Society of London. Series A, Mathematical and Physical Sciences (1934-1990)*, vol. 385, pp. 461-475, 1983.
- [146] M. Hammer, C. Monty, A. Endriss, and M. J. Hoffmann, "Correlation between Surface Texture and Chemical Composition in Undoped, Hard, and Soft Piezoelectric PZT Ceramics," *Journal of the American Ceramic Society*, vol. 81, pp. 721-724, 1998.
- [147] M. Karun and V. A. V., "Fracture Mechanisms in Ferroelectric-Ferroelastic Lead Zirconate Titanate (Zr: Ti=0.54:0.46) Ceramics," *Journal of the American Ceramic Society*, vol. 73, pp. 567-574, 1990.
- [148] E. Erdem, R.-A. Eichel, C. Fetzer, I. Dézsi, S. Lauterbach, H.-J. Kleebe, *et al.*, "Site of incorporation and solubility for Fe ions in acceptor-doped PZT ceramics," *Journal of Applied Physics*, vol. 107, p. 054109, 2010.
- [149] S. Puthucheri, P. K. Pandey, N. S. Gajbhiye, A. Gupta, A. Singh, R. Chatterjee, *et al.*, "Microstructural, Electrical, and Magnetic Properties of Acceptor-Doped Nanostructured Lead Zirconate Titanate," *Journal of the American Ceramic Society*, vol. 94, pp. 3941-3947, 2011.
- [150] H.-J. Kleebe, S. Lauterbach, L. Silvestroni, H. Kungl, M. J. Hoffmann, E. Erdem, *et al.*, "Formation of magnetic grains in ferroelectric  $\text{Pb}(\text{Zr}_{0.6}\text{Ti}_{0.4})\text{O}_3$  ceramics doped with  $\text{Fe}^{3+}$  above the solubility limit," *Applied Physics Letters*, vol. 94, p. 142901, 2009.

- [151] H. Zheng, I. M. Reaney, W. E. Lee, N. Jones, and H. Thomas, "Effects of Octahedral Tilting on the Piezoelectric Properties of Sr-Doped Lead Zirconate Titanate," *Ferroelectrics*, vol. 268, pp. 125-130, 2002/01/01 2002.
- [152] Z. Necira, A. Boutarfaia, M. Abba, H. Menasra, and N. Abdessalem, "Effects of Thermal Conditions in the Phase Formation of Undoped and Doped  $\text{Pb}(\text{Zr}_{1-x}\text{Ti}_x)\text{O}_3$  Solid Solutions," *Materials Sciences and Applications*, vol. 4, p. 5, 2013.
- [153] L. Kozielski, M. Adamczyk, J. Erhart, and M. Pawełczyk, "Application testing of Sr doping effect of PZT ceramics on the piezoelectric transformer gain and efficiency proposed for MEMS actuators driving," *Journal of Electroceramics*, vol. 29, pp. 133-138, 2012.
- [154] K. Ramam and M. Lopez, "Effect of strontium doping on dielectric, ferroelectric and piezoelectric properties of PLZTN ceramics," *Materials Science and Engineering: B*, vol. 145, pp. 41-47, 2007/12/20/ 2007.
- [155] K. Ramam and K. Chandramouli, "Dielectric and piezoelectric properties of combinatory effect of A-site isovalent and B-site acceptor doped PLZT ceramics," *Ceramics – Silikáty*, vol. 53, pp. 189-194, 2009.
- [156] S. FUSHIMI and T. IKEDA, "Phase Equilibrium in the System  $\text{PbO-TiO}_2\text{-ZrO}_2$ ," *Journal of the American Ceramic Society*, vol. 50, pp. 129-132, 1967.
- [157] Y. Nakamura, S. S. Chandratreya, and R. M. Fulrath, "Expansion during the reaction sintering of PZT," *Ceramurgia International*, vol. 6, pp. 57-60, 1980/04/01/ 1980.
- [158] B. Malič, D. Kolar, and M. Kosec, "Anomalous densification of complex ceramics in the initial sintering stage," in *Sintering Technology*, R. M. German, G. L. Messing, and R. G. Cornwall, Eds., ed New York: Marcel Dekker, 1996, pp. 69-76.
- [159] J. F. Fernández, C. Moure, M. Villegas, P. Durán, M. Kosec, and G. Drazic, "Compositional fluctuations and properties of fine-grained acceptor-doped PZT ceramics," *Journal of the European Ceramic Society*, vol. 18, pp. 1695-1705, 1998/11/01 1998.
- [160] A. I. Kingon, P. J. Terblanché, and J. B. Clark, "The control of composition, microstructure and properties of  $\text{Pb}(\text{Zr,Ti})\text{O}_3$  ceramics," *Materials Science and Engineering*, vol. 71, pp. 391-397, 1985/05/01/ 1985.
- [161] P. Klobes, K. Meyer, and R. G. Munro. (2006). *Porosity and Specific Surface Area Measurements for Solid Materials*. 960-17.
- [162] J. Peng, J. Zeng, G. Li, L. Zheng, X. Ruan, X. Huang, *et al.*, "Softening-hardening transition of electrical properties for  $\text{Fe}^{3+}$ -doped  $(\text{Pb}_{0.94}\text{Sr}_{0.05}\text{La}_{0.01})(\text{Zr}_{0.53}\text{Ti}_{0.47})\text{O}_3$  piezoelectric ceramics," *Ceramics International*, vol. 43, pp. 13233-13239, 2017/11/01/ 2017.
- [163] M. R. Soares, A. M. R. Senos, and P. Q. Mantas, "Phase coexistence region and dielectric properties of PZT ceramics," *Journal of the European Ceramic Society*, vol. 20, pp. 321-334, 2000/03/01/ 2000.
- [164] Geetika and A. M. Umarji, "The influence of Zr/Ti content on the morphotropic phase boundary in the PZT–PZN system," *Materials Science and Engineering: B*, vol. 167, pp. 171-176, 2010/03/25/ 2010.

- [165] P. G. Lucuta, F. L. Constantinescu, and D. Barb, "Structural Dependence on Sintering Temperature of Lead Zirconate-Titanate Solid Solutions," *Journal of the American Ceramic Society*, vol. 68, pp. 533-537, 1985.
- [166] F. Vasiliu, P. G. Lucuta, and F. Constantinescu, "Structure-sintering temperature relationship in PZT solid solutions at the morphotropic phase boundary," *physica status solidi (a)*, vol. 80, pp. 637-642, 1983.
- [167] T. Ikeda, "A Few Quarternary Systems of Perovskite Type  $A^{2+}B^{4+}O_3$  Solid Solutions," *Journal of the Physical Society of Japan*, vol. 14, pp. 1286-1294, 1959/10/15 1959.
- [168] M. S. da Silva, R. G. Dias, E. F. de Souza, M. Cilense, M. A. Zaghete, and A. A. Cavaleiro, "Effect of Strontium Doping on the Structural, Morphological, and Dielectric Properties of PZT Ceramics," *Materials Science Forum*, vol. 869, pp. 8-12, 2016.
- [169] V. Kalem, İ. Çam, and M. Timuçin, "Dielectric and piezoelectric properties of PZT ceramics doped with strontium and lanthanum," *Ceramics International*, vol. 37, pp. 1265-1275, 2011/05/01/ 2011.
- [170] H. Zheng, I. M. Reaney, W. E. Lee, N. Jones, and H. Thomas, "Effects of strontium substitution in Nb-doped PZT ceramics," *Journal of the European Ceramic Society*, vol. 21, pp. 1371-1375, 2001/01/01/ 2001.
- [171] H. Lu, U. Kenji, and N. Shōichiro, "On the Phenomenon of Morphotropic Tetragonal-Rhombohedral Phase Boundary in the Ferroelectric Ceramics," *Japanese Journal of Applied Physics*, vol. 17, p. 637, 1978.
- [172] K. P. Rema, V. K. Etacheri, and V. Kumar, "Influence of low trivalent iron doping on the electrical characteristics of PZT," *Journal of Materials Science: Materials in Electronics*, vol. 21, pp. 1149-1153, November 01 2010.
- [173] V. Sundar, N. Kim, C. A. Randall, R. Yimnirun, and R. E. Newnham, "The effect of doping and grain size on electrostriction in  $Pb(Zr_{0.52}Ti_{0.48})O_3$ ," in *ISAF '96. Proceedings of the Tenth IEEE International Symposium on Applications of Ferroelectrics*, 1996, pp. 935-938 vol.2.
- [174] B. M. Jin, J. Kim, and S. C. Kim, "Effects of grain size on the electrical properties of  $PbZr_{0.52}Ti_{0.48}O_3$  ceramics," *Applied Physics A*, vol. 65, pp. 53-56, July 01 1997.
- [175] F. Griggio and S. Trolier - McKinstry, "Grain size dependence of properties in lead nickel niobate-lead zirconate titanate films," *Journal of Applied Physics*, vol. 107, p. 024105, 2010.
- [176] M. Demartin and D. Damjanovic, "Dependence of the direct piezoelectric effect in coarse and fine grain barium titanate ceramics on dynamic and static pressure," *Applied Physics Letters*, vol. 68, pp. 3046-3048, 1996/05/20 1996.
- [177] D. Dragan and D. Marlyse, "Contribution of the irreversible displacement of domain walls to the piezoelectric effect in barium titanate and lead zirconate titanate ceramics," *Journal of Physics: Condensed Matter*, vol. 9, p. 4943, 1997.
- [178] D. M. Marincel, H. Zhang, A. Kumar, S. Jesse, S. V. Kalinin, W. M. Rainforth, *et al.*, "Influence of a Single Grain Boundary on Domain Wall Motion in Ferroelectrics," *Advanced Functional Materials*, vol. 24, pp. 1409-1417, 2014.

- [179] D. Berlincourt, "Piezoelectric ceramic compositional development," *The Journal of the Acoustical Society of America*, vol. 91, pp. 3034-3040, 1992.
- [180] R. S. Nasar, M. Cerqueira, E. Longo, J. A. Varela, and A. Beltran, "Experimental and theoretical study of the ferroelectric and piezoelectric behavior of strontium-doped PZT," *Journal of the European Ceramic Society*, vol. 22, pp. 209-218, 2002/02/01/ 2002.
- [181] Z. Q. Zhuang, M. J. Haun, S. Jang, and L. E. Cross, "Composition and temperature dependence of the dielectric, piezoelectric and elastic properties of pure PZT ceramics," *IEEE Transactions on Ultrasonics, Ferroelectrics, and Frequency Control*, vol. 36, pp. 413-416, 1989.
- [182] T. Fett and D. Munz, "Measurement of Young's moduli for lead zirconate titanate (PZT) ceramics," *ASTM Journal of Testing and Evaluation (USA)*, vol. 28, pp. 27-35.
- [183] CeramTec. (09/08/2018). *Lead Zirconate Titanate (PZT)*. Available: <https://www.ceramtec.com/competence/pzt-electro-ceramics/>
- [184] Mitutoyo. (2016). *Quick guide to surface roughness measurement*. 2229.
- [185] I. Inasaki, H. R. Meyer, F. Klocke, J. Shibata, G. Spur, H. K. Tonshoff, *et al.*, "4 - Grinding," in *Handbook of Ceramic Grinding & Polishing*, I. D. Marinescu, H. K. Tonshoff, and I. Inasaki, Eds., ed Norwich, NY: William Andrew Publishing, 1999, pp. 190-323.
- [186] OriginLab, "Algorithms (Distribution Fit)," in *Origin help*, ed, 2019.
- [187] NIST/SEMATECH. (2013). *e-Handbook of Statistical Methods*. Available: <http://www.itl.nist.gov/div898/handbook/>
- [188] T. Fett, D. Munz, and G. Thun, "Fracture toughness and R-curve behaviour of PZT," Forschungszentrum Karlsruhe GmbH1998.
- [189] T. Fett, D. Munz, and G. Thun, "Tensile and bending strength of piezoelectric ceramics," *Journal of Materials Science Letters*, vol. 18, pp. 1899-1902, 1999.
- [190] K. Zhang, F. W. Zeng, H. Wang, and H.-T. Lin, "Biaxial flexural strength of poled lead zirconate titanate under high electric field with extended field range," *Ceramics International*, vol. 39, pp. 2023-2030, 3// 2013.
- [191] H. Huang and P. Hing, "The relationship between the mechanical properties and microstructures of sintered PZT," *Journal of Materials Processing Technology*, vol. 89–90, pp. 538-543, 5/19/ 1999.
- [192] J. B. Quinn and G. D. Quinn, "A practical and systematic review of Weibull statistics for reporting strengths of dental materials," *Dental Materials*, vol. 26, pp. 135-147, 2010/02/01/ 2010.
- [193] W. D. Kingery, "Introduction to ceramics," H. K. Bowen and D. R. Uhlmann, Eds., 2nd ed. / W.D. Kingery, H.K. Bowen, D.R. Uhlmann. ed. New York, Chichester: Wiley-Interscience, 1976.
- [194] T. Fett, D. Munz, and G. Thun, "Nonsymmetric deformation behavior of several PZT ceramics," *Journal of Materials Science Letters*, vol. 18, pp. 1641-1643, October 01 1999.
- [195] A. d. Nádai, *Theory of flow and fracture of solids*. New York: McGraw-Hill, 1950.

- [196] T. Fett, D. Munz, and G. Thun, "Nonsymmetric Deformation Behavior of Lead Zirconate Titanate Determined in Bending Tests," *Journal of the American Ceramic Society*, vol. 81, pp. 269-272, 1998.
- [197] Y.-H. Seo, A. Benčan, J. Koruza, B. Malič, M. Kosec, and K. G. Webber, "Compositional Dependence of R-curve Behavior in Soft  $\text{Pb}(\text{Zr}_{1-x}\text{Ti}_x)\text{O}_3$  Ceramics," *Journal of the American Ceramic Society*, vol. 94, pp. 4419-4425, 2011.
- [198] R. W. Rice, "Relation of tensile strength-porosity effects in ceramics to porosity dependence of Young's modulus and fracture energy, porosity character and grain size," *Materials Science and Engineering: A*, vol. 112, pp. 215-224, 1989/06/01/ 1989.
- [199] R. W. Rice, S. W. Freiman, and P. F. Becher, "Grain - Size Dependence of Fracture Energy in Ceramics: I, Experiment," *Journal of the American Ceramic Society*, vol. 64, pp. 345-350, 1981.
- [200] Z. Zhang and R. Raj, "Influence of Grain Size on Ferroelastic Toughening and Piezoelectric Behavior of Lead Zirconate Titanate," *Journal of the American Ceramic Society*, vol. 78, pp. 3363-3368, 1995.
- [201] F. Meschke, A. Kolleck, and G. A. Schneider, "R-curve behaviour of  $\text{BaTiO}_3$  due to stress-induced ferroelastic domain switching," *Journal of the European Ceramic Society*, vol. 17, pp. 1143-1149, // 1997.
- [202] P. Zhang, S. X. Li, and Z. F. Zhang, "General relationship between strength and hardness," *Materials Science and Engineering: A*, vol. 529, pp. 62-73, 2011/11/25/ 2011.
- [203] R. Favaretto, D. Garcia, and J. A. Eiras, "Effects of  $\text{WO}_3$  on the microstructure and optical transmittance of PLZT ferroelectric ceramics," *Journal of the European Ceramic Society*, vol. 27, pp. 4037-4040, 2007/01/01/ 2007.
- [204] H. Kiyoshi, S. Masahiro, K. Toshihiko, and T. Kunisaburo, "Electrical and Mechanical Properties of  $\text{Pb}(\text{Zr},\text{Ti})\text{O}_3$  Ceramics Related to Mn Ion Diffusion," *Japanese Journal of Applied Physics*, vol. 32, p. 4227, 1993.
- [205] H. L. Zhang, J. F. Li, B. P. Zhang, and W. Jiang, "Enhanced mechanical properties in Ag-particle-dispersed PZT piezoelectric composites for actuator applications," *Materials Science and Engineering: A*, vol. 498, pp. 272-277, 2008/12/20/ 2008.
- [206] Y.-H. Seo, K. G. Webber, A. Benčan, J. Koruza, B. Malič, M. Kosec, *et al.*, "Deconvolving Ferroelastic and Phase Transformation Toughening in  $\text{Pb}(\text{Zr}_{1-x}\text{Ti}_x)\text{O}_3$  and  $\text{Pb}_{1-y}\text{La}_y(\text{Zr}_{1-x}\text{Ti}_x)\text{O}_3$ ," *Journal of the American Ceramic Society*, vol. 95, pp. 3713-3715, 2012.
- [207] J. L. Jones and M. Hoffman, "R-Curve and Stress–Strain Behavior of Ferroelastic Ceramics," *Journal of the American Ceramic Society*, vol. 89, pp. 3721-3727, 2006.
- [208] S. K. Nag and D. C. Agrawal, "Piezoelectric and mechanical properties of ceria-doped lead zirconate titanate ceramics," *Journal of Materials Science*, vol. 27, pp. 4125-4130, August 01 1992.